Investigations of New Methods of Synthesis, Phenomena and Novel Properties of Nanocarbons and Other Nanomaterials

A THESIS SUBMITTED FOR DEGREE OF

Doctor of Philosophy

By

Rakesh Voggu

Chemistry and Physics of Materials Unit
Jawaharlal Nehru Centre for Advanced Scientific Research
(A Deemed University)
Bangalore – 560 064

June 2010

అమ్మ, నాన్న...

Declaration

I hereby declare that the thesis entitled ***"Investigations of New Methods of Synthesis, Phenomena and Novel Properties of Nanocarbons and Other Nanomaterials"*** is an authentic record of research work carried out by me under the supervision of Prof. C. N. R. Rao, FRS, at the Chemistry and Physics of Materials Unit, Jawaharlal Nehru Centre for Advanced Scientific Research, Bangalore, India and that it has not been submitted elsewhere for the award of any degree or diploma.

In keeping with the general practice of reporting scientific observations, due acknowledgement has been made whenever the work described is based on the findings of other investigators. Any oversight due to error of judgement is regretted.

Rakesh Voggu

Certificate

I hereby certify that the matter embodied in this thesis entitled ***"Investigations of New Methods of Synthesis, Phenomena and Novel Properties of Nanocarbons and Other Nanomaterials"*** has been carried out by Mr. Rakesh Voggu at the Chemistry and Physics of Materials Unit, Jawaharlal Nehru Centre for Advanced Scientific Research, Bangalore, India under my supervision and it has not been submitted elsewhere for the award of any degree or diploma.

Prof. C. N. R. Rao

Acknowledgements

First and foremost, I would like to thank my research supervisor Prof. C. N. R. Rao, FRS without whom none of this would have been possible. I am indebted to him for taking me into his research group, and teaching me how to appreciate science, to perform research, to communicate ideas, and to have a vision for the future. Not only has he been an excellent teacher and mentor, but also a valuable moral support on the personal front. I am fortunate to know him as a great scientist and above all a very kind human being, who has taught me to always look at the bright side. The strong scientific foundation that he has given me will continue to guide and inspire me in my future career.

I would like to thank Mrs. Indumati Rao and Mr. Sanjay for their encouraging words and hospitality.

It has been a great pleasure working with Dr. A. Govindaraj. I am extremely grateful to him for teaching me the various aspects of experimental research.

I would like thank to all my collaborators, Prof. S. Chandrasekaran (IISc), Prof. Swapan K. Pati, Prof. N. Kumar (RRI), Dr. Subi J. George (NCU), Prof. K. S. Narayan.

I would like to thank P. Suguna (IISc), Dr. K. Biswas, Dr. C. S. Rout, B. Das, K. S. Subrahmanyam, N. Varghese, K. Venkata Rao, Sabyasachi, Dr. Ikram, Piyush and Santhosh for working with me on various problems.

I would like to thank all my past and present lab mates, Dr. Vivek, Leela, Subbu, Ramakrishna, Dr. Prabhakar Rao, Dr. Gomathi, Dr. Kalyani, Neenu, Barun, Dr. Chandu, Bhat, Dr. Claudy, Anupama,Urmi, Dr. Beheraji, Dr. Thiru, Dr. Gautam, Shireen, Jyoti, Kalyan, Basant, Sandeep, Dr. Latte, Dr. Prasanth, Dr. Sundarayya, Dr. Nagaraju, Dr Angshuman, Manjunatha, Bello, Rajasekharyya and Anirban for their constant cheerful company and help in various occasions.

I am extremely thankful to Prof. S. Chandrasekaran (IISc) for allowing me to work in his lab and providing me an opportunity to learn basic synthetic techniques during my first year of PhD. I would like to thank SCN lab members Suguna, Nazir, Siva Priya, Nilesh, Gundappa, Suresh,Gopinath for their help.

I thank Prof. A. Sundaresan, Mr. Pranab and Mr. Nitesh for magnetic measurements.

I am thankful to Usha Madam, Anil, Vasu, Selvi and Dr. Basavaraj (VEECO) for their help with the various characterization techniques.

I am thankful to the faculty members of JNCASR. In particular, I would like to thank Prof. G. U. Kulkarni, Prof. Swapan K. Pati, Prof. S. Balasubramanian , Prof. K. S. Narayan, Prof. A. Sundaresan, and Prof. M. Eswaramoorthy for their courses.

I am thankful to the past and present chairmen of CPMU for allowing me to utilize the various facilities in the center.

I would like to thank academic and administrative staff for their support, in particular senior administrative officer A.N. Jayachandra.

I thank Mrs. Shashi, Mrs. Sudha, Mrs. Aruna (ICMS), Mr. Gowda Mr. Victor and Mr. Xavier for their help. I thank Mr. Srinath and Mr. Srinivas for technical help. I thank Mr. Arokiyanathan, Mr. Narasimhamoorthy and Mr. Sunil for their help. I am thankful to all the library and computer lab staff for their help.

I express my deep gratitude to all the Professors of School of Chemistry, University of Hyderabad for their guidance and encouragements towards research life, in particular Prof. T. P. Radhakrishnan.

I thank my M. Sc friends Mitta, Srikanth, Srinivasa Reddy, Lakshmi Narayana, Prasanth, S. Ravi, Babavali, Malga, Ramakrishna, Dey, Kishore, Shinto, Nagaraju, Jaggu, Shiva, Prasad, Venkata Ram, Pavan for making my M.Sc days memorable.

Special thanks to friends and batchmates Krishna, Leela, Subbu, Sai, KKR, Venkat Rao, Barun, Bhat, Vivek, Kurra, Jayaram, Pandu, Sharma, Sandeep, Srinu, Anil, Migfar, Dinesh, Guru, Pranab, Shipra, Madhu, Toutam, Gomathi, Prabhakar Rao, Reji, Kalyani (JNC), Suresh anna, Sriman, Nazir, Sai (IISc)….

Finally, I wish to express my gratitude to my family members without their support and encouragement, this study would not have been possible.

The short, yet long endeavour of Ph.D. has been made possible because of the help, advice, suggestions and support provided by multiple hands. I have taken this opportunity to mention a few of them. However, my sincere thanks extend to everyone who has played a role in making this dream a reality.

Preface

This thesis consists of seven Chapters. Chapter 1 gives a brief overview of nanomaterials. Chapter 2 consists of two parts of which Part 1 describes efforts towards phase transfer of nanocrystals of gold and CdSe from aqueous or organic medium to a fluorous medium and solubilization of ZnO nanorods and carbon nanotubes in a fluorous medium. Part 2 deals with the one-step synthesis of fluorous-capped nanoparticles of metal chalcogenides such as CdSe, CdS, PbSe, ZnSe and of metal oxides such as γ-Fe_2O_3 and ZnO and of bimetallic FePt.

Chapter 3 describes the use of the Huisgen cycloaddition reaction to generate assemblies of metal (gold) and semiconductor (CdSe) nanoparticles as well as to covalently attached SWNT-gold and -CdSe nanoparticle composites. Connecting carbon nanotubes by click chemistry is also reported.

Investigations on the dependence of magnetic and optical properties of nanoparticles with interparticle distance are discussed in Chapter 4. Magnetic properties are examined with FePt nanoparticles while spectroscopic properties are examined in the case of CdSe nanoparticles.

Chapter 5 consists of two parts with Part 1 dealing with a spectroscopic study of charge-transfer interactions of electron-withdrawing (nitrobenzene, TCNQ and TCNE) and electron-donating (TTF and aniline) molecules with single-walled carbon nanotubes (SWNTs). In Part 2, the effect nanoparticles of metals such as gold and platinum on the electronic structure of SWNTs has been studied by Raman spectroscopy.

Chapter 6 consists of three parts. Part 1 describes the separation of metallic and semiconducting SWNTs based on molecular charge-transfer while Part 2 deals with a novel method for the synthesis of metallic SWNTs by an arc-discharge method. An arc-discharge method has also been employed to prepare Y-junction SWNTs (Part 3).

In Chapter 7, sensitivity of the electronic structure of graphene towards various electron-donor and –acceptor molecules has been studied by Raman and optical absorption spectroscopy as well as electrical resistivity measurements.

Contents

CHAPTER 1

Nanomaterials: A Brief Overview

1.1 Preamble

In December 1959, in his famous lecture “There's Plenty of Room at the Bottom" given at Caltech, Richard Feynman imagined the possibility to manufacture objects at the nanometer scale (1 nm = 10^{-9} m) by manipulating matter atom by atom (1). This revolutionary idea paved the way to envision systems designed and engineered at the ultimate length scale relevant to material science. Such systems have become a reality today and the efforts to understand, build and use them encompass what is called nanotechnology. Today, nanoscience and nanotechnology constitute very active and promising multidisciplinary research areas, bringing together scientists and engineers from several fields like physics, chemistry, materials science, electronics, biology and medicine. A strong focus is given to the understanding of the correlations between the structure of a material at the atomic level and its optical, chemical and electronic properties. But nanoscience and nanotechnology also aim at developing and improving techniques for manufacturing nanomaterials for new applications.

The Technical Committee (TC229) for nanotechnologies standardization of the International Organization for Standardization (ISO) defines nanotechnology that includes either or both of “understanding and control of matter and processes at the nanoscale, typically, but not exclusively, below 100 nanometers in one or more dimensions where the onset of size-dependent phenomena usually enables novel applications” or “utilizing the properties of nanoscale materials that differ from the

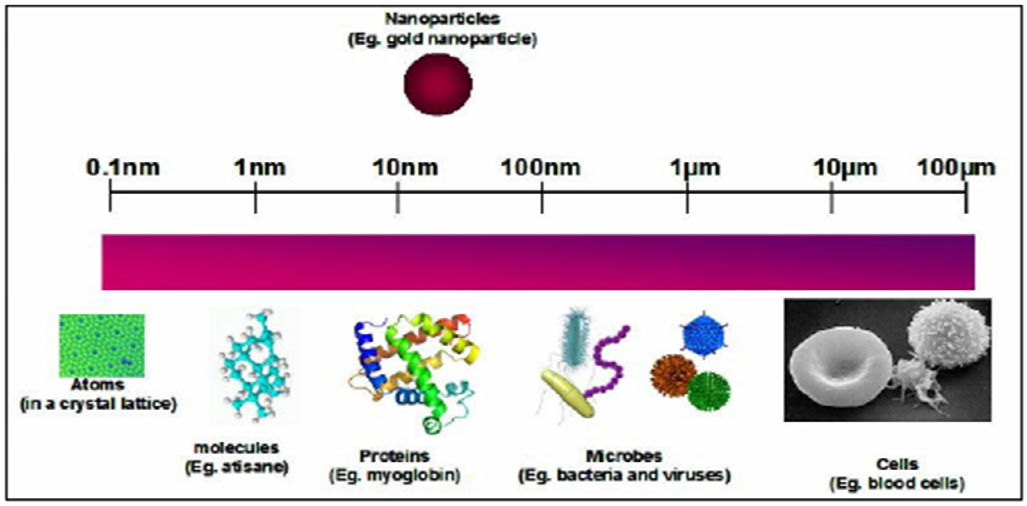

Figure 1.1: Nanoparticles in comparison with other biological entities.

properties of individual atoms, molecules, and bulk matter, to create improved materials, devices, and systems that exploit these new properties. Figure 1.1 shows nanoparticles (NPs) in comparison with other biological entities.

Nanomaterials include zero-dimensional (0D) nanocrystals, one-dimensional (1D) nanowires and nanotubes and two-dimensional (2D) nanofilms and nanowalls. Table 1.1 lists the typical nanomaterials of different dimensions (2).

Intensive studies of physiochemical properties of nanomaterials are carried out over the past decades have revealed a large number of unusual characteristics such as chemical, electrical, mechanical, optical, magnetic, optoelectronic and magneto-optical properties (3-5) of nanomaterials that are significantly different from those observed for bulk materials. These properties of nanomaterials are very useful in photo electronics (6, 7), catalysis (8), single electron transistor and light emitting diode (9), nonlinear optical devices (9). Magnetic nanoparticles are being used in memory storage devices (10), magnetic resonance image enhancement (11) and could probably be employed in interesting applications such as magnetic refrigeration (12). Other than these, nanomaterials have potential applications in synthesis of advanced materials, energy

Table 1.1: Examples of nanomaterials (From ref. 2).

	Size (approx.)	*Materials*
Nanocrystals and clusters (quantum dots)	Diam. 1-10 nm	Metals, semiconductors, magnetic materials
Other nanoparticles	Diam. 1-100 nm	Ceramic oxides
Nanowires	Diam. 1-100 nm	Metals, semiconductors, oxides, sulfides, nitrides
Nanotubes	Diam. 1-100 nm	Carbon, layered metal chalcogenides
Nanoporous solids	Pore diam. 0.5-10 nm	Zeolites, phosphates etc.
2-Dimensional arrays (of nanoparticles)	several nm^2-μm^2	Metals, semiconductors, magnetic materials
Surfaces and thin films	thickness 1-1000 nm	A variety of materials
3-Dimensional structures (superlattices)	Several nm in three dimensions	Metals, semiconductors, magnetic materials

storage devices (13), electronic and optical display, chemical and bio-sensors as well as bio-medical devices (2, 14). In this Chapter 1 gives a brief summary of current understanding on synthetic methodologies, phenomenon and properties associated with various nanomaterials such as metal, semiconductor, oxide and magnetic nanoparticles as well as carbon nanotubes and graphene.

1.2 Size Matters: Why Nanomaterials are Different

Gold is known as a shiny, yellow noble metal that does not tarnish, has a face centered cubic structure, is non-magnetic and melts at 1336 K. However, a small sample of the same gold is quite different, providing it is tiny enough: 10 nm particles absorb green light and thus appear red. The melting temperature decreases dramatically as the size goes down. Moreover, gold ceases to be noble, and 2–3 nm nanoparticles are excellent catalysts which also exhibit considerable magnetism. At this size they are still metallic, but smaller ones turn into insulators. Their equilibrium structure changes to icosahedral symmetry, or they are even hollow or planar, depending on size (15, 16). In another context, it is well known that diamond and graphite are different allotropic forms of carbon completely different, which have distinctly different structures,

bonding characteristics and therefore chemical and physical properties. The discovery of carbon wonder materials fullerene (C_{60}, C_{70} and others), carbon nanotubes which can be regarded as rolled-up graphite sheets of cylindrical shape with single or multiple layer walls and recent addition graphene, a single sheet of graphite, exhibiting amazing properties. The same is true with various metal, semiconductor and oxide nanoparticles. One important thing is that bonding in a small metal or semiconductor cluster is different from that in the bulk. Moreover, an atom at the smooth surface of a sizable single crystal is different from an atom at the surface of a small cluster of the same element. The properties of a surface atom of a small metal cluster depend on the type of support on which it sits or whether the cluster is doped with one or a few atoms of a different element.

Evidence for such effects has been available for long time, but only over the last one or two decades have the experimental methods become available which allow chemists to synthesize nanomaterials in a controlled and reproducible way and to investigate their properties by direct observation of individual clusters or by electrically contacting them using techniques like scanning tunneling or atomic force microscopy (14-16). The availability of size as a new parameter that permits the tuning of chemical properties has tremendously extended the potential of chemistry.

There are basically two types of size-dependent effects: smoothly scalable ones which are related to the fraction of atoms at the surface, and quantum effects which show discontinuous behavior due to completion of shells in systems with delocalized electrons (15-17).

1.2.1 Surface Effects

The surface of a sphere scales with the square of its radius r, but its volume scales with r^3. The total number of atoms N in sphere scales linearly with volume. The

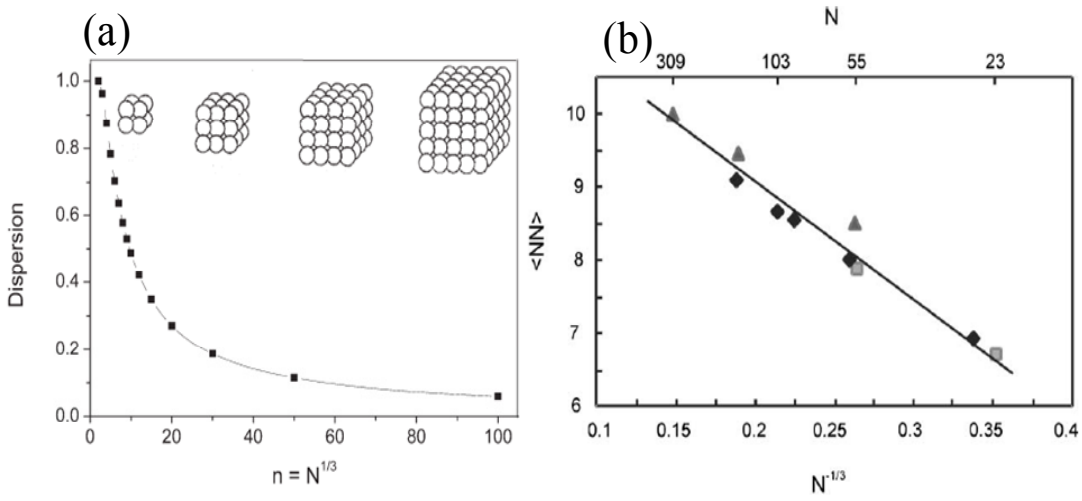

Figure 1.2: Evolution of the dispersion F as a function of n for cubic clusters up to n=100 ($N=10^6$). (b) Calculated mean coordination number <NN> as a function of inverse radius, represented by $N^{-1/3}$, for magnesium clusters of different symmetries (From ref. 15).

fraction of atoms at the surface is called dispersion F, and it scales with surface area divided by volume, i.e. with the inverse radius or diameter, and thus also with $N^{-1/3}$. Basically the same relation holds for long cylinders of radius r and for thin plates of thickness d. The size dependence of dispersion is illustrated in Figure 1.2 (a) for cubes of n atoms along an edge and a total of $N = n^3$ atoms, where the number of atoms at the surface is 6n corrected for double counts at the 12 edges and for reinstalling the 8 corners. For large N the edge and corner corrections become negligible, leading to the $N^{-1/3}$ scaling:

$$F = \frac{6n^2 - 12n + 8}{n^3} = \frac{6}{N^{1/3}}\left(1 - \frac{2}{N^{1/3}} + \frac{8}{6N^{2/3}}\right) \approx \frac{6}{N^{1/3}}$$

All properties which depend on the dispersion of a particle lead to a straight line when plotted against r^{-1}, d^{-1}, or $N^{-1/3}$.

Atoms at the surface have fewer direct neighbors than atoms in the bulk. Therefore, particles with a large fraction of atoms at the surface have a low mean coordination number (which is the number of nearest neighbors). In fact, the dispersion and the mean coordination number <NN> obey the same scaling law and are equivalent measures of

surface effects. The linearity of a plot of <NN> against $N^{-1/3}$ is shown in Figure 1.2 (b) for small clusters of Mg atoms in various packing symmetries (18). In the limit of infinitely large clusters the line extrapolates to <NN> = 12, the coordination number of close packed spheres in the bulk. Because of this lower coordination and unsatisfied bonds, surface atoms are less stabilized than bulk atoms. The smaller a particle, the larger the fraction of atoms at the surface, and the higher the average binding energy per atom. The surface-to-volume ratio scales with the inverse size, and therefore there are numerous properties which obey the same scaling law. Among them are the melting and other phase transition temperatures (19-21). Edge and corner atoms have an even lower coordination and bind foreign atoms and molecules more tightly. With fewer atoms a phase transition is less well defined, it is therefore no longer sharp. The Gibbs phase rule loses its meaning because phases and components are no longer properly distinguishable. Small clusters behave more like molecules than as bulk matter (19). The coordination number is also limited in narrow pores. The solubility of salts in pore confined water, the melting point and even the critical point of a fluid are therefore greatly reduced (22). There are numerous other concepts of thermodynamics which can break down, in particular when the system of interest consists of a single isolated cluster with a small number of atoms (23-26).

1.2.2 Quantum Effects

Atoms have their well known atomic orbitals. Depending on the extent of overlap in a solid they remain mostly unperturbed, as in noble gases, or they combine to extended band structures, as in metals or semiconductors. The core orbital's are confined to a relatively small volume and remain localized (atom-like). Each of N atoms contributes with its atomic states to a band so that, although the width of a band increases slightly when more atoms are added, the density of states (DOS) within a band is basically

proportional to the number of atoms of an ensemble with an extended band-like state. The band width amounts typically to a few eV. Thus, the DOS is on the order of N per eV, which is very large for a bulk amount of matter (N≅ Avogadro's number, N_A) but low for small clusters.

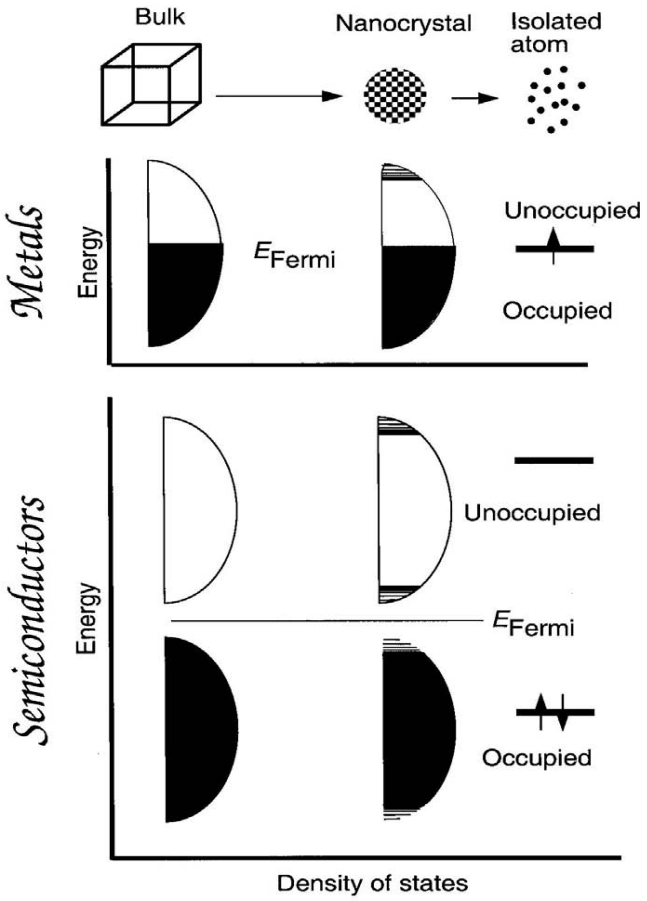

Figure 1.3: Schematic illustration of density of states (DOS) of metal and semiconductors nanocrystals (From ref. 2).

The DOS basically scales smoothly with size, but with a scaling law that is different from that found from surface effects. It is described to a first approximation by the " particle in a box" model in which the size of the box is given by the size of the particle. Discontinuities come in when the states are populated with electrons: for highly symmetric systems there are degenerate states, and when one of these is filled the next electron has to go into the next state of higher energy. Discontinuities come in when the

states are populated with electrons: for highly symmetric systems there are degenerate states, and when one of these is filled, the next electron has to go into the next state of higher energy. An important threshold is reached when the gap between the highest occupied and the lowest unoccupied state (called the Kubo gap δ) equals thermal energy (27). When electrons get thermally excited across the Kubo gap, a low temperature insulator becomes a semiconductor and at higher temperatures a metal; and also magnetic properties of small clusters can change dramatically. This non-metal-to-metal transition can take place within a single incompletely filled band, or when two bands begin to overlap because of band broadening. In case of semiconductors, a reduction in the size of the system causes the energy levels at the band edge to become discrete, with a inter level spacing similar to metals. This effectively increases the band gap of the semiconductor. Because of the quantized states of electrons and holes, these nanocrystallites are often called quantum dots, pseudo-atoms or superatoms. The schematic illustration of density of states in metal and semiconductor clusters are shown in Figure 1.3.

The density of states (DOS), ρ(E), of inorganic crystals simultaneously evolves from continuous levels into discrete states as the dimensionality is decreased from 3D to 0D as described by the relationship:

$$\rho(E) \approx E^{D/2-1}$$

(where, D = dimensionality; see in Figure 1.4) (28). For example, for a 3D bulk material, the DOS is proportional to the square route of the energy, E. For a system with confinement in one dimension (2D film or quantum well), the DOS is a step function. For systems with confinement in two dimension (a 1D system or quantum wire), the DOS has a peculiarity. For system with confinement in three dimension (0D materials or QDs), the DOS has a shape of δ-function. The DOS strongly influences the electronic

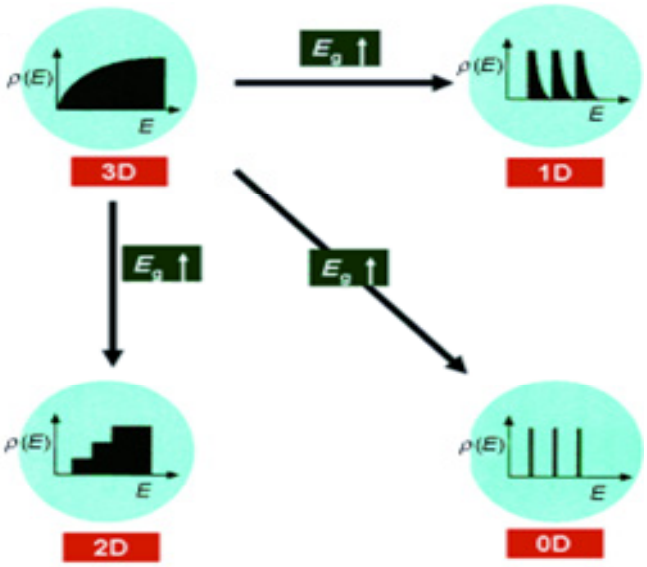

Figure 1.4: Density of states (DOS) of different dimensions (From ref. 28).

and optical properties of metal as well as semiconductors. The size dependence of the HOMO–LUMO band gap is best seen in the luminescence properties of semiconductor nanoparticles (3). Clusters may have to be regarded as pseudo-atoms, with the important difference that the cluster orbital momentum should be expected to be much larger than or atoms, because it scales with the square of the radius (29). It is quite likely that the orbital momentum has important implications for the magnetic character of the cluster (30, 31). Ionization potentials and electron affinities can be tuned between the atomic values and the work function of the bulk material by variation of the cluster size (18, 32). These same properties relate to the availability of electrons for forming bonds or getting involved in redox reactions. Therefore, the catalytic activity and the selectivity become functions of size (33-35).

1.3 Metal Nanoparticles:

Metal nanoparticles have been made since ancient history. One famous example is the fourth century Lycurgus cup, which features a curious optical property: in reflected

light it appears green, but in transmitted light it appears red (Figure 1.5 (a)) (*36*). Recent transmission electron microscopy (TEM) studies revealed metal nanoparticles embedded in the glass are responsible for the coloring (Figure 1.5 (b)) (*37*). The nanoparticle sizes range from 20 to 100 nm, and most are made of alloyed Au and Ag. Very few other dichronic Roman glasses exist, suggesting that the fabrication process was not well understood at the time. Although there are many other examples of Roman and medieval colored glass, these are due to metal compounds or oxides and not metal nanoparticles. It is now understood that the nanoparticles in the Lycurgus cup were formed by precipitation form the glass melt, as evidenced by the relatively high nonparticulate Ag content of the glass. The addition of Ag and Au to the glass mix may

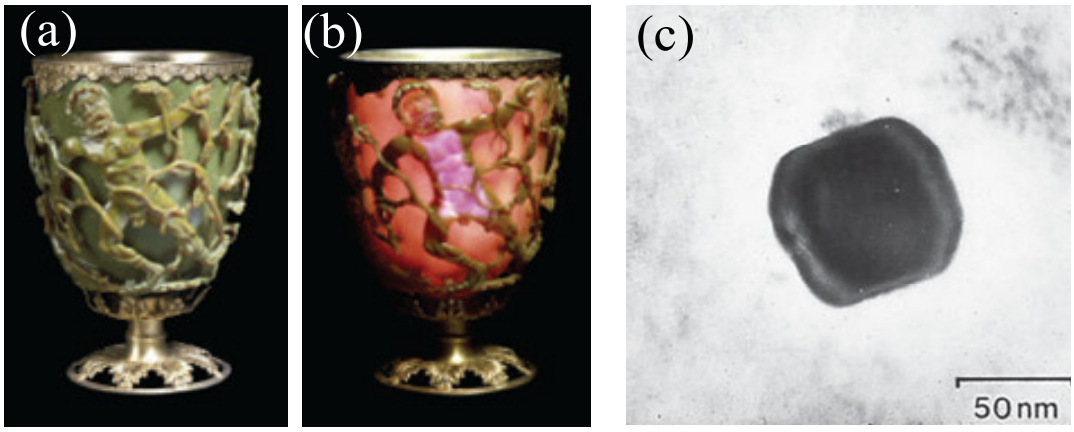

Figure 1.5: Photograph of Lycurgus cup (a) illuminated from the front (reflected light), and (b) from behind (transmitted light) (From ref. 36). (c) Transmission electron microscopy (TEM) image of a silver-gold alloy particle within the glass of the Lycurgus cup (From ref. 37).

have been accidental, or part of a more traditional coloring method. The technique does not seem to have outlasted the fourth century, and was not again rediscovered until the seventeenth century with the invention of ruby glass. Unlike the Lycurgus cup process, the ruby glass process was well understood and widely used, particularly in Victorian times. Another form of metal nanoparticle, colloidal Au solutions were known from around the fourth or fifth century B. C. (as 'potable gold'). Later uses included the coloring of ceramics and fabrics, for example the seventeenth century dye known as

purple of Cassius. However it was not until the nineteenth century that cause of the color of ruby glass and purple of Cassius was attributed to the size of the gold particles.

1.3.1 Synthesis

In recent decades research into metal nanoparticles has greatly intensified. This is largely due to the development of improved synthetic processes which enable precise control over nanoparticle size and shape, and therefore precise control over optical properties (*2, 14*). Additionally, metal nanoparticles can now be made in large quantities at low cost, therefore expanding the range of possible applications. Many synthetic process are available, ranging from the simple annealing of thin film to exotic methods such as fungus-mediated synthesis (*38*).

The most common method of synthesis of metal nanocrystals is the reduction of metal salts in the presence of suitable capping agents such as polyvinylpyrrolidone (PVP). Solvothermal and other reaction conditions are employed for the synthesis, to exercise control over their size and shape of the nanocrystals (*39*). The popular citrate route to colloidal Au, first described by Hauser and Lynn (*40*), involves the addition of chloroauric acid to a boiling solution of sodium citrate (*41, 42*). The average diameter of the nanocrystals can be varied over the 10–100 nm range by varying the concentration of reactants. Au nanocrystals with diameters between 1 and 2 nm are obtained by the reduction of $HAuCl_4$ with tetrakis(hydroxymethyl)-phosphonium chloride (THPC) which also acts as a capping agent (*43*). Following the early work of Brust and co-workers (*44*), the general practice employed to obtain organic-capped metal nanocrystals is to use a biphasic mixture of an organic solvent and the aqueous solution of the metal salt in the presence of a phase-transfer reagent. The metal ion is transferred across the organic-water interface by the phase transfer reagent and subsequently reduced to yield sols of metal nanocrystals. Metal

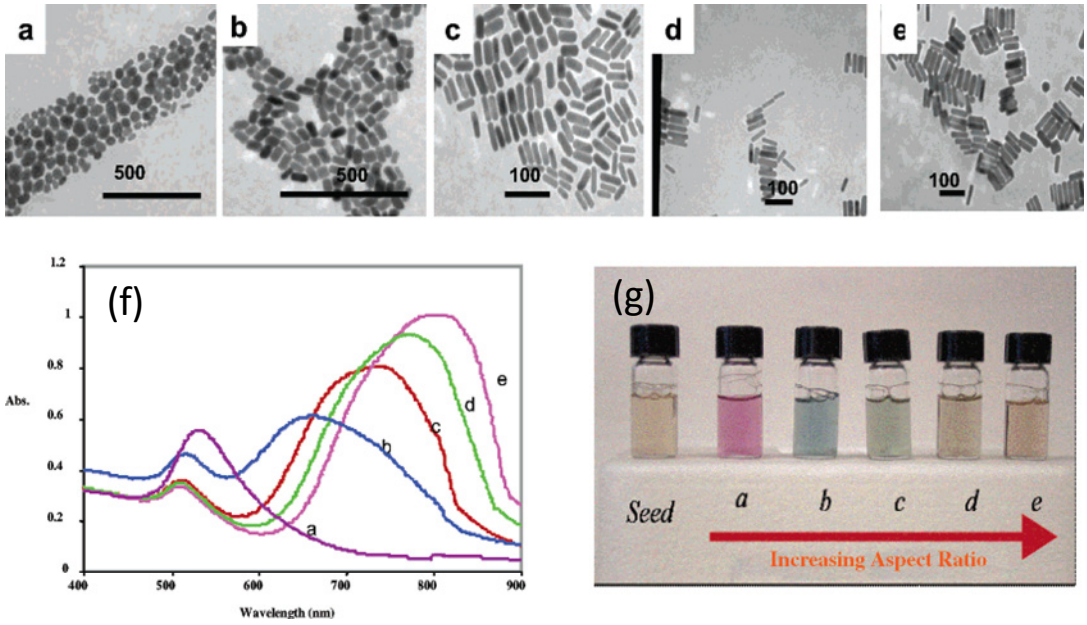

Figure 1.6: Transmission electron micrographs (a-e), optical spectra (f), and photographs of (g) aqueous solutions of gold nanorods of various aspect ratios. Seed sample: aspect ratio 1; sample a, aspect ratio 1.35 (0.32; sample b, aspect ratio 1.95 (0.34; sample c, aspect ratio 3.06 (0.28; sample d, aspect ratio 3.50 (0.29; sample e, aspect ratio 4.42 (0.23. Scale bars: 500 nm for a and b, 100 nm for c, d, e (From ref. 56).

nanocrystals in the aqueous phase can also be transferred to a nonaqueous medium by using alkanethiols to obtain organosols (*45, 46*). This method has been used to thiolize Pd nanocrystals with magic numbers of atoms (*47, 48*). A method to produce gold nanocrystals free from surfactants would be to reduce $HAuCl_4$ by sodium napthalenide in diglyme (*49*). Ag nanocrystals have been prepared in nanoscale by using dimethylformamide as both a stabilizing agent and a capping agent (*50*). Au and Ag are the most commonly studied metals for chemical synthesis, but nanoparticles of a wide range of other metals can also be synthesized, often by using analogous methods. By using tetrabutylammonium borohydride or its mixture with hydrazine, Jana and Peng (*51*) obtained monodisperse nanocrystals of Au, Cu, Ag, and Pt. Nanoparticles of Rh and Ir have been prepared by the reduction of the appropriate compounds in the ionic liquid, 1-n-butyl-3-methylimidazolium-hexafluorophosphate, in the presence of hydrogen (*52*). Synthesis and

functionalization of gold nanoparticles in ionic liquids is also reported, wherein the colour of the gold nanoparticles can be tuned by changing the anion of ionic liquid (*53*). The synthetic aspects of magnetic metallic nanoparticles will be discussed later in this chapter.

Shape-controlled synthesis has received widespread interest due to the importance of anisotropic nanoparticles in their structural, optical, electronic, magnetic, and catalytic properties, as well as their potential applications (*39, 54, 55*). By suitable choice of experimental conditions and additives, non-spherical shape of nanoparticles such as rods, wires, tubes and concentric core-shell structures have been successfully synthesized and they are found to possess properties which depend not only on the size but also on other topological aspects. Gold nanorods have drawn the most attention because they can be synthesized using a relatively simple process such as wet chemical methods and the rational control over the aspect ratio is possible (Figure 1.6) (*56*). To date, the main methods to synthesize gold nanorods include porous aluminum template methods (*57*), electrochemical methods (*58*), photochemical methods (*59*), and the seed-mediated growth method (*60*). Of all these methods, the seed-mediated growth method is especially appealing and widely adopted because it is very simple and flexible in fabricating different aspect ratios of gold nanorods and keeping a relatively high yield. Generally, the seed-mediated growth method includes two steps: synthesis of seeds and the growth of seeds. The former is done by using a strong reducing agent to reduce a metal salt solution in aqueous medium so as to get a certain size of spherical gold nanoparticles, which are defined as gold seeds. After the gold seeds are formed, the next step is to add them into the surfactant, which acts as a soft template to direct seed growth. During the growth, another weak reducing agent is necessary to guarantee the reduction of gold salt. To get a high yield of tailored gold nanorods by this method,

several parameters such as the seeds themselves (size and aging time), use of $AgNO_3$, use of cetyltrimethylammonium bromide (CTAB), pH, temperature, among others must be carefully considered before preparation because the formation mechanism of gold nanorods is very complicated; a slight variation will affect the size and shape of the gold nanorods (*61*).

1.3.2 Optical Properties:

Small metal particles exhibit complex optical and physical properties. Their small sizes (< 100 nm) cause strong confinement of the electrons, giving rise to fascinating effects not observed in the bulk material. The most striking phenomenon encountered in metal nanoparticles is electromagnetic resonances due to the collective oscillation of the conduction electrons. The excitation of localized surface plasmons on metal nanoparticles can be qualitatively understood by considering the particle as a simple oscillator. An external electric field is able to displace the free electrons in a metal nanoparticle with respect to the fixed ionic core. This displacement sets up a restoring force, leading to coherent, resonant oscillation of charge density (Figure 1.7) (*62*). These localized surface plasmon resonances (SPR) induce a strong interaction with light, and the wavelength at which this resonance occurs depends on the local environment, shape, size and orientation of the particle (*63, 64*). This section describes the optical properties of metal nanoparticles in particular gold nanoparticles and nanorods.

Absorption by small metal sphere: We are concerned with solutions containing small nanocrystals. These particles do not sediment and the solution is optically and spatially homogeneous. In a dilute colloidal solution containing *N* particles per unit

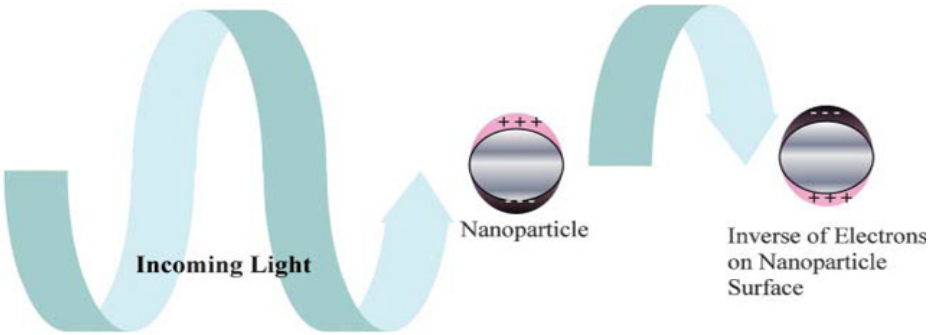

Figure 1.7: Origin of surface plasmon resonance due to coherent interaction of the electrons in the conduction band with light (From ref. 62).

volume, the measured attenuation of light of intensity I_0, over a path length x cm in a spectrophotometer is given in differential form as:

$$\frac{dI(x)}{dx} = -NC_{ext}\ I(x) \tag{1.1}$$

Which shows that the rate of loss of photons is proportional to the light intensity at distance x into the medium, and also to the number density of light extinguishing particles. Integration gives the solution absorbance:

$$A = \log_{10}\frac{I_0}{I(x)} = \frac{NC_{ext}\,x}{2.303} \tag{1.2}$$

where C_{ext} is the extinction cross-section of a single particle. For spherical particles with a wavelength-dependent dielectric function $\varepsilon(\lambda) = \varepsilon'(\lambda) + i\varepsilon''(\lambda)$, embedded in a medium of dielectric function ε_{m}, C_{ext} is given by (*65*) :

$$C_{ext} = \frac{2\pi}{k^2}\sum_{n=1}^{n=\infty}(2n+1)Re|\{a_n + b_n\}| \tag{1.3}$$

Where $$k = 2\pi\frac{\sqrt{\varepsilon_m}}{\lambda} \tag{1.4}$$

and a_n and b_n are the scattering coefficients, which are functions of the particle radius and λ in terms of Ricatti–Bessel functions. The extinction cross-section of a particle is often normalized to give the extinction cross-section per unit area:

$$Q_{ext} = \frac{C_{ext}}{\pi R^2} \tag{1.5}$$

Conventionally, chemists measure the extinction coefficient of a solution in units of M^{-1} cm^{-1}, where the concentration is the molar metal atom concentration. For particles of radius R (cm), this quantity is related to Q_{ext} by:

$$\mathcal{E}(M^{-1}cm^{-1}) = \frac{3\times10^{-3}V_m Q_{ext}}{(4\times2.303R)} \tag{1.6}$$

where V_m (cm^3 mol^{-1}) is the molar volume of the metal. Bohren and Huffman provide various approximations that may be used instead of the full series expansion (*65*). In particular, for very small particles where kR«1, only the first few terms are important in these equations.

$$a1 = -\frac{i2x^3}{3}\frac{m^2-1}{m^2+2} - \frac{i2x^5}{5}\frac{(m^2-2)(m^2-1)}{(m^2+2)^2} + \frac{i4x^6}{9}\left[\frac{m^2-1}{m^2+2}\right]^2 + O(x^7) \tag{1.7}$$

$$a2 = -\frac{i2x^5}{15}\frac{m^2-1}{2m^2+2} + O(x^7) \tag{1.8}$$

$$b1 = -\frac{ix^5}{45}(m^2-1) + O(x^7) \tag{1.9}$$

$$b1 = O(x^7) \tag{1.10}$$

Here m is the refractive index of the material relative to the medium, i.e., $m = n/n_{med}$ and $x = kR = 2\pi n_{med}R/\lambda$. If we retain just the first term in a_1, then Eq. (1.3) becomes:

$$C_{ext} = \frac{24\pi^2R^3\mathcal{E}_m^{3/2}}{\lambda}\frac{\mathcal{E}''}{(\mathcal{E}' + 2\mathcal{E}_m)^2 + \mathcal{E}''^2} \tag{1.11}$$

This equation can also be obtained by purely electrostatic arguments, and a succinct derivation is given elsewhere (*66*). The C_{ext} scales as R^3, while the number density decreases as R^3 for a given amount of colloidal material. Hence, the molar absorption coefficient is independent of particle size. This is borne out for particles in the range up to about 30 nm, where scattering begins to be significant. For very small particles, <5–10 nm in diameter, the material properties themselves change, and this results in changes to the dielectric function, $\varepsilon(\lambda)$, and hence to the colloid optical properties. An interesting feature of Eq. (1.11) is that there is no absorption if $\varepsilon'' = 0$ but there is also

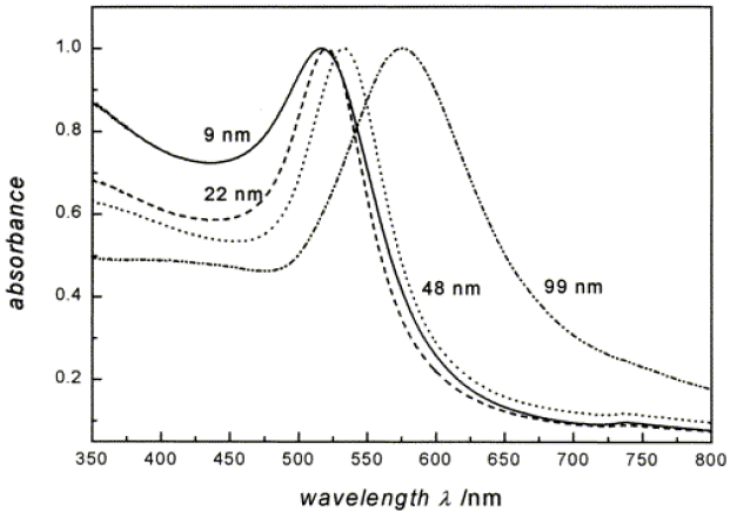

Figure 1.8: Optical absorption spectra of Au nanospheres of different size ranging from 9-99 nm (From ref. 68).

no absorption if $\varepsilon''=\infty$. In the first case, the particle is simply non-absorbing, while in the second case, it reflects all incident radiation.

Mie was able to explain some of the anomalous and striking colors exhibited by small metal particles, particularly those of gold or silver (*67*). In these measurements, it is assumed that the refractive index and absorption coefficient of the dispersed particles are known. The reason that metals exhibit such strong optical effects is due to the dynamic response of the electrons. The dielectric function is related to the complex refractive index, n, through $\varepsilon(\lambda)=(n + ik)^2$. For metals, the dielectric function typically takes the form:

$$\mathcal{E}'(\lambda) = \mathcal{E}(\lambda) - \frac{\lambda^2}{\lambda_p^2} \tag{1.12a}$$

$$\mathcal{E}''(\lambda) = \frac{\lambda(\lambda^2 + \lambda_d^2)}{\lambda_p^2 \lambda_d} \tag{1.12b}$$

The first term in Eq. (1.12a) is the short wavelength dielectric constant, which considers all UV absorption bands.

$$\lambda_p = \frac{2\pi c}{\omega_p} = \sqrt{\frac{4\pi^2 c^2 m \mathcal{E}_0}{Ne^2}} \tag{1.13}$$

The plasma wavelength, λ_p, is characteristic for each metal, and is a function of only the electron density, N, and the effective mass of electrons, m, in the material. λ_d is the damping constant of the conduction electrons. Surface plasmon absorption due to the confined excitation of conduction electrons in small particles occurs because the dielectric function $\varepsilon(\lambda)$ can take negative values, leading to poles in the value of a_1. The position of the surface plasmon absorption band of small gold spheres is given to a good approximation by the condition:

$$\mathcal{E}1 = -2\mathcal{E}_m \tag{1.14}$$

Here, $\varepsilon_m = n^2_{med}$ is the dielectric function of the (nonabsorbing) solvent, and ε_1 is the real part of the dielectric function of the metal at that energy or wavelength. Previous work suggests that the dielectric data obtained from reflectivity measurements on bulk metal may be in error by about 1–3%. Figure 1.8 shows the optical absorption spectra of Au nanospheres of different size ranging from 9-99 nm (*68*).

Absorption by small metal ellipsoids: In 1912, Gans predicted (*69*) that for very small ellipsoids, where the dipole approximation holds, the surface plasmon mode would split into two distinct modes. This is a consequence of the surface curvature, which determines classically the restoring force or depolarization field that acts on the confined conduction electron population. He quantified the response as a function of the ellipsoid aspect ratio. The electron microscopy reveals that most nanorods are more like cylinders or sphero-capped cylinders than ellipsoids. However, an analytical solution for such shapes is not possible. Solutions have been found for the case of an infinite cylinder and for oblate and prolate ellipsoids. In explaining the optical properties of these small rods, it has been common to treat them as ellipsoids (*61, 70*), which allows the Gans formula to be applied. The polarizability of an ellipsoid is given by:

$$\alpha_{x,y,z} = \frac{4\pi abc(\mathcal{E}_{Au} - \mathcal{E}_m)}{3\mathcal{E}_m + 3L_{x,y,z}(\mathcal{E}_{Au} - \mathcal{E}_m)} \tag{1.15}$$

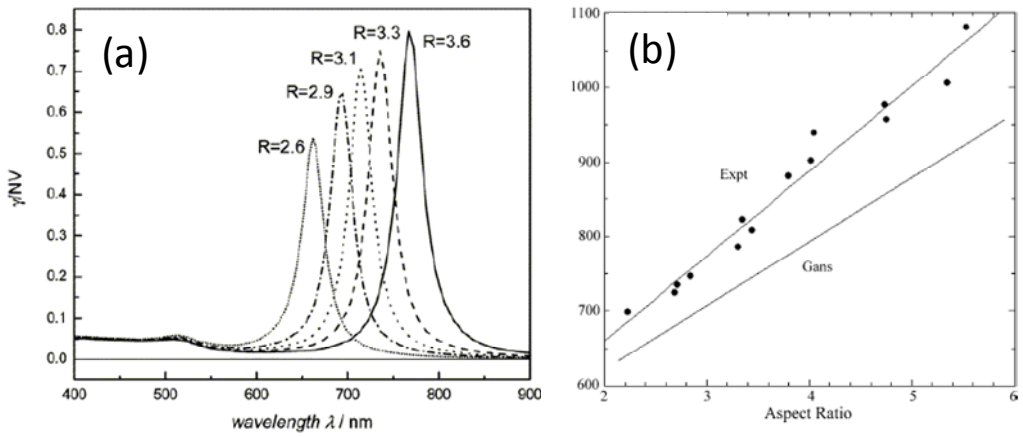

Figure 1.9: (a) Simulated spectra of the long-axis SPR mode for gold nanorods of different aspect ratio, showing the shape tunability of the optical resonance in the visible-near infrared region. (b) Experimental plot of the surface plasmon longitudinal band position vs. aspect ratio for pure gold rods in water. (From ref. 71).

Here a, b and c refer to the length of the ellipse along the x, y and z axes ($a > b = c$), ε_{Au} the dielectric function of Au, ε_m the dielectric constant of the medium at optical frequencies and $L_{x,y,z}$ is the depolarization factor for the respective axis, which is given by:

$$L_x = \frac{1-e^2}{e^2}\left(-1+\frac{1}{2e}\ln\frac{1+e}{1-e}\right); \quad L_{y,z} = \frac{(1-L_x)}{2} \tag{1.16}$$

here, e is the rod ellipticity given by $e^2 = 1-(b/a)^2$. For a sphere $e = 0$ and $L = 1/3$. The polarizability is related directly to the extinction of light by $C_{ext} = kI(\alpha)$.

In the vast majority of the studies Gans' theory has successfully explained the qualitative optical properties of gold nanorods.

The effect of aspect ratio. Gan's equation predicts how the plasmon mode peak position varies with aspect ratio for small ellipsoids embedded in the same medium. The easiest way to visualize this is to plot the depolarization factor L in Eq. (1.16) versus the value of the dielectric function at the peak.

A common observation from combining electron microscopy sizing of Au nanocrystals with spectral measurements is an almost linear correlation between peak position and aspect ratio (Figure 1.9) (*71*). Small changes in aspect ratio lead to drastic changes in transmitted colors. The fact that the plasmon band appears to be drastically red-shifted from the positions predicted by the Gans model, yet still displays the linearity expected from Eqs. (1.15) and (1.16), led El-Sayed and co-workers to propose (*72*) that the water layers around the rods were polarized and had a substantially higher refractive index than water. In addition to the aspect ratio, optical properties of gold nanorods depends on refractive index of the solvent, the effect of dielectric shell layer and the polarization of the excited light.

1.4 Semiconductor Nanoparticles:

Semiconductor Nanoparticles has been under the researcher's constant scrutiny since the 1980's due to the sensitivity of their optical spectra to size and shape. Semiconductor nanocrystals are usually referred to quantum dots, whose charge carriers, i.e. their wave functions, are confined in all three spatial directions, so their energy becomes quantized (*73*). The confinement can be based on electrostatic potentials (generated by external electrodes, doping, strain, impurities), the presence of an interface between different semiconducting materials (e.g. in core shell systems), the presence of the semiconductor surface (e.g. of nanocrystals in an amorphous matrix), or a combination of these. By adjusting the shape, size, and confinement potential of quantum dots one is able to tailor their electronic as well as their optoelectronic properties (*73*). In electronic applications they have been proven to operate like a single-electron transistor and show the Coulomb blockade effect. Furthermore, quantum dots have been suggested as implementations of qubits for quantum information processing. Other semiconducting nanostructures besides quantum dots are quantum wires (e.g.

carbon nanotubes), which confine the charge carriers in two spatial directions and allow free propagation in the third (*74*) and quantum wells, which confine the charge carriers in one direction and allow free propagation in two directions (*75*). Most of the studies of semiconductor NPs are of interdisciplinary character and are devoted to investigation of their colloidal solutions. To date, NPs of II-VI and III-V groups like CdSe, CdS, ZnSe, ZnS and InAs and number of other semiconductors such as ZnO, SiO_2, MoS_2, GaP, GaN, PbI_2, have been synthesized and investigated their properties and applications.

1.4.1 Synthesis:

Since the first application of the pyrolysis method to the synthesis of of CdSe NPs in the early nineties by Murray et al. (*76*), there has been significant amount of work improving and modifying the NP synthesis. NPs of CdSe, CdTe, CdS, PbS, PbSe, PbTe, ZnS, ZnSe, InAs and InP are all routinely made as are core/shell combination such as CdSe/ZnS and CdTe/CdSe (*77, 78*). In another method nanocrystals of metal chalcogenides are generally prepared by the reaction of metal salts with an appropriate sulfiding or seleniding agent under solvothermal or thermolysis conditions. Thus, toluene-soluble CdSe nanocrystals with a diameter of 3 nm have been prepared solvothermally by reacting cadmium stearate with elemental Se in toluene in the presence of tetralin (*79*). Decomposition of single molecular precursors provides convenient and effective routes for the synthesis of metal chalcogenide nanocrystals (*80, 81*). In addition, metal chalcogenides of different shapes and composition have been created such as CdTe and CdSe tetrapods (*82*), CdSe/CdTe nanobarbells (*83*), PbTe cubes and even CdSe hyperbranched structures (*84*).

Metal oxide NPs are mainly prepared by the solvothermal decomposition of organometallic precursors. ZnO NPs have been synthesized from the cupferron complex by a solvothermal route in toluene solution treatment of metal acetylacetonates under

solvothermal conditions produces NPs of metal oxides such as Ga_2O_3, ZnO and cubic In_2O_3 (*85*). It has been found that reactions of alcohols such as ethanol and t-butanol with Zn powder readily yield ZnO NPs (*86*).

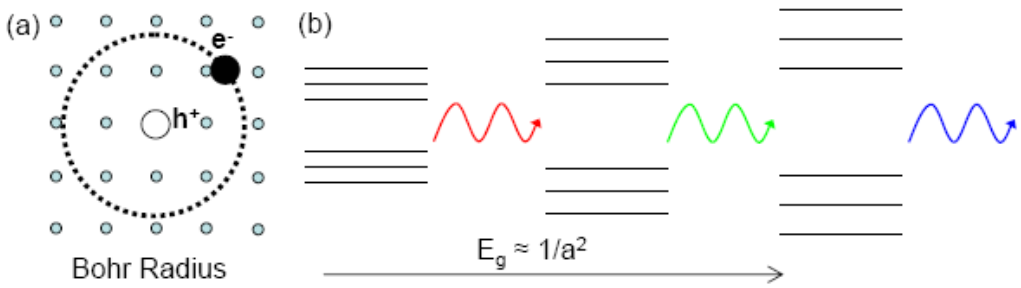

Figure 1.10: (a) Bohr radius of an exciton and (b) the effect of quantum confinement on the band structure and emission of a nanocrystals.

1.4.2 Optical Properties:

When a semiconductor absorbs light, the energy of the photon is used to promote an electron to the conduction band and a hole is left behind in the valence band. This electron-hole pair is termed as an exciton, and it is bound through a coulomb attraction of the negatively charged electron to the positively charged hole. The distance between the electron and hole of the exciton in the semiconductor lattice termed the exciton Bohr radius (Figure 1.10), similar in concept to the Bohr radius of an electron orbiting the nucleus in an atom. When the dimensions of a semiconductor become smaller than the exciton Bohr radius, the exciton is physically confined. The physical confinement of the exciton results in changes in the energetic spectrum of the semiconductor (*87, 88*). As the size of the semiconductor becomes smaller, the energy gap between the conduction and valence bands increases. In general, the relationship between band gap energy and particle size goes roughly like that of a particle in a box, $E_g \sim 1/a^2$, where a is the radius of the particles. The physical confinement also results in quantization of the continuous energy levels of the conduction and valence bands. The quantization of the energy bands is one reason NPs are often called 'artificial atom'. The absorption spectrum of a

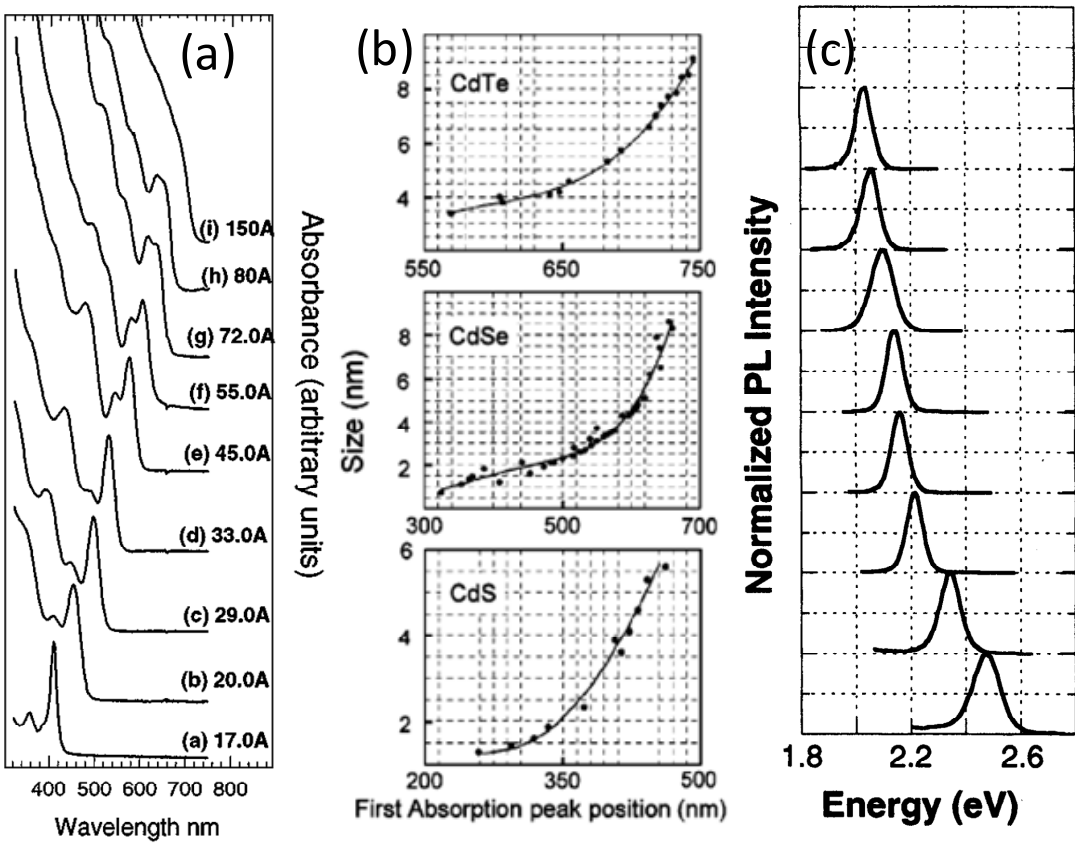

Figure 1.11: (a) Optical absorption spectra for a series of sizes of monodisperse CdSe nanocrystals. (From ref. 89). (b) First absorption peak change vs. the size of nanocrystals of CdS, CdSe and CdTe. (From ref. 97). (c) PL spectra of different size of CdSe nanocrystals. (From ref. 98).

NPs exhibits the effects of quantization as it contains the features resulting from the transitions between the quantized states (Figure 1.11 (a)) (*89*).

While the blue shift of the band gap energy and quantization of energy levels are general effect of confinement, the exact energy level spacing and optical effects are specific to a semiconductor material. The emission and absorption properties depend on other factors such as the Bohr radius of the given semiconductor, the effective masses of the electron and hole, and the shape of the nanoparticle. In CdSe, the effective mass of the hole is six times that of the electron (*90*) which results in closer spacing between the quantized states of the valence band than the conduction band. In PbSe, the electron and hole effective masses are equal (*90*) and the quantized energy levels in the conduction and valence bands are spaced equally. In addition, the sensitivity of the band gap energy

blue shift to NP size which is materials dependent. The emission from monodisperse semiconductor nanocrystals such as CdSe is intense, narrow and can be brought about by excitation in a broad range of wavelengths (Figure 1.11 (c)). The Bohr radius in CdSe is ~ 6 nm and so by tuning the NP diameter from 1.2-11.5 nm, the emission can be experimentally varied from 410 nm – 670 nm. In PbSe the Bohr radius is 23 nm and the emission can be experimentally tuned from 1.1 μm (2.6 nm) to 2.2 μm (9.5 nm) (*90*). Finally, NP shape can also affect the optical properties. When CdSe nanorods (NRs) grow longer than 12 nm they are no longer confined in one of the dimension. Absorption is dominated by radial confinement along the diameter of the NR and so the absorbance spectrum remains the same despite change to the rod length (*91*). 1D confinement does effect exciton fine structure and results in linearly polarized emission from the NRs (*92*). For CdSe tetrapods, the features in the absorption spectrum also depend only on the diameter of the NP core and not the length of the arms (*82*). The quantum confinement in semiconductor NPs results in the changes in the absorption and emission characteristics of semiconductor. However, the results of confinement are extremely material dependent allowing for the creation of particles with new and interesting optical and electrical properties.

The quantitative dependence of the minimum electronic excitation energy of a nanoparticle on its size can be approximately calculated taking into account the relation between the uncertainty in the position (Δx) and the uncertainty in the momentum (Δp) of the exciton in a macroscopic crystal and in a nanoparticle:

$$\Delta p \Delta x \geq \frac{\hbar}{2} \tag{1.17}$$

The delocalized exciton has no fixed position in the periodic potential of the macroscopic crystal, whereas its energy (E) and momentum ($p=\hbar k$) are strictly fixed, and at small k,

$$E = \frac{\hbar^2 k^2}{2\mu}, \tag{1.18}$$

where μ is the effective mass of the exciton (*93*). For a nanoparticle, the uncertainty in the position of the exciton depends on the characteristic size of the nanoparticle Δx=d.

Assuming that the relation between the energy and momentum is independent of the particle size, the exciton energy will change in inverse proportion to the square of the characteristic size of the nanoparticle.

A more rigorous analysis of the effect of the size on the energy of excitonic excitation of spherical nanoparticles (E_n) gives the following relationship:

$$E_n=E_m+E_l\ , \tag{1.19}$$

where E_m is the energy of the interband transition in a macroscopic semiconductor, E_l is the energy of exciton localization in the nanoparticle:

$$E_1 = \frac{h^2 n^2}{8R^2\mu} - \frac{1.78e^2}{\mathcal{E}R} - 0.248E_R^* \tag{1.20}$$

where n is an integer, R is the radius of the nanoparticle, $\mu = (m_e^{-1} + m_h^{-1})^{-1}$ (m_e and m_h are the electron and hole effective mass, respectively), $\mathcal{E}$ is the dielectric constant of the semiconductor, and E_R^* is the effective Rydberg energy (*94, 95*). The first term on the right of the equation is predominant, and its nature was considered above, the second term takes into account the Coulomb interaction between the electron and hole inside the nanoparticle, and the third term is responsible for the spatial correlation. The n values larger than 1 in Eq. (1.20) correspond to the exciton transitions to higher excited states. In the case of anisotropic semiconductors, the electron and hole effective masses depend on the direction of motion and Eq. (1.20) becomes more complex with allowance for this anisotropy (*96*).

$$E_{n_x,n_y,n_z} = \frac{h^2}{8}\left(\frac{n_x^2}{\mu_x L_x^2} + \frac{n_y^2}{\mu_y L_y^2} + \frac{n_z^2}{\mu_z L_z^2}\right) - \frac{1.78e^2}{\varepsilon R} - 0.248E_R^* \quad (1.21)$$

where n_x, n_y, and n_z are integers; m_x, m_y, and m_z are the effective masses of the exciton along the corresponding directions, and L_x, L_y, and L_z are the dimensions of the nanoparticle.

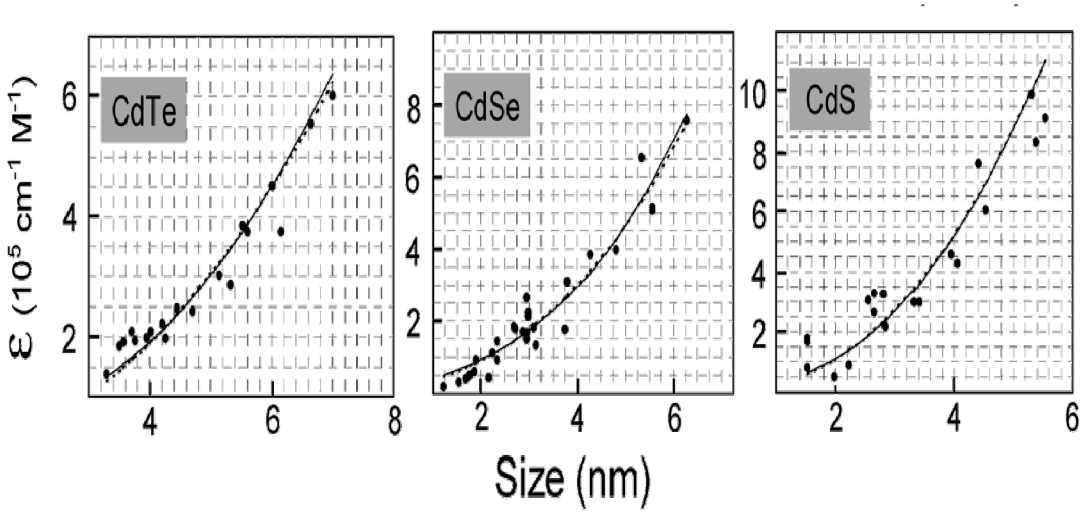

Figure 1.12: Extinction coefficient × 10^5 cm^{-1} M^{-1} of particles at the first absorption peak position curves for CdTe, CdSe, and CdS nanocrystals as a function of size (From ref. 97).

Optical absorption spectroscopy is used extensively for the characterization of the semiconductor nanoparticles, since they exhibit strong and unique absorption in the visible region. Optical absorption spectroscopy is highly sensitive to dimension, morphology and surface modification of the nanoparticles. A distinct red shift is observed with increase in the size of the particles and features of the exciton peak vary with the morphology and the surface modification of the nanoparticles. The first exciton peak also can be used to calculate the energy difference between the highest occupied molecular orbital (HOMO) and the lowest unoccupied molecular orbital (LUMO). This energy difference is referred to as band gap. The concentration of the CdSe nanoparticles was calculated by using the classic Beer-Lamberts law.

$$A = \xi bC \quad (1.22)$$

Where A is absorbance with no units, ξ is molar extinction coefficient in liter mol^{-1} cm^{-1}, b is the path length in cm and C is concentration in mol $litre^{-1}$.

However, the extinction coefficient of nanoparticles were found to vary with the size of the nanoparticles. Peng et al. (*97*) experimentally determined the extinction coefficients of cadmium chalcogenides, using the wavelength at which the first exciton peak occurred (Figure 1.12).

Recombination of light-generated charges results in luminescence of nanoparticles (*98*). In this case, the blue shift is also observed as the nanoparticle size decreases. The luminescence of ZnO (*99, 100*), ZnS (*101*), CdS (*102*) and CdSe (*103*) has been studied in detail. The luminescence spectra of colloidal CdSe solutions are shown in Figure 1.11 (c). It can be seen that the decrease in the nanoparticle size results in a shift of the luminescence spectra towards the short-wavelength region. The kinetics of the luminescence decay of nanoparticles is nonexponential and the characteristic time of decay for nanoparticles of the same size depends on the luminescence wavelength. The shorter-lived luminescence corresponds to a higher energy of the emitted light quantum. The dependence of the lifetime of the excited state on the wavelength is explained by the contribution of the Coulomb interaction between the electron and hole to the energy of the emitted light quantum (*104*):

$$h\upsilon = E - (D_+ - D_-) + \frac{e^2}{\varepsilon R_h} \qquad (1.23)$$

where E is the minimum excitation energy of nanoparticles, D_- and D_+ are the depths of the electron and hole traps, respectively, and R_h is the distance between the electron and hole. If the electron - hole recombination follows the tunnel mechanism, then the pairs with small R_h emit light faster and at higher energies than the pairs with larger R_h.

1.5 Magnetic Nanoparticles:

Magnetism has fascinated us for thousands of years, but it is only recently that we began to realize that magnetism is, to a large extent, a nanoscale phenomenon (*105*). The atomic exchange interaction that defines ferromagnetism is typically on the length scale of 10 nm for most materials (*106*). The competition between the exchange interaction and magnetic anisotropy leads to domain formation, with a domain wall width also in the nanometer region. When the dimensions of the materials become comparable to these length scales, new properties begin to emerge, such as enhanced magnetic moments (*107, 108*), exchange coupled dynamics (*109*), quantization of spin waves (*110, 111*) and giant magnetoresistance (*112, 113*). These new properties lead to potential applications in permanent magnets, multi-terabit/in^2 data storage devices (*114*), new magnetic refrigeration systems (*115*), enhancing agents for magnetic resonance imaging (*116*) and targeted drug delivery (*117*). Research and applications of these unique features of magnetic nanostructures start with the material synthesis and fabrication. During the past two decades, chemical synthesis has demonstrated to be a powerful and rapid venue to obtain large quantities of nanosize building blocks in a single reaction. The magnetic nanostructures obtained through colloidal chemistry have better crystallinity, and are typically much smaller in size than what are typically achieved using top-down lithographic techniques. Particle size can be tuned through varying synthetic conditions. This has provided tremendous opportunities to investigate the transition of magnetism from the atomic scale to the bulk level.

1.5.1 Synthesis:

The recent advances in synthesis of various magnetic nanoparticles by colloidal chemical approaches offer the capability to precisely control the size of magnetic nanoparticles from 2 to 20 nm in diameters. Various synthetic strategies for preparation of

magnetic nanoparticles have been investigated, including chemical co-precipitation, sonochemical reactions, sol-gel, microwave heating, mechanochemical, micelle microemulsion, hydrothermal, and ball milling (*118, 119*). Compared to other methods, chemical synthesis has often been found the best method for the production of high- quality magnetic nanoparticles. Typically, these approaches involve either rapid injection of reagents into hot solution containing surfactants followed by aging at a high temperature, or the mix of reagents at a low temperature and then slow increase of the temperature under controlled conditions. For example thermal decomposition of dicobaltoctacarbonyl or reduction of cobalt salts generated spherical cobalt nanoparticles with various crystal structures (*120, 121*). Some research groups have made nanoparticles of iron oxide and other related iron or cobalt containing alloys by simultaneously reaction the precursors of the constituents (*118*). Many different ferrite nanoparticles were synthesized by the thermal decomposition of organometallic precursors followed by oxidation or low-temperature reactions inside reverse micelles. Many groups have contributed on the synthesis of metal magnetic nanoparticles. In 1999, Bawendi group reported the synthesis of Co nanoparticle with a new phase from the thermal decomposition of dicobalt octacarbonyl in tricoctylphosphine oxide (*122*). Murray *et al.* at the IBM Watson research center has studied the synthesis of monodisperse metallic magnetic nanoparticles intensively (*123*). Hyeons *et al.* in Seoul National University synthesized monodispere iron nanoparticles via the high temperature (300 ^{0}C) aging of an iron-oleic acid metal complex; which was prepared by the thermal decomposition of $Fe(CO)_5$ in the presence of oleic acid at 100 ^{0}C (*124*). The major disadvantage of metallic magnetic nanoparticles is their susceptibility to oxidation because of their high surface/volume ratio and high reactivity. Alloy magnetic nanoparticles and metal oxide nanoparticles are preferred in many studies because of

their relative stability in ambient conditions. Sun et al. developed a general method to synthesize monodisperse iron-platinum alloy nanoparticles by simultaneous reduction of platinum acetylacetonate and the thermal decomposition of $Fe(CO)_5$ in the presence of oleic acid and oleyl amine (*125*). Weller *et al.* developed the synthesis of monodisperse, highly crystalline $CoPt_3$ nanoparticles by reduction of $Pt(acac)_2$ and thermo-decomposition of $Co_2(CO)_8$ in the presence of 1-adamantanecarboxylic acid (*126*). Sun and coworkers also developed the synthesis of monodisperse magnetite (Fe_3O_4) nanoparticles by a high temperature solution phase reaction of $Fe(acac)_3$ and 1,2 hexadecanediol in presence of oleic acid and oleylamine as surfactants (*127*). In another method, monodisperse iron nanoparticles were first synthesized, and then they were transformed to monodisperse γ-Fe_2O_3 nanocrystals by controlled oxidation using trimethly amine N-oxide as a mild oxidant (*124*).

1.5.2 Special Features of Magnetic Nanoparticles:

Two key issues dominate the magnetic properties of nanoparticles: finite-size effects and surface effects which give rise to various special features, as summarized in Figure 1.13. Finite-size effects result, for example, from the quantum confinement of the electrons, whereas typical surface effects are related to the symmetry breaking of the crystal structure at the boundary of each particle. The two most studied finite-size effects in nanoparticles are the single domain limit and the superparamagnetic limit. In large magnetic particles, it is well known that there is a multidomain structure, where regions of uniform magnetization are separated by domain walls. The formation of the domain walls is a process driven by the balance between the magnetostatic energy (ΔE_{MS}), which increases proportionally to the volume of the materials and the domain-wall energy (E_{dw}), which increases proportionally to the interfacial area between

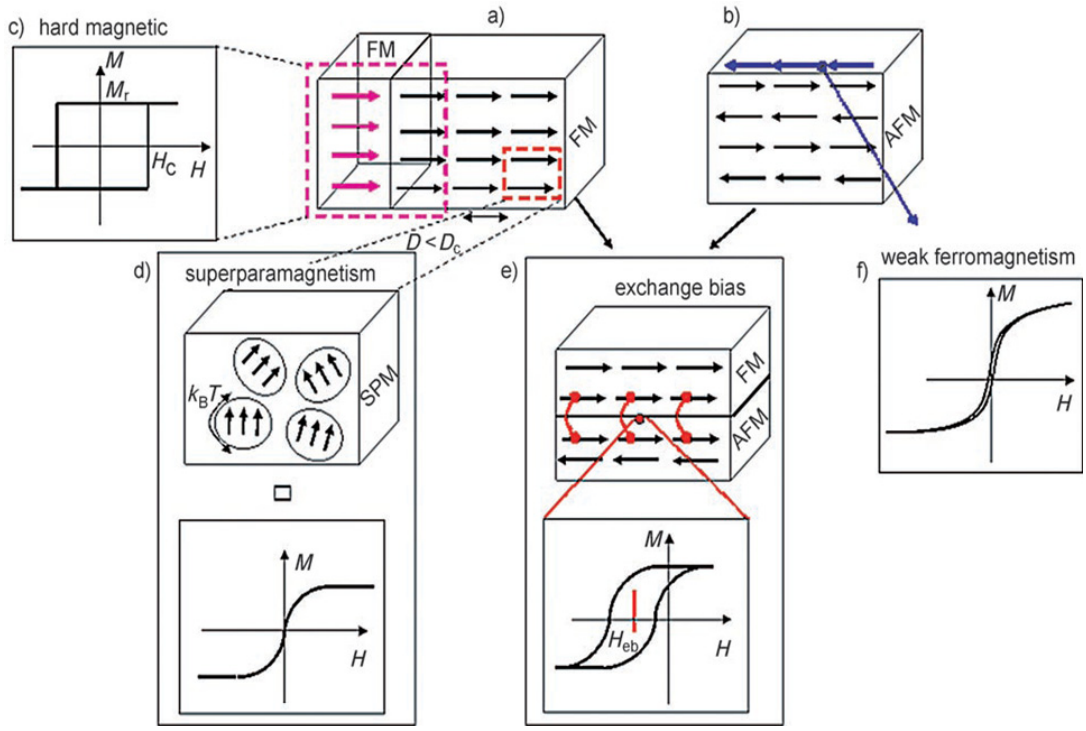

Figure 1.13: The different magnetic effects occurring in magnetic nanoparticles. The spin arrangement in (a) a ferromagnet (FM) and (b) an antiferromagnet (AFM); D=diameter, D_c=critical diameter. (c) a combination of two different ferromagnetic pahses. (d) An illustration of the magnetic moments in a superparamagnet (SPM). (e) The interaction (exchange coupling; linked red dots) at the interface between a ferromagnet and an antiferromagnet produces the exchange bias effect. (f) Pure antiferromagneic nanoparticles could exhibit superparamagnetic relaxation as well as a net magnetization arising from uncompensated surface spins (From ref. 118).

domains. If the sample size is reduced, there is a critical volume below which it costs more energy to create a domain wall than to support the external magnetostatic energy (stray field) of the single-domain state. This critical diameter typically lies in the range of a few tens of nanometers and depends on the material. It is influenced by the contribution from various anisotropy energy terms. The critical diameter of a spherical particle, D_c, below which it exists in a single-domain state is reached when $\Delta E_{MS}=E_{dw}$, which implies

$$D_c \approx 18\frac{\sqrt{AK_{eff}}}{\mu_0 M^2} \qquad (1.24)$$

where A is the exchange constant, K_{eff} is anisotropy constant, μ_0 is the vacuum permeability, and M is the saturation magnetization. Typical values of D_c for some important magnetic materials are listed in Table 1.2 (*128*).

Table 1.2: Estimated single-domain size for different spherical particles (From ref. 118)

Material	D_c [nm]
hcp Co	15
fcc Co	7
Fe	15
Ni	55
$SmCo_5$	750
Fe_3O_4	128

The magnetization of a single-domain particle lies along the easy axis direction in the absence of applied magnetic field (*118, 129*). When a field is applied opposite to the direction of the magnetization, the magnetic moments rotate through the hard direction to a new easy direction. There is no domain structure change with this magnetization switching. It is always more difficult to overcome the anisotropy force that holds the magnetization in the easy direction to rotate the magnetization than to move a domain wall, thus, single-domain particles have a larger coercivity than multi-domain materials, as shown in Figure 1.14. Another source for the high coercivity in a system of small particles is the shape anisotropy.

Superparamagnetism: The phenomenon of superparamagnetism is observed in small single-domain particles and it occurs when the materials are composed of very small particles (usually below10 nm) (*118, 129*). The energy required to change the direction of magnetization of a crystallite is called the crystalline anisotropy energy, which

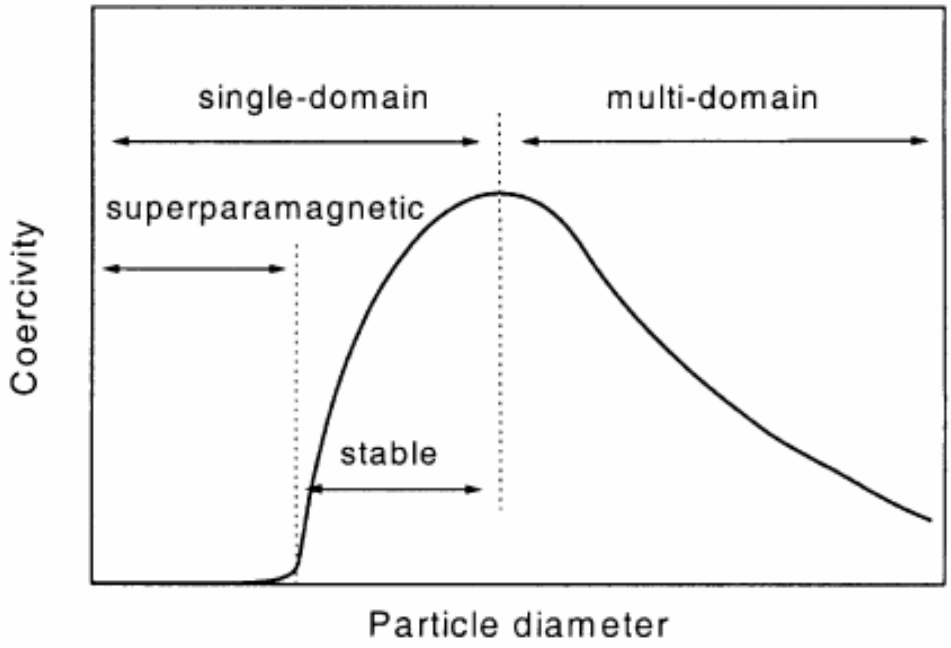

Figure 1.14: Variation of coercivity with particles diameter

depends on both the material properties and the particle size, as described in the following equation,

$$E_a = K_\mu V \tag{1.25}$$

where K_μ is the anisotropy energy density and V is the magnetic switching volume of the crystallite. As the crystallite size V decreases, so does the crystalline anisotropy energy. When the crystallite size reaches below a critical limit, the thermal energy is sufficient to overcome the coupling interactions between neighboring atoms even though the temperature is below the Curie or Neel temperature, which leads to the change in direction of magnetization of the entire crystallite. The resulting fluctuation of the magnetization direction causes the magnetic field to average to zero. The material behaves in a manner similar to paramagnetism, except that the magnetic moments of the entire crystallite tend to align under the magnetic field instead of each individual atom being independently influenced by an external magnetic field. A typical magnetization curve measured from

superparamagnetic materials is shown in Figure 1.13 (d). This superparamagnetic size limit can be estimated by the Neel relaxation time equation given below, (*130*)

$$t_{rel} = \tau_o \exp\left(\frac{K_\mu V}{k_B T}\right) \tag{1.26}$$

where τ_o is the relaxation time factor of the order of 10^{-9} seconds and $k_B T$ is the thermal energy with the Boltzmann constant k_B. When the magnetic measurement time $t_{mes} < t_{rel}$, the sample belongs to ferromagnetism. And when, $t_{mes} > t_{rel}$ it belongs to superparamagnetism. Therefore, the ratio of crystalline anisotropy energy $K_\mu V$ to the thermal energy $k_B T$ should satisfy the condition below for the superparamagnetic size limit,

$$\frac{K_\mu V}{k_B T} \geq ln\left(\frac{t_{meas}}{\tau_o}\right) \tag{1.27}$$

In the case of high-K_μ magnetic materials such as FePt, $SmCo_5$ and CoPt, etc., in order to maintain the thermal stability of the single-domain nanoparticles, this ratio should satisfy, (*114, 131, 132*)

$$\frac{K_\mu V}{k_B T} \geq 60 \tag{1.28}$$

Therefore, we can estimate the superparamagnetic size limit D_s by assuming the cubic shape of grains (*133*),

$$D_s = \left(\frac{60 \cdot k_B T}{K_\mu}\right)^{\frac{1}{3}} \tag{1.29}$$

As for FePt nanoparticles, taking K_μ=6.6~10×10^7 erg/cm^3, T=300 K and $k_B T$=3.77×10^{-14} erg, the superparamagnetic size limit D_s is 2.8~3 nm at room temperature (*133-135*). This theoretical superparamagnetic size limit also predicts that FePt nanoparticles below a critical size limit cannot convert to hard magnetic phase (*133*). This transition size limit has

been proved to be well matched with the range of the superparamagnetic size limit, theoretically and experimentally (*136*).

1.6 Carbon Nanostructures:

Carbon occurs in many forms, and the dependence of the properties of each form on its special structure makes carbon a truly unique building block for nanomaterials. For this reason carbon has been investigated for more than half a century. Three types of nanocarbons have emerged in the last 25 years. These are fullerenes, carbon nanotubes and graphene. Fullerenes are zero-dimensional molecular compounds, while carbon nanotubes are one-dimensional materials. Graphene is a two-dimensional network of carbon atoms with fascinating properties. All the three nanocarbons contain sp^2 carbon atoms and one would expect certain similarities in the properties of these nanocarbons.

The most famous of this class of molecules is the spherical Buckyball C_{60}, which has a bond structure analog to the seams of an old fashioned soccer ball connecting the 12 heptagonal and 20 hexagonal leather patches. After this discovery, it became evident that sp^2-hybridized graphene layers exist not only as planar honeycomb sheets like in graphite but also as spherically curved and closed cages (*137*). Later, in 1991, Sumio Iijima (*138*) discovered a cylindrical form of the buckyball, known as carbon nanotube. These new members of the fullerene family fall into two broad categories: single-walled carbon nanotubes (SWNT) consisting of one graphene sheet rolled into a cylinder and multi-walled carbon nanotubes (MWNT) made of several concentric SWNTs. The recent addition to carbon nanostructures family, graphene has been discovered by Geim and co-workers at the University of Manchester (*139, 140*). Figure 1.15 shows how single graphene sheet can be wrapped, rolled or stacked to generate those materials.

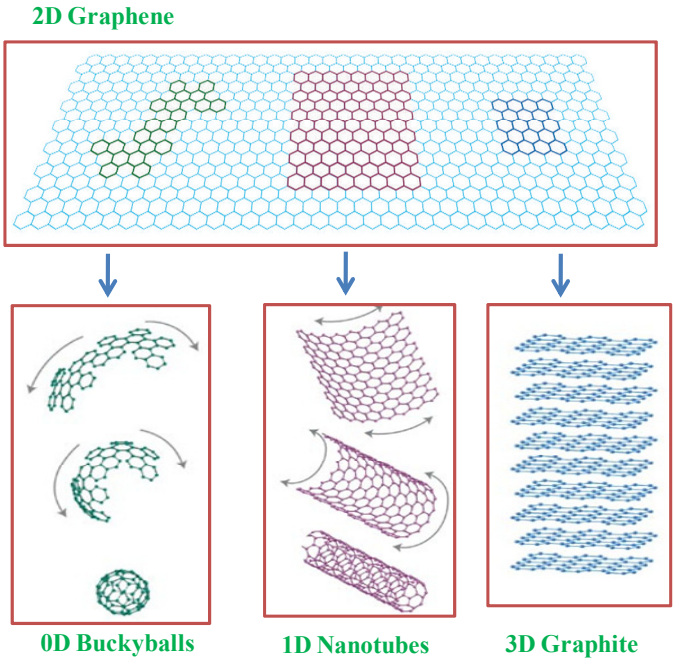

Figure 1.15: Graphene: mother of all graphitic forms. It can be wrapped up into 0D buckyballs, rolled into 1D nanotubes or stacked into 3D graphite (From ref. 158).

1.6.1 Carbon Nanotubes

These new members of the fullerene family fall into two broad categories: single-walled carbon nanotubes (SWNT) consisting of one graphene sheet rolled into a cylinder and multi-walled carbon nanotubes (MWNT) made of several concentric SWNTs. The outstanding mechanical and electronic properties of SWNTs have been largely investigated and today still constitute the object of intensive research activities. Notably, a SWNT can be viewed as the prime example for a molecular one dimensional electronic system and can be used for the realization of future SWNT-based quantum devices. In the following paragraphs, we are going to give a short introduction to the synthesis, structure and electronic properties of SWNTs.

Synthesis: Carbon nanotubes (CNTs) can be synthesized by various methods with arc-discharge, laser ablation and chemical vapor deposition (CVD) being the principal ones (Figure 1.16) (*141*). In these methods, the carbon nanotubes (SWNTs or/and MWNTs) are grown from the condensation of a carbon-containing phase in as most of

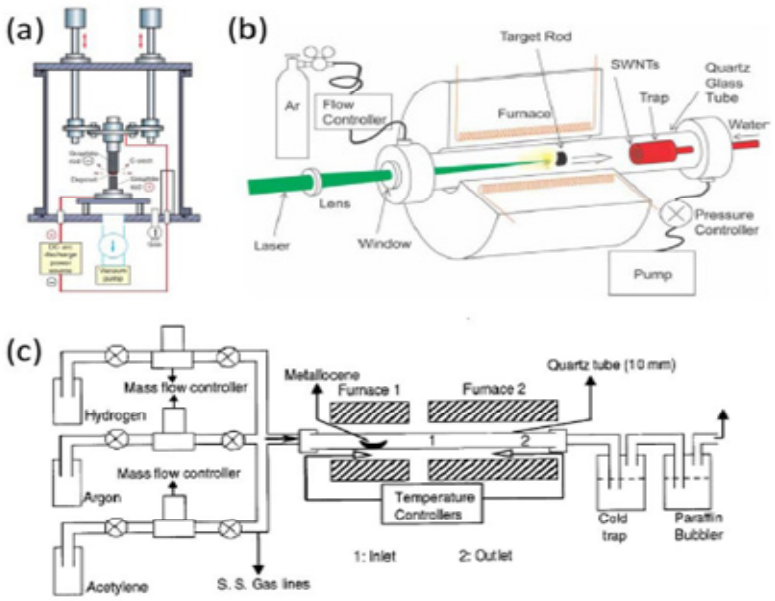

Figure 1.16: Schematic diagrams of (a) arc-discharge chamber, (b) high temperature laser ablation and (c) organometallic pyrolysis experimental set-up (From ref. 141).

the cases in the presence of metallic catalysts like Fe, Ni or Co. The produced SWNTs mostly bunch in the form or ropes with tens of individual nanotubes close-packed via Vander-Waals interactions. Originally developed for the synthesis of fullerenes, arc discharge technique produce carbon soot containing many interesting carbon nanostructures including CNTs, as discovered by Iijima in 1991 (*138*). Besides its pioneering role for the synthesis of CNTs, arc discharge evolved as a trustful technique for the mass production of CNTs (*142, 143*).

Synthesis of CNTs via laser ablation of a graphite target is similar to arc discharge since the carbon source in both techniques is graphite. For the synthesis of CNTs by the laser ablation technique a continuous or pulsed laser is used, which is directed at a graphite target located in a heated quartz tube at around 1200 ^{0}C. The quartz tube is continuously flushed with argon or helium gas under reduced pressure and the sublimed carbon species along with metal clusters are transported by the gas flow and recombine on a cold finger to form bundles of CNTs. If the graphite target with transition metals

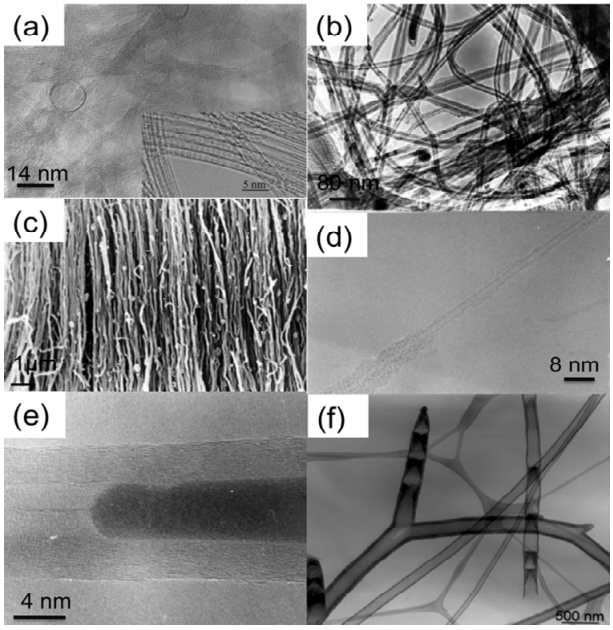

Figure 1.17: Electron microscope images of (a) SWNTs prepared by arc-discharge process, (b) MWNTs, (c) aligned MWNT bundles, (d) SWNTs, (e) Fe-filled MWNTs and (f) Y-junction carbon nanotubes prepared by organometallic route respectively. Inset in (a) shows C_{60} filled SWNTs, carbon "peapods" (From ref. 141).

like nickel and cobalt is a prerequisite for the synthesis of SWNTs (*144*). Chemical vapor deposition (CVD) is another important method used for the production of carbon nanotubes. The main requirements for the CVD or plasma enhanced chemical vapor deposition (PECVD) synthesis of CNTs are a hydrocarbon gas, a metal catalyst and a plasma or thermal energy source. Contrary to arc discharge and laser ablation techniques, CVD requires a metal catalyst for the synthesis of MWNTs as well as SWNTs (*145, 146*). The SWNTs can also produced by the high pressure CO disproportionation process (HiPCO) (*147*), which belongs to the CVD family. In CVD, a flowing hydrocarbon gas is decomposed at a growth temperature between 500 and 1000 ^{0}C. The precipitation of carbon from the saturated phase on the metal catalyst particles leads to the formation of a tubular carbon solid. In the HiPCO technique, the SWNTs are produced by flowing CO, which is the carbon feedstock, mixed with a small amount of iron-containing catalyst precursor $Fe(CO)_5$ through a heated reactor. In this process CO disproportionate, simultaneously $Fe(CO)_5$ decomposes and produces

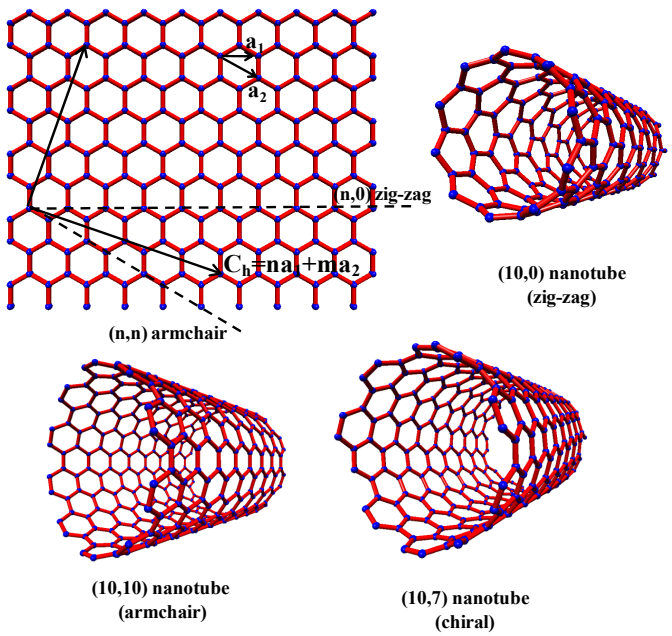

Figure 1.18: Schematic representation of the relation between nanotubes and graphene.

nacent Fe clusters, both of which react to yield SWNTs. The diameter of SWNT produced by the HiPCO technique are generally smaller (typically ~ 1 nm) than for arc-discharge and laser ablation (typical diameters ranging from 1 to 1.6 nm). Figure 1.17 shows TEM images of carbon nanotubes prepared by different methods.

As produced raw material can contain a high degree of impurities, being mainly metal particles and amorphous carbon. These impurities can be removed to a great extent, *e.g* by metal catalyzed oxidation (*147*) or by hydrogen treatment. Controlling the chirality of CNTs is of great importance, since CNTs are either metallic or semiconducting depending on the chirality and many applications require CNTs with controlled electrical properties. Furthermore, recent promising progresses have been made in separating SWNTs according to their chirality (*n,m*) (*148*). This is of prime importance towards the realization of future SWNT-based technologies. The recent progress in the selective synthesis as well as separation of SWNTs will be discussed in Chapter 6.

Structure and characterization: A SWNT can be visualized by cutting C_{60} across the middle and adding a cylinder of graphene of the same diameter. If the C_{60} is bisected normal to a five-fold axis, an armchair tube is obtained and if it is bisected normal to a threefold axis, a zigzag tube is formed. In addition, a variety of chiral tubes can be obtained with the screw axis along the axis of the tube (armchair and zigzag nanotubes are achiral). Nanotubes can be defined by a chiral angle θ and C_h a chiral vector given by equation (1.30) where $a_1$and a_2 are unit vectors in a 2D graphene lattice (see Figure 1.18), while n and m are integers.

$$C_h = na_1 + ma_2 \tag{1.30}$$

The vector C_h connects two crystallographically equivalent sites on a 2D graphene sheet while the chiral angle is the angle it makes with respect to the zigzag direction (Figure 1.18). A tube is formed by rolling up the graphene sheet such that the two points connected by the chiral vector coincide. The nanotube can be specified by the pair of integers (n,m), which have a wide range of values. For the armchair nanotubes, n= m ≠ 0 while n ≠ 0, m =0 for the zigzag nanotubes. For a nanotube defined by the index (n, m), the diameter, d, and chiral angle, θ, are given by the equations (1.31) and (1.32), where a = 1.42 Å and $0 \leq \theta \leq 30^o$.

$$d = a \cdot (m^2 + m \cdot n + n^2)^{1/2}/\pi \tag{1.31}$$

$$\theta = arctan(-(3)^{1/2} \cdot m)/2n + m) \tag{1.32}$$

The MWNTs consist of capped concentric cylinders separated by 3.45 Å, which is close to the separation between the (002) planes in graphite. The carbon nanotubes are capped by dome-shaped hemispherical fullerene-type units. The capping unit consists of pentagons and hexagons. SWNTs have defects like bends, which are due the presence of pentagons and heptagons on opposite side of the tube (*149*). The electronic structure of SWNTs is closely related to its structure. The basic electronic band structure of

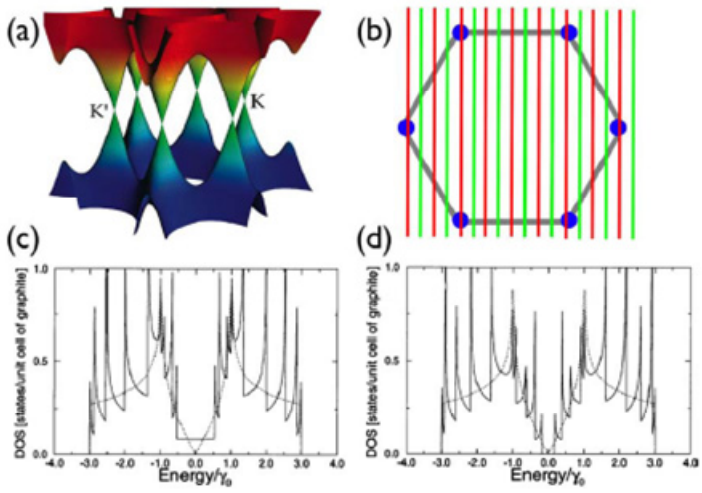

Figure 1.19: (a) Three-dimensional plot of the π and π^* graphene energy bands and (b) a 2D projection with the allowed 1D wave vectors k for a metallic (red) and semiconducting (green) SWNTs. The hexagon defines the first Brillouin zone of a graphene sheet, and the black dots in the corners are the K_B points. (c) and (d) density of states plot for metallic and semiconducting SWNTs respectively (From ref. 187).

SWNTs can be derived from a graphene sheet while neglecting hybridization effects due to the finite curvature of the tube structure. Graphene is a semi-metal with valence and conduction bands are degenerate only at six corners (K_B) of the hexagonal first Brillouin zone (see Figure 1.19 (a)). The Fermi surface of the graphene sheet is thus reduced to these six points. In SWNTs, the wave vector k is quantized along the circumferential direction due to periodic boundary condition, $k.\ C_h = 2\pi q$, were q is any integer. Therefore, only a particular set of states, which are parallel to the corresponding tube axis with a spacing of 2/d, are allowed as evident from Figure 1.19 (b). On the basis of this simple scheme, if one of the allowed wave vectors passes through a Fermi level K_B of the graphene sheet, the SWNT should be metallic, and otherwise it should be semiconducting (*150-152*). SWNTs are metallic when (n - m)/3 is an integer, and otherwise they are semiconductors. Low-temperature scanning tunneling microscopy (STM) and scanning tunneling spectroscopy (STS) studies of SWNTs have shown the size-specific transport properties in agreement with theoretical predictions(*153, 154*).

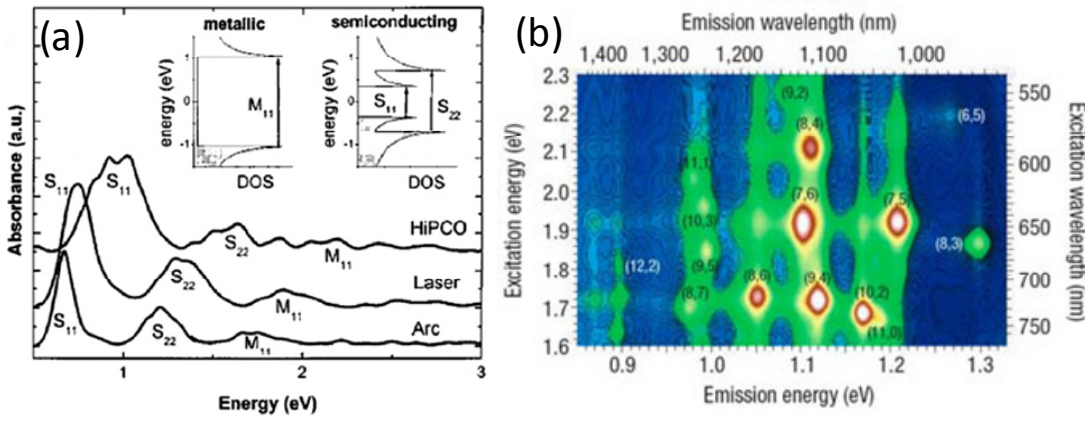

Figure 1.20: (a) Optical absorption spectra of films of purified SWNTs. Here S and M stand for electronic transitions of semiconducting and metallic SWNTs respectively. (b) 2D photoluminescence map of HiPCO SWNTs. (From ref. 156).

Optical absorption and fluorescence spectroscopy has also been used to study SWNTs. All the optical spectroscopic processes in semiconducting SWNTs and most in metallic SWNTs are attributed to transitions between corresponding van Hove singularities. The presence of energy gaps is induced by features such as doping, curvature and bundling. A small energy gap at the Fermi level opens up in the case of metallic nanotubes due to the curvature of the graphene sheet (*155*). Typical optical absorption spectra of SWNTs in shown in Figure 1.20 (a) (*156*). The near-infrared transitions designated at S_{11} and S_{22} arise from the inter-van Hove energy levels in semiconducting SWNTs while metallic SWNTs exhibit absorption bands (M_{11}) in the visible region. Metallic SWNTs show a band (M_{00}) in the infrared spectrum (100 cm^{-1}) which arises due to the small gap near the Fermi level (attributed to effects of finite curvature and broken symmetry). The absorption spectra of SWNTs show a blue shifted as the diameter of the nanotube decreases.

Bundled SWNTs do not exhibit photoluminescence as the electron-hole pair non-radiatively decay due to the presence of metallic SWNTs in the bundles. Photoluminescence is only observed when the nanotubes are individualized and the

process occurs in three steps: (a) an absorption of light at S_{22} followed by (b) a relaxation from S_{11} using a phonon-electron interaction, and (c) a spontaneous emission at E_{11}. The photoluminescence emission is possible with the S_{11} transition while a wide range of wavelengths are useful for excitation. As the energy of the van-Hove singularities maxima are mainly dependent on the nanotube chirality, the (n,m) values of the different nanotubes present in a sample can be characterized using two-dimensional photoluminescence mapping. A typical photoluminescence map of HiPCO SWNTs is shown in Figure 1.20 (b). Diffraction methods have also been used to probe the structure and properties of carbon nanotubes. Electron diffraction studies establish the presence of helicity (*157*). The XRD pattern of MWNTs show only the (hk0) and (00l) reflections but no (hkl) reflections. Raman spectroscopy is an important tool to characterize carbon nanotubes. It will be discussed in section 1.6.3.

1.6.2 Graphene:

Graphene is the name given to a flat monolayer of carbon atoms tightly packed into a two-dimensional (2D) honeycomb lattice, and is a basic building block for graphitic materials of all other dimensionalities (*158*). Theoretically, graphene has been studied for sixty years and is widely used for describing properties of various carbon-based materials. Graphene was an academic material as it was widely believed that 2D crystals are unstable. Geim and co-workers (*139*) in 2005 showed that a single layer of graphene is indeed stable, thus opening a new area of fascinating physics and chemistry

Synthesis: A large majority of the studies of graphene have been directed towards synthesis (Chart 1). Since micromechanical cleavage of HOPG was first employed to obtain single layer graphene (SG), various methods including epitaxial growth on an insulator surface such as SiC and chemical vapor deposition (CVD) on surfaces of transition metals such as Ni and Cu have been employed (*159, 160*). We find that

Chart 1: Various Synthetic methods of graphene.

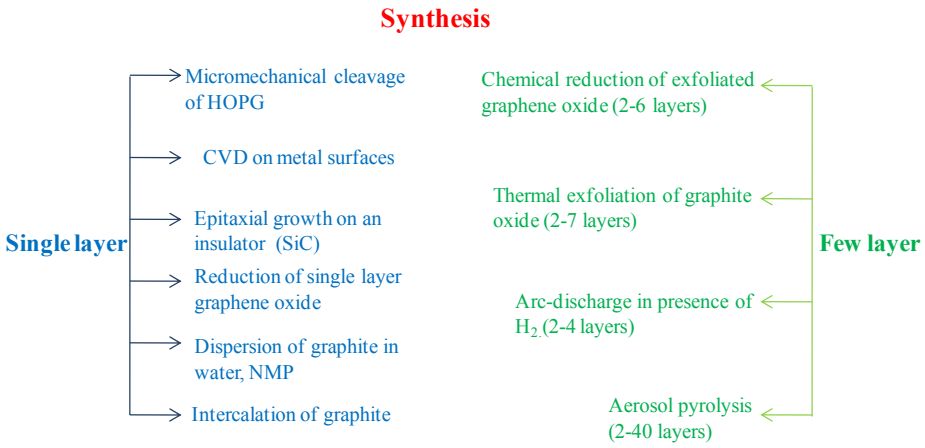

graphene layers can be grown on different transition metal substrates by decomposing a variety of hydrocarbons such as methane, ethylene, acetylene and benzene with the number of layers varying with the hydrocarbon and reaction parameters. Hydrazine reduction of single layer graphene oxide seems to be an effective means of obtaining a dispersion of SG in solvents such as DMF. Many of the above methods are, however, not suitable to make large quantities of graphene samples. Bi- and few-layer graphenes can be obtained by different chemical procedures such as thermal exfoliation of graphite oxide, reduction of graphene oxide with reducing agents such as hydrazine under microwave irradiation, and microwave solvothermal treatment of graphene oxide (*159, 160*). The most common method of preparing graphene samples seems to be through the reduction of graphene oxide.

There are a few studies directed towards the formation of carbon nanoscrolls (CNSs) from graphene. Because of the novel scroll topology, properties of CNSs differ from those of SWNTs and MWNTs. CNSs provide interlayer galleries that can be intercalated with donors and acceptors and may be of value in energy storage in supercapacitors or batteries, in addition to exhibiting novel electronic and optical properties as predicted (*161*). The scrolls can be prepared by ultrasonication of potassium intercalated graphite (*162*) or by simply dipping the single-layer graphene

deposited on substrate in isopropyl alcohol (*163*). Developing an efficient approach to roll chemically derived graphene to CNSs would be worthwhile. Transformation of graphene oxide to carbon nanotubes and carbon nanoparticles is induced by ultrasonication under acidic conditions (*164*). In this one-pot transformation, two-dimensional sheets, susceptible to acid cutting, are decomposed into polyaromatics in concentrated acid in minutes. Polyaromatics are further reconstituted by acid dehydration reactions to form carbon nanoparticles and nanotubes. There is much to be done on such transformation as well as on CNSs. Arc-discharge of graphite rod in hydrogen atmosphere has been used for preparing graphene containing 2-4 layers on a relatively large-scale. An important aspect of the arc-discharge method is its use in doping graphene with boron and nitrogen.

Structure and characterization: A single atomic sheet of graphene is the mother of all graphitic allotropes, since it is the elementary building block of graphite as well as CNTs and even fullerenes if pentagons are introduced in the hexagonal lattice. Stacking two sheets of graphene produces graphite by definition, but the physical properties of stacks consisting of less than ten graphene sheets are significantly different from the physical properties of bulk graphite.

Therefore, a different terminology is applied to distinguish several classes of graphene stacks. Depending on their dimensions and physical properties, graphene stacks are classified into three categories: single layer graphene, few layer graphene or FLG and graphite. Graphite is the three-dimensional equivalent resulting from stacking the strictly two-dimensional crystalline graphene. The definitions of graphite and graphene are solely based on structural differences and are therefore inappropriate to denote stacks of less than ten graphene layers, whose structure resembles graphite but whose physical properties correspond more to graphene than to graphite. This class of graphitic

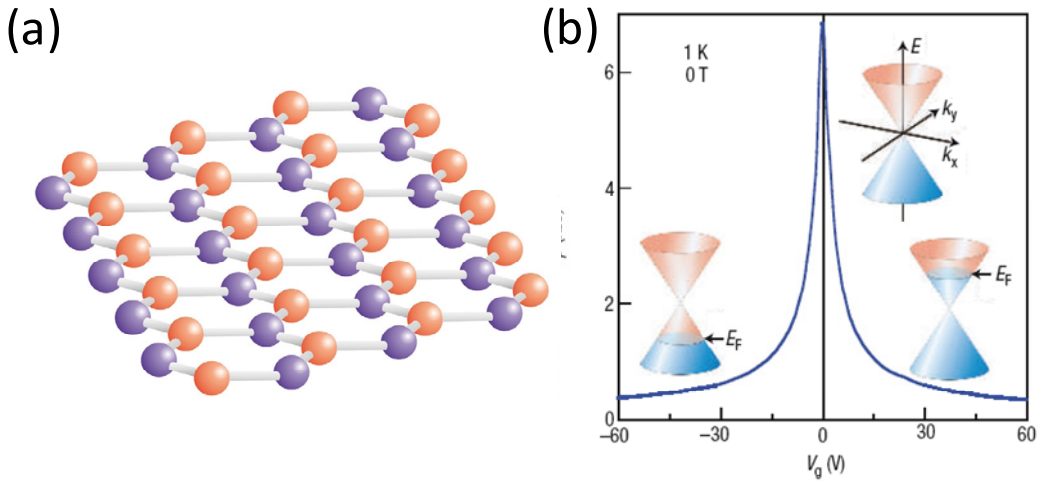

Figure 1.21: (a) Crystallographic structure of graphene. Atoms from different sublattices (A and B) are marked by different colors (From ref.175). (b) Ambipolar electric field effects in single-layer graphene. The conical low-energy spectrum $E(k)$ indicates changes in the position of the Fermi energy E_F with changing gate voltage V_g (From ref. 158).

material is therefore denoted by the term few layer graphene or FLG. Graphene, FLG and graphite are the three classes of planar graphitic structures.

Single layer graphene is defined as a two-dimensional carbon crystal with a strictly hexagonal lattice structure. But perfect two-dimensional crystals cannot exist in the free state, as first theoretically established by Peierls (*165, 166*) and Landau (*167*) more than 70 years ago. They showed that thermal fluctuations should destroy long-range order, resulting in curling of a two-dimensional lattice at finite temperature. Mermin and Wagner further confirmed these findings and extended the proof to two dimensional crystals in general (*168, 169*). Numerous experiments have validated the theoretical conclusions, presenting thermodynamical instabilities in thin films unless the films constitute a three-dimensional system (*170, 171*).

However, although theory forbids strictly two-dimensional crystals, it does allow structural deformations, like bending, to stabilize atomically thin graphene in the third dimension (*171*). High resolution TEM and electron diffraction studies have confirmed the deformation of suspended graphene by periodic rippling of the surface (*172*). This

intrinsic microscopic roughening results in an average out of plane curvature, corresponding to a surface normal deviation of about 5^{o}. Even though these are large values, they do not immediately cause plastic deformation and generation of defects (*173*).

Graphene has two atoms per unit cell, which results in two 'conical' points (*K* and *K'*) per Brillouin zone where the band crossing occurs (*174*). Figure 1.19 (a) gives an illustration of the band structure of graphene (*175*). The charge carriers in graphene are described by a Dirac-like equation as a consequence of graphene's crystal structure. This consists of two equivalent carbon sublattices A and B (Figure 1.21 (a)) (*175*). Quantum-mechanical hopping between these sublattices leads to the formation of two energy bands, and their intersection near the edges of the Brillouin zone yields the conical energy spectrum. As a result, quasiparticles in graphene exhibit a linear dispersion relation $E = \hbar k \upsilon_F$, as if they were massless relativistic particles (for example, photons) but the role of the speed of light is played here by the Fermi velocity $\upsilon_F \approx c/300$. Because of this linear spectrum, one can expect that quasiparticles in graphene behave differently from those in conventional metals and semiconductors, where the energy spectrum can be approximated by a parabolic (free electron-like) dispersion relation. Graphene shows a pronounced ambipolar electric field effect (*158*) as the charge carriers can be tuned continuously between electrons and holes in very high concentrations and mobilities even under normal conditions which do not depend much on temperature. The conical low energy spectrum $E(k)$ indicates changes in the position of the Fermi energy E_F with changing gate voltage V_g in Figure 1.21 (b). Although some semiconductors (namely, InSb) exhibit high mobility at room temperature, graphene has drawn special attention as it exhibits room temperature quantum Hall effect (QHE). An equally important reason for the interest in graphene is the unique nature of its charge

carriers. Graphene is an exception to other materials as its charge carriers mimic relativistic particles which is described by the Dirac equation (*176*) rather than the Schrödinger equation (*177, 178*). Graphene's honeycomb lattice generates a new quasiparticle which can be described by the (2+1)-dimensional Dirac equation at low energy. These quasiparticles, called z mass-less Dirac fermions which can be depicted as electrons that have lost their rest mass m_o or as neutrinos that gained the electron charge e.

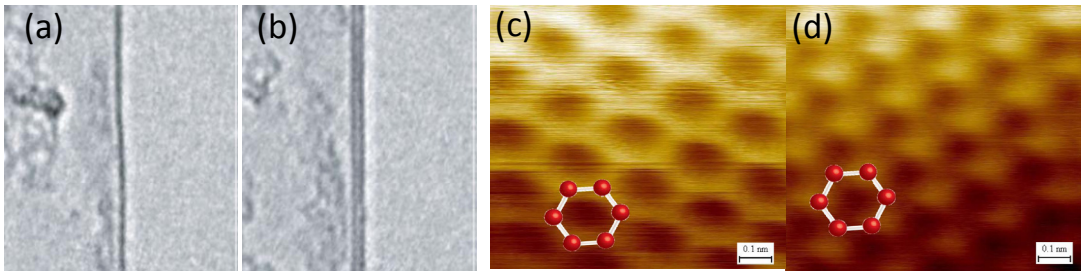

Figure 1.22: TEM (From ref. 172) (a & b) and STM (From ref. 179) (c & d) images of (a) & (c) single and (b) & (d) bi-layer graphene.

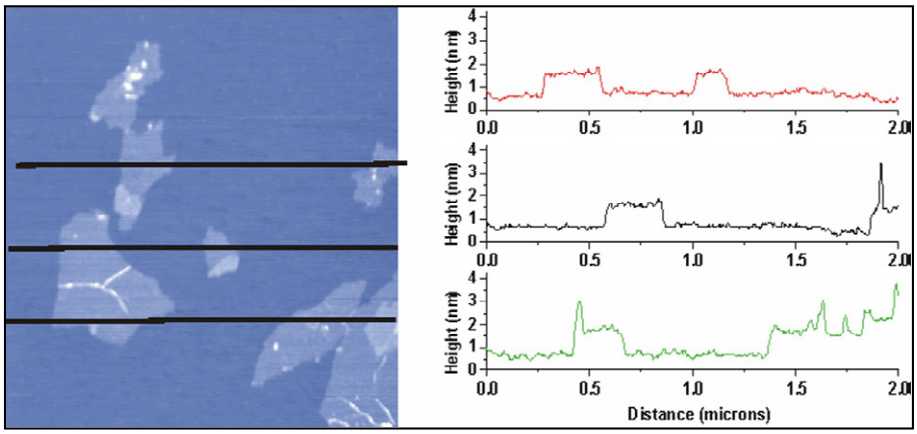

Figure 1.23: A non-contact mode AFM image of exfoliated graphene oxide sheets with three height profiles acquired in different locations (From ref. 180).

Graphene is characterized by different microscopy and related techniques. While transmission electron microscopy (TEM) and scanning electron microscopy (SEM) are used to obtain graphene morphology, scanning tunneling microscopy (STM) and atomic force microscopy (AFM) are used to observe the atomic arrangement and the layer thickness of graphene. TEM images of single and bi-layer graphene is shown in Figure

1.22 (a) & (b) (*172*). Moreover, TEM image of few-layer graphene gives the idea of number of layers present. Scanning Tunneling Microscopy (STM) is also a good technique to have an idea of graphene topology. Figure 1.22 (c) shows the STM image of a single layer graphene which displays the honeycomb structure expected for the full hexagonal symmetry of an isolated graphene monolayer, while few layer graphene exhibits totally different STM topography, displaying the reduced threefold symmetry characteristic of the surface of bulk graphite shown in Fig 1.22 (d) (*179*). AFM can be used to measure the thickness of graphene sheets. The height profile analysis of AFM images gives a clear idea about the number of layers present in graphene. Figure 1.23 shows AFM images of exfoliated graphene oxide sheets with three height profiles acquired in different regions of a sample comprising of mostly individual graphene sheets (*180*). Raman spectroscopy is an important tool to study and characterize graphene. It will be discussed in next section.

1.6.3 Raman spectroscopy of carbon nanotubes and graphene:

Raman spectroscopy has historically played an important role in the study and characterization of graphitic materials (*181-184*), being widely used in the last four decades to characterize pyrolytic graphite, carbon fibers, glassy carbon, pitch based graphitic foams, nanographite ribbons, fullerenes, carbon nanotubes, and graphene. For sp^2 nanocarbons, Raman spectroscopy can give information about crystallite size, clustering of the sp^2 phase, the presence of sp^3 hybridization and chemical impurities, mass density, optical energy gap, elastic constants, doping, defects and other crystal disorder, edge structure, strain, number of graphene layers, nanotube diameter, nanotube chirality and metallic vs. semiconductor behavior. The following paragraphs we describe three aspects of Raman spectra (see Figure 1.24), which are sensitive enough to provide unique information about the similarities and differences between the various

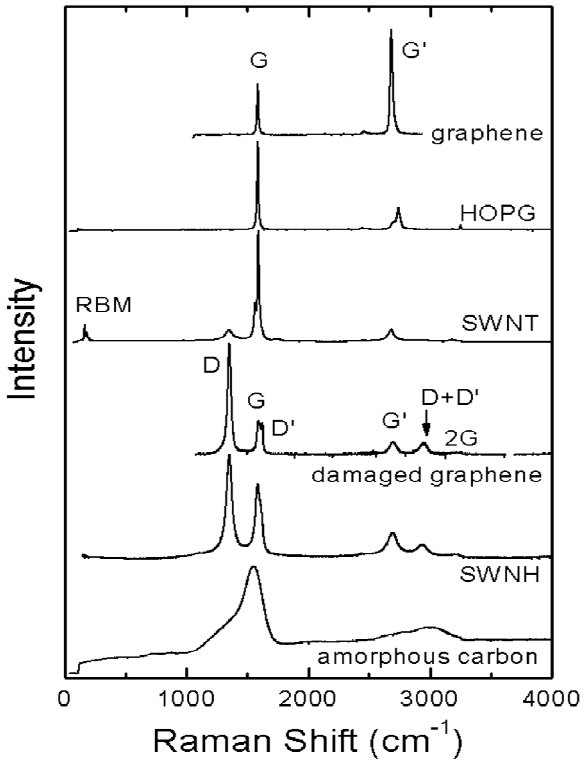

Figure 1.24: Raman spectra from different types of sp^2 nanocarbons (From ref. 183).

carbon nanostructures. The various Raman features are discussed including the G-band at ~ 1582 cm^{-1}, which is common to all sp^2 carbon forms, the radial breathing mode (RBM) that makes the diameter and optical transition energy analysis of nanotubes possible, and the D and G′ bands that are significant in providing information about the electronic and geometrical structure through the double resonance process

The G-band: The stretching of the C-C bond in graphitic materials gives rise to the so-called G-band Raman feature which is common to all sp^2 carbon systems (see Figures 1.24 and 1.25). This spectral feature is similar for graphenes and nanotubes but yet has properties capable of distinguishing one carbon nanotstructure from another. When the bond lengths and angles of graphene are modified by strain, caused by the interaction with a substrate or with other graphene layers or due to external perturbations, the hexagonal symmetry of graphene is broken (*182, 185*). The G-band is, therefore, highly sensitive to strain effects in sp^2 nanocarbons and can be used to probe any modification to the flat geometric structure of graphene, such as the strain induced by external forces,

by one graphene layer on another in few layer graphene or in multiwall nanotubes, or even by the curvature of the side wall when growing a SWNT. Curvature effects, such as occur in carbon nanotubes, give rise to multiple peaks in the G-band spectrum for a SWNT (*186*), while a single peak ($\omega_G \approx 1582$ cm^{-1}) is observed for a 2D graphene sheet (see Figure 1.25) (*187, 188*). Up to six G-band phonons are Raman allowed in chiral SWNTs, although two of them (the totally symmetric A_1 modes, see Figure 1.25) usually dominate the spectra (*187, 188*). This curvature dependence generates diameter dependence, thus making the G band a probe also for the tube diameter, while the G-band dependence on externally induced strain is very rich and is still controversial (*189*).

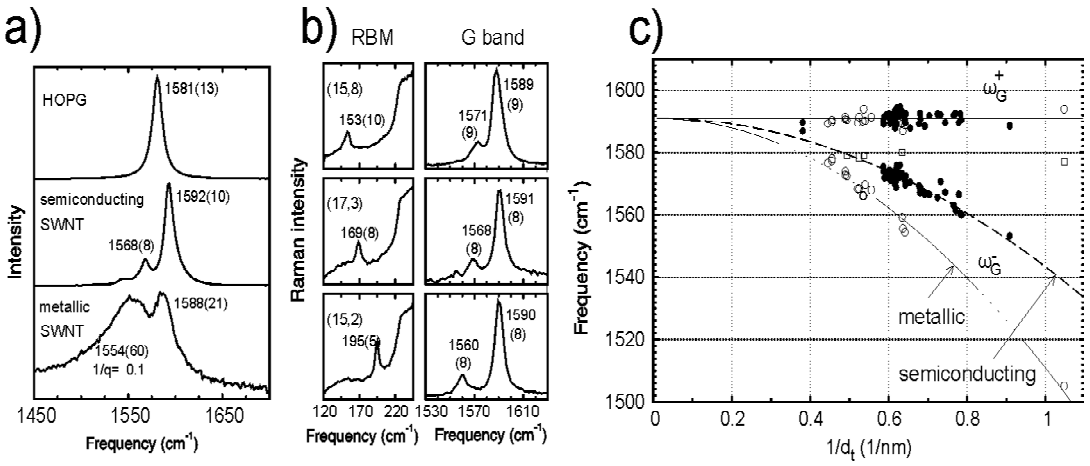

Figure 1.25: (a) The G-band for highly oriented pyrolytic graphite (HOPG), one semiconducting SWNT, and one metallic SWNT. (b) The RBM and the G-band Raman spectra for three semiconducting isolated SWNTs with the indicated (*n*,*m*) values. (c) Frequency vs $1/d_t$ for the two most intense G-band features (ω_G^- and ω_G^+) from isolated SWNTs (From ref. 188).

The coupling between electrons and phonons in nanocarbons (*190, 191*) is especially interesting because of the breakdown of the adiabatic approximation, thus changing both the electron energies (the Peierls instability) and the phonon energies (Kohn anomaly effect) in somewhat different ways, thereby providing tools for studying differences in the properties of different carbon nanostructures. Since these effects are

strongly dependent on the Fermi level and temperature, the G band becomes a probe for the doping of nanocarbons, thereby allowing study of their electronic dispersion relations. The Kohn anomaly is observed in metallic and semimetallic systems, where real electron-hole pair creation can occur by a phonon excitation ($p\omega_G$) process, thus strongly influencing the G-band frequency and the spectral width of graphene and metallic SWNTs. These effects in metallic SWNTs are stronger than those in graphene because of the quantum confinement effect, and this process depends sensitively on diameter and chiral angle (*192*). In graphenes these effects depend sensitively on the number of graphene layers. Semiconducting SWNTs also exhibit a phonon energy renormalization due to electron-phonon coupling, but this renormalization effect is weaker than that in graphene and for metallic SWNTs, and furthermore no real anomaly associated with ($E_g > p\omega_G$) takes place for S-SWNTs. Consequently, while the G band line width in graphene and metallic SWNTs is strongly sensitive to whether or not the Fermi energy matches the energy of the Kohn anomaly, (*192*) in semiconducting SWNTs the G band line width is basically independent of doping.

The radial breathing mode (RBM): The radial breathing mode is especially important in two ways: (1) for the determination of the diameter of a nanotube through the dependence of ω_{RBM} on d_t, and (2) for relating the ω_{RBM} and the resonant optical transition energies E_{ii} for a given tube.

Experimental data on the radial breathing mode frequency taken by many authors have been fit that using the relation $\omega_{RBM} = A/d_t + B$. For water-assisted super-growth samples, values of $A = (227.0 \pm 0.3)$ nm·cm^{-1} and $B = (0.3 \pm 0.2)$ cm^{-1} are obtained. This result is in remarkably good agreement with elasticity theory (*193*) parameterized by the graphite elastic properties, thus directly connecting one-dimensional carbon nanotubes and their two-dimensional counterpart graphene from which nanotubes are conceptually

derived. The vanishing value of B is in accordance with the limit d_t for appropriate for a graphene sheet. However, all the other ω_{RBM} results in the literature are up-shifted from these values of A and B, due to the vander Waals interaction with the environment, and can be generally described by

$$\omega_{RBM} = \frac{227}{d_t}\sqrt{1 + C_e d_t^2} \tag{1.32}$$

where the parameter C_e in eq. 1.32 describes environmental effects (*193*). It is intriguing that the super growth sample is the only sample showing the pristine-like behavior, while the measured free-standing tubes show the highest level of environmental changes. However, the detailed science behind the specific values of C_e has not yet been adequately addressed.

RBM bands have been important for understanding the effect of tube-tube interaction within multi-walled carbon nanotubes, the prototype material for studying such interactions being double-wall carbon nanotubes (DWNTs). Finally, through the RBM resonance window analysis, we can also study the (n,m) dependence of the optical transition energies (E_{ii}). This analysis reveals a great deal of information that goes beyond the simple tight binding model, including σ-π hybridization and the science of excitons. Though some aspects of the experiments can be interpreted within the context of a simple, noninteracting electron model (*194, 195*), it has become increasingly clear that electron-electron interactions also play an important role in determining the optical transition energies.

Dispersive *G′*-band (2D band): the double resonance process: All kinds of sp^2 carbon materials exhibit a strong Raman feature which appears in the range 2500-2800 cm^{-1}, as shown in Figure 1.24. Together with the G band (1582 cm^{-1}), this spectrum is a Raman signature of graphitic sp^2 materials and is called the G′ band (also called 2D

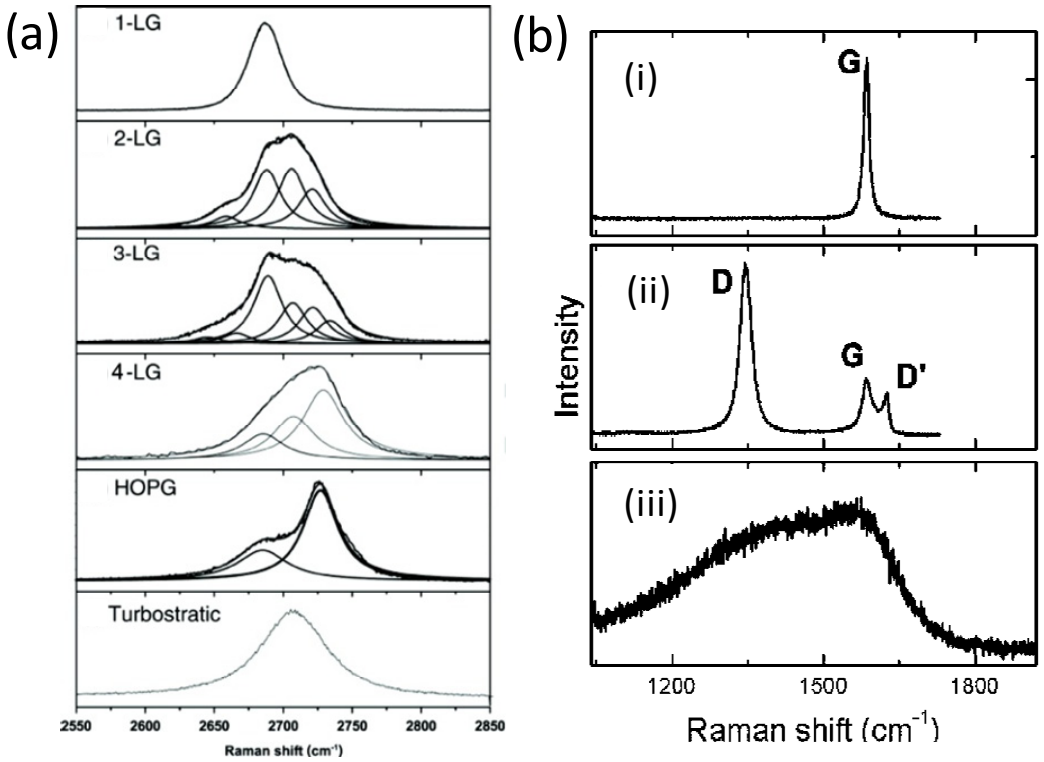

Figure 1.26: (a) The G′ (2D-band) spectra for graphene as a function of the number of layers (From ref. 182). (b) The first-order Raman spectrum of (i) crystalline graphene, (ii) defective graphene, and (iii) and fully disordered single-layer graphene deposited on a SiO_2 (From ref. 190).

band) to emphasize that it is a Raman-allowed mode for sp^2 carbons. Interestingly, the G′ band is a second-order two-phonon process and, intriguingly, it exhibits a strong frequency dependence on the excitation laser energy E_{laser}. This dispersive behavior ($\omega G' = \omega G'(E_{laser})$) is unusual in Raman scattering, since Raman-active mode frequencies usually do not depend on E_{laser}. The G′ band in particular is a second-order process related to a phonon near the K point in graphene, activated by double resonance (DR) processes (*196*), which are responsible for its dispersive nature and cause a strong dependence on any perturbation to the electronic and/or phonon structure of graphene. For this reason, the G′ feature provides a very sensitive probe for characterizing specific sp^2 nanocarbons. For example, the G′ band can be used for differentiating between single and double- layer graphene with AB interlayer stacking (*182*) and for probing aspects of the electronic structures of SWNTs.

Figure 1.26 (a) shows the dependence of the G′ band on the number of layers (*182*). While 1-LG exhibits a single very intense Lorentzian peak, fitting the 2-LG G′-band requires four Lorentzians, which are related to the four possible double resonance scattering processes, rather than to one possible process for 1-LG, resulting from the splitting of the π electronic structure of graphene when a second layer is added. With an increase in the number of layers, the number of DR scattering processes increases, and eventually the line shape converges to graphite, where only two peaks are observed (*182*). Carbon nanotubes show a very special G′ feature, where the number of peaks and their frequencies depend on (*n*,*m*) due to both curvature-induced strain and quantum confinement effects (*186*). Recently it was shown that the G′ feature can be used to assign p- and n-type doping in SWNTs, where the spectra from one single dopant attached to an individual tube was observed using both near-field Raman microscopy and spectroscopy (*197*).

Disorder-induced D band: The presence of disorder in sp^2-hybridized carbon systems leads to rich and intriguing phenomena in their resonance Raman spectra, thus making Raman spectroscopy one of the most sensitive and informative techniques to characterize disorder in sp^2 carbon materials. The D-band generally appears around 1350 cm^{-1}. Raman spectroscopy has thus become a key tool and is widely used to identify disorder in the sp^2 network of different carbon structures, such as diamond like carbon, amorphous carbon, nanostructured carbon, as well as carbon nanofibers, nanotubes, and nanohorns (*184, 198*). Figure 1.25 (b) shows Raman spectrum of graphene which gives good indication of D-band evolution in crystalline graphene induced by the ion bombardment procedure (*199*) .

REFERENCES

1. R. P. Feynman, *J. Microelectromech. Syst.* **1**, 60 (1992).
2. C. N. R. Rao, A. Mueller, A. K. Cheetham, Eds., *The chemistry of nanomaterials. synthesis, properties and applications*, vol. 1-2 (Wiley-VCH, Weinheim, 2004), vol. 1-2.
3. A. P. Alivisatos, *Science* **271**, 933 (1996).
4. H. Weller, *Angew. Chem., Int. Ed* **32**, 41 (1993).
5. V. L. Colvin, A. N. Goldstein, A. P. Alivisatos, *J. Am. Chem. Soc.* **114**, 5221 (1992).
6. V. L. Colvin, M. C. Schlamp, A. P. Alivisatos, *Nature* **370**, 354 (1994).
7. Y. Wang, N. Herron, *J. Phys. Chem.* **95**, 525 (1991).
8. G. Schmid, *Chem. Rev.* **92**, 1709 (1992).
9. Y. Wang, *Acc. Chem. Res.* **24**, 133 (1991).
10. J. L. Simonds, *Phys. Today* **48**, 26 (1995).
11. J. W. M. Bulte *et al.*, *Invest. Radiol.* **29**, S214 (1994).
12. R. D. McMichael, J. J. Ritter, R. D. Shull, *37th Annual conference on magnetism and magnetic materials* **73**, 6946 (1993).
13. P. V. Kamat, *J. Phys. Chem. C* **111**, 2834 (2007).
14. C. N. R. Rao, P. J. Thomas, G. U. Kulkarni, *Nanocrystals: synthesis, properties and applications*. (Springer, 2007).
15. E. Roduner, *Chem. Soc. Rev.* **35**, 583 (2006).
16. E. Roduner, *Nanoscopic Materials: Size-Dependent Phenomena*. (The Royal Society of Chemistry Cambridge, 2006).
17. J. Jortner, *Z. Phys. D:At., Mol. Clusters* **24**, 247 (1992).
18. A. Kohn, F. Weigend, R. Ahlrichs, *Phys. Chem. Chem. Phys.* **3**, 711 (2001).
19. K. M. Unruh, T. E. Huber, C. A. Huber, *Phys. Rev. B* **48**, 9021 (1993).
20. S. L. Lai, J. Y. Guo, V. Petrova, G. Ramanath, L. H. Allen, *Phys. Rev. Lett.* **77**, 99 (1996).
21. K. Koga, T. Ikeshoji, K.-i. Sugawara, *Phys. Rev. Lett.* **92**, 115507 (2004).
22. L. D. Gelb, K. E. Gubbins, R. Radhakrishnan, M. Sliwinska-Bartkowiak, *Rep. Prog. Phys.* **62**, 1573 (1999).
23. A. Ramírez-Hernández, H. Larralde, F. Leyvraz, *Phys. Rev. Lett.* **100**, 120601 (2008).

24. M. Hartmann, G. Mahler, O. Hess, *Phys. Rev. Lett.* **93**, 080402 (2004).
25. M. Schmidt *et al.*, *Phys. Rev. Lett.* **86**, 1191 (2001).
26. A. K. Starace *et al.*, *J. Chem. Phys.* **131**, 044307 (2009).
27. P. P. Edwards, R. L. Johnston, C. N. R. Rao, in *Metal Clusters in Chemistry,* P. Barunstein, G. Oro, P. R. Raithbay, Eds. (Wiley-VCH, Weinheim, 1998).
28. Y.-w. Jun, J.-s. Choi, J. Cheon, *Angew. Chem., Int. Ed* **45**, 3414 (2006).
29. V. Kresin, *Phys. Rev. B* **38**, 3741 (1988).
30. X. Liu, H. Dilger, R. A. Eichel, J. Kunstmann, E. Roduner, *J. Phys. Chem. B* **110**, 2013 (2006).
31. N. Watari, S. Ohnishi, *Phys. Rev. B* **58**, 1665 (1998).
32. D. E. Bergeron, A. W. Castleman, Jr., T. Morisato, S. N. Khanna, *Science* **304**, 84 (2004).
33. B. Yoon *et al.*, *Science* **307**, 403 (2005).
34. M. Haruta, *Catal. Today* **36**, 153 (1997).
35. C. J. H. Jacobsen *et al.*, *J. Am. Chem. Soc.* **123**, 8404 (2001).
36. I. Freestone, N. Meeks, M. Sax, C. Higgitt, *Gold Bulletin* **40**, 270 (2007).
37. D. J. Barber, I. C. Freestone, *Archaeometry* **32**, 33 (1990).
38. P. Mukherjee *et al.*, *Nano Lett.* **1**, 515 (2001).
39. C. Burda, X. Chen, R. Narayanan, M. A. El-Sayed, *Chem. Rev.* **105**, 1025 (2005).
40. E. A. Hauser, J. E. Lynn, *Experiments in Colloid Chemistry*. (MacGraw-Hill, New York, 1940).
41. J. Turkevich, P. C. Stevenson, J. Hillier, *J. Discuss. Farad. Soc.* **11**, 55 (1951).
42. B. V. Enüstün, J. Turkevich, *J. Am. Chem. Soc.* **85**, 3317 (1963).
43. D. G. Duff, A. Baiker, P. P. Edwards, *Langmuir* **9**, 2301 (1993).
44. M. Brust, M. Walker, D. Bethell, D. J. Schiffrin, R. Whyman, *Chem. Commun.*, 801 (1994).
45. K. V. Sarathy, G. Raina, R. T. Yadav, G. U. Kulkarni, C. N. R. Rao, *J. Phys. Chem. B* **101**, 9876 (1997).
46. K. V. Sarathy, G. U. Kulkarni, C. N. R. Rao, *Chem. Commun.*, 537 (1997).
47. P. J. Thomas, G. U. Kulkarni, C. N. R. Rao, *J. Phys. Chem. B* **104**, 8138 (2000).
48. T. Teranishi, M. Miyake, *Chem. Mater.* **10**, 594 (1998).

49. M. Schulz-Dobrick, K. V. Sarathy, M. Jansen, *J. Am. Chem. Soc.* **127**, 12816 (2005).
50. I. Pastoriza-Santos, L. M. Liz-Marzin, *Langmuir* **18**, 2888 (2002).
51. N. R. Jana, X. Peng, *J. Am. Chem. Soc.* **125**, 14280 (2003).
52. G. S. Fonseca, A. P. Umpierre, P. F. P. Fichtner, S. R. Teixeira, J. Dupont, *Chem. Eur. J.* **9**, 3263 (2003).
53. H. Itoh, K. Naka, Y. Chujo, *J. Am. Chem. Soc.* **126**, 3026 (2004).
54. Y. Yin, A. P. Alivisatos, *Nature* **437**, 664 (2005).
55. X. Younan, X. Yujie, L. Byungkwon, E. S. Sara *Angew. Chem., Int. Ed* **48**, 60 (2009).
56. C. J. Murphy *et al.*, *J. Phys. Chem. B* **109**, 13857 (2005).
57. C. A. Foss, G. L. Hornyak, J. A. Stockert, C. R. Martin, *J. Phys. Chem.* **96**, 7497 (1992).
58. S.-S. Chang, C.-W. Shih, C.-D. Chen, W.-C. Lai, C. R. C. Wang, *Langmuir* **15**, 701 (1999).
59. F. Kim, J. H. Song, P. Yang, *J. Am. Chem. Soc.* **124**, 14316 (2002).
60. N. R. Jana, L. Gearheart, C. J. Murphy, *Adv. Mater.* **13**, 1389 (2001).
61. X. Huang, S. Neretina, M. A. El-Sayed, *Adv. Mater.* **21**, 4880 (2009).
62. S. Eustis, M. A. El-Sayed, *Chem. Soc. Rev.* **35**, 209 (2006).
63. P. Mulvaney, *Langmuir* **12**, 788 (1996).
64. K. L. Kelly, E. Coronado, L. L. Zhao, G. C. Schatz, *J. Phys. Chem. B* **107**, 668 (2002).
65. C. F. Bohren, D. R. Huffman, *Absorption and Scattering of Light by Small Particles*. (Wiley, New York, 1983).
66. L. Genzel, T. P. Martin, U. Kreibig, *Z. Phys. B* **21**, 339 (1975).
67. G. Mie, *Ann. Phys.* **25** 377 (1908).
68. S. Link, M. A. El-Sayed, *J. Phys. Chem. B* **103**, 4212 (1999).
69. R. Gans, *Ann. Phys.* **37**, 881 (1912).
70. C. A. Foss, G. L. Hornyak, J. A. Stockert, C. R. Martin, *J. Phys. Chem.* **98**, 2963 (1994).
71. S. Link, M. A. El-Sayed, *J. Phys. Chem. B* **109**, 10531 (2005).
72. S. Link, M. B. Mohamed, M. A. El-Sayed, *J. Phys. Chem. B* **103**, 3073 (1999).
73. F. o. H. Julien, A. Alexandrou, *Science* **282**, 1429 (1998).
74. U. Zulicke, *Science* **295**, 810 (2002).

75. M. Sundaram, S. A. Chalmers, P. F. Hopkins, A. C. Gossard, *Science* **254**, 1326 (1991).
76. C. B. Murray, D. J. Norris, M. G. Bawendi, *J. Am. Chem. Soc.* **115**, 8706 (1993).
77. B. O. Dabbousi *et al.*, *J. Phys. Chem. B* **101**, 9463 (1997).
78. M. A. Hines, P. Guyot-Sionnest, *J. Phys. Chem.* **100**, 468 (1996).
79. U. K. Gautam, M. Rajamathi, F. Meldrum, P. Morgan, R. Seshadri, *Chem. Commun.* 629 (2001).
80. B. Ludolph, M. A. Malik, P. O'Brien, N. Revaprasadu, *Chem. Commun.*, 1849 (1998).
81. N. Pradhan, S. Efrima, *J. Am. Chem. Soc.* **125**, 2050 (2003).
82. L. Manna, D. J. Milliron, A. Meisel, E. C. Scher, A. P. Alivisatos, *Nat. Mater.* **2**, 382 (2003).
83. J. E. Halpert, V. J. Porter, J. P. Zimmer, M. G. Bawendi, *J. Am. Chem. Soc.* **128**, 12590 (2006).
84. A. G. Kanaras, C. Sannichsen, H. Liu, A. P. Alivisatos, *Nano Lett.* **5**, 2164 (2005).
85. N. Pinna, G. Garnweitner, M. Antonietti, M. Niederberger, *J. Am. Chem. Soc.* **127**, 5608 (2005).
86. L. S. Panchakarla, A. Govindaraj, C. N. R. Rao, *J. Cluster Sci.* **18**, 660 (2007).
87. L. E. Brus, *J. Chem. Phys.* **79**, 5566 (1983).
88. A. L. Efros, M. Rosen, *Phys. Rev. B* **58**, 7120 (1998).
89. C. B. Murray, C. R. Kagan, M. G. Bawendi, *Annu. Rev. Mater. Sci.* **30**, 545 (2003).
90. H. Landolt, R. Bornestein, *Numerical Data and Functional Relationships in Science and Technology*. (Springer-Verlag, Berlin, 1961).
91. X. Peng *et al.*, *Nature* **404**, 59 (2000).
92. J. Hu *et al.*, *Science* **292**, 2060 (2001).
93. R. S. Knox, *Theory of Excitons*. (Academic Press, New York, 1963).
94. Y. Kayanuma, *Phys. Rev. B* **38**, 9797 (1988).
95. L. E. Brus, *J. Chem. Phys.* **80**, 4403 (1984).
96. C. J. Sandroff, D. M. Hwang, W. M. Chung, *Phys. Rev. B* **33**, 5953 (1986).
97. W. W. Yu, L. Qu, W. Guo, X. Peng, *Chem. Mater.* **15**, 2854 (2003).
98. X. Peng, J. Wickham, A. P. Alivisatos, *J. Am. Chem. Soc.* **120**, 5343 (1998).

99. S. Hotchandani, P. V. Kamat, *J. Phys. Chem.* **96**, 6834 (1992).
100. P. V. Kamat, B. Patrick, *J. Phys. Chem.* **96**, 6829 (1992).
101. W. G. Becker, A. J. Bard, *J. Phys. Chem.* **87**, 4888 (1983).
102. M. Haase, H. Weller, A. Henglein, *J. Phys. Chem.* **92**, 4706 (1988).
103. K. R. Gopidas, P. V. Kamat, *Mater. Lett.* **9**, 372 (1990).
104. N. Chestnoy, T. D. Harris, R. Hull, L. E. Brus, *J. Phys. Chem.* **90**, 3393 (1986).
105. A. Aharoni, *Introduction to the Theory of Ferromagnetism*. (Clarendon Press, Oxford, 2001).
106. R. Skomski, *J. Phys.: Condens. Matter* **15**, R841 (2003).
107. J. P. Bucher, D. C. Douglass, L. A. Bloomfield, *Phys. Rev. Lett.* **66**, 3052 (1991).
108. I. M. L. Billas, A. Chatelain, W. A. de Heer, *Science* **265**, 1682 (1994).
109. E. E. Fullerton, J. S. Jiang, C. H. Sowers, J. E. Pearson, S. D. Bader, *App. Phys. Lett.* **72**, 380 (1998).
110. S. Jung, B. Watkins, L. DeLong, J. B. Ketterson, V. Chandrasekhar, *Phys. Rev. B* **66**, 132401 (2002).
111. U. Ebels *et al.*, *Phys. Rev. B* **64**, 144421 (2001).
112. A. E. Berkowitz *et al.*, *Phys. Rev. Lett.* **68**, 3745 (1992).
113. J. Q. Xiao, J. S. Jiang, C. L. Chien, *Phys. Rev. Lett.* **68**, 3749 (1992).
114. D. Weller, A. Moser, *IEEE Trans. Mag.* **35**, 4423 (1999).
115. R. D. Shull, *IEEE Trans. Mag.* **29**, 2614 (1993).
116. L. X. Tiefenauer, G. Kuehne, R. Y. Andres, *Bioconjugate Chem.* **4**, 347 (1993).
117. C. R. Martin, P. Kohli, *Nat. Rev. Drug Discov.* **2**, 29 (2003).
118. L. An-Hui, E. L. Salabas, S. Ferdi, *Angew. Chem., Int. Ed* **46**, 1222 (2007).
119. X.-M. Lin, A. C. S. Samia, *J. Magn. Magn. Mater.* **305**, 100 (2006).
120. Z. L. Wang, Z. Dai, S. Sun, *Adv. Mater.* **12**, 1944 (2000).
121. C. Petit *et al.*, *Adv. Mater.* **11**, 1198 (1999).
122. P. D. Dmitry, M. G. Bawendi, *Angew. Chem., Int. Ed* **38**, 1788 (1999).
123. C. T. Black, C. B. Murray, R. L. Sandstrom, S. Sun, *Science* **290**, 1131 (2000).
124. T. Hyeon, S. S. Lee, J. Park, Y. Chung, H. B. Na, *J. Am. Chem. Soc.* **123**, 12798 (2001).
125. Y. Cui, Q. Wei, H. Park, C. M. Lieber, *Science* **293**, 1289 (2001).
126. E. V. Shevchenko *et al.*, *J. Am. Chem. Soc.* **124**, 11480 (2002).
127. S. Sun *et al.*, *J. Am. Chem. Soc.* **126**, 273 (2003).

128. X. Batlle, A. Labarta, *J. Phys. D: Appl. Phys* **35**, R15 (2002).
129. B. D. Cullity, *Introduction to Magnetic Materials*. (Addison-Wesley Publishing 1972).
130. William Fuller Brown, Jr., *37th Annual conference on magnetism and magnetic materials* **30**, S130 (1959).
131. H. N. Bertram, H. Zhou, R. Gustafson, *IEEE Trans. Mag.* **34**, 1845 (1998).
132. S. H. Charap, P. L. Lu, Y. He, *IEEE Trans. Mag.* **33**, 978 (1997).
133. D. Weller *et al.*, *IEEE Trans. Mag.* **36**, 10 (2000).
134. T. Mahalingam, et al., *J. Phys.: Condens. Matter* **15**, 2561 (2003).
135. Y. H. Huang, Y. Zhang, G. C. Hadjipanayis, D. Weller, *37th Annual conference on magnetism and magnetic materials* **93**, 7172 (2003).
136. R. V. Chepulskii, W. H. Butler, *Phys. Rev. B* **72**, 134205 (2005).
137. W. Kratschmer, L. D. Lamb, K. Fostiropoulos, D. R. Huffman, *Nature* **347**, 354 (1990).
138. S. Iijima, *Nature* **354**, 56 (1991).
139. K. S. Novoselov *et al.*, *Proc. Natl. Acad. Sci. U.S.A.* **102**, 10451 (2005).
140. K. S. Novoselov *et al.*, *Nature* **438**, 197 (2005).
141. C. N. R. Rao, A. Govindaraj, *Nanotubes and Nanowires*. (Royal Society of Chemistry, Cambridge, 2005).
142. D. T. Colbert *et al.*, *Science* **266**, 1218 (1994).
143. C. Journet *et al.*, *Nature* **388**, 756 (1997).
144. T. Guo, P. Nikolaev, A. Thess, D. T. Colbert, R. E. Smalley, *Chem. Phys. Lett.* **243**, 49 (1995).
145. A. Moisala, A. G. Nasibulin, E. I. Kauppinen, *J. Phys.: Cond. Matt.* **15**, S3011 (2003).
146. P. B. Balbuena *et al.*, *J. Nanosci. Nanotechnol.* **6**, 1247 (2006).
147. I. W. Chiang *et al.*, *J. Phys. Chem. B* **105**, 8297 (2001).
148. M. S. Arnold, A. A. Green, J. F. Hulvat, S. I. Stupp, M. C. Hersam, *Nat. Nanotechnol.* **1**, 60 (2006).
149. S. Iijima, *MRS Bulletin* **19**, 43 (1994).
150. J. W. Mintmire, B. I. Dunlap, C. T. White, *Phys. Rev. Lett.* **68**, 631 (1992).
151. N. Hamada, S.-i. Sawada, A. Oshiyama, *Phys. Rev. Lett.* **68**, 1579 (1992).

152. R. Saito, M. Fujita, G. Dresselhaus, M. S. Dresselhaus, *Appl. Phys. Lett.* **60**, 2204 (1992).
153. J. W. G. Wilder, L. C. Venema, A. G. Rinzler, R. E. Smalley, C. Dekker, *Nature* **391**, 59 (1998).
154. T. W. Odom, J.-L. Huang, P. Kim, C. M. Lieber, *Nature* **391**, 62 (1998).
155. M. Ouyang, J.-L. Huang, C. M. Lieber, *Acc. Chem. Res.* **35**, 1018 (2002).
156. M. A. Hamon *et al.*, *J. Am. Chem. Soc.* **123**, 11292 (2001).
157. S. Amelinckx, et al., *Rep. Prog. Phys.* **62**, 1471 (1999).
158. A. K. Geim, K. S. Novoselov, *Nat. Mater.* **6**, 183 (2007).
159. C. N. R. Rao, A. K. Sood, K. S. Subrahmanyam, A. Govindaraj, *Angew. Chem. Int. Ed* **48**, 7752 (2009).
160. S. Park, R. S. Ruoff, *Nat. Nanotechnol.* **4**, 217 (2009).
161. S. F. Braga *et al.*, *Nano Lett.* **4**, 881 (2004).
162. L. M. Viculis, J. J. Mack, R. B. Kaner, *Science* **299**, 1361 (2003).
163. X. Xie *et al.*, *Nano Lett.* **9**, 2565 (2009).
164. S. Wang *et al.*, *J. Am. Chem. Soc.* **131**, 16832 (2009).
165. R. E. Peierls, *Ann. Inst. Henri Poincare* **5**, 177 (1935).
166. R. E. Peierls, *Helv. Phys. Acta* **7**, 81 (1934).
167. L. D. Landau, *Phys. Z. Sowjetunion* **11**, 26 (1937).
168. N. D. Mermin, *Phys. Rev.* **176**, 250 (1968).
169. N. D. Mermin, H. Wagner, *Phys. Rev. Lett.* **17**, 1133 (1966).
170. J. W. Evans, P. A. Thiel, M. C. Bartelt, *Surf. Sci. Rep.* **61**, 1 (2006).
171. M. Zinke-Allmang, L. C. Feldman, M. H. Grabow, *Surf. Sci. Rep.* **16**, 377 (1992).
172. J. C. Meyer *et al.*, *Nature* **446**, 60 (2007).
173. J. Y. Huang *et al.*, *Nature* **439**, 281 (2006).
174. J. C. Slonczewski, P. R. Weiss, *Phys. Rev.* **109**, 272 (1958).
175. M. I. Katsnelson, *Mater. Today* **10**, 20 (2008).
176. G. W. Semenoff, *Phys. Rev. Lett.* **53**, 2449 (1984).
177. J. González, F. Guinea, M. A. H. Vozmediano, *Phys. Rev. Lett.* **77**, 3589 (1996).
178. M. I. Katsnelson, K. S. Novoselov, A. K. Geim, *Nat. Phys.* **2**, 620 (2006).
179. E. Stolyarova *et al.*, *Proc. Natl. Acad. Sci. U.S.A.* **104**, 9209 (2007).
180. S. Stankovich *et al.*, *Carbon* **45**, 1558 (2007).

181. M. S. Dresselhaus, G. Dresselhaus, K. Sugihara, I. L. Spain, H. A. Goldberg, *Graphite Fibers and Filaments*. (Springer-Verlag, Berlin, 1988), vol. 5.
182. L. M. Malard, M. A. Pimenta, G. Dresselhaus, M. S. Dresselhaus, *Phys. Rep.* **473**, 51 (2009).
183. M. S. Dresselhaus, A. Jorio, M. Hofmann, G. Dresselhaus, R. Saito, *Nano Lett.* **10**, 751(2010).
184. A. C. Ferrari, J. Robertson, *Phil. Trans. R. Soc. Lond. A* **362**, 2477 (2004).
185. Z. H. Ni *et al.*, *ACS Nano* **2**, 2301 (2008).
186. M. S. Dresselhaus, G. Dresselhaus, R. Saito, A. Jorio, *Phys. Rep.* **409**, 47 (2005).
187. M. S. Dresselhaus, P. C. Eklund, *Adv. Phys.* **49**, 705 (2000).
188. M. S. Dresselhaus, G. Dresselhaus, A. Jorio, A. G. Souza Filho, R. Saito, *Carbon* **40**, 2043 (2002).
189. S. B. Cronin *et al.*, *Phys. Rev. Lett.* **93**, 167401 (2004).
190. O. Dubay, G. Kresse, H. Kuzmany, *Phys. Rev. Lett.* **88**, 235506 (2002).
191. S. Piscanec, M. Lazzeri, F. Mauri, A. C. Ferrari, J. Robertson, *Phys. Rev. Lett.* **93**, 185503 (2004).
192. K.-i. Sasaki *et al.*, *Phys. Rev. B* **77**, 245441 (2008).
193. P. T. Araujo *et al.*, *Phys. Rev. B* **77**, 241403 (2008).
194. A. Jorio *et al.*, *Phys. Rev. B* **71**, 075401 (2005).
195. G. G. Samsonidze *et al.*, *Appl. Phys. Lett.* **85**, 5703 (2004).
196. R. Saito *et al.*, *Phys. Rev. Lett.* **88**, 027401 (2001).
197. I. O. Maciel *et al.*, *Nat. Mater.* **7**, 878 (2008).
198. M. A. Pimenta *et al.*, *Phys. Chem. Chem. Phys.* **9**, 1276 (2007).
199. M. M. Lucchese *et al.*, *Carbon* **48**, 1592 (2010).

CHAPTER 2

Use of Fluorous Chemistry for the Synthesis and Purification of Nanomaterials

Summary*

This chapter deals with the synthesis and purification of nanomaterials using fluorous chemistry. Fluorous chemistry, involving the use of a fluorous label for the functionalization of a substrate and a fluorous solvent for extraction of the functionalized substrate, is shown to be effective in solubilizing gold and CdSe nanoparticles in a fluorous medium, through phase transfer from an aqueous or a hydrocarbon medium. While these nanoparticles were functionalized with a fluorous thiol, single-walled carbon nanotubes and ZnO nanorods could be solubilized in a fluorous medium by reacting them with a fluorous amine.

By making use of the fact that perfluorohydrocarbon and hydrocarbon solvents become miscible at high temperatures, highly pure inorganic nanoparticles capped with fluorous labels have been generated in a one-step synthesis. By employing this procedure, we have prepared nanoparticles of metal chalcogenides such as CdSe, CdS, PbSe, ZnSe and of metal oxides such as γ-Fe_2O_3 and ZnO and of bimetallic FePt in one pot.

Papers based on these studies have appeared in Journal of Physical Chemistry B (Letter) (2006) and Dalton Transactions (communication) (2010)

2.1 Introduction

Fluorous synthesis is a recent addition to the arsenal of synthetic and separation techniques which integrates solution phase reaction conditions with phase tag separation (*1-5*). The fluorous medium constitutes a liquid phase which is orthogonal to organic and aqueous liquid phases. The technique is attractive, since fluorous-tag compounds can be quickly separated from the untagged compounds. Separation and recovery in fluorous chemistry generally utilizes fluorous/organic as well as fluorous/aqueous extraction, since the fluorous phase forms a layer distinct from both aqueous and hydrocarbon layers (see Figure 2.1). One generally attaches the substrate to a fluorous phase label that has sufficient fluorine content and the product extracted into a perfluorohydrocarbon. Such separation is based on fluorine-fluorine interaction between the fluorous reagent and the fluorous separation medium. It is also to be noted that perfluorohydrocarbons provide the most nonpolar medium possible, since they have very low refractive indices (~1.2), even compared to hydrocarbons such as toluene

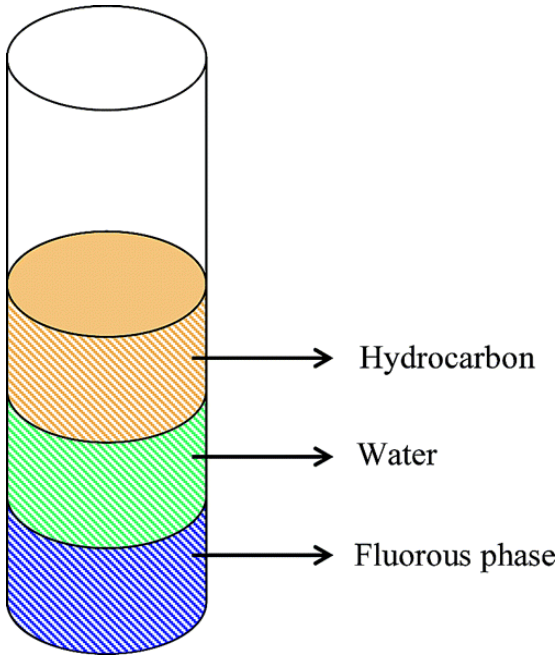

Figure 2.1: Schematic showing three immiscible layers of a hydrocarbon, water and a fluorocarbon.

(~1.4). We considered it rewarding to explore how fluorous chemistry can be used effectively for the synthesis and separation/solubilization of nanocrystals, oxide nanorods and carbon nanotubes. Another interesting property of perfluorocarbon is the fact that perfluorohydrocarbons (PFC) and hydrocarbons become miscible at high temperatures and become biphasic only on cooling to room temperature. Temperature dependent miscibility represents one of many types of thermomorphic behavior (*5*). We have used this thermomorphic behavior for one-step synthesis cum purification of inorganic nanoparticles.

In the literature, nanoparticles have been obtained in aqueous and hydrocarbon media in different ways. Thus, Brust *et al*. (*6*) synthesized thiol-derivatized gold nanoparticles in a two-phase liquid-liquid system by transferring the metal salt from the aqueous medium to toluene using tetraoctylammoniumbromide as the phase-transfer reagent. Thiol derivatized nanoparticles of Au, Pt and Ag have been prepared as organosols by the acid-facilitated transfer of the nanoparticles from a hydrosol to a toluene layer containing an alkanethiol (*7*). Schulz-Dobrick *et al*. (*8*) have dispersed gold nanoparticles prepared by the reduction of tetrachloroaurate by sodium naphthalide in diglyme in various hydrocarbon solvents. Recently Ying *et al*. (*9*) developed general phase-transfer protocol for metal ions and its application in nanocrystal synthesis. Fluorous capped nanoparticles are of special interest due to their high purity as well as the superhydrophobic nature (*10, 11*). Fluorinated alkanethiol stabilized gold and silver nanoparticles have been prepared in a fluorocarbon solvent (*12, 13*). A number of other fluorous capped nanoparticles (*5*) and self assembled monolayers (SAM) (*14*) on planar surfaces based on fluorous ligands or stabilizing coatings have been reported, including Ir, Pt, Pd and FePt (*10, 15-18*). Fluorinated alkylthiol protected gold nanoparticle film has been used as vapor sensor (*19*). Fluorous chemistry has been effectively used to separate metallic from semiconducting single-walled carbon nanotubes (SWNTs) (*20*).

In another report cycloaddition of fluorinated olefins has been used for converting as-grown commercial SWNT mats into high-mobility semiconducting tubes with high yield and without further need for carbon nanotube separation (*21*). We report the scope of the present investigations in the next section.

2.2 Scope of the present investigations

Nanoparticles of different materials have been synthesized by various chemical as well as physical methods. There are only few reports on the synthesis of fluorous capped nanoparticles but phase transfer of such nanoparticles from an aqueous or a hydrocarbon medium to a fluorous phase has not been examined. We have used two novel strategies for the synthesis and phase transfer of fluorous capped nanostructures. The first strategy is based on the fact that, fluorine-fluorine interaction between the fluorous reagent and the fluorous separation medium. This process is shown to be effective in solubilizing gold and CdSe nanoparticles in a fluorous medium, through phase transfer from an aqueous or a hydrocarbon medium using fluorous thiol. Single-walled carbon nanotubes and ZnO nanorods have been solubilized in a fluorous medium by reacting them with a fluorous amine. We have followed the phase transfer process by optical absorption spectroscopy, scanning electron microscopy (SEM), transmission electron microscopy (TEM) and Raman spectroscopy.

The second strategy employed by us is based on the fact that fluorous and organic solvents usually mix at elevated temperature. We have prepared nanoparticles of metal chalcogenides such as CdSe, CdS, PbSe, ZnSe and of metal oxides such as γ-Fe_2O_3 and ZnO and of bimetallic FePt. The synthesized nanoparticles have been characterized by optical absorption spectroscopy, photoluminescence spectroscopy, transmission electron microscopy. Magnetic measurements have been studied for γ-Fe_2O_3 and of bimetallic FePt.

2.3 Experimental

2.3.1 Phase transfer of nanocrystals, nanorods, and nanotubes

Gold nanoparticles: To transfer gold nanoparticles from an aqueous to a perfluorohexane medium, the gold nanoparticles are prepared by literature procedure (*22, 23*). In a typical preparation, a hydrosol containing small clusters of Au was first prepared by the reduction of chloroaurate ions (0.55 ml of 25 mM aqueous solution) using partially hydrolysed tetrakis(hydroxymethyl)phosphoniumchloride (THPC), having prepared the latter by adding 1 ml of a fresh 50 mM solution of THPC in water to 47 ml of 6.38 mm NaOH solution. To the gold sol so obtained, a solution of 10 µl of heptadecafluoro-1-decanthiol (HDFD) in 25 ml of perfluorohexane was added at room temperature, to obtain two immiscible layers consisting of the transparent fluorous phase containing the thiol on the bottom and the colored hydrosol at the top. To this biphasic mixture, 30 ml of conc. HCl was added under vigorous stirring. This resulted in a remarkably swift movement (within 5 min) of the Au nanoparticles to the fluorocarbon layer containing the thiol. Clearly, the gold particles have an inherent attraction to the thiol molecules. This could be seen vividly by the complete transfer of color across the interface to the fluorocarbon layer as shown in Figure 2.2 (a).

We have also been able to carry out the phase transfer of gold nanoparticles from toluene to the fluorous phase. For this purpose, we prepared an organosol of gold nanoparticles in toluene by transferring gold nanoparticles from the aqueous medium to the toluene medium by following the literature procedure (*7*), but by using the fluorous thiol. We added a solution of 10 µl of HDFD in 20 ml of perfluorohexane to 10 ml of the thiolated gold sol in toluene under vigorous stirring. Within 5 min, the thiolated gold nanoparticles were completely extracted into the perfluorohexane medium, as can be seen from Figure 2.2 (b).

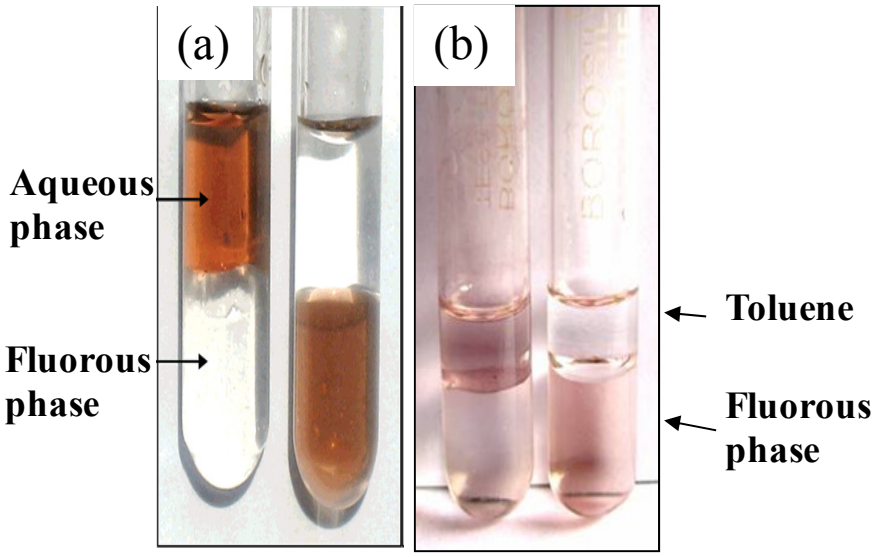

Figure 2.2: Photographs showing transfer of gold nanoparticles (color) (a) from an aqueous medium to fluorous medium and (b) from toluene to the fluorous medium

CdSe nanoparticles: Phase transfer of an organosol of CdSe in a hydrocarbon solvent to the fluorous medium could be carried out as follows. CdSe nanoparticles of 2.5 nm diameter were prepared by reacting cadmium stearate (50 mg, 0.07 mmol) with selenium (6 mg, 0.07 mmol) and tetralin (7.5 µl, 0.05 mmol) in 20 ml of toluene in the presence of HDFD (5.5 µl, 0.02 mmol) for 5 h at 250 °C in a Teflon-lined stainless steel autoclave (40 ml capacity) (*24*).

CdSe nanoparticles of 4.5 nm diameter were prepared by increasing the concentrations of cadmium stearate to 1 g (1.4 mmol), selenium to 120 mg (1.4 mmol), tetralin to 150 µl (1 mmol), and HDFD to 110 µl (0.4 mmol) keeping the amount of toluene and reaction conditions constant. We obtained two different colored CdSe nanoparticles which were precipitated by adding 2-propanol and redispersed in toluene. Upon adding the toluene solution of HDFD-capped CdSe nanoparticles (10 ml) to 10 ml of perfluorohexane under vigorous stirring, we observed a complete transfer of the particles from toluene to the perfluorohexane medium. This can be seen from the Figure 2.3.

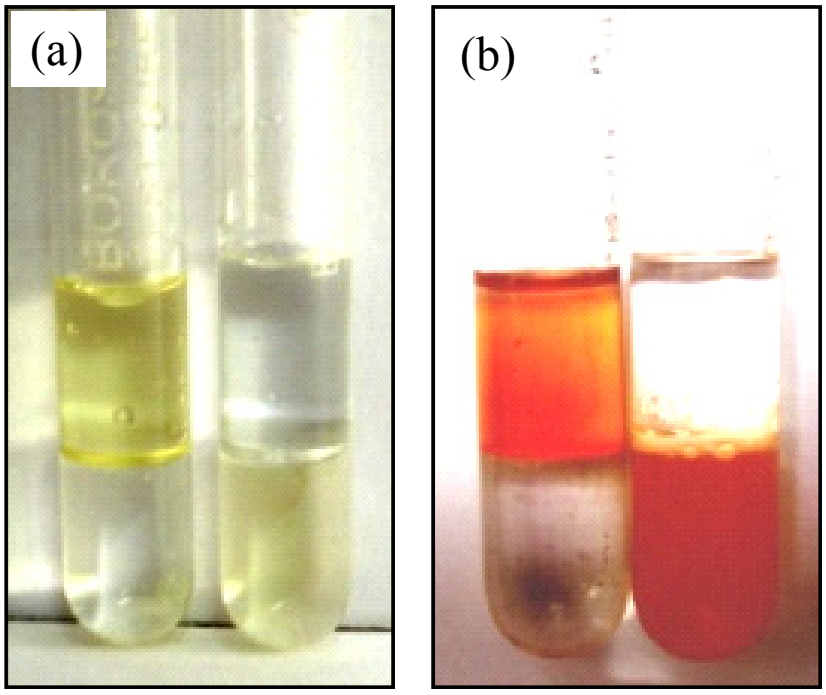

Figure 2.3: Photographs showing transfer of CdSe nanoparticles with average diameter (a) 2.5 nm and (b) 4.5 nm from toluene (upper layer) to perfluorohexane (lower layer).

Single-walled carbon nanotubes: We could solubilize purified single-walled carbon nanotubes (SWNTs) (*25*) in the fluorous medium by reacting them with heptadecafluoroundecylamine. For this purpose, we first prepared SWNTs by the arc discharge method and purified them by HNO_3 and H_2 treatment (*25*). To solubilize the nanotubes, 1.5 mg of SWNTs, 22 μl of the heptadecafluoroundecylamine (SWNTs /amine, 2:1), and 3 ml of perfluorohexanne were sealed in a 7 ml Teflon-lined stainless steel autoclave and heated at 130 °C for 48 h. This process produced a clear solution of SWNTs in perfluorohexane.

Zinc oxide nanorods: We prepared ZnO nanorods by the solvothermal decomposition of 250 mg (0.911 mmol) of zinc acetate dihydrate in the presence of 6 ml (0.102 mmol) of ethylenediamine, 3 ml (0.05 mmol) of ethanol, and 2 ml of Triton X-100 at 335 °C for 5 h in a swagelok autoclave (20 ml capacity) (*26*). The ZnO nanorods were washed several times with ethanol and precipitated by centrifuging. To solubilize

ZnO nanorods in perfluorohexane, 2 mg of ZnO nanorods, 12 µl of heptadecafluoroundecylamine (ZnO nanorods/amine, 1:1), and 3 ml of perfluoro-hexane were sealed in a 7 ml Teflon-lined stainless steel autoclave and heated at 130 °C for 48 h. This process produced a clear solution of ZnO nanorods in perfluorohexane.

2.3.2 One-step synthesis fluorous-capped inorganic nanoparticles

The synthetic procedure involves first taking appropriate metal precursors and other reagents in a hydrocarbon solvent such as toluene. To this mixture, the required quantity of the fluorous label (which caps the product) is added along with perfluorohexane. The reaction is carried out under solvotheramal or refluxing conditions (Figure 2.4). We have used perfluorodecanethiol as the capping agent for metal chalcogenides, heptadecafulorodecylamine for ZnO, and perfluorodecanoic acid for γ-Fe_2O_3 and FePt.

Metal chalcogenides: In a typical procedure to prepare fluorous-capped metal chalcogenides (CdSe, CdS, PbSe and ZnSe), the metal cupferronate or acetylacetonate (0.07 mmol) is taken along with selenium or sulphur (0.07 mmol), tetralin (7.5 µl) and a small quantity of perfluorodecanethiol (200 µl) in a mixture of 10 ml toluene and 10 ml perflurohexane (*24, 27*). The reaction mixture which was biphasic at room temperature was sealed in a stainless steel 30 ml teflon-lined autoclave and placed in an air oven preheated to 250ºC for 5h. After the reaction was complete, the autoclave was allowed to cool to room temperature and the contents were then transferred to a vial. The resulting product consisted of two layers with the perfluorodecanethiol-capped nanoparticles present in the perfluorohexane layer.

γ- Fe_2O_3 nanoparticles: Synthesis of fluorous-capped γ- Fe_2O_3 nanoparticles was carried out by the following procedure (*28*). Around 0.2 ml of $Fe(CO)_5$ (1.5mmol) was added to a mixture of 10 ml of dioctyl ether,10 ml of perfluorohexane and 1 g of perfluorodecanoic acid at 100ºC. The resulting mixture was heated to 250ºC and kept at

that temperature for 2 h. During this time, the initial orange color turned black. The reaction mixture was allowed to cool to room temperature. The iron nanoparticles in perfluorohexane upon exposure to air got oxidized to γ-Fe_2O_3 nanoparticles.

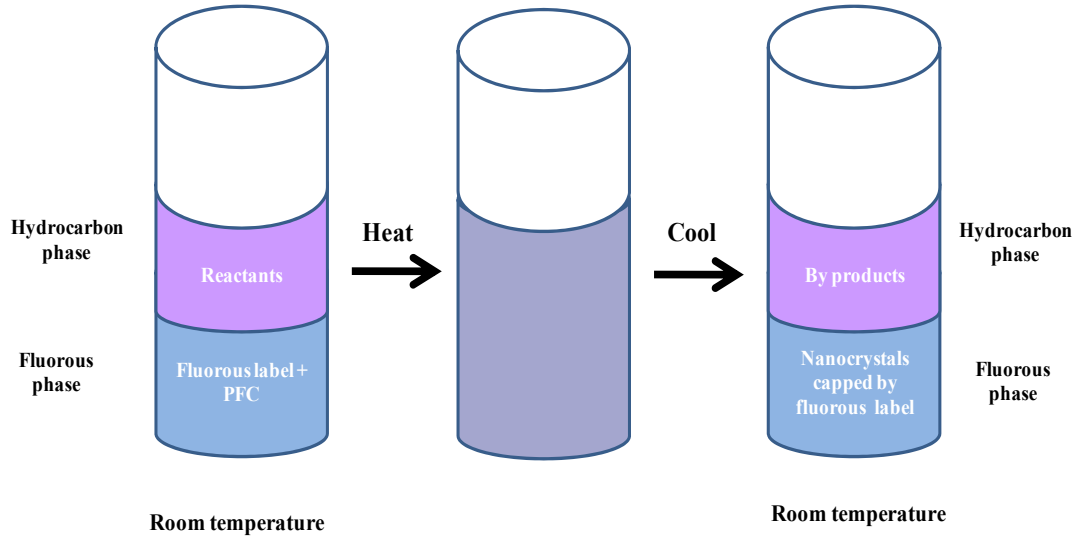

Figure 2.4: Schematic showing the thermomorphic nature of fluorous and hydrocarbon solvents. (Note that colors of different phases are given for visualization purpose only)

ZnO nanoparticles: Fluorous-capped ZnO nanoparticles (*29, 30*) were prepared starting with a mixture of 7.5 mg of $Zn(acac)_2$ with 150 mg of heptadecafluorodecylamine in the presence of 7.5 ml toluene and 10 ml perfluorohexane. The mixture was sealed in a stainless steel 25 ml teflon-lined autoclave placed for 20 h in an hot-air oven preheated to 250 ºC. On cooling, ZnO nanoparticles capped with heptadecafluorodecylamine dispersed in the denser fluorocarbon medium were obtained.

FePt nanoparticles: Fluorous-capped FePt nanoparticles were prepared as follows (*31*). Under a flow of nitrogen, $Pt(acac)_2$ (0.5 mmol) was mixed with benzyl ether (10 ml) and heated to 100 ºC. To this mixture, $Fe(CO)_5$ (1 mmol), heptadecafluoro-decylamine (5 mmol, 500 µl) perfluorodecanoic acid (5 mmol) and perfluorohexane (10 ml) were added under a flow of nitrogen. The mixture was heated to 250 ºC at a

heating rate of ~15 ºC/min to assure complete decomposition of $Fe(CO)_5$, and then mixture was refluxed for 1 hour. The reaction mixture was then cooled to room temperature to obtain pure FePt particles capped with heptadecafluorodecyl amine and perfluorodecanoic acid dispersed in perfluorohexane.

2.3.3 Techniques used for characterization

Powder X-ray diffraction

X-ray diffraction (XRD) patterns of the nitrides were recorded using Cu Kα radiation on a Rich-Siefert XRD-3000-TT diffractometer

Optical absorption and photoluminescence spectroscopy

The optical absorption spectroscopy measurements were performed using a Perkin-Elmer Lambda 900 UV/VIS/NIR spectrometer. Photoluminescence spectra of these solutions were recorded with a Perkin-Elmer model LS55 luminescence spectrometer.

Transmission electron microscopy

For transmission electron microscopy (TEM), perfluorohexane and aqeous dispersions of the samples were dropped onto the holey carbon-coated Cu grids, and the grids were allowed to dry in the air. The grids were examined using a JEOL (JEM3010) microscope operating with an accelerating voltage of 300 kV.

Magnetic characterization

Powder samples of the as-prepared nanoparticles were subjected to magnetic characterization using the VSM in PPMS (Physical Properties Measurement System).

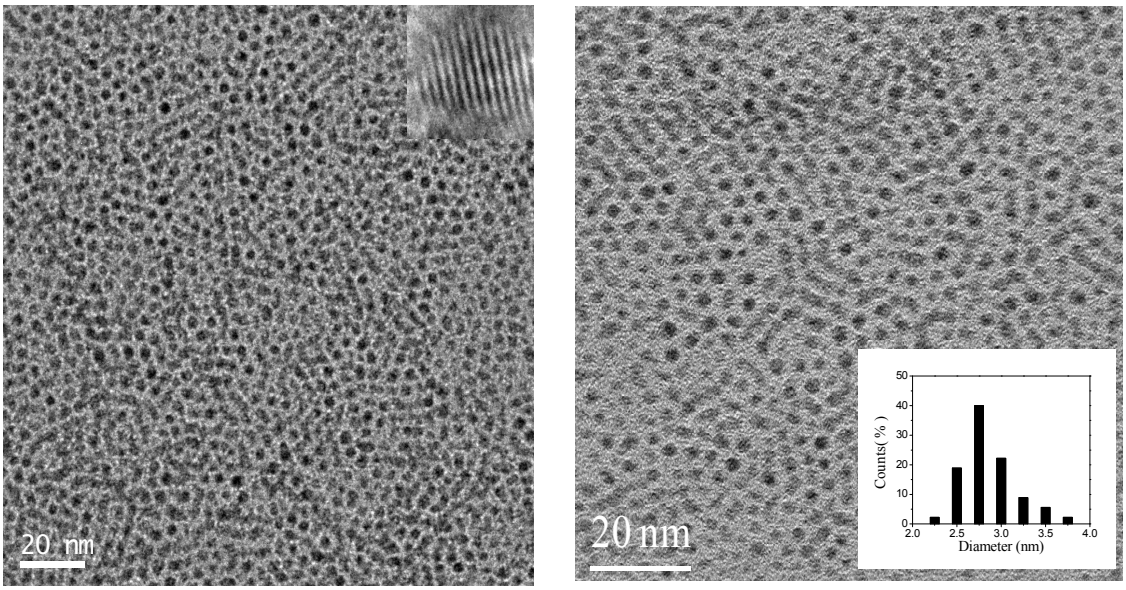

Figure 2.5: TEM image with a size distribution histogram as an inset of ~ 3 nm gold nanoparticles.

2.4 Results and discussion

2.4.1 Phase transfer of nanocrystals, nanorods and nanotubes

We shall first present the use of fluorous chemistry with gold nanoparticles. The transfer of gold nanoparticles from an aqueous to a perfluorohexane medium was described in the experimental section. In Figure 2.5, we show the transmission electron microscope (TEM) images of the gold nanoparticles from perfluorohexane solution, which reveals that the particles have an average diameter close to 3 nm. TEM images display a part of the regularly packed monolayer, which consists of monodisperse nanoparticles. Interestingly, these monolayers were extended over a wide area on the transmission electron microscopy (TEM) grid. The monolayer formed by gold nanoparticles is in hexagonal packing. Though several defects are visible in this image, they were generated by the electron beam irradiation. The formation of such a uniform monolayer is ascribed to the remarkably low surface tension and display high interfacial tension of perfluorohexane (16.2 mN/m), which can spread over the wide area of the

carbon grid with a uniform thickness. The constant interparticle distance in the hexagonal packed monolayer is attributable to the rigid fluorocarbon chains, which are radially organized around the nanoparticles.

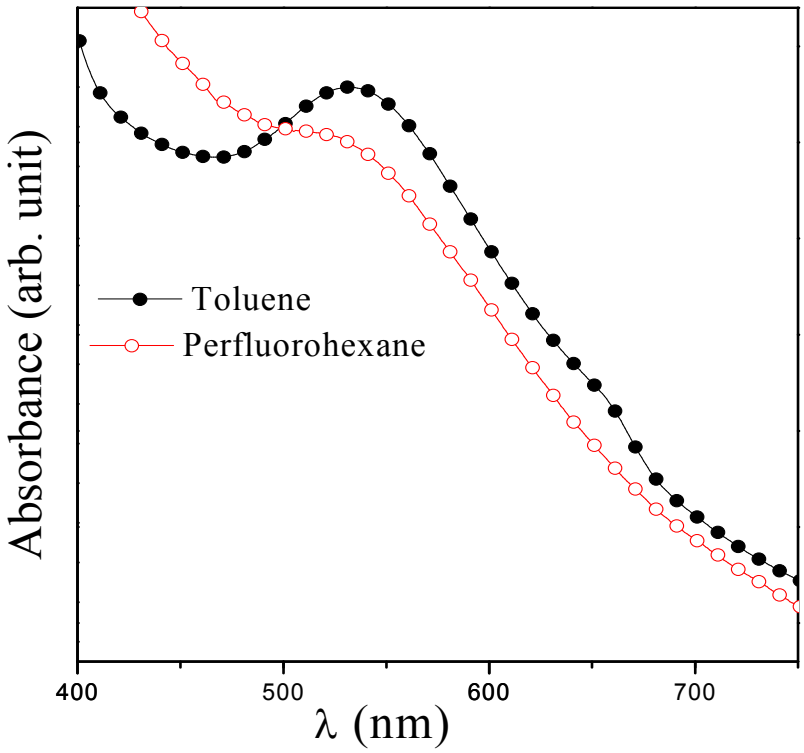

Figure 2.6: Optical absorption spectra of gold nanoparticles in toluene and in perfluorohexane.

The optical absorption spectra of the Au nanoparticles (Figure 2.6) in perfluoro-hexane shows the characteristic plasmon band at 520 nm. We have also been able to carry out the phase transfer of gold nanoparticles from toluene to the fluorous phase. For this purpose, we prepared an organosol of gold nanoparticles in toluene by transferring gold nanoparticles from the aqueous medium to the toluene medium using the procedure given in the experimental section. The optical absorption spectra of the gold nanoparticles in toluene and perfluorohexane are shown in Figure 2.6, with the absorption maximum in the fluorous solvent being blue shifted compared to that in toluene, due to the lower refractive index of perfluorohexane.

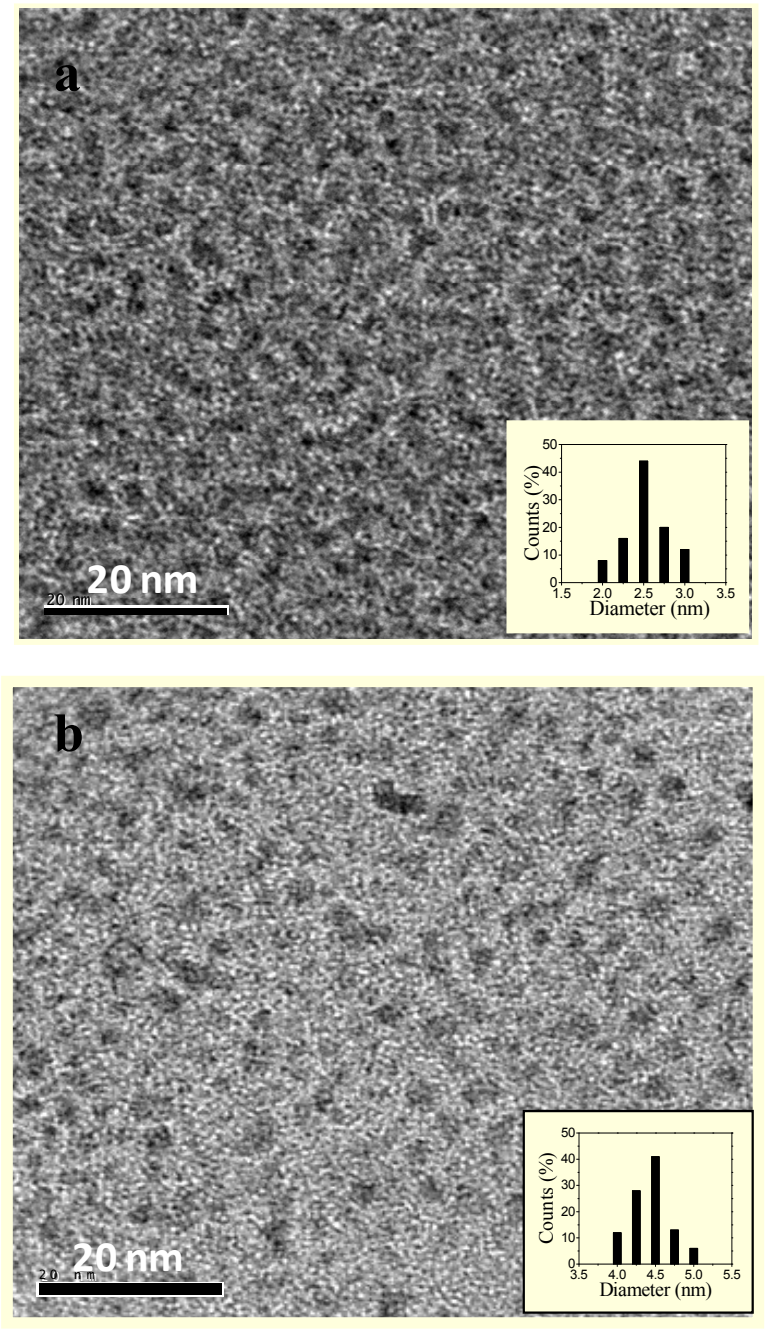

Figure 2.7: TEM images with size distribution histograms as insets of CdSe nanopaticles of average diameters of (a) 2.5 nm and (b) 4.5 nm solubilized in perfluorohexane.

Phase transfer of an organosol of CdSe in a hydrocarbon solvent to the fluorous medium could be carried out using the procedure given in the experimental section. We have prepared the two different sizes of CdSe nanoparticles by varying the reactant concentrations. Figure 2.7 (a) and (b) shows the TEM images with size distribution

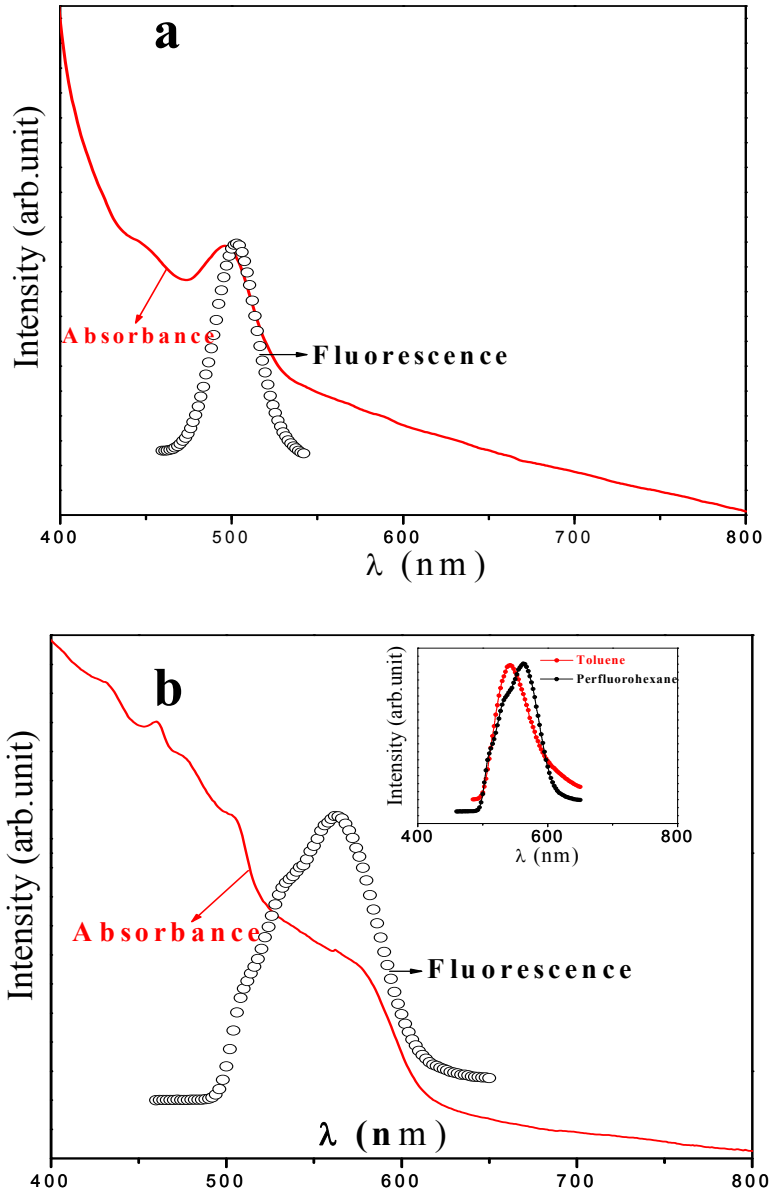

Figure 2.8: Optical absorption spectra and photoluminescence spectra of CdSe nanoparticles of average diameter of (a) 2.5 nm and (b) 4.5 nm in perfluorohexane. The inset in part b shows the PL emission spectra of 4.5 nm CdSe nanoparticles in toluene and perfluorohexane.

histograms (insets) of the 2.5 nm (yellow) and 4.5 nm (red) CdSe nanoparticles solubilized in perfluorohexane. The Figure 2.3 shows the photographs of the yellow and red CdSe nanoparticles transferred completely from toluene to the fluorous medium. Figure 2.8 (a) and (b) shows the optical absorption and photoluminescence (PL) spectra of the 2.5 and 4.5 nm CdSe nanoparticles solublilized in perfluorohexane. The optical

absorption spectrum of the 2.5 nm CdSe nanoparticles clearly shows an absorption band at 495 nm. The band is red shifted in the case of the 4.5 nm CdSe nanoparticles. The PL band of the 4.5 nm CdSe nanoparticles is also red shifted compared to that of the 2.5 nm nanoparticles. The inset in Figure 2.4 (d) compares the PL spectra of the CdSe nanoparticles in toluene and perfluorohexane solutions, showing a shift in the PL maximum due to the different refractive indices of the two liquids.

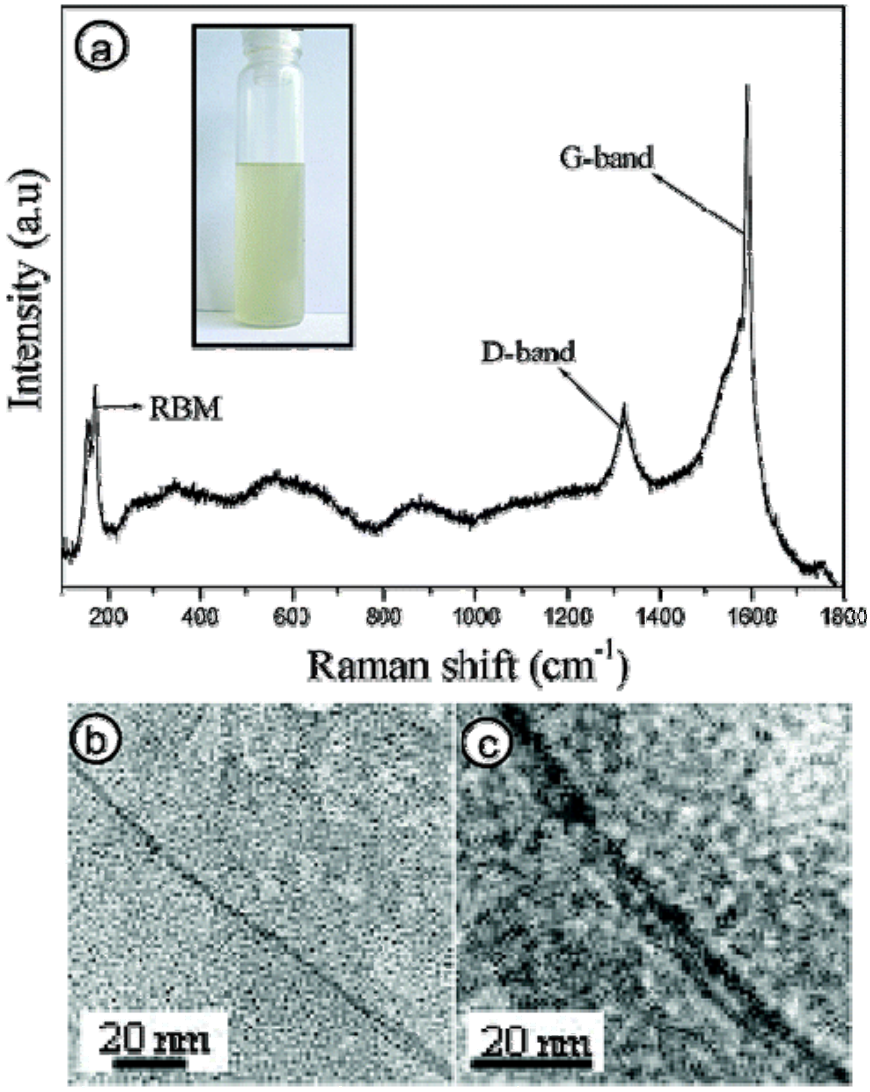

Figure 2.9: (a) Raman spectrum of SWNTs solubilized in perfluorohexane. The inset in part a shows the photograph of solution of SWNTs in perfluorohexane. TEM images of the solubilized SWNTs are shown in parts (b) and (c).

We could solubilize purified SWNTs (*25*) in the fluorous medium by reacting them with heptadecafluoroundecylamine. The process given in the experimental section produced a clear solution of SWNTs in perfluorohexane, as can be seen from Figure 2.9 (a). The solubilization of SWNTs appears to occur by the interaction of the -NH_2 groups of the amine with the -COOH groups present in the surface of the SWNTs (zwitterions type), as proposed by Chen *et al.* (*32*). The Raman spectrum of the solution gives the bands of SWNTs, especially the radial breathing modes (155 and 177 cm^{-1}). The D band arises due to defect introduced by acid functionalization. The TEM images in Figure 2.9 (b) and (c) show the presence of debundled SWNTs in the fluorous medium.

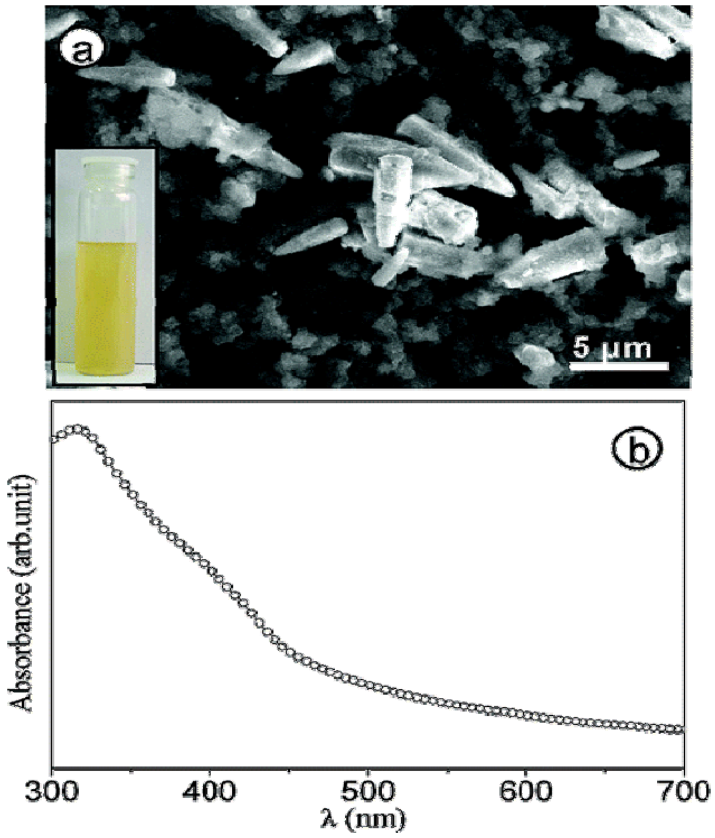

Figure 2.10: (a) SEM images of ZnO nanorods solubilized in perfluorohexane. The inset in part (a) shows the photograph of the solution of ZnO nanorods in perfluorohexane. (b) Optical absorption spectra of the solubilized ZnO nanorods.

We have extended the method of solubilization of SWNTs to oxide nanorods. This process produced a clear solution of ZnO nanorods in perfluorohexane. Scanning electron microscope (SEM) images shown in Figure 2.6 (a) indicate the presence of ZnO nanorods in perfluorohexane medium. In the inset of this figure, we show the photograph of the solution of ZnO nanorods in perfluorohexane. Figure 2.6 (b) shows the UV-vis absorption spectrum of ZnO nanorods solubilized in perfluorohexane.

The phase transfer protocols developed here can be applied to different nanostructures. The method employed here requires appropriate fluorous label for functionalization of a substrate and a fluorous solvent for extraction of the functionalized substrate. The fluorocarbon extracts only the species attached to the fluorous label, the process enables us to obtain solely one product in pure state.

2.4.2 One-step synthesis of fluorous-capped inorganic nanoparticles

A TEM image of perfluorodecanethiol capped CdSe nanoparticles dispersed in perfluorohexane obtained by the procedure reported in experimental section is shown in the Figure 2.11. The TEM image shows a narrow size distribution of nanoparticles, the average diameter of nanoparticles being around 4 nm. The photograph shown as an inset of Figure 2.11 (a) reveals a reddish brown solution of the fluorous-capped CdSe nanoparticles in the perfluorohexane layer. The XRD profile indicates that it has cubic zinc blende structure rather than the usual hexagonal wurtzite structure. Figure 2.12 (a) shows the optical absorption spectrum and the photoluminescence (PL) spectrum of the 4 nm CdSe nanoparticles. The absorption spectrum shows a band at 545 nm and the PL spectrum shows a band at 554 nm (excitation at 430 nm) characteristic of the 4 nm particles (*33*). The narrow PL band reflects the nearly monodisperse nature of the sample. The absorption and PL bands of the CdSe nanoparticles are red-shifted due to

the highly nonpolar nature of the perfluorohydrocarbon. The powder XRD pattern of the nanoparticles acquired in transmission mode is displayed in Figure 2.13 indexed to zinc blend structure.

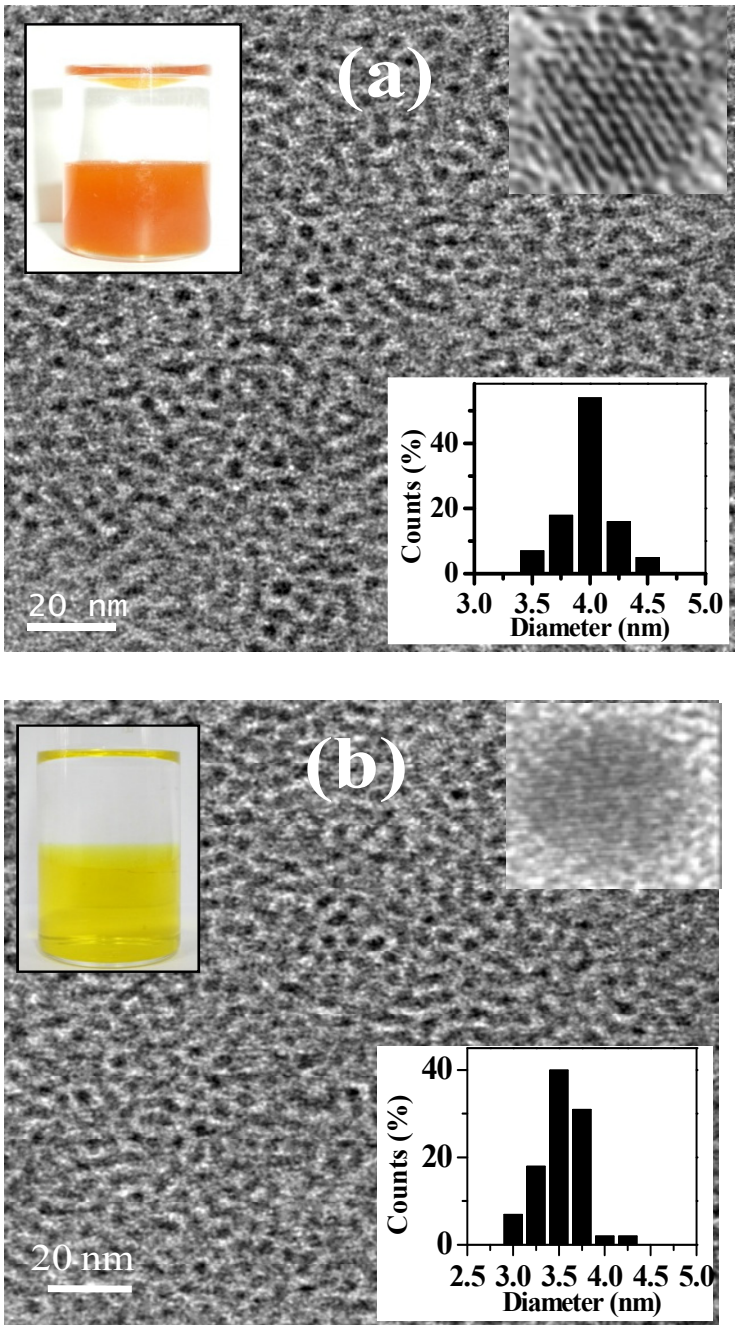

Figure 2.11: TEM images of (a) 4 nm CdSe and (b) 3.5 nm CdS nanoparticles with size distribution histograms as inset. Photographs of the dispersions of the nanoparticles in PFC are also given as insets. HRTEM images are also shown as insets.

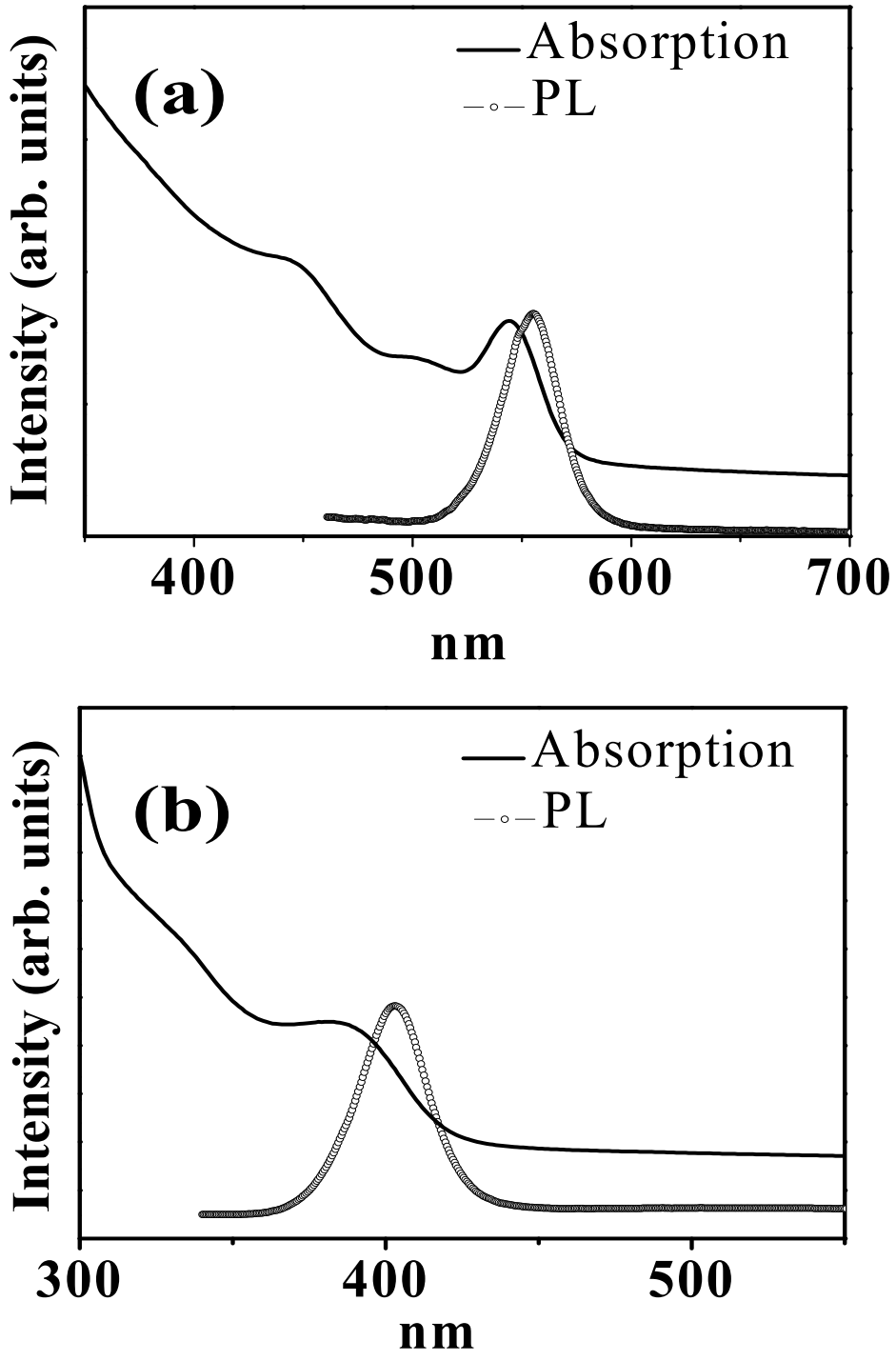

Figure 2.12: Optical absorption and photoluminescence spectra of (a) 4 nm CdSe and (b) 3.5 nm CdS nanoparticles.

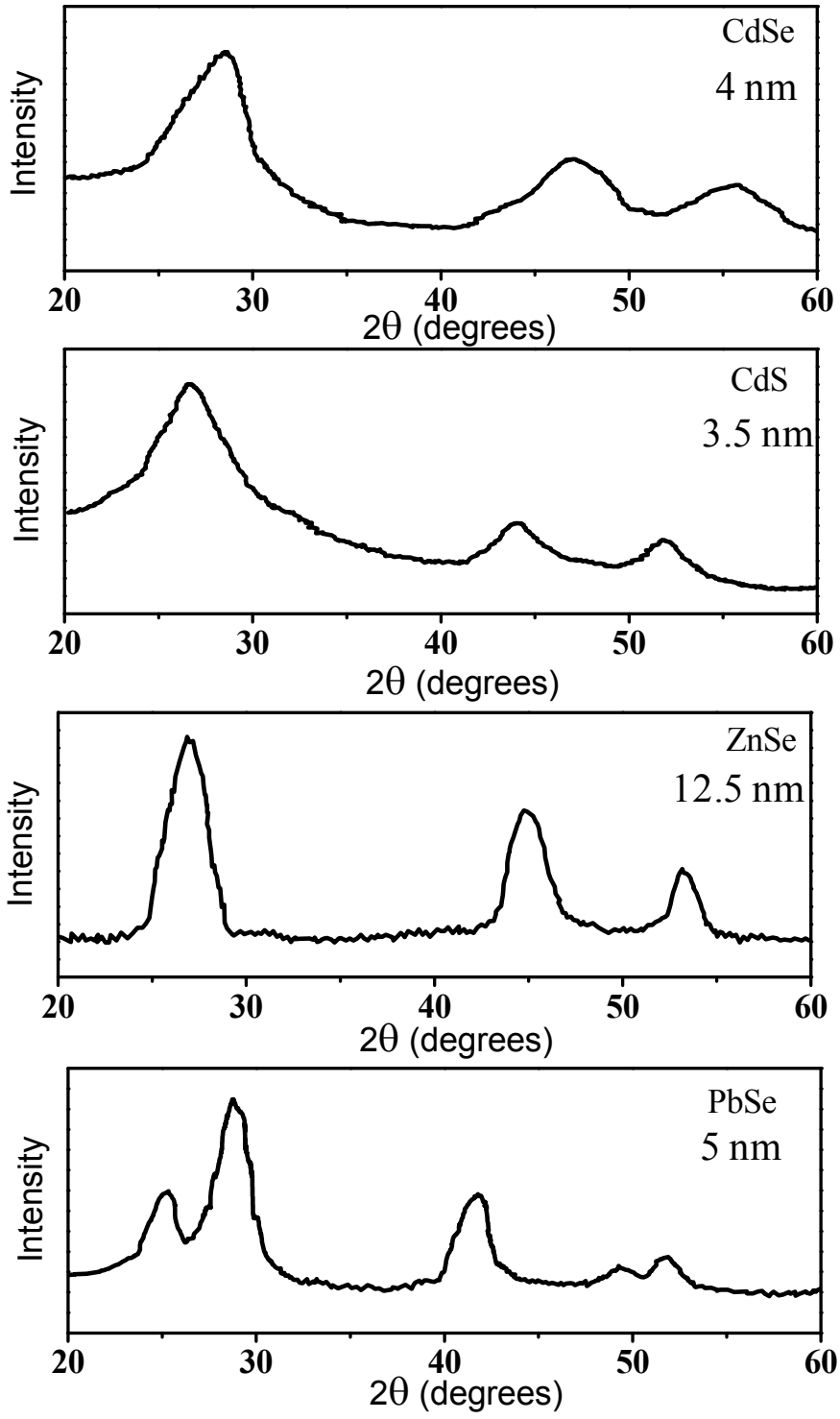

Figure 2.13: X-ray diffraction patterns of metal chalcogenides nanocrystals.

A TEM image of CdS nanoparticles capped with perfluorodecanethiol, prepared by a procedure similar to that of CdSe is shown in Figure 2.11 (b). The average diameter of the nanoparticles is around 3.5 nm. The photograph of the solution in perfluorohexane is shown as the inset of Figure 2.11 (b) reveals the yellow color of the dispersion. The optical absorption spectrum and the PL spectrum of the CdS nanoparticles are shown in Figure 2.12b. The absorption spectrum, characteristic of 3.5 nm CdS particles, shows a band at 395 nm while the PL spectrum shows a band at 403 nm (excitation at 320 nm) (*34*). The XRD pattern can be indexed to a cubic zinc blende structure (Figure 2.13).

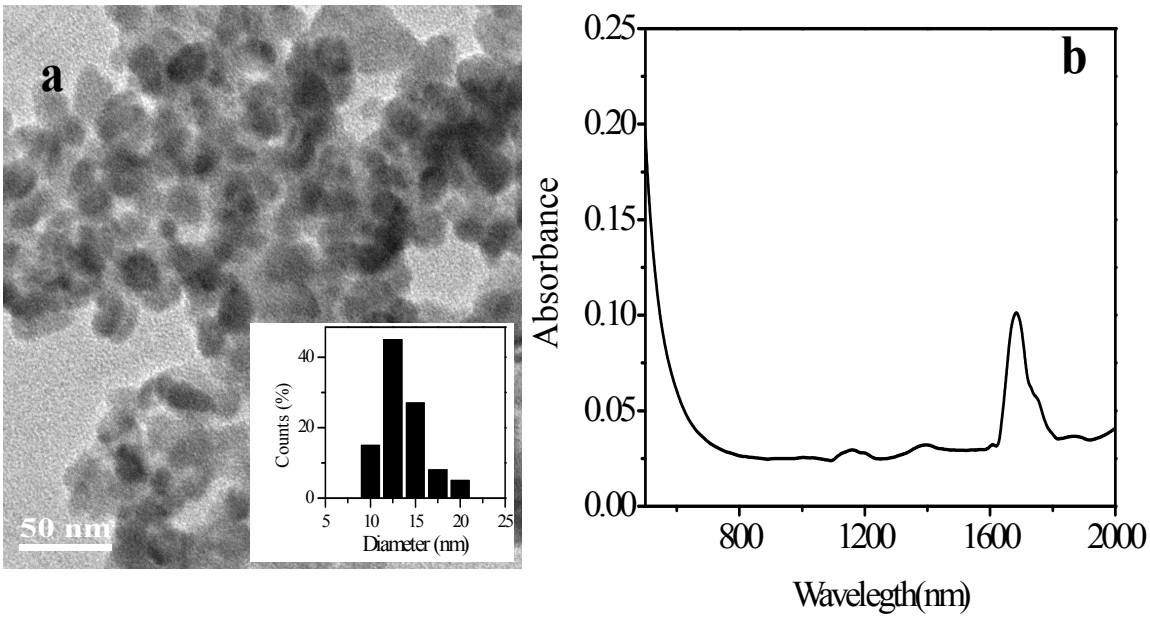

Figure 2.14: (a) TEM images of PbSe nanoparticles with size distribution histograms as inset. (b) Optical absorption and photoluminescence spectra of PbSe nanoparticles.

We have obtained PbSe and ZnSe nanoparticles by employing procedures similar to those for the Cd chalcogenide nanoparticles. Figure 2.14 (a) show the TEM image of PbSe nanocrystals with average diameter of around 12.5 nm. Optical absorption spectrum of the PbSe nanoparticles shows a first exciton peak around 1680 nm (Figure 2.14 (b)) (*35*). The TEM image of 5 nm ZnSe nanoparticles has been shown

in the Figure 2.15 (a). The optical absorption spectrum of the ZnSe nanoparticles shows a band at 400 nm and a photoluminescence band at 407nm (Figure 2.15 (b)) (*36*). The powder XRD patterns of ZnSe was indexed on the cubic zinc blende structure where as PbSe was indexed on the rock salt structure.

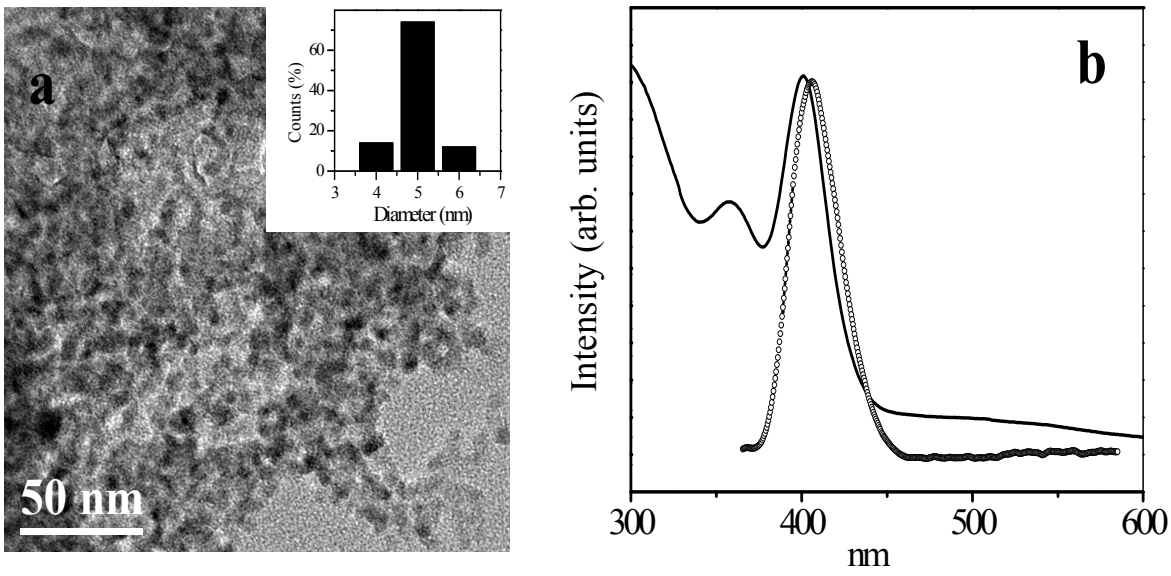

Figure 2.15: (a) TEM images of ZnSe nanoparticles with size distribution histograms as inset. (b) Optical absorption and photoluminescence spectra of ZnSe nanoparticles.

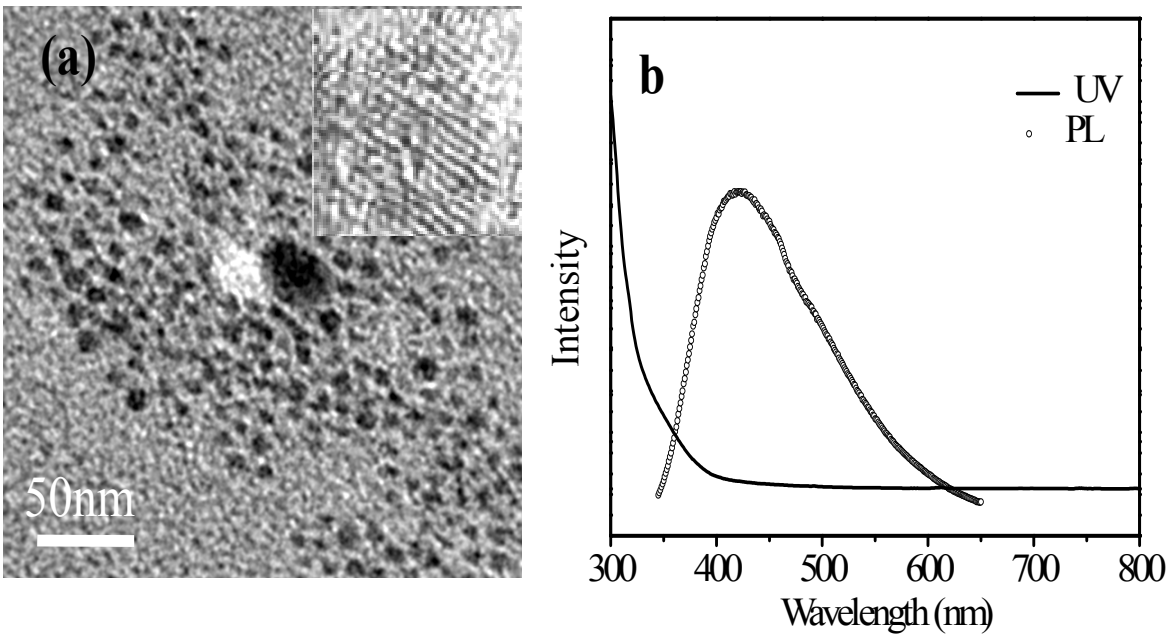

Figure 2.16: (a) TEM and (b) optical absorption and photoluminescence spectra of 8 nm ZnO nanoparticles.

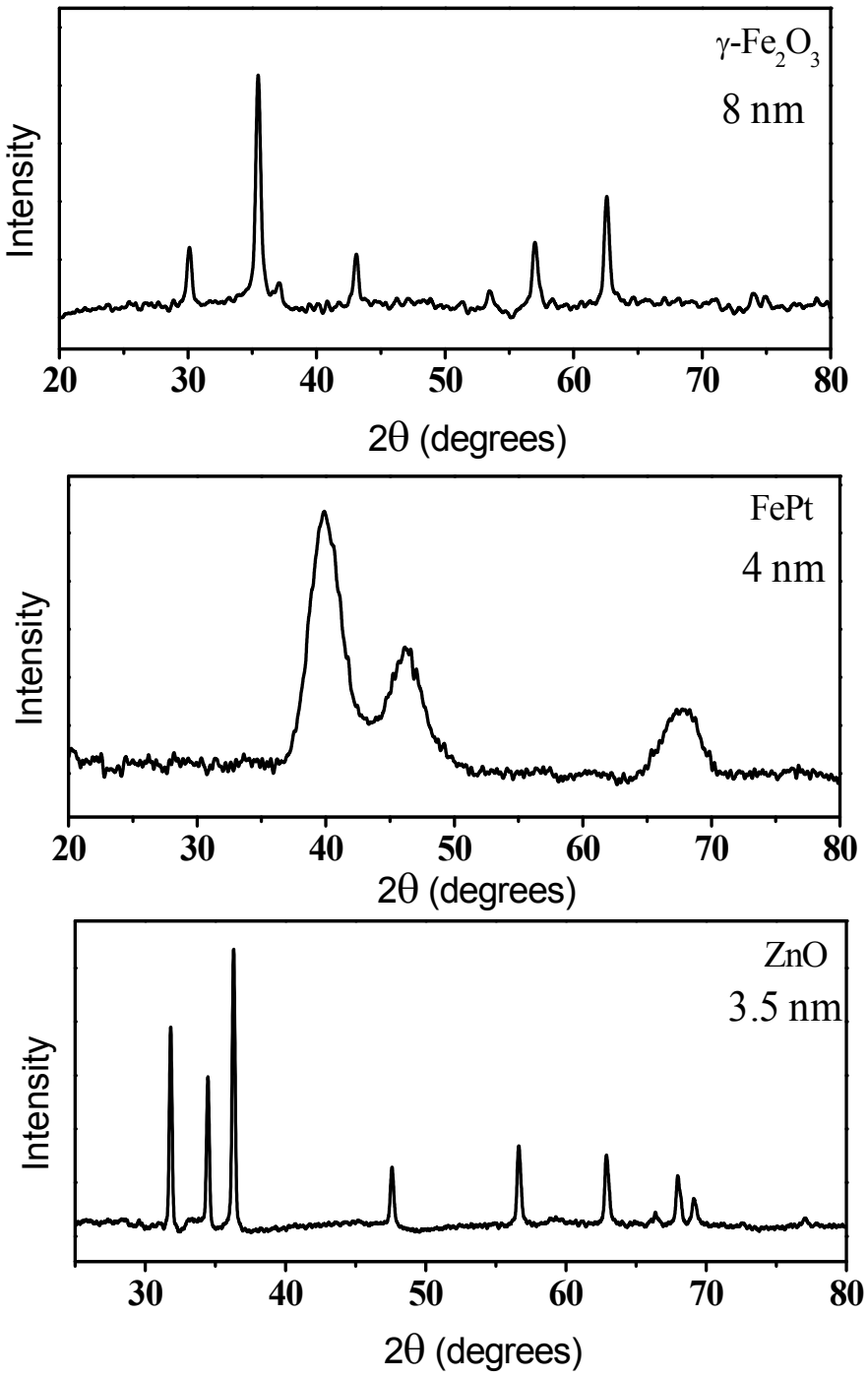

Figure 2.17: X-ray diffraction patterns of ZnO, FePt and γ-Fe_2O_3 nanocrystals.

Heptadecafluorodecylamine capped ZnO nanoparticles were prepared by the nonhydrolytic decomposition of zinc acetylacetonate. In Figure 2.16 (a) we show a TEM image of ZnO nanoparticles with an average diameter of 8 nm dispersed in perfluorohexane. XRD pattern shows ZnO nanoparticles had the wurtzite structure (Figure 2.17). The optical absorption spectrum in Figure 2.16 (b) shows an

absorption band edge around 330 nm *(29, 30)*. The PL spectrum shows a broad blue-green emission band at above 430 nm. A broad blue-green emission band above 430 nm is attributed to a singly charged oxygen vacancy, which results from the recombination of a photogenerated hole with a charge state of the specific defect, such as oxygen vacancies, or resulted from the surface deep traps.

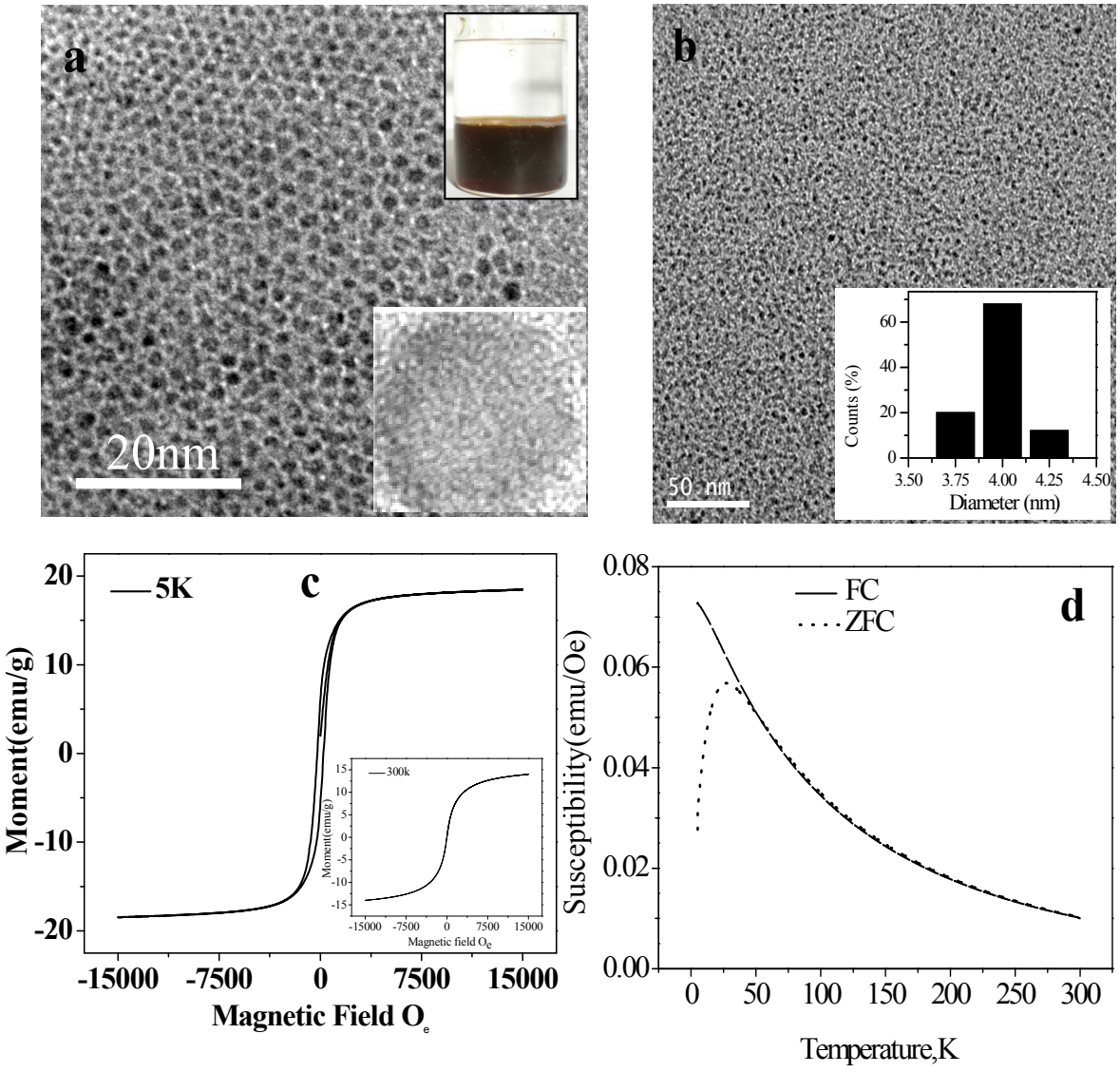

Figure 2.18: (a) and (b) show TEM images of 4 nm γ-Fe_2O_3.(c) Magnetic hysteresis at 5 K exhibited by 4 nm γ-Fe_2O_3 nanoparticles and (d) Zero-field cooled (ZFC) and field cooled (FC) magnetic susceptibility data as a function of temperature for γ-Fe_2O_3 . Inset of (a) shows the photograph of the dispersions of the nanoparticles in PFC . Inset of (b) show the size distribution of γ-Fe_2O_3 nanoparticles from TEM and (b) show high resolution TEM image . Inset of (c) shows the magnetic hysteresis at 300 K exhibited by 4 nm γ-Fe_2O_3 nanoparticles.

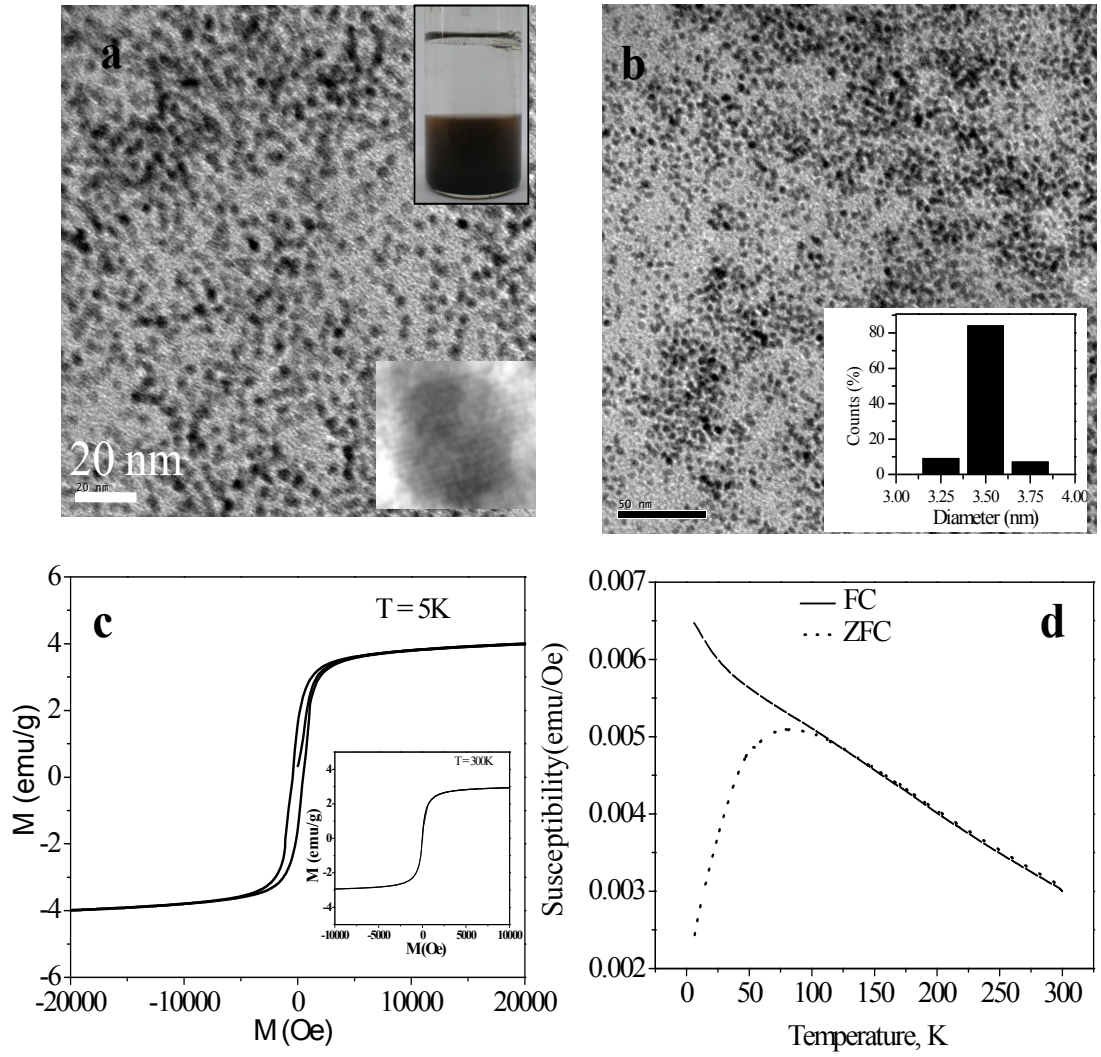

Figure 2.19: (a) and (b) show TEM images of 3.5 nm FePt (c) Magnetic hysteresis at 5 K exhibited by 3.5 nm FePt nanoparticles and (d) Zero-field cooled (ZFC) and field cooled (FC) magnetic susceptibility data as a function of temperature for FePt. Inset of (a) shows the photograph of the dispersions of the nanoparticles in PFC . Inset of (b) show the size distribution of FePt nanoparticles from TEM . Inset of (c) shows the magnetic hysteresis at 300 K exhibited by 3.5 nm FePt nanoparticles.

By the thermal decomposition of $Fe(CO)_5$, we have obtained perfluorodecanoic acid-capped γ-Fe_2O_3 dispersed in perfluorohexane. A TEM image of the nanoparticles is shown in Figure 2.18 (a) and (b). The as prepared γ-Fe_2O_3 nanoparticles are monodisperse with a diameter around 4 nm. Figure 2.17 shows the XRD pattern of iron oxide nanoparticles. γ-Fe_2O_3 nanoparticles exhibit superparamagentic behavior at 300K

(inset Figure 2.18 (c)). At 5 K (Figure 2.16 (c)) the nanoparticles exhibit the hysteresis behavior expected for particles below their blocking temperature. Magnetic susceptibility measurements show divergence between field-cooled (FC) and zero field-cooled (ZFC) measurements with a blocking temperature of 23K (at 100 Oe) as shown in the Figure 2.18 (d) (*28*).

FePt nanoparticles were prepared by thermal decomposition of $Fe(CO)_5$ and reduction of $Pt(acac)_2$ in benzyl ether. In Figure 2.19 (a) and (b), we show a TEM image of 3.5 nm heptadecafluorodecylamine-capped FePt nanoparticles. The FePt nanoparticles show XRD patterns corresponding to the FCC structure (Figure 2.17). The reflections are broad due to the small particle size. At 5 K (Figure 2.19 (c)) the nanoparticles exhibit the hysteresis behaviour expected for particles below their blocking temperature. FePt nanoparticles show superparamagnetic behavior at room temperature and divergence between FC and ZFC measurements with a blocking temperature of 75 K (at 100 Oe) as shown in Figure 2.19 (d) in agreement with the literature value (*31*).

2.5 Conclusions

We have successfully demonstrated that by using a fluorous label and a fluorous solvent, we can affect the phase transfer of gold and CdSe nanoparticles from an aqueous or hydrocarbon medium to the fluorous phase. Single-walled carbon nanotubes and ZnO nanorods can be solubilized in a fluorous solvent after interaction with a fluorous amine. Phase transfer of the nanostructures to a fluorous solvent represents solubilization in a highly nonpolar solvent, accompanied by purification. The high nonpolarity of the fluorocarbon makes it possible to study the optical and other properties of nanostructures in a medium of very low refractive index. Since the fluorocarbon extracts only the species attached to the fluorous label, the process enables

one to obtain solely one product in the pure state. We believe that fluorous chemistry may have practical utility in carrying out studies of nanostructures.

We have extended the use of fluorous chemistry to synthesize pure fluorous-capped inorganic nanoparticles by a one step procedure. This procedure conveniently uses the fact that hydrocarbons and perfluorohydrocarbons become fully miscible at high temperatures. This feature has enabled us to extract fluorous-capped inorganic nanoparticles in perfluorohydrocarbons, having prepared them in mixture of hydrocarbon and perfluorohydrocarbon at high temperatures. It is noteworthy that the nanoparticles are nearly monodisperse and highly pure. The method can be used for the synthesis of variety of fluorous-capped inorganic nanostructures dispersed in perfluorohydrocarbons.

REFERENCES

1. A. Studer *et al.*, *Science* **275**, 823 (1997).
2. P. C. Dennis, *Angew. Chem., Int. Ed.* **37**, 1174 (1998).
3. W. Zhang, *Chem. Rev.* **104**, 2531 (2004).
4. J. Yoshida, K. Itami, *Chem. Rev.* **102**, 3693 (2002).
5. A. Gladyz, D. P. Curran, I. T. Horvath, *Handbook of Fluorous Chemistry*. (Wiley-VCH Verlag GmbH, Weinheim, Germany, 2004).
6. M. Brust, M. Walker, D. Bethell, D. J. Schiffrin, R. Whyman, *J. Chem. Soc. Chem. Commun.* 801 (1994).
7. K. V. Sarathy, G. U. Kulkarni, C. N. R. Rao, *Chem. Commun.* 537 (1997).
8. M. Schulz-Dobrick, K. V. Sarathy, M. Jansen, *J. Am. Chem. Soc.* **127**, 12816 (2005).
9. J. Yang, E. Sargent, S. Kelley, J. Y. Ying, *Nat. Mater.* **8**, 683 (2009).
10. Y. Ofir, B. Samanta, P. Arumugam, V. M. Rotello, *Adv. Mater.* **19**, 4075 (2007).
11. K. Biswas, C. N. R. Rao, *J. Colloid Interface Sci.* **333**, 404 (2009).
12. T. Yonezawa, S. Onoue, N. Kimizuka, *Adv. Mater.* **13**, 140 (2001).
13. T. Yonezawa, S. Onoue, N. Kimizuka, *Langmuir* **17**, 2291 (2001).
14. D. Barriet, T. R. Lee, *Curr. Opin. Colloid Interface Sci.* **8**, 236 (2003).
15. P. S. Shah, S. Husain, K. P. Johnston, B. A. Korgel, *J. Phys. Chem. B* **105**, 9433 (2001).
16. P. S. Shah, S. Husain, K. P. Johnston, B. A. Korgel, *J. Phys. Chem. B* **106**, 12178 (2002).
17. P. S. Shah, J. D. Holmes, R. C. Doty, K. P. Johnston, B. A. Korgel, *J. Am. Chem. Soc.* **122**, 4245 (2000).
18. M. Tristany *et al.*, *Chem. Mater.* **18**, 716 (2006).
19. J. Im, A. Chandekar, J. E. Whitten, *Langmuir* **25**, 4288 (2009).
20. S. Ghosh, C. N. R. Rao, *Nano Research* **2**, 183 (2009).
21. M. Kanungo, H. Lu, G. G. Malliaras, G. B. Blanchet, *Science* **323**, 234 (2009).
22. D. G. Duff, A. Baiker, P. P. Edwards, *J. Chem. Soc. Chem. Commun.*, 96 (1993).
23. C. N. R. Rao, V. Vijayakrishnan, H. N. Aiyer, G. U. Kulkarni, G. N. Subbanna, *J. Phys. Chem.* **97**, 11157 (1993).
24. U. K. Gautam, R. Seshadri, M. Rajamathi, F. Meldrum, P. Morgan, *Chem. Commun.*, 629 (2001).

25. S. R. C. Vivekchand, A. Govindaraj, M. M. Seikh, C. N. R. Rao, *J. Phys. Chem. B* **108**, 6935 (2004).
26. N. Varghese, L. S. Panchakarla, M. Hanapi, A. Govindaraj, C. N. R. Rao, *Mater. Res. Bull.* **42**, 2117 (2007).
27. U. K. Gautam, R. Seshadri, C. N. R. Rao, *Chem. Phys. Lett.* **375**, 560 (2003).
28. L. E. Euliss *et al.*, *Nano Lett.* **3**, 1489 (2003).
29. N. Pinna, G. Garnweitner, M. Antonietti, M. Niederberger, *J. Am. Chem. Soc.* **127**, 5608 (2005).
30. Y.-S. Fu *et al.*, *J. Am. Chem. Soc.* **129**, 16029 (2007).
31. M. Chen, J. P. Liu, S. Sun, *J. Am. Chem. Soc.* **126**, 8394 (2004).
32. J. Chen *et al.*, *J. Phys. Chem. B* **105**, 2525 (2001).
33. B. K. H. Yen, N. E. Stott, K. F. Jensen, M. G. Bawendi, *Adv. Mater.* **15**, 1858 (2003).
34. W. W. Yu, X. Peng, *Angew. Chem., Int. Ed.* **41**, 2368 (2002).
35. J. S. Steckel, S. Coe-Sullivan, V. Bulovic, M. G. Bawendi, *Adv. Mater.* **15**, 1862 (2003).
36. M. A. Hines, P. Guyot-Sionnest, *J. Phys. Chem. B* **102**, 3655 (1998).

CHAPTER 3

Assembling Covalently Linked Nanocrystals and Carbon Nanotubes Through Click Chemistry

Summary*

The click reaction involving the Huisgen 1, 3-cycloaddition reaction between azide and ethynyl groups has been employed to obtain assemblies of nanostuctures. The click reaction between gold nanorods capped with azidoalkane- and alkyne-thiols yields chains and complex assemblies, accompanied by a large red shift of the longitudinal surface plasmon band. A similar reaction between CdSe nanocrystals results in a splitting of the photoluminescence band, possibly due to exciton splitting. Carbon nanotubes decorated by covalently linked gold and CdSe nanoparticles have been obtained through click chemistry. We have also attempted to interconnect carbon nanotubes by click chemistry.

A Paper based on this study has appeared in Chemical Physics Letters (2007)

3.1 Introduction

Click chemistry provides reliable and selective reactions for synthesizing new compounds and to generate combinatorial libraries (*1*) and the method enabled a novel style of organic synthesis. The term click chemistry defines a chemical reaction which is versatile and clean, with simple workup and purification procedures. Among the large collection of organic reactions, Huisgen cycloaddition, 1,3-dipolar cycloaddition between azide and acetylene derivatives in the presence of Cu(I) catalyst, represents the most effective reaction of click chemistry. The 1,3-dipolar cycloaddition reaction of a 1,3-dipole to a dipolaropile (i. e. an acetylene or alkene) for the synthesis of five-membered heterocycles are ubiquitous transformations in synthetic chemistry (*2, 3*). Recently, the Sharpless (*4*) and Meldal (*5*) groups have reported the dramatic rate enhancement (up to 10^7 times) and improved regioselectivity of the Huisgen 1,3-dipolar cycloaddtion reaction of an organic azide to a terminal acetylene to afford, regiospecifically, the 1,4-disubstituted 1,2,3,-trizaole in the presence of a Cu (I) catalyst (Scheme 3.1). The classical non-catalysed process proceeds by a concerted mechanism under thermal conditions to afford mixture 1,4- and 1,5- disubstituded 1,2,3-triazole regioisomers. The Cu (I)-catalysed 1,3-dipolar cycloaddition reaction has successfully fulfilled the requirement of click chemistry as prescribed by Sharpless and within the past few years has become a premier component of the click chemistry paradigm (*1*). Azides and acetylenes are by definition kinetically stable entities possessing high built-in energy and are tolerant to a wide range of synthetic conditions (*6*). Within a short time-frame, click chemistry has proven to be of remarkable utility and broad scope not only in an organic synthesis, but in chemical biology, drug discovery (*7*), polymer and materials science (*8*).

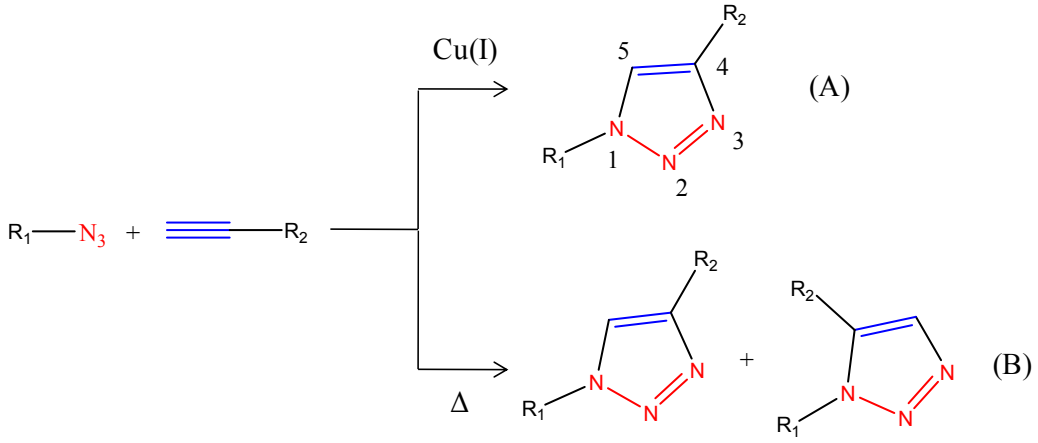

Scheme 3.1

Nanostructures of different inorganic and carbon materials possessing different dimensionalities have been synthesized and characterized in the last few years. Several of these nanostructures are found to have exciting properties with potential applications. The surface plays an important role in the properties of nanomaterials, including the solubility, reactivity, stability, melting point, and electronic structure (*9*). At the same time, the surface is the connection of the nanoparticles to other materials and objects and plays a vital role in the construction of superlattices, in the fabrication of new devices and in the conjugation with target molecules for drug delivery applications (*10*). Thus, the chemical modification of the surface of nanoparticles is a very important field. During growth of the nanoparticles, stabilizing agents are present to prevent nanoparticle aggregation and precipitation. Various organic and inorganic materials have been utilized as capping materials on the surface of nanoparticles through covalent or ionic interactions (*11, 12*). Besides modifying the properties of the bare nanoparticles, they also play a role as the connecting media of the nanoparticles to the outside world. For example, in the superlattices of nanoparticles, they define the interparticle distances between nanoparticles (*13*). On the other hand, in nanoparticle based drug delivery, they connect the nanoparticles to the therapeutic agents and to interconnect the different nanostructures (*14*).

Assembly of colloidal metallic, semiconducting quantum dots, or insulating inorganic particles into one-, two- and three dimensional superstructures has received increased interests over the last decade. This is due to their potential uses as smart materials and devices as they are characteristic of ordered structures with collective physical properties from the individual particles and the interparticle coupling (*15*). Assemblies can be liquid-crystal structures in solution, crystals, or precipitates separated from solution phase or ordered arrays supported on liquid or solid phase. Assembly approaches include spontaneous self-assembly, chemical driving assembly, template-directed patterning, and physical methods such as polymer stretching and electric field induction (*10, 16*).

Carbon nanotubes possess exceptional electronic, mechanical, chemical, and optical properties, which render them particularly promising materials in the areas of solar energy conversion electronic, and sensing as well as biological applications (*17*). Functionalization and solubilization are important aspects of the chemistry of CNTs and these chemical manipulations are essential for many of the applications. Derivatization of CNTs gives products with sidewall substituents, wrapped with polymers, with inclusion of guest molecules and attaching various inorganic nanoparticles (*18*). The approaches can be divided into covalent functionalization and noncovalent interaction of the SWNT sidewalls. Covalent functionalization include direct addition of fluorine atoms, cycloaddition reactions, radical and nucleophilic additions to side walls of nanotubes (*17, 19*). Another method is to introduce carboxylic groups on the side walls of SWNTs by oxidation. The carboxylic acid groups can further attached with various organic molecules by means of amide/ester linkages or carboxylate-ammonium salt ionic interactions. Attachment of various chemical molecules or other nanomaterials might be convenient way to modify the electronic structure of carbon nanotubes (*17, 19*).

Finding the new strategies to functionalize and assemble the nanostructures is an active area of research. We report the scope of the present investigations in the next section.

3.2 Scope of the present investigations

There are various reports in the literature to functionalize and assemble nanostructurues. We considered click chemistry as a possible means to assemble or link various types of nanostructures. An important click reaction is the Cu- catalyzed 1, 3-dipolar cycloaddition reaction between azido and ethynyl groups to form the 1,2,3-triazole ring, investigated in detail by Huisgen (*20, 21*). While this reaction has been used to functionalize nanoparticles (*22*) and single-walled carbon nanotubes (SWNTs) (*23*), it has not been exploited for assembling nanostructures. We have employed the cycloaddition reaction to generate assemblies of metal nanoparticles, semiconductor nanoparticles as well as covalently attached SWNT – metal nanoparticle composites. The methodology employed in the present study was as follows. An azidoalkane derivative containing a terminal SH or NH_2 group is attached to a nanostructure, **A**, while an alkyne with a SH or NH_2 group is attached to another nanostructure, **B**. Reaction between **A** and **B** gives rise to 1, 2, 3-triazole, thereby causing a covalently attached assembly of the nanostructures. The occurrence of the click reaction is readily ascertained by the absence of the characteristic stretching mode frequencies of the azido and acetylenic units as well as changes in the NMR spectra.

This chapter deals with the Husigen cycloadditon reaction in the case of gold nanorods, gold nanoparticles and CdSe nanocrystals to produce covalently linked assemblies. Carbon nanotubes decorated by covalently linked gold nanoparticles have also been produced by this means.

3.3 Experimental

The following bifunctional molecules had been synthesizes and used for assembling and functionalization of different nanostructures.

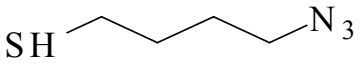

4-azidobutane-1-thiol

(A)

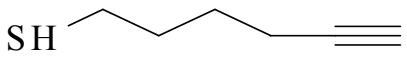

hex-5-yne-1-thiol

(B)

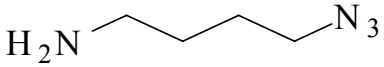

4-azidobutan-1-amine

(C)

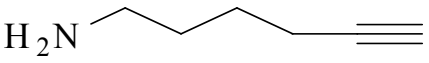

hex-5-yn-1-amine

(D)

Synthesis of 4-azidobutane-1-thiol

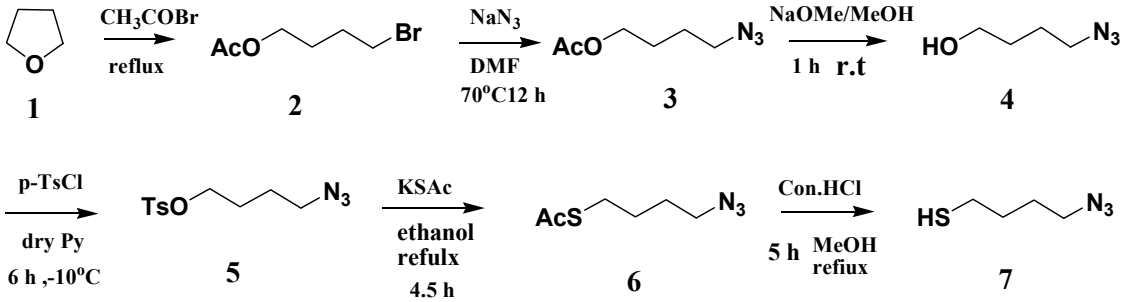

Dropwise addition of CH_3COBr (2.9 g, 235 mmol) to THF **1** (2.5 g, 359 mmol) which was stirring with $ZnCl_2$ (0.005 g, 0.037 mmol) at 0 ºC and allowed the stirring for overnight followed by refluxing for 2 h, cooled, diluted with DCM then washed with water and saturated aqueous $NaHCO_3$. The organic layer was dried over Na_2SO_4, and evaporated in *vacuo* to give 97 % of **2.** NaN_3 (6.9 g, 107.5 mmol) was added to the solution of (1.0 g, 76.8 mmol) **2** in DMF (150 ml) and refluxed for 12 h afforded **3** in 82 %. By treating azide **3** (2000 mg, 12.7 mmol) with NaOMe/MeOH (1.5 ml) for 1 h gave **4** in 71.4 %. *p*- TsCl (3.2 g, 17.0 mmol) was added to the solution of **4** (1.6 g, 14.1 mmol) in Py (7 ml) at -10 ºC, stirred for 6 h to give 65.7 % of **5.** KSAc (364 mg, 3.2 mmol) was added to the solution (0.718 g, 2.6 mmol) of **5** in ethanol (7 ml), and

refluxed for 4.5 h to from 88 % of **6**, then by refluxing (0.757 g, 4.3 mmol) of **6** Conc.HCl (4 ml) in MeOH (78 ml) for 5 h then extracted with ether, dried over Na_2SO_4 and evaporated in *vacuo* afforded 78 % of **7.** The NMR spectrum of **7** is shown in the Figure 3.1

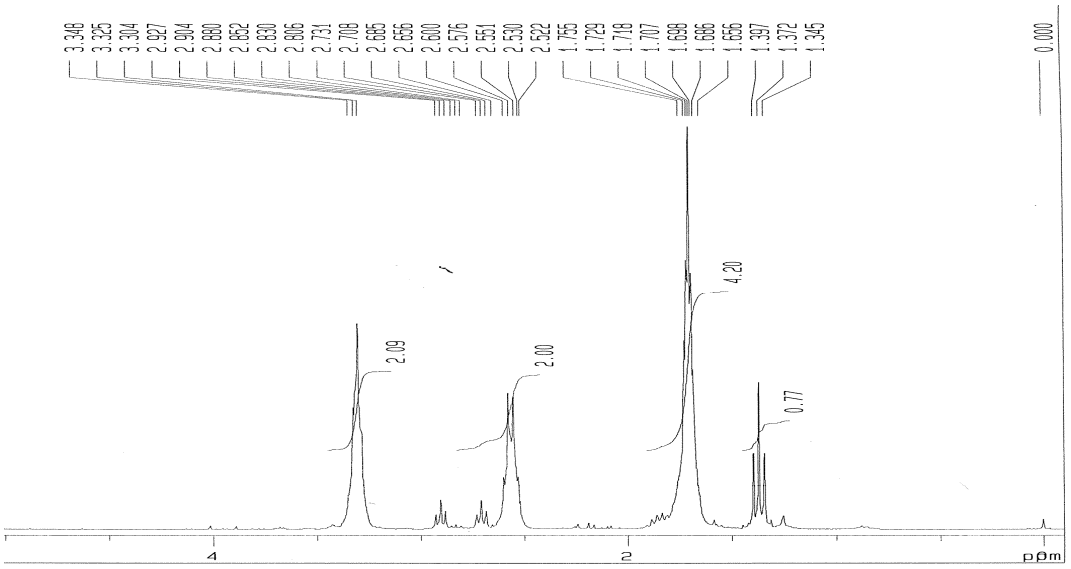

Figure 3.1: NMR spectrum of the compound **7**.

Synthesis of hex-5-yne-1-thiol

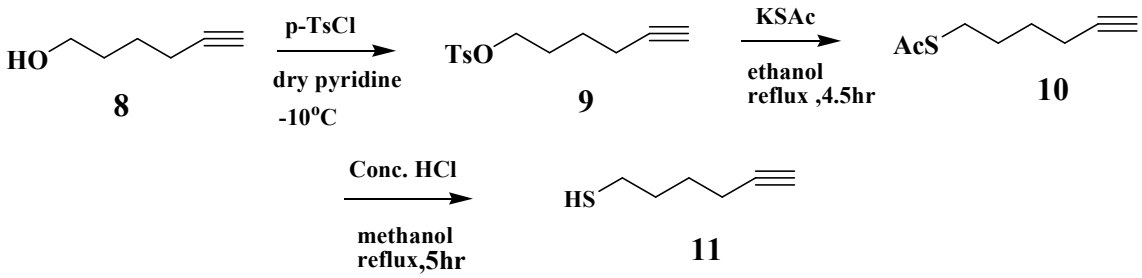

To the solution of 5-hexyn-1-ol (2.1 g, 21.3 mmol) **8** in Py (10 ml) at -10 ºC, *p*-TsCl (4.8 g, 25.6 mmol) was added and allowed to stir for 4 h which on dilution with DCM, dried over Na_2SO_4 and evaporated in *vacuo* gave 90.5 % of **9**, by refluxing (0.740 g, 2.9 mmol) of **9** with KSAc (0.401 g, 3.5 mmol) in ethanol (6 ml) for 4.5 h gave 56.6 % of **10.** (0.581 g, 3.7 mmol) of **10** was refluxed with conc. HCl (3 ml) in MeOH (66.8 ml)

for 5 h extracted with ether, dried over Na_2SO_4 and evaporated in *vacuo* afforded 68 % of **11.** The NMR spectrum of **11** is shown in the Figure 3.2.

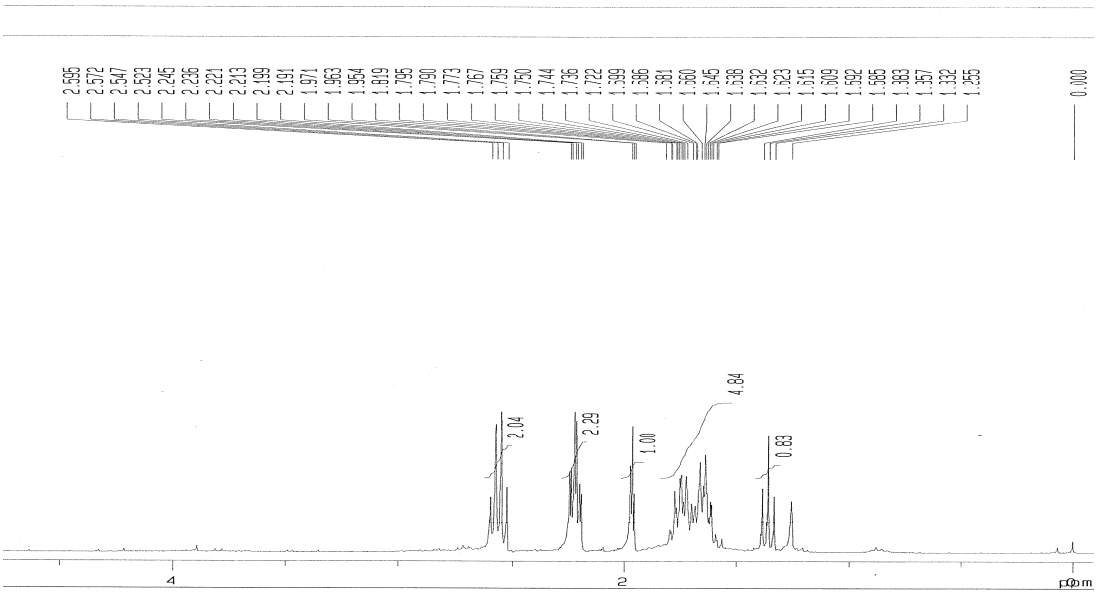

Figure 3.2: NMR spectrum of the compound **11**.

Synthesis of 4-azidobutane-1-amine

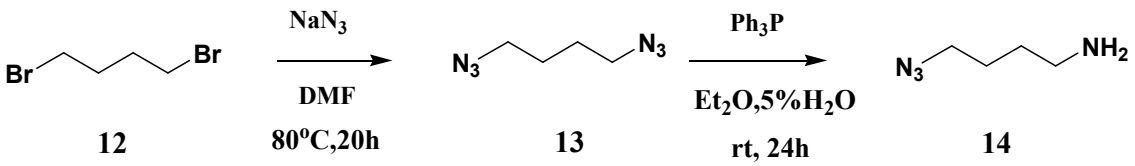

12 **13** **14**

To the solution of dibromobutane (5 g, 23.16 mmol) **12** in dry DMF (50 ml), NaN_3 was added and the resultant mixture was heated 80°C for 20h yields 86 % of **13**.(*24*) To a solution of diazidoalkane **13** (0.4 mol) in Et_2O (250 ml):EtOAc (250 ml) and 5% HCl (400 ml) was added, further triphenylphosphine (0.39 mol) was added in small portions for 1 h at 0°C and then the mixture was stirred for 24 h at room temperature. The organic layer was discarded and the aqueous layer was washed twice with DCM (150 ml). The resulting aqueous phase was carefully basified with NaOH and then extracted with DCM (3×200 ml). The combined extracts were dried with sodium sulfate and evaporated to give pure azidoaminoalkane **14** in 90% yields. The NMR spectra of **14** is shown in the Figure 3.3

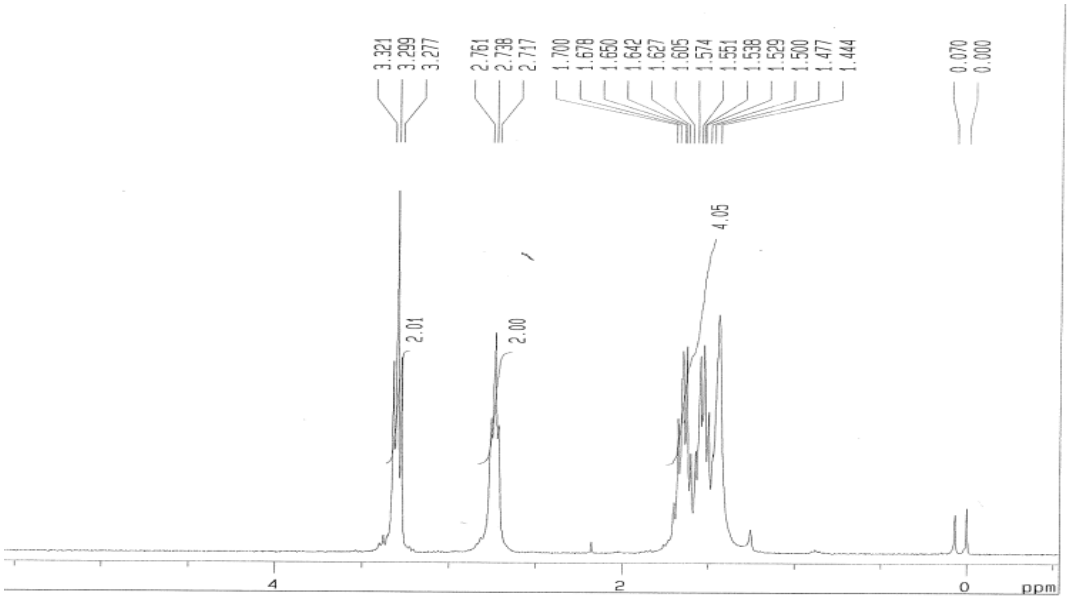

Figure 3.3: NMR spectrum of the compound **14**.

Synthesis of hex-5-yne-1-amine

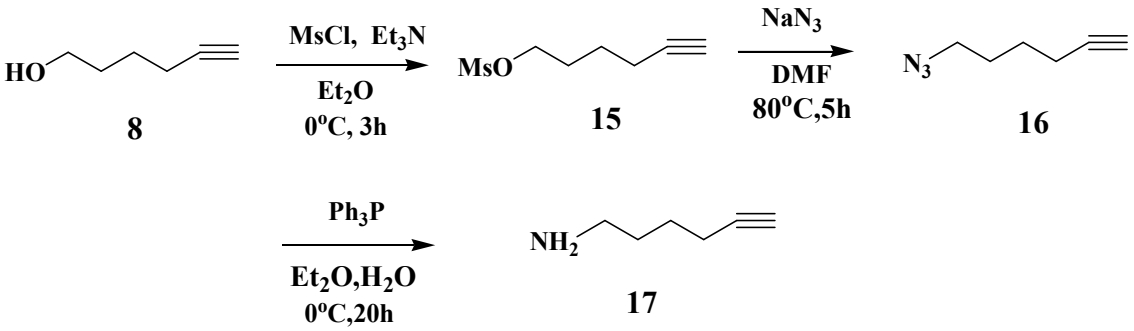

Methanesulfonylchloride (3.501 g, 30.5 mmol) was added drop wise to a stirred solution of 5-hexyn-1-ol **8** (2.000 g, 20.3 mmol) and Et_3N (3.086 g, 30.5 mmol) in anhydrous ether (20 ml) at 0 ºC and stirred for 3 h to yield 80 % of **15**. Sodiun azide was added to a solution of the mesylate **15** (4.000 g, 22.7 mmol) in anhydrous DMF (18 ml). The mixture was stirred for 3.5 h at 67 ºC to yield 70 % of **16**. To the solution of azide **16** (0.900 g, 0.73 mmol) in ether (6 ml) at 0 ºC**,** PPh_3 (1.915 g, 0.73 mmol) was added and allowed to stir for 1.5 h water (0.33 ml) was added and stirred for 16 h and the reaction mixture was extracted with ether dried over Na_2SO_4 and evaporated to yield 21.1 % of substituted amino alkyne **17**.

Synthesis of gold nanorods

Gold nanorods were prepared by photochemical procedure of Kim *et al. (25)*. A quantity of 3 ml of an aqueous solution of 0.08 M hexadecyltrimethylammonium bromide (CTAB) and 0.42 mg/ml tetradodecylammonium bromide was used as the growth solution. Hydrogen tetrachloroaurate (0.25 ml of 0.024 M, $HAuCl_4.3H_2O$) was added to the solution as the precursor of gold, and 0.065 ml of acetone and 0.045 ml of cyclohexane were added to loosen the micellar structure. 0.01 M silver nitrate ($AgNO_3$) aqueous solution was added to the solution. The solution was irradiated with a 254 nm UV light for about 30 h. The resulting solution was centrifuged at 3000 rpm for 10 min, and the supernatant was collected, which was centrifuged again at 10000 rpm for 10 min. The precipitate was collected and redispersed in deionized water.

Synthesis of gold nanoparticles

Gold nanoparticles were prepared by the following literature procedure (*26*). Successive charging of a vessel (e.g. a 100-ml round-bottomed flask), while stirring, with 45.5 ml of water and then, portions of aqueous solutions of sodium hydroxide (0.2 M, 1.5 ml), the reducing agent THPC (1 ml of a solution of 1.2 ml of 80% aqueous solution diluted to 100 ml with water), and the metal salt chloroauric acid (2 ml of dark-aged stock solution, 25 mM) results in the formation of orange-brown hydrosols of gold nanocrystals.

Synthesis of CdSe nanoparticles

CdSe nanoparticles were prepared by solvothemal method as reported in the literature (*27*). In a typical reaction 1.36 g (2 mmol) of $[Cd(Stea)_2]$, 0.158 g (2 mmol) of Se, 0.2 g (1.5 mmol) of tetralin and 0.1 g (0.5 mmol) of dodecanethiol were taken in 50 ml of toluene in a stainless steel autoclave (*ca.* 70% filling, Teflon gasket) and placed in an oven that had been preheated to 250 °C. After 5 h the autoclave was removed and

cooled to room temperature. The solid product obtained by precipitation as mentioned in the text was dried at 50 °C in air overnight.

Synthesis of single-walled carbon nanotubes (SWNTs)

Arc discharge SWNTs (arc SWNTs) were synthesized by the method as reported by Journet *et al. (28)* using a composite rod containing Y (1 at.%) and Ni (4.2 at.%) as the anode and a graphite rod as the cathode, under a helium pressure of 660 torr with a current of 100 A and 30 V. The nanotubes were heated in air at 300 ^{o}C for 12 h and then stirred in conc. HNO_3 at 60 ^{o}C for 24 h in order to dissolve the metal nanoparticles. The product was washed with distilled water, dried, dispersed in ethanol under sonication, and filtered using Millipore (0.3 μm) filter paper. The filtered product was dried in an oven at 100 ^{0}C for 2 h. The sample was heated to 1000 ^{o}C in a furnace at a rate of 3 ^{o}C per minute, in flowing hydrogen at 100 sccm and held at that temperature for 2 h. The resulting sample was again stirred in conc. HNO_3 at 60 ^{o}C for 3 h and finally heated in a furnace at 1000 ^{o}C for 2 h in flowing hydrogen (100 sccm).

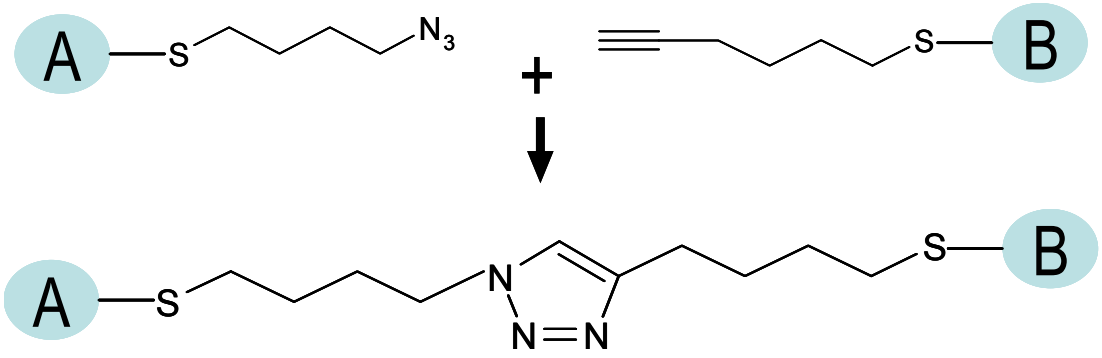

Figure 3.4: Schematic of click reaction between nanostructures.

Assembling gold nanorods, gold nanoparticles and CdSe nanoparticles by click chemistry

Thiol capped gold and CdSe nanoparticles were prepared by the reaction of fixed quantities of the nanoparticles in an 1:4 acetonitrile–water mixture (1.5 ml) with 100 µlsolution 1 µM of the thiol. The cycloaddition reaction of the capped nanocrystals was

carried out with equimolar concentrations (1:1) of A and B. In some of the reactions, the concentration of A was kept constant and the concentration of B was varied. The click reaction was carried out by the addition of equimolar mixture of $CuSO_4$ and sodium ascorbate which acts as a catalyst.

Attaching gold and CdSe nanoparticles to SWNTs

In order to prepare SWNT–Au and CdSe nanocrystal composites, SWNTs were functionalized by amidobutane (with a terminal azide group) as follows. First the SWNTs were treated with 3:2 volume ratio of conc. H_2SO_4 and conc. HNO_3 for about 1 hour to introduce carboxyl functional groups to the side walls of the SWNTs and SWNTs solution was filtered using PTFE membrane followed by washing with water. Acid-treated SWNTs were reacted with thionyl chloride at 65 ^oC for about 20 hours, followed by reaction with 4-azidobutan-1-amine. These SWNTs were reacted with hexynethiol- capped Au and CdSe nanocrystals. The click reaction was carried out by the addition of equimolar mixture of $CuSO_4$ and sodium ascorbate which acts as a catalyst.

Interconnection of SWNTs

In order to interconnect the SWNTs, two separate portions of SWNTs were attached with molecular linkers **C** and **D** by the procedure described in the previous section. The click reaction was carried out by the addition of equimolar mixture of $CuSO_4$ and sodium ascorbate which acts as a catalyst.

3.3.3 Techniques used for characterization

Transmission electron microscopy

For transmission electron microscopy (TEM), dispersions of the samples were dropped onto the holey carbon-coated Cu grids, and the grids were allowed to dry in the

air. The grids were examined using a JEOL (JEM3010) microscope operating with an accelerating voltage of 300 kV.

Optical absorption and photoluminescence spectroscopy

The optical absorption spectroscopy measurements were performed using a Perkin-Elmer Lambda 900 UV/VIS/NIR spectrometer. Photoluminescence spectra of these solutions were recorded with a Perkin-Elmer model LS55 luminescence spectrometer.

Infrared spectroscopy

Infrared (IR) spectra of the precursors were recorded with a Bruker FT-IR spectrometer.

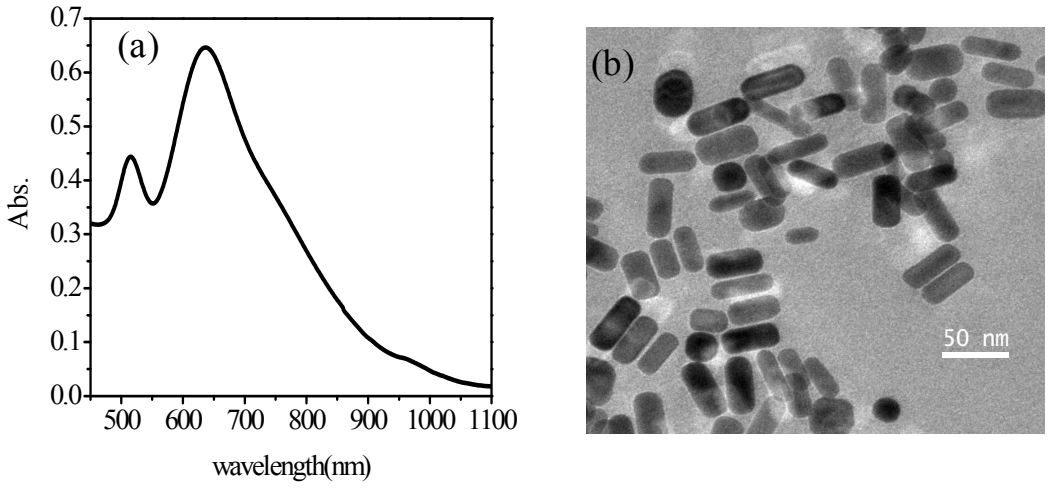

Figure 3.5: (a) Optical absorption spectra and (b) TEM of gold nanorods.

3.4 Results and discussion

Gold nanorods of aspect ratios 2.4 were synthesized by following the photochemical method reported by Yang and co-workers (*25*). In order to assemble gold nanorods by the click reaction, one batch of nanorods capped with 4-azidobutane-1-thiol, A, and another with hex-5-yn-1-thiol, B, were reacted in the acetonitrile-water mixture under

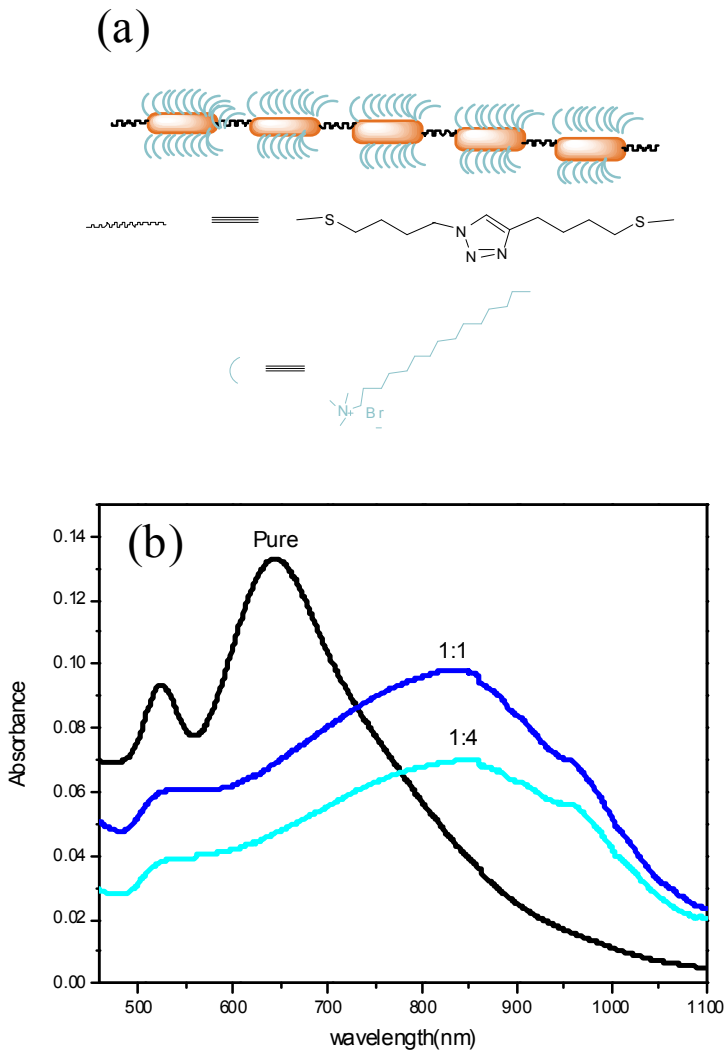

Figure 3.6: (a) schematic of gold nanorod assembly by click chemistry. (b) Optical absorption spectra of gold nanorods after the click reaction (at two different (1:1 and 1:4) concentrations of A and B).

standard conditions (*29*). The occurrence of the click reaction was established by infrared spectroscopy. The product of the reaction was investigated by electronic absorption spectroscopy and transmission electron microscopy. Figure 3.6 (b) compares the electronic absorption spectra of the gold nanorods before and after the click reaction between the A and B type nanorods. Isolated gold nanorods show transverse and longitudinal plasmon bands around 520 nm and 630 nm respectively (see Figure 3.5(a)). After the cycloaddition reaction, the spectra show a broad band centered around 800-

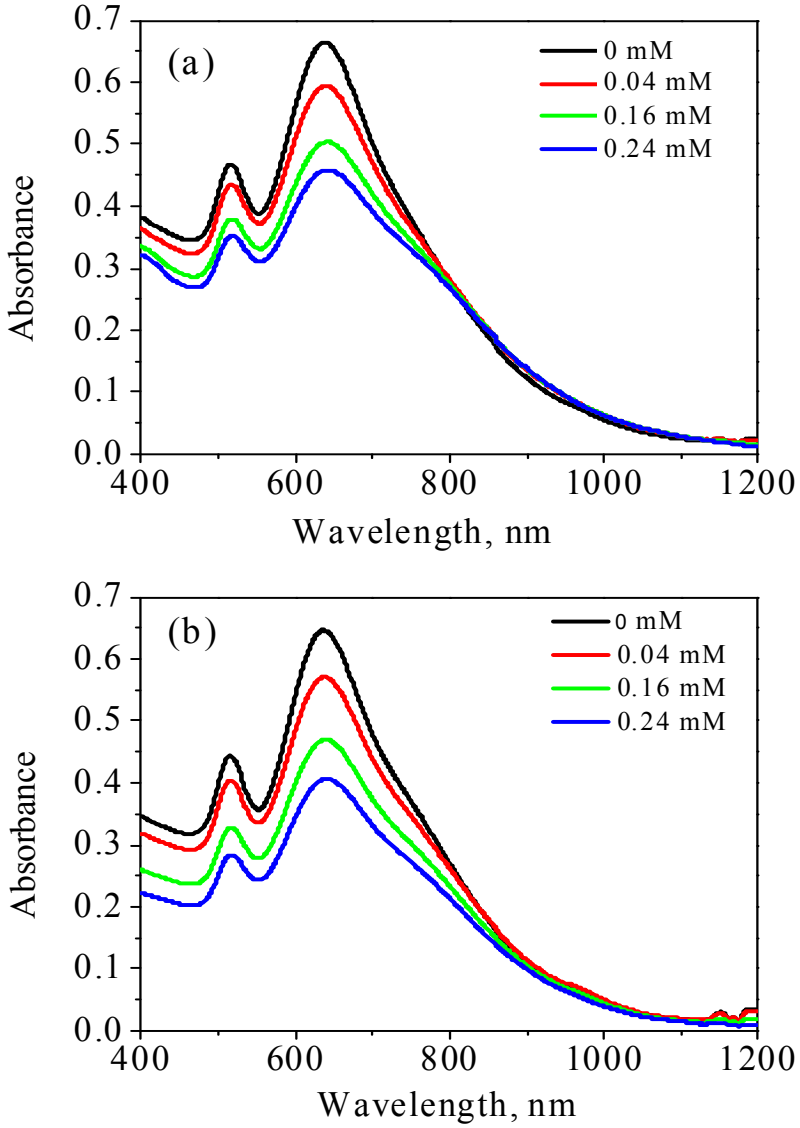

Figure 3.7: Optical absorption spectra of gold nanorods with the addition of different concentration of (a) hex-5-yen-1-thiol (b) 4-azidobutane-1-thiol.

850 nm due to the longitudinal surface plasmon absorption. The transverse band remaining at 520 nm (Figure 3.6(b)). The position of longitudinal band changed only little with the relative concentrations of the A and B used in the click reaction. The formation of the new red-shifted band can be explained on the basis of inter plasmon coupling in assembled nanorods. In the case of gold nanorods, there are two modes of plasmon oscillations (transverse and longitudinal) and each of these modes can couple with plasmon oscillations of the neighboring rods. In the present study, we observe a

selective coupling of the longitudinal plasmon band whereas the transverse plasmon band remains more or less unaffected. The addition of 4-azidobutane-1-thiol or hex-5-yn-1-thiol to gold nanorods does not result in the change in the position of longitudinal plasmon band (Figure 3.7). There is only small decrease in the plasmon bands with the addition of either thiols due to the damping of the plasmon oscillation leading to the slight broadening of its band. The damping of the plasmon band by introducing thiol groups has been reported in the past (*30*).

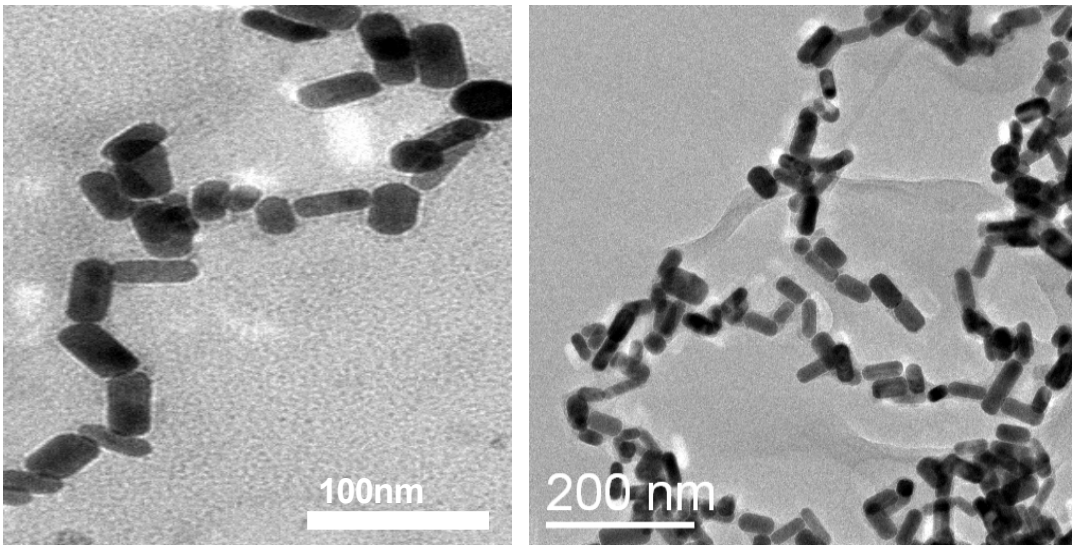

Figure 3.8: TEM images of chain-like assemblies of gold nanorods obtained after the click reaction with 1:1 concentrations of A and B.

The above results suggest that click reaction leads to the coupling of the longitudinal plasmon oscillation, resulting from an end-to-end assembly of gold nanorods as previously observed for other bifunctional ligands (thioalkyl carboxylic acids, (*31*) cysteine, and glutathione (*32*)) (Figure 3.6(a)). Interplasmon interaction was also observed by linearly assembling Au nanorods on multiwall carbon nanotubes (*33*). In Figures 3.5 (b) & 3.8, we show the transmission electron microscope (TEM) images of the gold nanorods before and after the cycloaddition reaction. After the reaction, the image shows chains of nanorods. Thus, the shift in the electronic absorption spectrum to

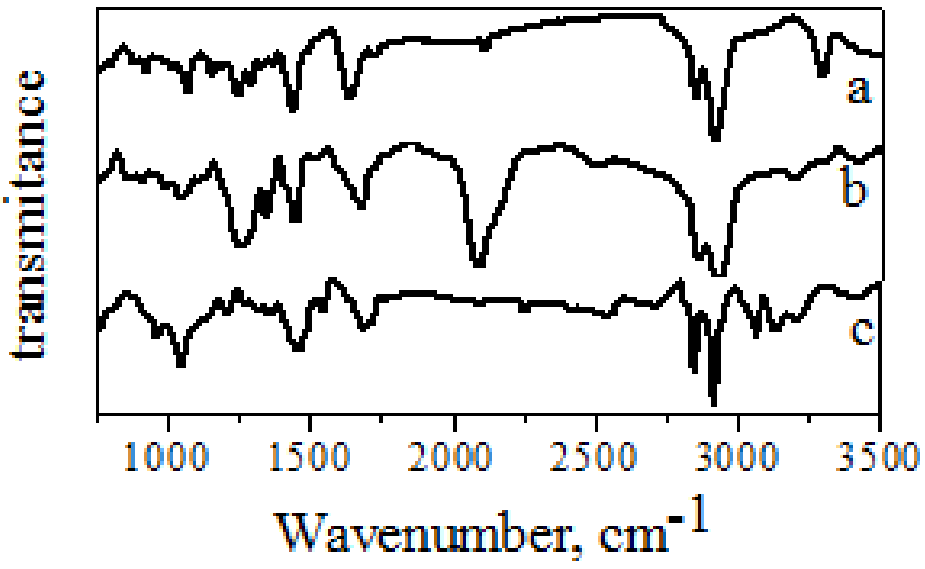

Figure 3.9: Infrared spectra in the 1000-2500cm^{-1} region (a) of the hexynethiol-capped gold nanorods, B, showing the C≡C stretching bond at 2109 cm^{-1}, (b) of the azidothiol-capped gold nanorods, A, showing the asymmetric azide stretching band at 2092 cm^{-1} and (c) of the product of the click reaction (1:1 of A and B) showing the absence of the bands due to the azide and C≡C stretching modes.

longer wavelengths is accompanied by the assembly of nanorods forming chains. The reason for obtaining chains of gold nanorods through click chemistry is because the ends of the nanorods comprise (111) faces of gold which favor thiol binding (*16*). The capping agents at the edges of Au nanorods can play a major role in the linear organization. Most of the reports on the synthesis of Au nanorods involve the presence of a cationic surfactant, cetyltrimethylammonium bromide (CTAB), and a cosurfactant in certain cases. Several mechanisms have been suggested for explaining the seed-mediated growth of Au nanorods. surfactant-directed nanorod growth mechanism was proposed by Murphy and co-workers which involves the differential blocking of certain crystallographic facets of Au nanorod ({100} or {110}) by CTAB which promotes the anisotropic growth of the {111} edges (*34*). An alternate mechanism involving the electric field directed growth of Au nanorods was proposed by Perez-Juste et al. which suggests that the Au(III) ions were initially bound to CTAB which upon reduction to

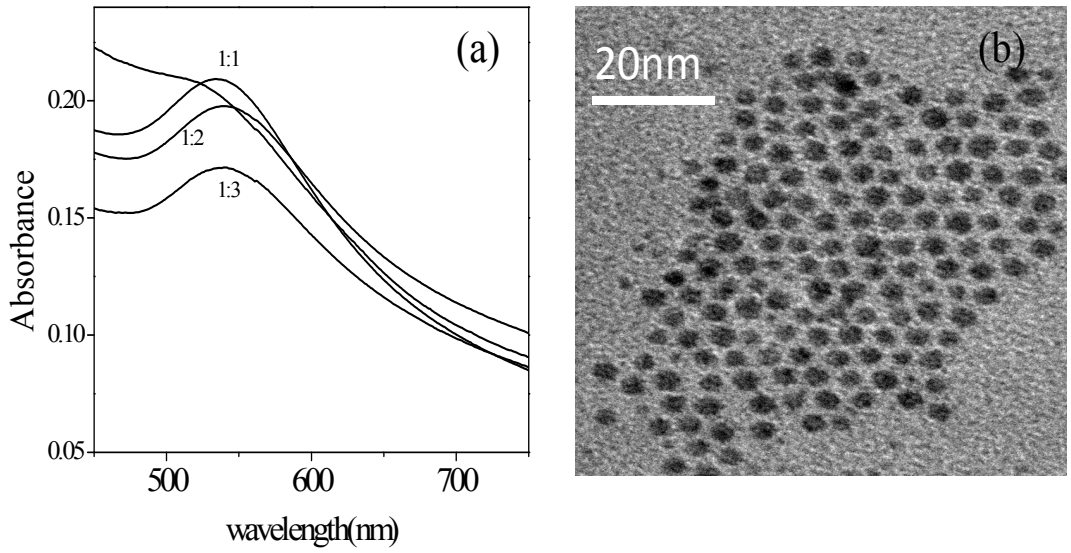

Figure 3.10: (a) Electronic absorption spectra of gold nanocrystals (2.5 nm diameter) and after click reactions at different concentrations of A and B. (b) Typical TEM image of the nanocrystals after the click reaction.

Au(I) ions interact more strongly with the CTAB micelle (*35*). According to this mechanism, the slow collision frequencyof Au(I) bound CTAB and the enhanced electric field at the tips allow the reduction of Au(I) at the termini. In the present case, we have adopted a photochemical method for the synthesis of Au nanorods by using CTAB as the surfactant and tetraoctylammonium bromide as the cosurfactant (*25*). At the growing edges of nanorods, the capping agents may be loosely bound and the organic thiols possessing short alkyl chains may diffuse faster and more efficiently into the micellar shell resulting in the organization of Au nanorods. To ensure that the changes in the electronic absorption spectra and the assemblies of nanorods seen in the TEM images were the result of the click reaction, we recorded infrared spectra before and after reaction. The spectra in Figure 3.9 clearly show the absence of the azide and acetylenic stretching frequencies at 2092 cm^{-1} and 2109 cm^{-1} respectively.

We have carried out the click reaction between spherical gold nanocrystals (2.5 nm). Optical absorption spectra show a small red-shift of the plasmon band after the click

reaction compared to the as synthesized nanoparticles (Figure 3.10 (a)). The TEM image as shown in Figure 3.10 (b) shows an organized assembly of the nanocrystals.

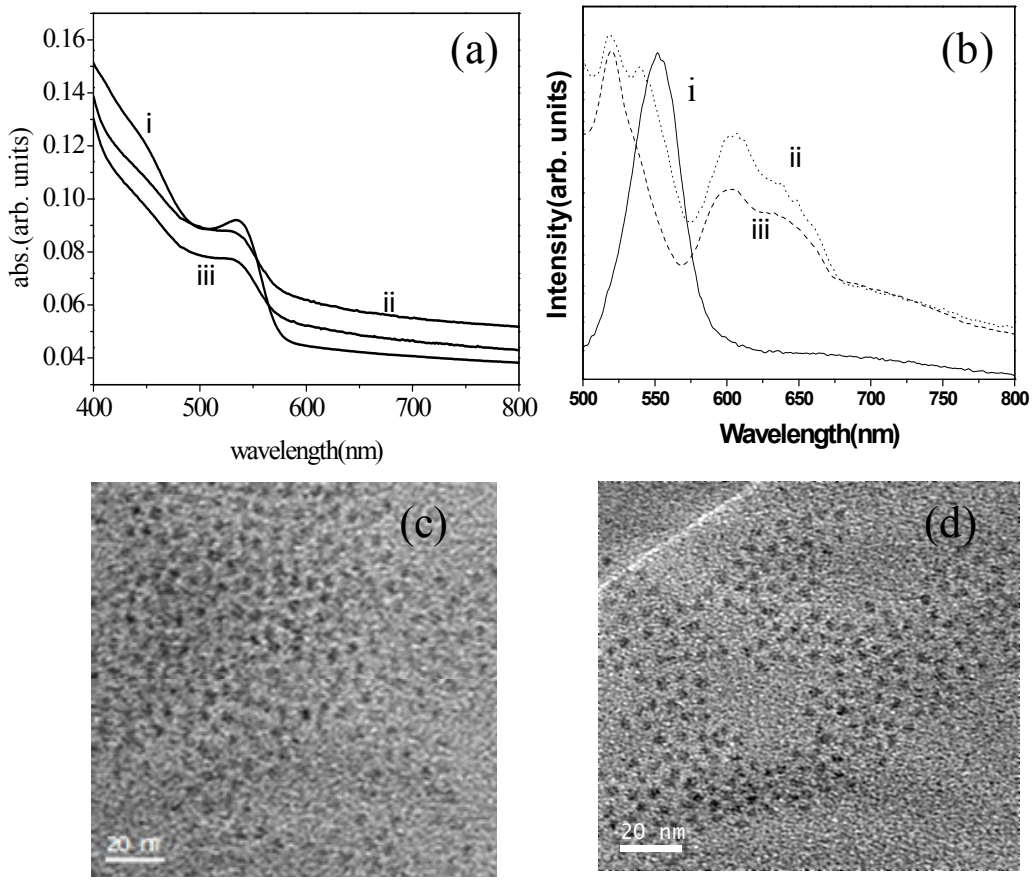

Figure 3.11: (a) Optical absorption and (b) photoluminescence spectra of CdSe nanocrystals before (i) and after (ii & iii) click reaction. (c) and (d) shows typical TEM images after click reaction.

The click reaction between spherical CdSe nanocrystals functionalized with the azido and ethynyl thiols gives rise to the cycloaddition products as verified by infrared spectroscopy. In Figure 3.11 (a) we show the optical absorption spectra of CdSe nanoparticles before and after click reaction. In Figure 3.11(b), we compare typical photoluminescence (PL) spectra of the click reaction product with the spectrum of the CdSe nanocrystals before the reaction. The product of the click reaction shows two broad bands, one at 518 nm and another centered at 620 nm while the isolated thiol-capped nanocrystals give a band at 550 nm. The two bands in Figure 3.11 (b) are not

due to two types of species since we observe one band at a lower wavelength and another at a higher wavelength relative to the band exhibited by the isolated CdSe nanocrystals. Theoretical calculations suggest that the change in the PL spectrum is due to dipolar coupling between neighboring nanocrystals giving rise to exciton splitting somewhat similar to Davydov splitting in CdS nanocrystals (*36, 37*). These features in the PL spectrum were found in the products obtained with different relative concentrations of the azidothiol and alkynethiol capped CdSe nanocrystals. The TEM image of the CdSe nanocrystals subjected to click reaction showed 3D periodic arrays (Figure 3.11(c) and (d)).

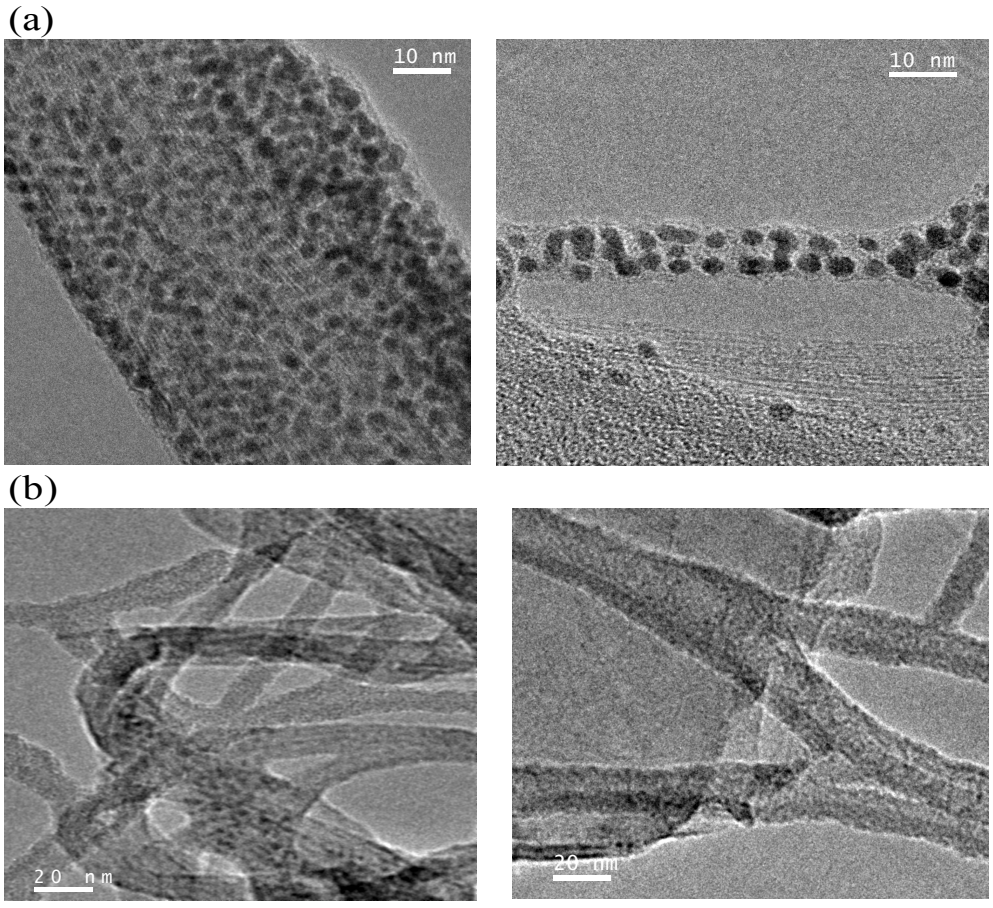

Figure 3.12: TEM images showing covalently attached (a) gold and (b) CdSe nanocrystals over SWNTs.

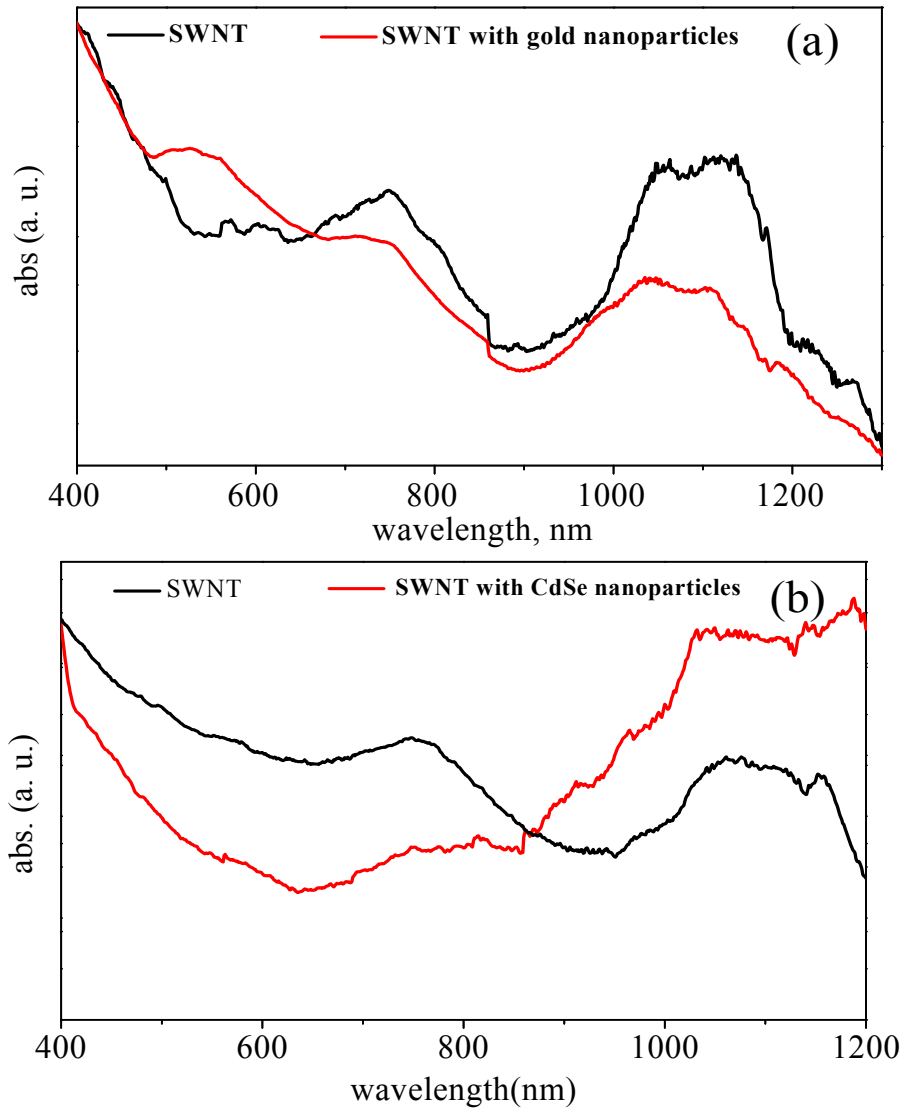

Figure 3.13: Optical absorption spectra of SWNTs (black) and SWNTs covalently attached with (a) gold and (b) CdSe nanoparticles (red).

In order to link SWNTs with gold or CdSe nanocrystals, SWNTs functionalized by the aminobutane with a terminal azido group were reacted with Au or CdSe nanocrystals capped with the hex-5-yne-1-thiol in the acetonitrile – water mixture. This reaction yielded SWNT–Au and SWNT-CdSe nanocomposites where in the gold or CdSe nanoparticles decorate the SWNTs uniformly. This can be seen in the TEM images shown in Figure 3.12. These images demonstrate the success of click chemistry

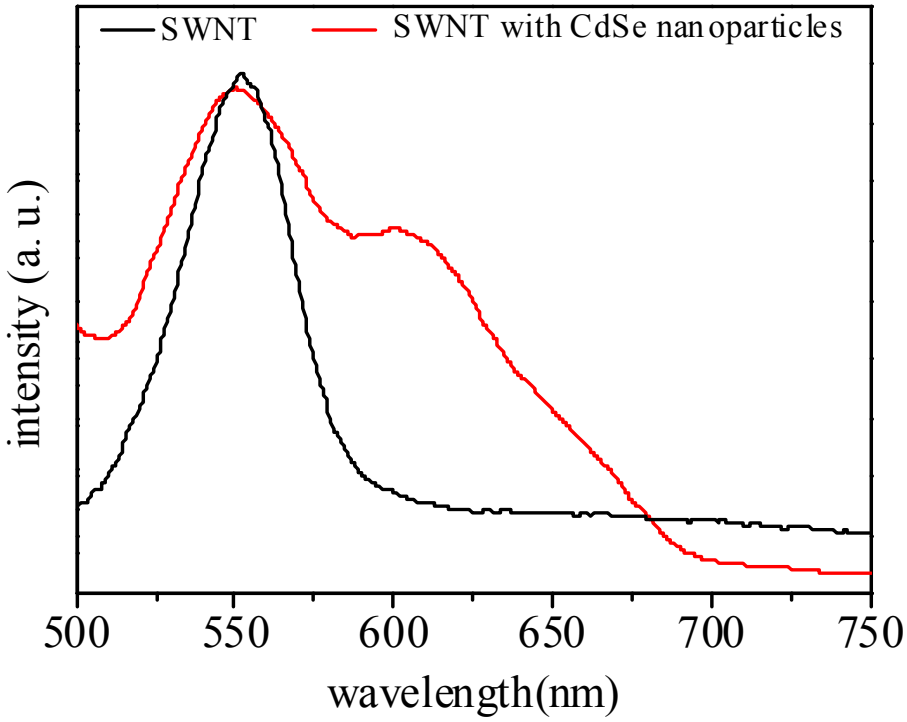

Figure 3.14: Photoluminescence spectra of CdSe (black) and CdSe attached to SWNTs (red).

in generating assemblies comprising covalently linked SWNT –metal or -semiconductor nanoparticle composites. Linking gold and CdSe nanoparticles with SWNTs causes perturbation in the optical absorption spectra of the nanotubes as can be seen from Figure 3.13. Pristine SWNTs show bands around 750 nm (M_{11}) corresponding to the metallic nanotubes and around 1040 nm (S_{22}) and 1880 nm (S_{11}) due to the semiconducting species arising from Van-Hove singularities in the optical absorption spectra. In case of gold nanoparticles attachment with SWNTs, intensity of S_{22} band of SWNTs decreases relative to M_{11} band, where as opposite effect is seen in CdSe nanoparticles attached with SWNTs. Gold nanoparticles attached with SWNTs show broad plasmon band centered around 549 nm, which is red shifted compared to the pristine gold nanoparticles (520 nm) (Figure 3.13(a)). Photoluminescence spectra of

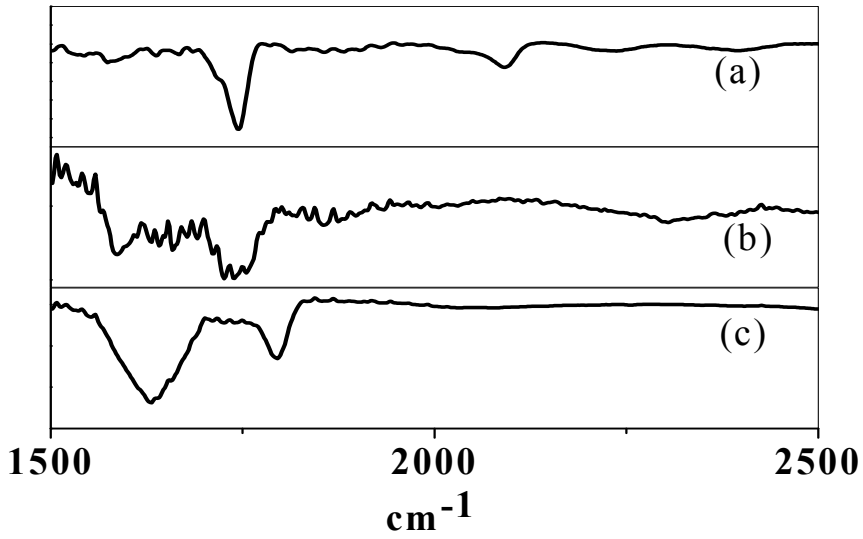

Figure 3.15: IR spectra of SWNTs functionalized with (a) 4-azidobutan-1-amine and (b) hex-5-yn-1-amine. (c) IR spectra of SWNTs after intelinking by click chemistry.

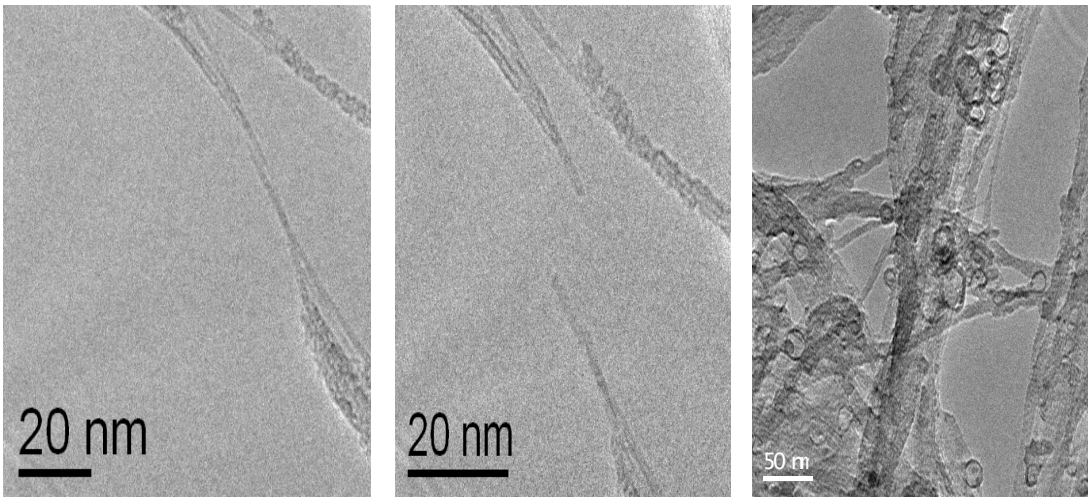

Figure 3.16: TEM images of SWNTs interlinked by click chemistry.

CdSe nanoparticles attached with SWNTs is shown in the Figure 3.14, which shows an additional band centred around 602 nm.

Intermolecular carbon nanotubes junctions were formed by coupling chemically functionalized nanotubes with linkers **C** and **D** by click reaction. The reaction was followed by IR spectroscopy (Figure 3.15). From The TEM images show the presence of end-to-end, end-to-side and side-to-side heterojunctions (Figure 3.16).

3.5 Conclusions

The above results demonstrate the efficacy and use of click chemistry in assembling covalently linked nanostructures. While alkanedithiols and thiolcarboxylic acids are known to assemble gold nanoparticles, the present method based on click chemistry is more general and can be used with carbon nanotubes, semiconductor nanoparticles and other nanostructures. It has been shown that the click reaction between spherical gold nanocrystals gives a product with a broad plasmon band accompanied by an organized assembly of the nanocrystals, instead of the chains obtained with the gold nanorods. The click reaction between capped CdSe nanocrystals causes changes in the photoluminescence spectra (This aspect will be discussed in the chapter 4). Click chemistry is also useful to prepare the composites of SWNTs with gold and CdSe nanocrystals.

REFERENCES

1. H. Kolb, M. G. Finn, K. B. Sharpless, *Angew. Chem. Int. Ed.* **40**, 2004 (2001).
2. R. Huisgen, *1,3-Dipolar Cycloaddition Chemistry*. A. Padwa, Ed., (Wiley, New York, 1984).
3. K. V. Gothelf, K. A. Jorgensen, *Chem. Rev.* **98**, 863 (1998).
4. V. R. Vsevolod, G. G. Luke, V. F. Valery, K. B. Sharpless, *Angew. Chem. Int. Ed.* **41**, 2596 (2002).
5. C. W. Tornoe, C. Christensen, M. Meldal, *J. Org. Chem.* **67**, 3057 (2002).
6. S. Bräse, C. Gil, K. Knepper, V. Zimmermann, *Angew. Chem. Int. Ed.* **44**, 5188 (2005).
7. H. C. Kolb, K. B. Sharpless, *Drug Discov. Today* **8**, 1128 (2003).
8. H. B. Wolfgang, S. Robert, *Macromol. Rapid Commun.* **28**, 15 (2007).
9. A. P. Alivisatos, *J. Phys. Chem.* **100**, 13226 (1996).
10. C. Burda, X. Chen, R. Narayanan, M. A. El-Sayed, *Chem. Rev.* **105**, 1025 (2005).
11. C. B. Murray, C. R. Kagan, M. G. Bawendi, *Annu. Rev. Mater. Sci.* **30**, 545 (2000).
12. M. L. Steigerwald *et al.*, *J. Am. Chem. Soc.* **110**, 3046 (1988).
13. C. B. Murray, C. R. Kagan, M. G. Bawendi, *Science* **270**, 1335 (1995).
14. C. B. Catherine, S. G. C. Adam, *J. Phys. D* **36**, R198 (2003).
15. S. K. Ghosh, T. Pal, *Chem. Rev.* **107**, 4797 (2007).
16. X. Huang, S. Neretina, M. A. El-Sayed, *Adv. Mater.* **21**, 4880 (2009).
17. C. N. R. Rao, A. Govindaraj, *Nanotubes and Nanowires: RSC Nanoscience & Nanotechnology series*. (Royal Society of Chemistry, Cambridge, 2005).
18. A. Hirsch, *Angew. Chem. Int. Ed.* **41**, 1853 (2002).
19. D. Tasis, N. Tagmatarchis, A. Bianco, M. Prato, *Chem. Rev.* **106**, 1105 (2006).
20. J. W. Lown, *1,3-Dipolar Cycloaddition Chemistry*. A. Padwa, Ed., (Wiley, New York, 1984).
21. R. Huisgen, *Pure. Appl. Chem.* **61**, 613 (1989).
22. D. A. Fleming, C. J. Thode, M. E. Williams, *Chem. Mater.* **18**, 2327 (2006).
23. H. Li, F. Cheng, A. M. Duft, A. Adronov, *J. Am. Chem. Soc.* **127**, 14518 (2005).
24. J. W. Lee, S. I. Jun, K. Kim, *Tetrahedron Lett.* **42**, 2709 (2001).
25. F. Kim, J. H. Song, P. Yang, *J. Am. Chem. Soc.* **124**, 14316 (2002).
26. D. G. Duff, A. Baiker, P. P. Edwards, *Chem. Commun.*, 96 (1993).

27. U. K. Gautam, M. Rajamathi, F. Meldrum, P. Morgand, R. Seshadria, *Chem. Commun.*, 629 (2001).
28. C. Journet *et al.*, *Nature* **388**, 756 (1997).
29. V. V. Rostovtsev, L. G. Green, V. V. Fokin, K. B. Sharpless, *Angew. Chem. Int. Ed.* **41**, 2596 (2002).
30. T. Linnert, P. Mulvaney, A. Henglein, *J. Phys. Chem.* **97**, 679 (1993).
31. K. G. Thomas, S. Barazzouk, B. I. Ipe, S. T. S. Joseph, P. V. Kamat, *J. Phys. Chem. B* **108**, 13066 (2004).
32. P. K. Sudeep, S. T. S. Joseph, K. G. Thomas, *J. Am. Chem. Soc.* **127**, 6516 (2005).
33. M. A. Correa-Duarte, J. Pérez-Juste, A. Sánchez-Iglesias, M. Giersig, L. M. Liz-Marzán, *Angew. Chem. Int. Ed.* **44**, 4375 (2005).
34. C. J. Murphy *et al.*, *J. Phys. Chem. B* **109**, 13857 (2005).
35. J. Pérez-Juste, L. M Liz-Marzán, S. Carnie, D. Y C Chan, P. Mulvaney, *Adv. Funct. Mater.* **14**, 571 (2004).
36. L. Cao *et al.*, *J. Chem. Phys.* **123**, 024702 (2005).
37. A. S. Davydov, *Theory of Molecular Excitons*. (Plenum, New York, 1971).

CHAPTER 4

Dependence of Magnetic and Optical Properties of Nanoparticles on the Interparticle Separation

Summary*

Dependence of the magnetic properties of FePt nanoparticles with an average diameter, D, of 5 nm and 1.5 nm on the interparticle separation, d, has been investigated by employing different spacer molecules. The blocking temperature and Curie-Weiss temperature decreases with increase in d while saturation magnetization increases with increase in d. The results are explained on the basis of a simple model for the case d<<D where the magnetic nanoparticles are treated as finite dipoles coupled through anisotropic multipolar interactions.

Different types of aggregates of CdSe nanoparticles have been assembled by using bridging molecules such as thiolcarboxylic acids and alkanedithiols as by well as the click reaction involving cycloaddition between azido and acetylenic groups. The aggregates show photoluminescence spectra different from the pristine CdSe nanocrystals. The simplest situation is one where the spectrum has two bands one at longer wavelengths and another at lower wavelengths arising from dimeric units. More complex spectra arise from higher aggregates, but there is always some symmetry in the band positions. Fluorescence decay measurements have been carried out on the different CdSe aggregates. The results are interpreted in terms of electronic coupling between the nanocrystals.

**** Papers based on these studies have appeared in Journal Physical Chemistry C (Letter) (2008) and Journal of Nanoscience and Nanotechnology (2009)***

4.1 Introduction

Nanoparticles show a number of properties that are either absent (*1, 2*) in or more efficient (*3*) than their bulk materials counterparts. It is well-established that individual nanoparticles can exhibit unique size-dependent electronic, optical, magnetic and photonic properties (*4*). It has become apparent that the properties of nanoparticle assemblies can differ from those of the isolated nanoparticles. If the interparticle distance is appropriate to encourage nanoscale cooperative processes (*5*) such as electron tunneling, dipolar coupling, and Forster energy transfer, photonic and electronic properties can be manipulated by controlling the distance between nanoparticles. In some cases, altogether new properties based upon collective nanoparticle behavior will arise. The realization of these properties in next-generation applications including catalysis (*6, 7*), optoelectronics (*8*), sensors (*9*) and medicine (*10, 11*), therefore requires methods for the precise spatial assembly of nanoparticles.

Some progress has been made in the development of self-organizing nanoparticle assemblies. The distance between nanoparticles has been controlled by grafting polymers to (*12*) or polymerizing polymers from (*13*) the nanoparticle surfaces, or by using a number of functional molecules, including alkanethiols (*14*), dendrimers (*15*), proteins (*16*), DNA (*17*) or difunctional linkers (*18, 19*), to mediate the nanoparticle self-assembly process. It has been demonstrated that magnetic properties can be manipulated in assemblies of superparamagnetic particles by using dendrimers to mediate the interparticle distances (*20*).

In this chapter, we present our investigations towards understanding magnetic and optical properties of nanoparticles by varying the interparticle distance. Magnetic properties are examined on FePt nanoparticles. While spectroscopic properties are

examined in the case of CdSe nanoparticles. We report the scope of the present investigations in the next section.

4.2 Scope of the Present Investigations

Recently, there has been an increasing attention to the formation of controlled assemblies of nanoparticles (*4, 21-23*), whose properties depend on the constituent particles as well as on the assembly parameters, such as interparticle distance and average particle environment. Plasmon waveguides (*24*), magnetic logic (*25*) and quantum cellular automata (*26*) are only a few examples of proposed devices that would be based on such assemblies. In case of all assemblies, one of the main goals is to create materials with novel properties, possibly not present in either the nanoparticle or the bulk form of the material.

Properties of magnetic nanoparticles have been investigated by several workers and some of the novel features exhibited by these materials have been known for some time (*27*). For example, nanoparticles of antiferromagnetic materials are expected to show a small net magnetic moment due to finite size effects (*28*). Such a behavior has been found in nanoparticles of oxides such as MnO, CoO and NiO (*29, 30*). A problem of considerable interest related to magnetic nanoparticles is the dependence of their properties on the interparticle separation. It is commonly believed that the variation in properties such as the blocking temperature, T_B, with the interparticle separation, d, is governed by dipolar interaction. There have been a few studies on this aspect in the last few years. Vestal *et al.* (*31*) have varied the interparticle distance in spinel ferrite nanoparticles by varying the concentration in solution, and found that T_B increases with the increase in concentration, suggesting there by that T_B increases with decrease in interparticle separation. A study of the magnetic interaction between iron oxide nanoparticles by Frankamp *et al.* (*20*) through dendrimer-mediated self-assembly has

shown that T_B decreases with increase in interparticle separation. These authors comment on how their results deviate from the dependence predicted on the basis of dipolar interaction between the magnetic nanoparticles. DNA-assembled FePt nanoparticles exhibit a decrease in T_B compared to the pristine ones (*17*). An increase in T_B with increase in interparticle separation seems to have been observed in chains of 13 nm γ-Fe_2O_3 nanoparticles prepared by using 11-(10-carboxy-decyldisulfanyl)-undecanoic acid (*32*). Clearly, the nature of dependence of T_B of magnetic nanoparticles on the interparticle separation, d, is not understood. We felt that this may be because one has not employed the correct model to interpret magnetic properties as a function of d. We would expect the interaction would be essentially dipolar if d is large relative to the particle diameter, D. The interaction would, however, be multipolar if d is small compared to D.

Scheme 4.1:

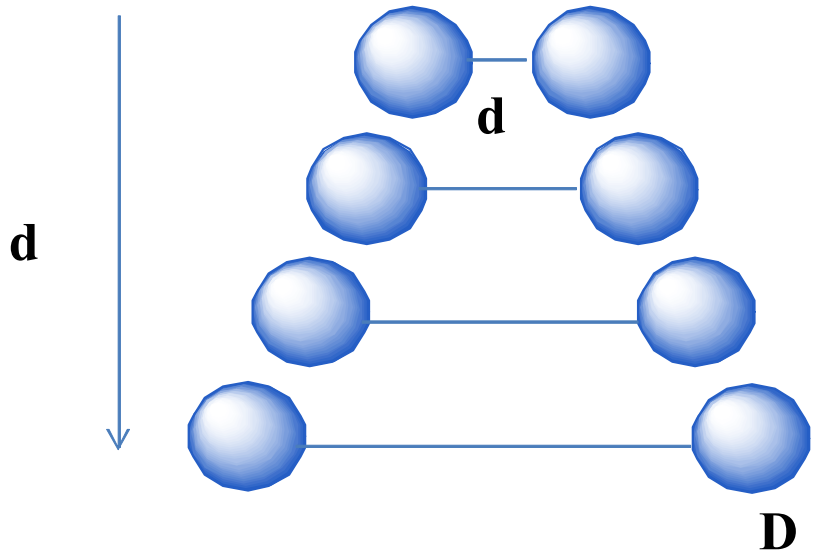

We have carefully investigated the variation of the magnetic properties of FePt nanoparticles (D=5nm) as a function of interparticle separation, by varying d by using alkanedithiols (Scheme 4.1) and other capping agents. The 5nm FePt particles are superparamagnetic at 300K and show magnetic hysteresis at low temperatures (*33, 34*).

Zero-field cooled magnetization data show a maximum in magnetization at the blocking temperature, T_B. We have determined the variation of T_B, the Curie-Weiss temperature, θ, and the saturation magnetization, M, with the interparticle separation, and discussed the observed trends in the light of a simple model. It may be noted that the variation of magnetization or the Curie-Weiss temperature with d has not been examined in any of the studies reported in the literature.

Understanding electronic interactions between two or more semiconductor nanocrystals is of considerable academic as well as technological interest. Optoelectronic properties of nanostructures containing nanocrystals which are electronically coupled have been investigated (*27, 35-38*). There has been some attempt recently to study optical spectra of CdS nanocrystal aggregates prepared by using oleic acid, in comparison with the spectrum of isolated nanocrystals (*39*). This study by Cao *et al.* has shown the presence of multi-exciton interaction leading to new absorption and emission bands. The excitonic interaction in the aggregates shows Davydov splitting due to dipole–dipole interaction (*40*). Koole and coworkers (*41, 42*) examined the optical spectra of CdTe nanocrystals linked by flexible and rigid dithiol molecules and found shifts in the emission spectra due to the linking of nanocrystals and fast initial decay due to exciton electronic transfer between the quantum dots. While the above studies are indicative of electronic coupling in the semiconductor nanocrystal aggregates, the spectra reported are not sufficiently informative in describing specific effects due to electronic interaction and to relate them to the state of aggregation. Due to the importance of this problem, we have investigated the electronic emission spectra of CdSe nanocrystals linked by different types of molecules, having characterized the aggregates by transmission electron microscopy.

In order to obtain different types of CdSe aggregates, we have used mercaptopropionic acid and alkanedithiols with different alkane chain lengths as the

linker molecules. We have also employed the click reaction involving Huisgen cycloadditon between azide and acetylenic groups yielding a 1, 2, 3-triazole to link the nanocrystals. The manner of linkage formed by mercaptopropionic acid, by alkanedithiols and by the click reaction are shown below in 1, 2 and 3 respectively. Here the circles correspond to CdSe nanocrystals.

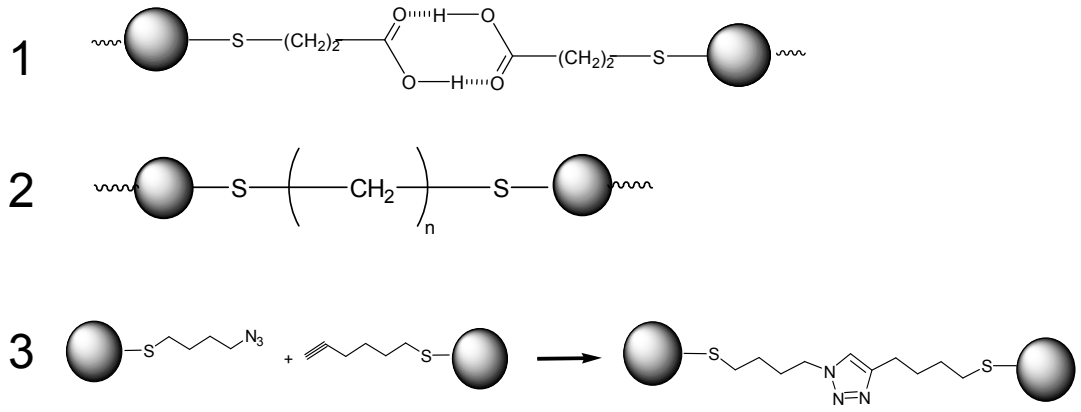

4.3 Experimental

4.3.1 Preparation of magnetic nanoparticles and assembly

Synthesis of FePt nanoparticles: FePt nanoparticles with an average diameter 5 and 1.5 nm were prepared by the procedure described by Nandwana *et al.* (*34*). The 5 nm FePt nanoparticles were prepared as follows. Under a flow of nitrogen, $Pt(acac)_2$ (0.5 mmol) was mixed with benzyl ether (10 ml) and heated to 100 ^oC. Under a blanket of nitrogen, $Fe(CO)_5$ (1 mmol), oleyl amine (4 mmol) and oleic acid (4 mmol) were then added. The mixture solution was then heated to 240 ^oC and incubated at this temperature for one hour to assure complete decomposition of $Fe(CO)_5$, and then heated to reflux (300 ^oC). The mixture was kept refluxing at this temperature range for 2 hours. During this time, slow nitrogen flow was introduced from time to time to remove some low boiling by-products and to maintain the refluxing temperature around 300 ^oC. The reaction mixture was allowed to cool to room temperature by removing the heating source. The 20 ml of ethanol was added to the solution to precipitate the nanocrystals.

The nanocrystals were separated by centrifugation. The resulting balck precipitate was redispersed in hexane. We have obtained the 1.5 nm FePt nanoparticles by reducing all the precursor concentrations by one fourth. The precipitate of 5 nm and 1.5 nm nanoparticles (200 mg) capped with oleic acid and oleyl amine was redissovled in 20 ml of hexane (stock solution) for further studies.

FePt nanoparticles cross-linked by dithiols were prepared as follows. Alkanedithiols (1, 2-ethanedithiol, 1, 4-butanedithiol, 1,6-hexanedithiol and 1,8-octanedithiol) with specific concentrations mentioned in the section 4.4.1 were added to the 3 ml hexane stock solution of FePt to prepare cross linked FePt nanocrystals.

4.3.2 Synthesis of CdSe nanocrystals and their assemblies

Synthesis of CdSe nanoparticles: Red-emitting CdSe nanocrystals (~ 4 nm) were prepared by the solvothermal method starting with cadmium stearate, selenium, trioctylphosphine Oxide (TOPO) and tetralin in toluene solution following the procedure reported earlier (*43*). In a typical reaction 1.36 g (2 mmol) of [$Cd(St)_2$], 0.158 g (2 mmol) of Se, 0.2 g (1.5 mmol) of tetralin and 0.1 g (0.5 mmol) of dodecanethiol were taken in 50 ml of toluene in a stainless steel autocalve (*ca.* 70% filling, Teflon gasket) and placed in an oven that had been preheated to 250 ^{o}C. After 5 h the autoclave was removed and cooled to room temperature. The solid product obtained by precipitation as mentioned in the text was dried at 50 ^{o}C in air overnight. The precipitate of CdSe nanoparticles (18 mg) capped with TOPO was redissovled in 20ml of toluene (stock solution) for further studies.

Assemblies of CdSe nanoparticles were obtained by the use of mercaptopropionic acid as follows. 50 µl of the solution of CdSe nanoparticles solution in toluene taken in a glass vial and the toluene solvent evaporated under vacuum. The resulting CdSe QDs precipitate was solubulized in 3 ml of deonized water by the addition different concentrations of mercaptopropionic acid (2.5 mM, 5 mM, 7.5 mM and 10 mM) under

sonication. CdSe nanoparticles cross-linked by dithiols were prepared as follows. Toluene solution (10 μM) of alkanedithiol (1, 2-ethanedithiol, 1, 4-butanedithiol, 1,6-hexanedithiol and 1,8-octanedithiol) were added to the toluene solution of CdSe to prepare cross-linked CdSe nanocrystals. Solutions with different dithiol-nanocrystal ratios were prepared by adding a constant quantity of TOPO-capped CdSe QDs (50 μl) to 3 ml of toluene solution containing different concentrations of the dithiols. Covalent attachment of CdSe nanoparticles by click chemistry was accomplished as follows. For linking CdSe nanocrystals by the 1, 3-dipolar cycloaddition reaction, a stock solution of 25 μl of CdSe nanoparticles solubulized in toluene was added to 1.5 ml of the toluene solution (Solution A). 1.5 mlof solution A was taken in two different glass vials and 60 μl of 4-azidobutanethiol (**I**, 1 μM) was added to one and a known quantity (120 or 240 μl) of hex-5-yn-1-thiol (II**, 1** μM) to another. The resulting solutions of CdSe nanoparticles attached with the thiols **I** and **II** were mixed and the cycloadditon reaction carried out using CuI as the catalyst in the absence of external light. The preparation of various types of aggregates of CdSe nanocrystals described above were repeated several times and spectroscopic measurements carried out on the independent preparations.

4.3.3 Techniques used for characterization

Transmission electron microscopy

For transmission electron microscopy (TEM), dispersions of the samples were dropped onto the holey carbon-coated Cu grids, and the grids were allowed to dry in the air. The grids were examined using a JEOL (JEM3010) microscope operating with an accelerating voltage of 300 kV.

Optical absorption and photoluminescence spectroscopy

The optical absorption spectroscopy measurements were performed using a Perkin-Elmer Lambda 900 UV/VIS/NIR spectrometer. Photoluminescence spectra of these

solutions were recorded with a Perkin-Elmer model LS55 luminescence spectrometer. Photoluminescence (PL) experiments were performed using a Fluorolog-22 (Horiba-jobin Yvon) spectrofluorometer fitted with a Xenon lamp excitation source. Time resolved fluorescence measurements were carried out with time correlated single photon counting fluorescence spectrometer (IBH) by exciting the sample at 425 nm with Ti: Sapphire laser of pulse width 2 ps FWHM and the instrument response time of 50 ps. Fluorescence decay was measured at the front face configuration with suitable cutoff filters to avoid scattered light and the decay curve was analyzed using the software (DAS6, IBH).

Infrared spectroscopy

Infrared (IR) spectra of the precursors were recorded with a Bruker FT-IR spectrometer. The samples were prepared by grinding with KBr and pressing into a disk.

Magnetic characterization

Powder samples of the as-prepared nanoparticles were subjected to magnetic characterization using the VSM in PPMS (Physical Properties Measurement System).

4.4 Results and discussion

4.4.1 Dependence of the properties of magnetic nanoparticles on the interparticle separation

FePt nanoparticles with an average diameter 5 nm and 1.5 nm were prepared by the procedure described by Nandwana *et al.* (*34*). Transmission electron microscopy (TEM) was employed to determine the average size of the particles (Figure 4.1). When the 5 nm FePt nanoparticles were prepared in the presence of the oleyl amine and oleic

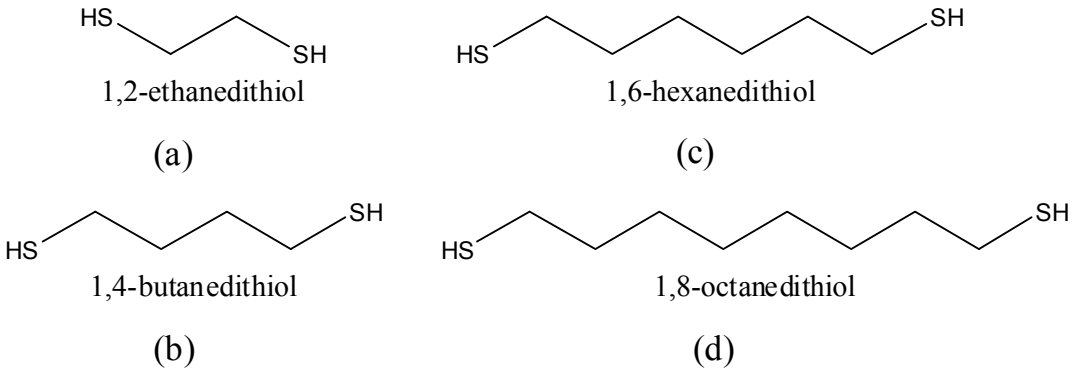

Scheme 4.2: Different alkanedithiols used to vary interparticle separation.

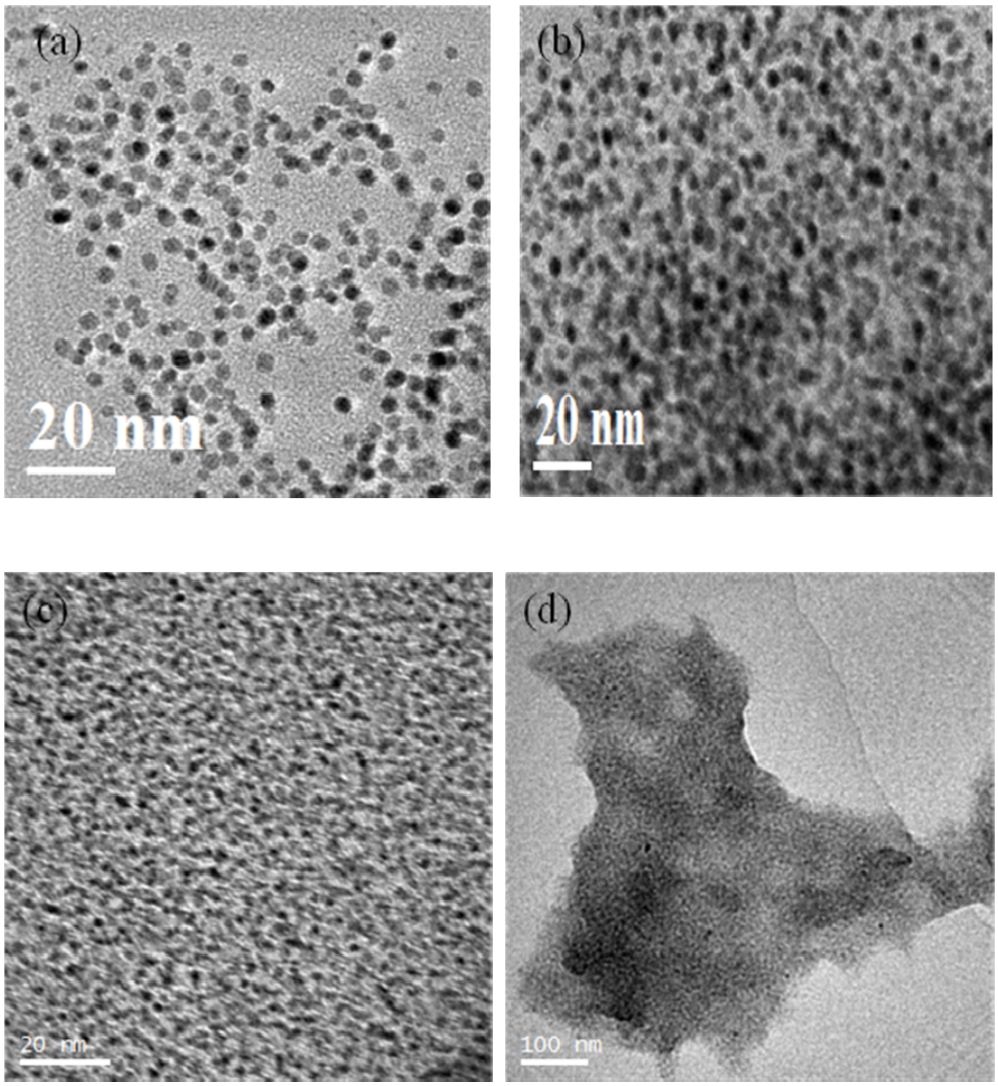

Figure 4.1: TEM images of (a) & (b) 5 nm and (c) & (d) 1.5 nm FePt nanoparticles linked by low ethanedithiol (a&c) and high ethanedithiol (b & d) concentrations.

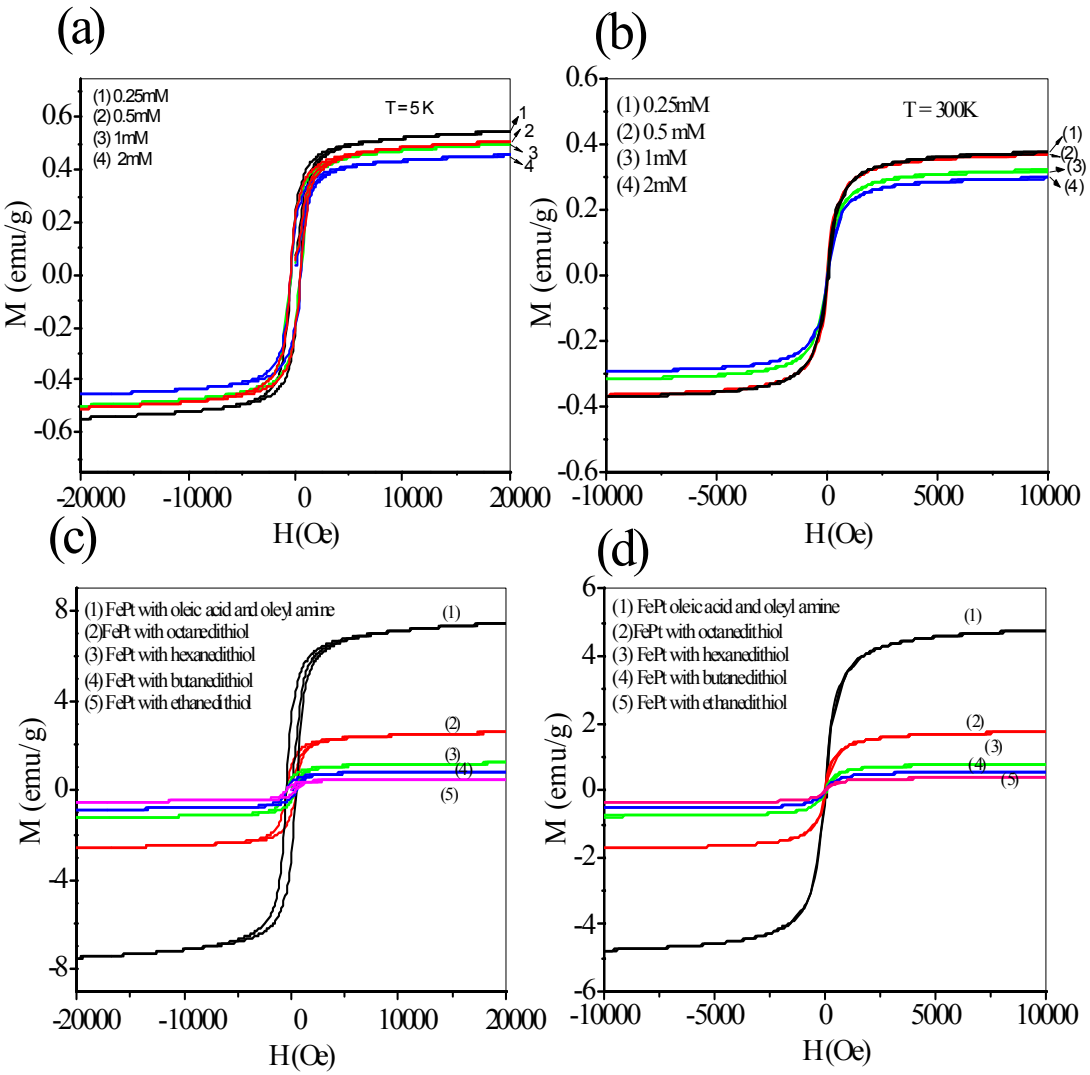

Figure 4.2: Magnetic hysteresis exhibited by 5 nm FePt nanoparticles at (a) & (c) 5 K and (b) & (d) 300 K with different concentrations of ethanedithiol ((a) & (b)) and with different interparticle separations ((c) & (d)).

acid, the interparticle separation was 2.4 nm. Oleyl amine and oleic acid are readily removed on the addition of alkanedithiols. We have used four alkanedithols (Scheme 4.2) namely 1,2-ethanedithiol, 1,4-butanedithiol, 1,6-hexanedithiol and 1,8-octanedithiol, to vary inteparticle separation (d). The dithiol binds two nanoparticles on either side, the interparticle separation being determined by the alkane chain length. To obtain alkanedithiol linked particles, a known quantity of 5 nm FePt nanoparticles was taken in a hexane solution of alkanedithiol of known concentration. The solid that

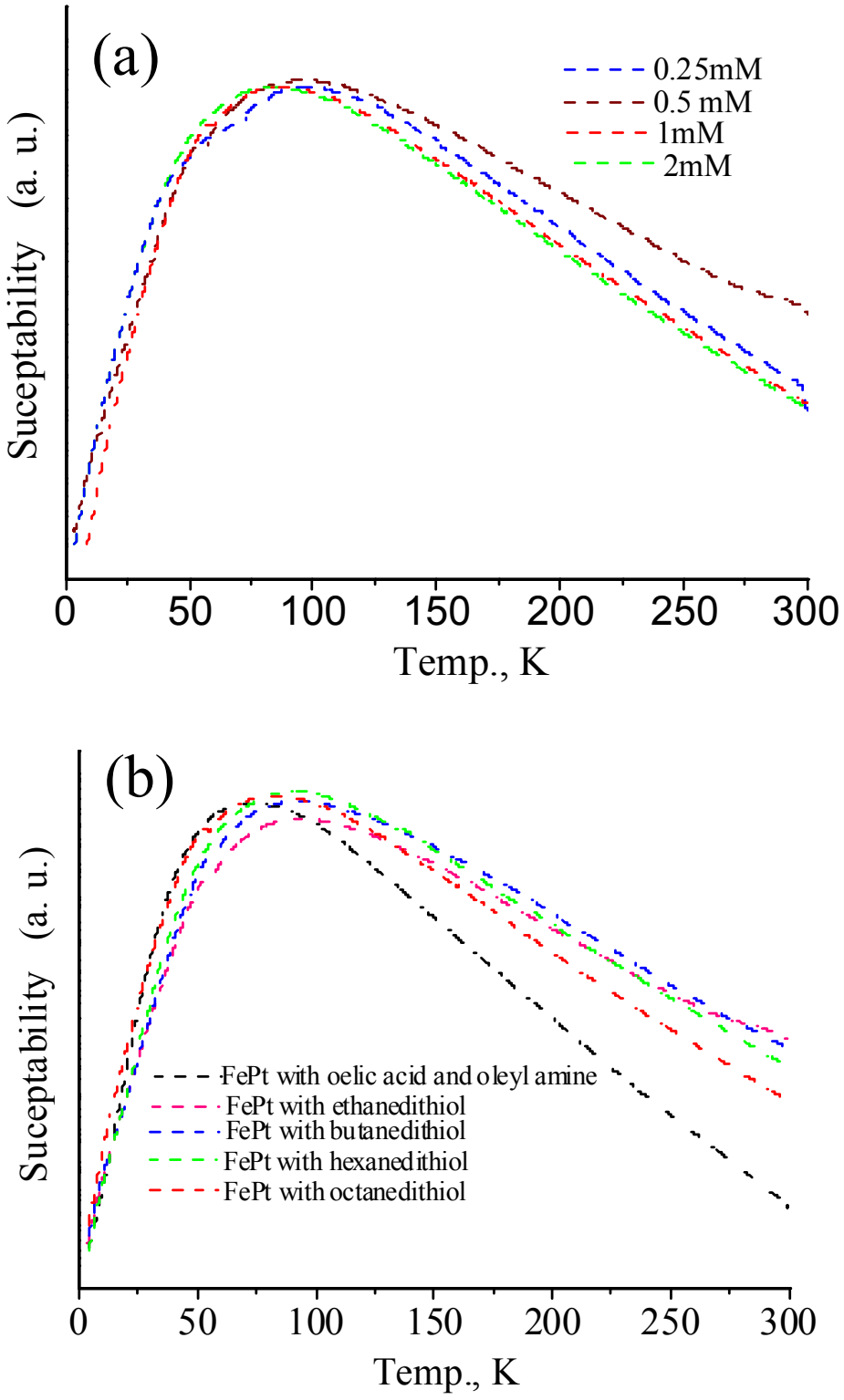

Figure 4.3: Temperature-variation of zero-field cooled magnetization of 5 nm FePt nanoparticles (a) with different concentrations of ethanedithiol and (b) linked with different alkanedithiols (having different interparticle distances).

precipitated out or obtained after evaporation of the solvent was used to measure the magnetic properties. The dependence of magnetic properties of 5 nm FePt were examined by the concentration variation of the dithiol. Figure 4.2 (a) & (b) shows the magnetic hysteresis of 5 nm FePt nanoparticles at 5 K and 300 K with different concentrations of ethanedithiol. It was found that the value of the magnetization varies only slightly with the alkanedithiol concentration (Figure 4.4 (a)). Figure 4.3 (a) shows the temperature variation of zero-field cooled (ZFC) magnetization of 5 nm FePt nanoparticles with different concentrations of ethanedithiol. The blocking temperature, T_B, in the zero-field cooled data, and the Curie-Weiss temperature, θ, obtained from high-temperature inverse susceptibility data, were in the range of 87±5 K and 95±5 K respectively over dithiol concentrations of 0.25 – 2 M (Figure 4.4 (b)). We have used a constant concentration of 0.5 mM of the alkanedithiols in the present study, since all the particles would be dithiol-linked at this concentration.

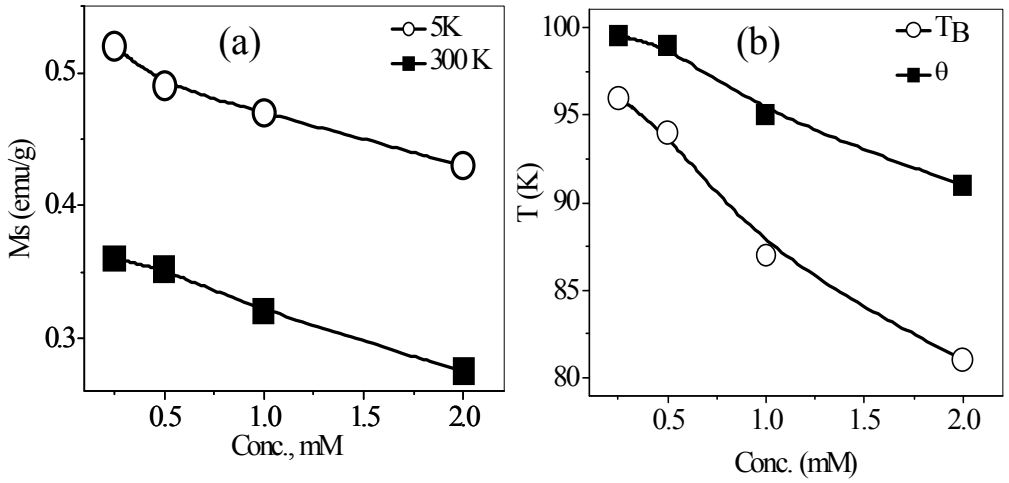

Figure 4.4: (a) variation of saturation magnetization at 5 K and 300 K and (b) variation of TB and θ with at different concentrations of ethanedithiol.

With the different spacer molecules employed by us, the interparticle separation could be varied between 0.4 and 2.4 nm (Figure 4.1). Figure 4.2 (c) & (d) shows the magnetic hysteresis of 5 nm FePt nanoparticles at 5 K and 300 K respectively with different interparticle separations (different dithiols). From Figure 4.2 (c) & (d) we

readily see that the nature of the hysteresis varies with d. Thus, the value of the saturation magnetization, M_S, increases with increase in d (Figure 4.5 (a)). From Figure 4.3 (b), we see that T_B shifts to lower temperatures with increase in d. Since the average diameter of the FePt nanoparticles, D, is 5nm, the spacer length, d, is always less than D (d<<D). It is impractical to have a situation where d>>D with alkanedithiols and such spacer molecules. Furthermore, nanoparticles with very small D do not possess the desirable magnetic properties. In Figures 4.5 (b) we show the variation of the blocking temperature, T_B, and the Curie–Weiss temperature, θ, respectively with the spacer length, d. The θ values were obtained from the high-temperature inverse susceptibility data. We see that T_B decreases with the increase in d. The nature of variation of T_B with d found here is comparable to that reported in the literature on the basis of concentration-dependence or of dendrimer-mediated assemblies (*20, 31*). The Curie-Weiss temperature, θ, varies with d in the same manner as T_B. This is interesting since θ is a thermodynamic quantity unlike T_B. In Figure 4.5 (a), we show the variation of the saturation magnetization, M_S, at 5 K with d, to demonstrate how M_s increases with d.

The decrease in T_B with increase in d can be understood on the basis of the model described by Dormann *et al.* (*44-46*) which predicts a decrease in the energy barrier with increase in d. However, the exact manner in which T_B varies with d is another matter. Theoretical calculations predict that T_B of magnetic particles interacting through dipolar coupling should follow an inverse cubic dependence on the interparticle separation (*47*). Our data as well as the literature data (*20*) do not follow the inverse cubic dependence. That is, the slope of the plot of log T_B against log d deviates significantly from d^{-3}. The possibility of d^6 dependence up to a spacing of 1.0 nm or so has been suggested (*20*). In other words, a modest increase in d has been considered sufficient to result in independent nanoparticles. The real situation, however, appears to be different.

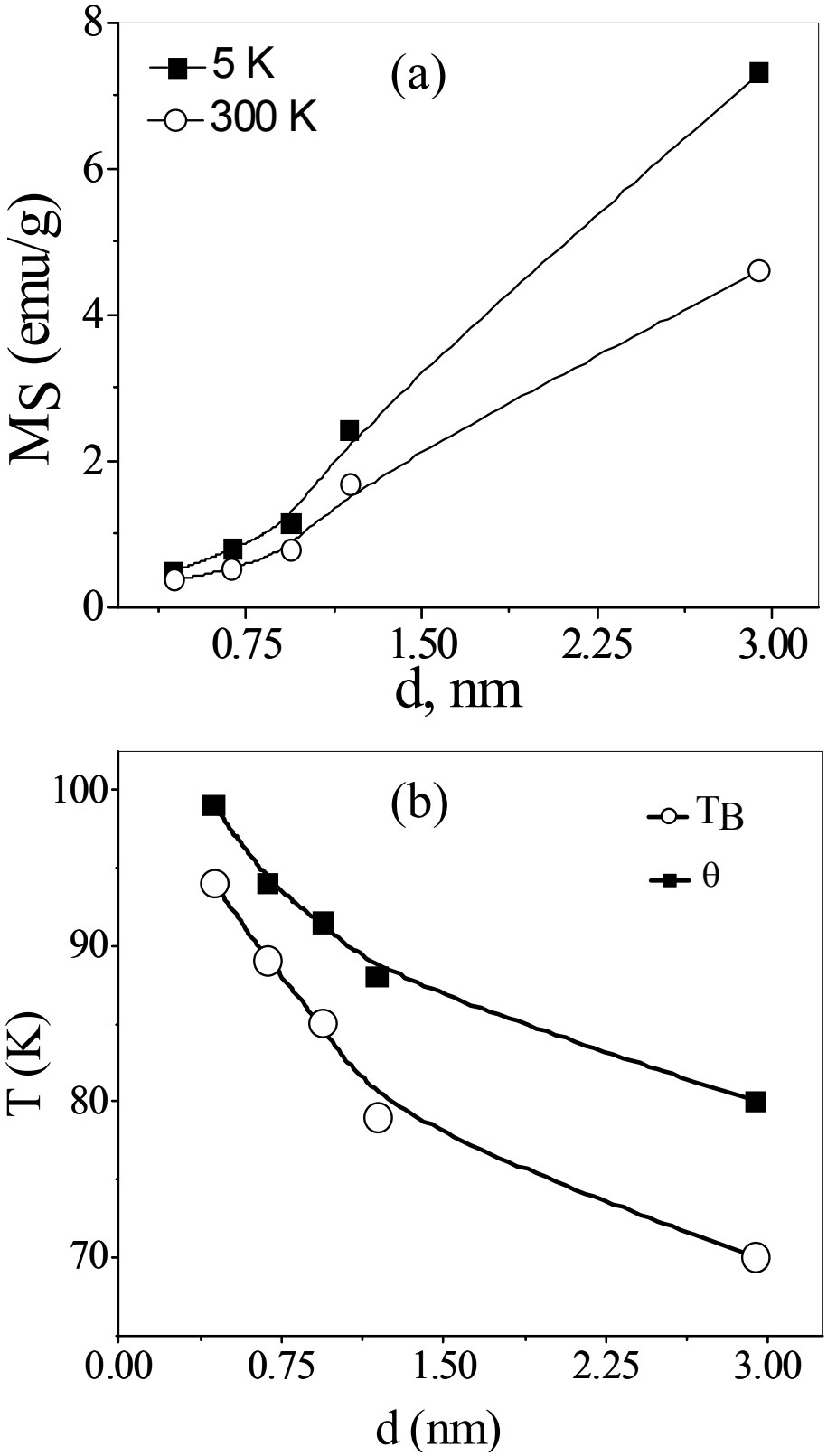

Figure 4.5: (a) Variation of saturation magnetization at 5 and 300 K and (b) variation of T_B and θ with interparticle separation, d.

In order to understand the nature of variation of T_B and θ with d, we have calculated the magnetostatic interaction energy between two identical, spherical nanoparticles as a function of the particle diameter, D, and the interparticle separation d, with D>d. We are dealing here with a multipolar finite magnets (*48*), with the purely dipolar behaviour dominating only in the limit of large separation *d*>>D. In deriving our expression for the normalized magnetostatic interaction energy, u, we take advantage of the fact that a uniformly magnetized spherical body of magnetic moment density, μ, is equivalent to a surface magnetic charge density $\sigma(\theta,\phi) = \mu\cos\theta$, where we have taken the direction of magnetization as the polar axis. The total magnetic moment is, given by, $M = \mu(4\pi/3)(D/2)^3$ which is the magnetic moment of the spherical single-domain nanoparticles. The problem of finding the interaction energy between two uniformly magnetized spheres reduces to that of evaluating the interaction energy of these two surface charge densities. It is essentially the product of these two densities divided by their relative distance apart, integrated over the respective spherical surfaces. For two antiparallel magnetized spheres in the broad-side on configuration, we obtain the following expression for u:

$$u = \frac{U(d,D,\mu)}{U_{dipolar}(d+D,0,\mu)} = \frac{9}{4\pi^2}\left(1+\frac{d}{D}\right)^3 \int_0^{\pi}\int_0^{\pi}\int_0^{2\pi}\int_0^{2\pi} \frac{\sin\theta_1 \sin\theta_2 \cos\theta_1 \cos\theta_2 \; d\theta_1 d\theta_2 d\phi_1 d\phi_2}{\sqrt{f(1,2)}}$$

,

where $f(1,2)$ =

$$\left[\left(1+\frac{d}{D}+\frac{1}{2}\sin\theta_1\sin\phi_1-\frac{1}{2}\sin\theta_2\sin\phi_2\right)^2+\left(\frac{1}{2}\sin\theta_1\cos\phi_1-\frac{1}{2}\sin\theta_2\cos\phi_2\right)^2 + \left(\frac{1}{2}\cos\theta_1-\frac{1}{2}\cos\theta_2\right)^2\right].$$

The above relation is exact. The normalization factor is the purely dipolar interaction energy for the two finite dipoles replaced by two point dipoles each of moment M placed at the centres of the respective spheres, *i.e.,* at a distance $d + D$

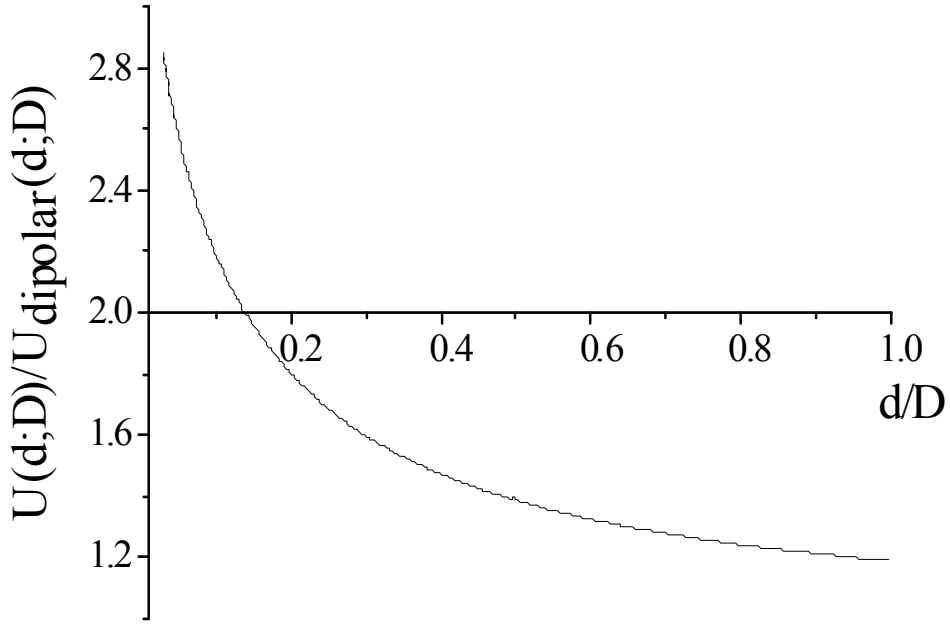

Figure 4.6: Plot of normalized magnetostatic energy U(d, D) for broad side on configuration (normalized) with respect to a point dipolar interaction at a distance (D+d) for the same μ value, against d/D.

apart. It may be noted that the above expression for the normalized interaction tends to unity as d/D → ∞ as it should. This is readily verified by expanding $1/\sqrt{f(1,2)}$ in powers of $(1+d/D)^{-1}$ and retaining the leading (nonzero) term obtained on performing the integrals of the trigonometric functions involved. The above expression can be simplified to a more tractable, but approximate form for numerical integration. In physical terms, here we essentially collapse the two uniformly magnetized finite-diameter spheres to two extended distributions of point dipoles along the line joining the two spheres in the broad-side on configuration. This gives the normalized interaction energy *u* as,

$$u \equiv \left(\frac{U(d,D,\mu)}{U_{dipolar}(d+D,0,\mu)} \right) \cong \left(\frac{9}{16} \right) \left(1+\frac{d}{D} \right)^3 \int_{-1}^{+1} \int_{-1}^{+1} dx_1\, dx_2 \left(\frac{(1-x_1^2)(1-x_2^2)}{\left(1+\frac{d}{D}-\frac{1}{2}(x_1-x_2) \right)^3} \right)$$

We see at once that, $u \rightarrow 1$, as $d/D \rightarrow \infty$. That is, at large distances, the finite dipoles act as point dipoles as expected. In Figure 4.6, we show the variation of normalized u with d/D. For fixed D, as in our experiments, it represents the variation of u with d. The above treatment ignores nonmagnetic contributions to the binding. It is, however, gratifying, given the simplicity of this minimal model, that the plot in Figure 4.6 contains essential features of the experimental results in Figures 4.5 (b). Thus, both T_B and θ decrease with increase in d just as the magnetostatic interaction energy in Figure 4.6. The initial fall in both cases is fast and then tends to level off for large d. This is understandable since T_B, is due to the energy barrier subtended by anisotropic interactions that render the arrested relaxation ultra slow for $T<T_B$ and must scale with u. Unlike the relaxational blocking temperature, the Curie-Weiss temperature is a thermodynamic quantity. It too, must track u, this being the only coupling energy scale in the problem responsible for the cooperative phenomenon. The observed decrease in the Curie-Wiess temperature with increasing d is qualitatively similar to what is expected.

The variation of the magnetization with d is rather subtle, but can be understood as follows. First, note that a conventional ferromagnetic system with its isotropic exchange coupling orders to saturation when a relatively small polarizing magnetic field is applied. In the present case, however, the anisotropic multi-polar magnetic coupling between the nanoparticles is in conflict with the effect of a polarizing field. This effectively reduces the saturation magnetization. In the simple case of two nanomagnets each of magnetic moment μ, in the broad-side-on configuration with the magnetostatic coupling U(d,D), the magnetic polarization M(d) induced by a polarizing field H is given by,

$$M(d) = [2\mu \sinh(2\ \mu H/kT)]/[\cosh(2\ \mu H/kT)+ \exp(2U(d.D)\ \mu^2)]$$

Clearly, the induced magnetization M(d) increases monotonically as the interparticle spacing d increases. Recall that U(d,D) decreases monotonically as d increases (Figure 4.6). In order to interpret this more explicitly for the saturation magnetization, $M_s(d)$, consider the high-field limit of 2 μH/kT >>1. Here,

$$M_s(d) \sim 2\mu \tanh(2\ \mu H/kT)\ [1-\{\ \exp(2U(d,D)\ \mu^2)/\ \cosh(2\ \mu H/kT)\}].$$

Accordingly, $M_s(d)$ increases with increasing spacing d (i.e., with decreasing U(d,D)). This is in qualitative agreement with the observed variation of saturation magnetization with d in Figure 4.5 (a).

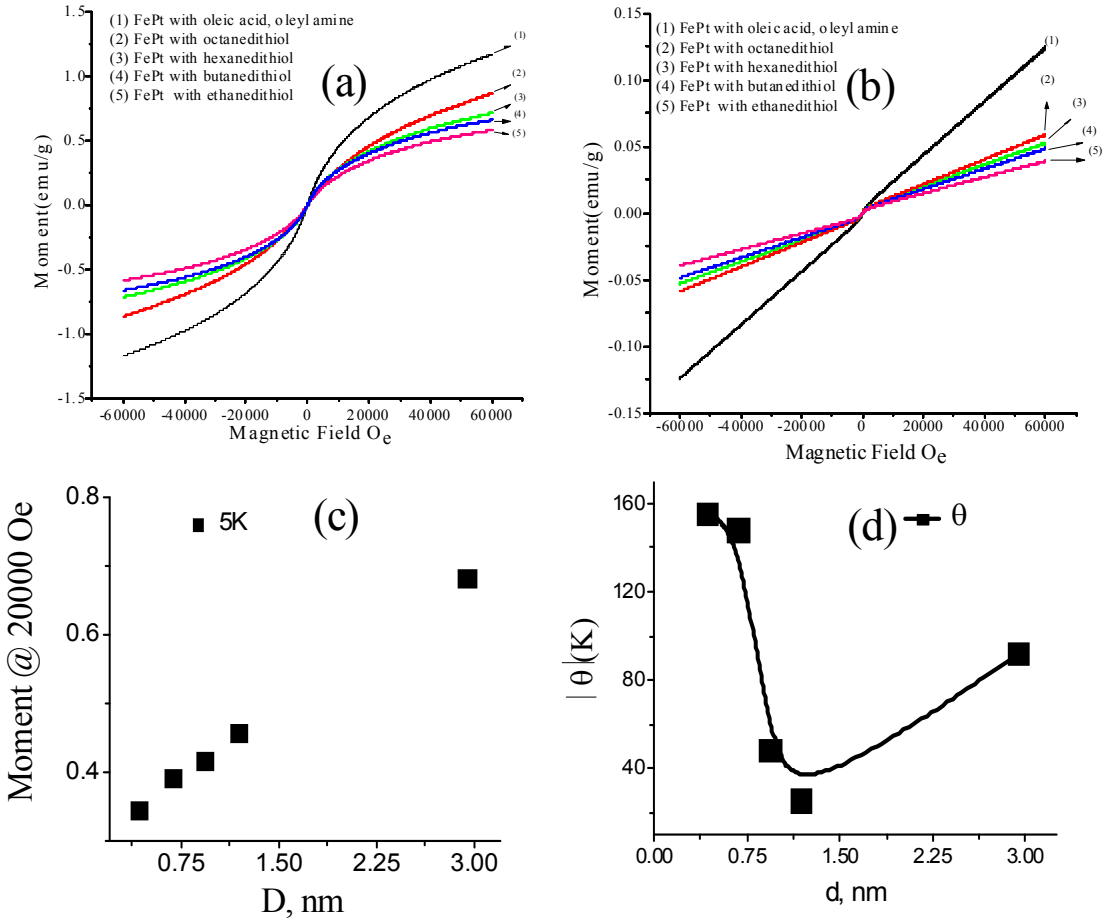

Figure 4.7: Magnetic hysteresis exhibited by 1.5 nm FePt nanoparticles at (a) 5 K and (b) 300 K with different interparticle separations. Variation of (c) magnetization (20000 Oe) at 5 K and (d) θ with the interparticle separation, d.

Encouraged by the results on 5 nm FePt nanoparticles with different alkanedithiols (where d<<D in all cases), we have studied magnetic properties of 1.5 nm FePt nanoparticles. In one case, the distance between the FePt nanoparticles is longer than the diameter 1.5 of FePT nanoparticles. The 1.5 nm FePt nanoparticles exhibits superparamagnetic behavior at 300 K and 5 K as can be seen from Figure 4.7 (a) & (b) . Figure 4.7 (c) shows the variation in the magnetization at 20000 Oe with the spacer length, d. Magnetization increases linearly with increase in the space length similar to the 5 nm FePt nanoparticles. In Figure 4.7 (d) we show the variation of the Curie – Weiss temperature, θ, with the spacer length, d for 1.5 nm FePt nanoparticles. The θ values were obtained from the high-temperature inverse susceptibility data. The θ value increases with increases in the interparticle separation until 1.5 nm. Interestingly above spacer length 1.5 nm, we observe decrease in the θ value with increase in d. It clearly shows multipolar behavior dominates when d<D where as dipolar behavior will dominate in case of d>D.

4.4.2 Effect of electronic coupling between CdSe nanocrystals on the photoluminescence spectra

Red-emitting CdSe nanocrystals (4 nm) were prepared by the solvothermal method starting with cadmium stearate, selenium, trioctylphoshine oxide (TOPO) and tetralin in toluene solution following the procedure reported earlier (*43*). We have characterized the CdSe nanoparticles by optical absorption and photoluminescence spectroscopy and TEM (Figure 4.8). In Figure 4.9 we show TEM images of various types of aggregates. Using mercaptopropionic acid, we obtain dimers and trimers as shown in the image in Figure 4.9 (a). The same type of image was formed when high concentrations of alkanedithiols were used as can be seen from the image in Figure 4.9 (b). Low concentrations of dithiols and click reaction give rise to larger aggregates as shown in Figures 4.9 (c) and (d) respectively. In Figure 4.10, we show the PL spectra of CdSe

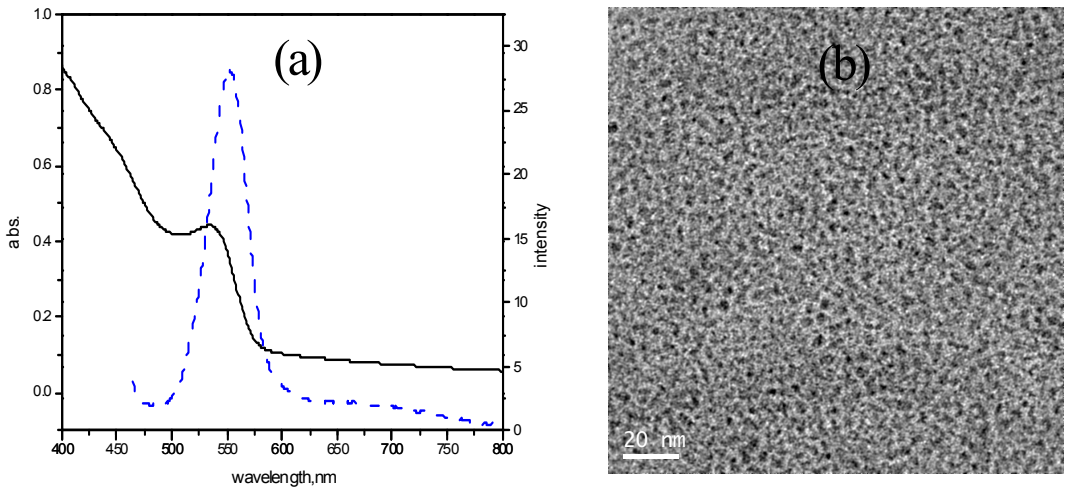

Figure 4.8: Optical absorption and photoluminescence spectra and (b) TEM image of CdSe nanoparticles

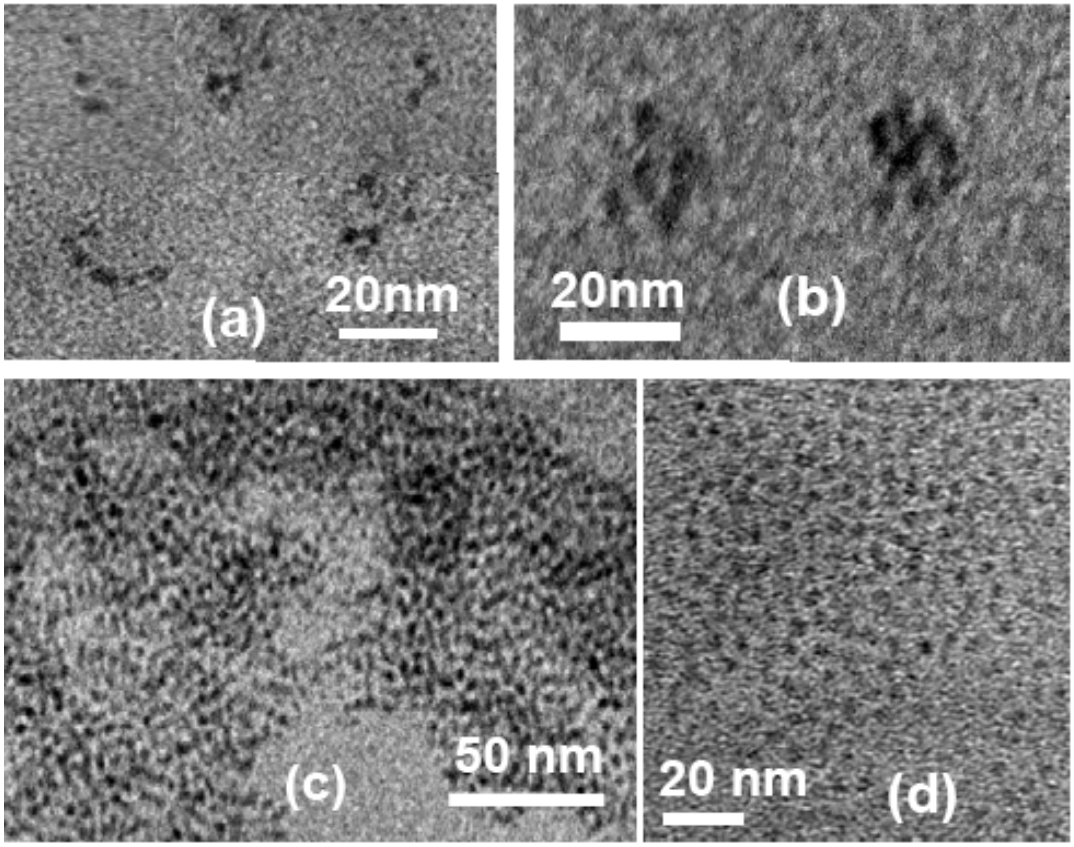

Figure 4.9: TEM images of CdSe aggregates formed by (a) mercaptopropionic acid, (b) by high concentrations of ethanedithiol, (c) low concentrations of alkane dithiols and (d) by Click reaction

nanocrystals with different concentrations of mercaptopropionic acid. The as prepared (pristine) CdSe nanoparticles show a broad band centered around 564 nm with

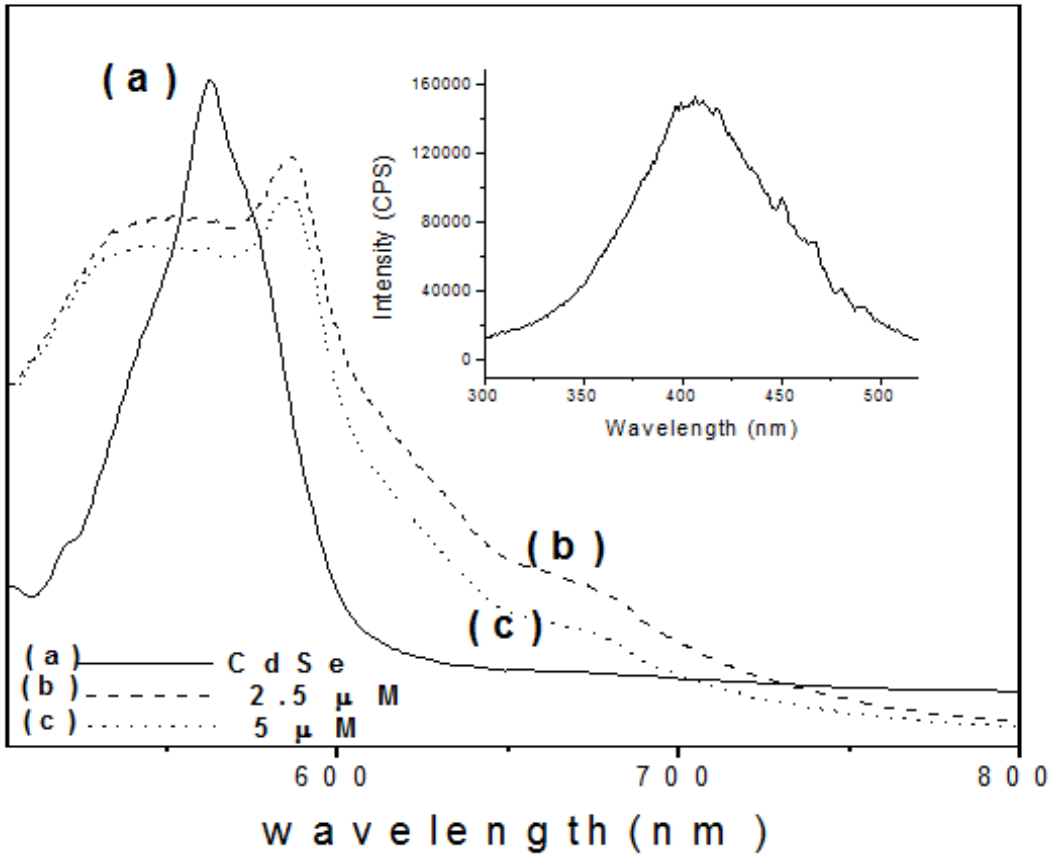

Figure 4.10: PL spectra of (a) the as-prepared (pristine) CdSe nanoparticles and (b) and (c) those linked by using different concentrations of mercaptopropionic acid (excitation wavelength 470 nm).There was negligible difference by varying the excitation wavelength in the 460–490 nm range. Inset gives the excitation spectrum corresponding to (b).

shoulders on either side in toluene solution. The shoulders arise from species of slightly smaller and larger particles and are eliminated in fully monodisperse preparations. The CdSe nanocrystals linked by mercaptopropionic acid show two distinct bands, one broad band at 536 nm, a sharper band of 586 nm and a prominent shoulder at 675 nm. In Figure 4.11, we show the PL spectra of CdSe nanocrystals obtained with high and low concentrations of ethanedithiol. At high concentration of ethanedithiol (Figure 4.11(b)), we find two distinct bands at 532 nm and 573 nm and a weak shoulder at 628 nm, as in the case of mercaptopropionic acid in Figure 4.10. At low concentrations of ethanedithiol, we find three bands for the nanocrystal aggregates at 515 nm, 530 nm and

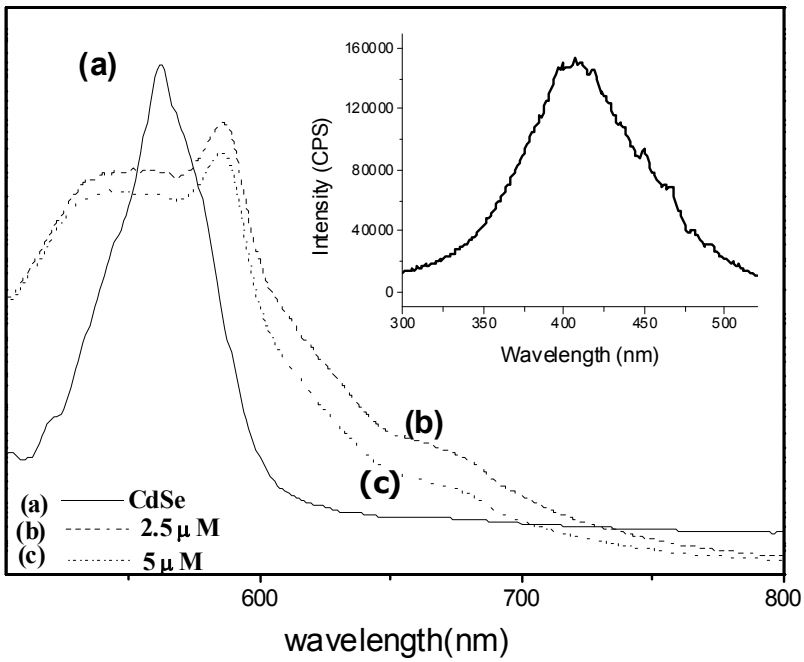

Figure 4.11: PL spectra of (a) the as-prepared CdSe nanoparticles and those of assembled particles by using (b) a high concentration (300 nM) of 1,2-ethanedithiol and (c) a low concentration (75 nM) of the dithiol. The spectra with other alkanedithiols were similar (excitation wavelength 470 nm). Inset gives the excitation spectrum corresponding to (b).

574 nm. The weak shoulder at 628 nm seems to persist here as well. With the other alkanedithiols, we obtained PL bands similar to those found with ethanedithiol at lower concentrations. Figure 4.12 shows the PL spectra of CdSe nanocrystal aggregates obtained by the click reaction. We obtain four bands, two at lower wavelength and two at higher wavelengths than the isolated CdSe nanocrystals. In Figure 4.13, we present a summary of the different types of PL spectra of the CdSe aggregates that we have obtained. These features were reproducible with independent preparations of the aggregates.

Since the CdSe Nanocrystals are known to show a sharp exciton band (*49*), it is appropriate to describe the interaction between bridge-connected nanocrystallites by the dipole-dipole interaction model. In this picture, the excitons are assumed to be located in each nanocrystal and are stable at room temperature (*50, 51*). The distance between

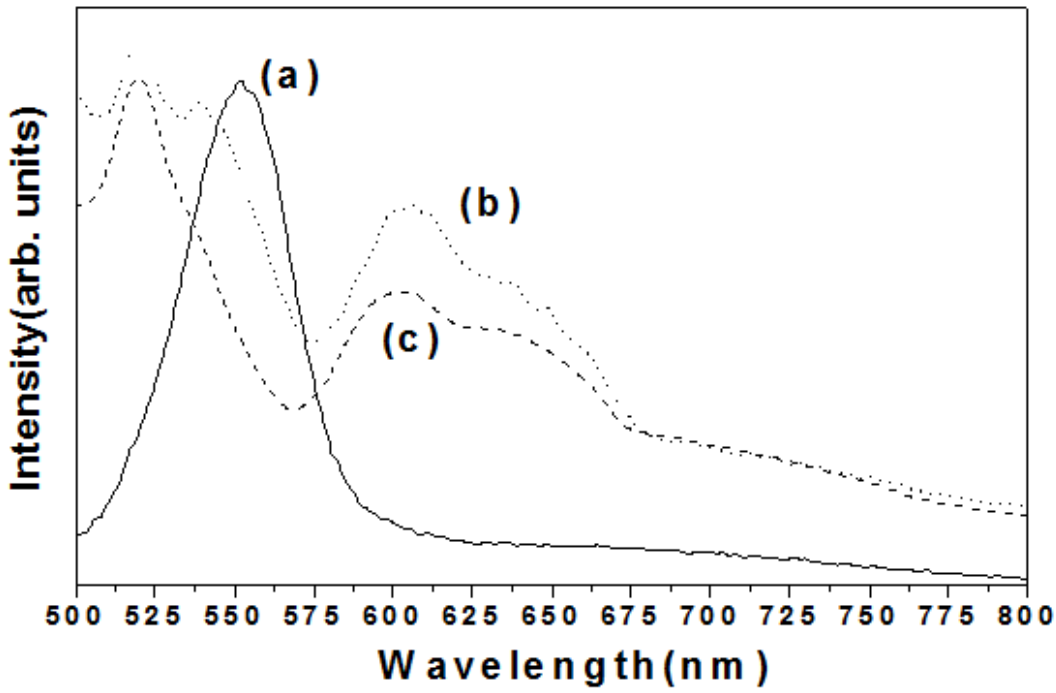

Figure 4.12: PL spectra of (a) the as-prepared CdSe nanocrystals, and (b), (c) those linked by click reaction at different relative concentrations of the azido and alkyne thiol linked particles (excitation wavelength 450 nm).

nearest neighbors is assumed to be such that there is no charge transfer and thereby no mixing of their orbitals. The exciton coupling can then be approximated by dipole-dipole interaction of the form $\mu_{ge}^{i}.\ \mu_{ge}^{j}/r^3-(\mu_{ge}^{i}.r)(\mu_{ge}^{j}.r)/r^5$, where μ_{ge}^{i} is the transition dipole moment between the ground state and the dipole allowed excited state for the i^{th} nanocrystal and the r is the distance between the i^{th} and j^{th} nanocrystals. Both the transition dipole and the dipolar axis (r in the numerator) are vectorial quantities. The magnitude of the interaction term will therefore, depend crucially on the relative orientations of the semiconductor dipoles as well as on the axis joining their centers of mass. This is, however, a purely quasi classical vector treatment and only electrostatic interactions are considered between the transition moments (*52, 53*).

Let us consider that the dipolar axis of a CdSe nanocrystal makes an angle Φ with the nanocrystal axis, and the dipolar axes make an angle θ with each other in a dimer configuration with two CdSe nanocrystals. The exciton splitting from dipole-dipole

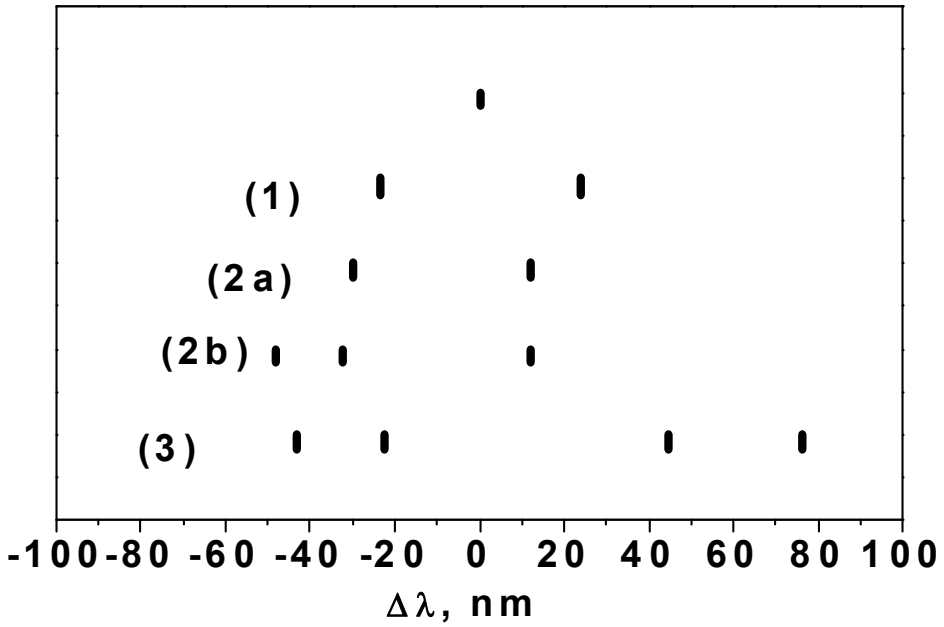

Figure 4.13: Summary of the PL spectral characteristics of the as prepared of CdSe nanocrystals and those of the aggregates obtained by using, (1) the mercaptopropionic acid (having dimers, trimers), (2a) high alkanedithiol concentration (with dimers and trimers), (2b) low dithiol concentration (with larger aggregates) and (3) the click reaction (with larger aggregates). The features shown here were found with repeated measurements on independent preparations, with different excitation wavelengths. (In 1, (2a) and (2b) the band red-shifted to the longest wavelength appears as weak shoulder.

interaction potential can then be written as $\Delta E = \mu^2/r^3 (\cos(\theta)-3\cos^2(\Phi))$ (*52, 53*). If the two nanocrystal sizes are different, μ^2 should be replaced by $\mu_1\mu_2$ and the $\cos^2(\Phi)$ by $\cos(\Phi_1)\cos(\Phi_2)$, corresponding to two (labeled 1 and 2) nanocrystals. In such a situation, the level splitting would give rise to excitations with two possible luminescence peaks. For an ideal situation, where the dipole vectors of the nanocrystallites form head-to-tail arrangements ($\Phi=0^o$), the ground state is stabilized due to favorable dipole-dipole attraction, while the excited states split into two states. Since the interaction is attractive for this case, light emission would occur only from the

lowest excited state. Clearly the emission energy is lower than that of the isolated crystals and this mode of aggregation therefore leads to a red shift in the luminescence spectra. In the case of repulsion ($\Phi=180^{o}$), the picture would be exactly opposite. For intermediate angular orientations of the dipoles, both the excited states may emit light, with varying oscillator strengths, depending on the extent of transition dipole combinations. For a trimer, similarly there will be three excited states which would split according to the dipolar arrangement and the extent of dipolar phase combinations. For a tetrameric structure, the four excitations can distinctly be different and luminescence may vary from each of the excitonic states depending on the dipolar combinations. The luminescence frequency and intensity will strongly depend on the size and shape of the nanoparticles and their dipolar alignments which in turn depend on the distance and the monomer dipole vector.

The band splitting observed in the experimental spectra (Figure 4.13) can be understood as follows. The luminescence intensity of the isolated CdSe nanocrystals is high, suggesting large oscillator strength due to a well-defined excitonic state with a large transition dipole moment. The numerator in the expression for ΔE plays the dominant role in the luminescence spectra. There are reports of large ground state dipole moments of CdSe nanocrystals due to high charging energy (*54*). Using quantum chemical calculations with the Gaussian codes at the 6-31g (d, p) level with B3LYP functional, Pati et al. optimized the ground state structure of a number of CdSe clusters with varying Cd and Se atoms. The dipole moment and the transition dipoles are found to vary with the number of Cd and Se atoms. For systems with an optical gap of the order of 530 nm, the ground state and the transition state dipole moments are found to be 8 Debye and 2.3 Debye respectively. Interestingly, we find that the dipole vectors lie along the perpendicular direction to the CdSe nanocrystals ($\theta=90^{o}$).

As found experimentally with almost all the bridging molecules that we have employed, the red-shifted bands show high intensities, suggesting a strong in-phase dipolar combination in the CdSe nanocrystallite aggregates. Since the level splitting is proportional to the inverse cube of the center of mass distance between the nanocrystallites, the frequency splitting of the band is small.

In case 1 of Figure 4.13, the red and blue shifts from the band due to the pristine CdSe nanocrystals are 22nm and 28nm respectively. The shifts are similar in case 2a as well (Figure 4.13), with one blue-shifted and one red-shifted bands. Assuming a linear structure, the distance for such splitting can be estimated from the dimer model to be of the order of 6-10 Å. In 2b of Figure 4.13, the monomer band splits into three peaks, one red-shifted by 11 nm and two blue-shifted, by 32 nm and 50 nm respectively. Finally, in 3 of Figure 4.13, the CdSe nanocrystals seem to form a network gives four bands, two red-shifted and two blue-shifted, from the band due to the pristine crystals. From our trimer and tetramer model analysis, we find that while the network in 3 of Figure 4.13 would consist of CdSe tetramers with almost a square geometry, the structure of 2b may have a triangular shape with all the sides being different. This can be seen in the symmetry of the red-shifted and blue-shifted peaks. In 3 of Figure 4.13, there is symmetry between the lower energy and higher energy red-shifted peaks with the corresponding blue-shifted peaks. Since such dipolar interaction can occur through space, the higher energy blue-shifted peaks and the asymmetry in splitting energies may arise from the closely spaced dimer, trimer and other higher order structures. It appears that, while the hydrogen bonded bridge in 1 and the dithiol bridge in 2a (Figure 4.13) produce structures closer to dimers, low concentrations of dithiols in 2b and the click reaction (see 2b and 3 representative of Figure 4.13), on the other hand, produce larger lattices with square units of CdSe nanocrystals. Note that the intensity variation is solely due to different phase combinations of the individual CdSe nanocrystalline transition

dipole moments, and that the large distance (>10 Å) lattice ordering has little or no effect on the splitting of the peaks. Thus, the luminescence bands provide an idea of the nanocrystalline lattice structure within the framework of dipolar coupling, although the real lattice structure may have larger dimensions. That such a variation

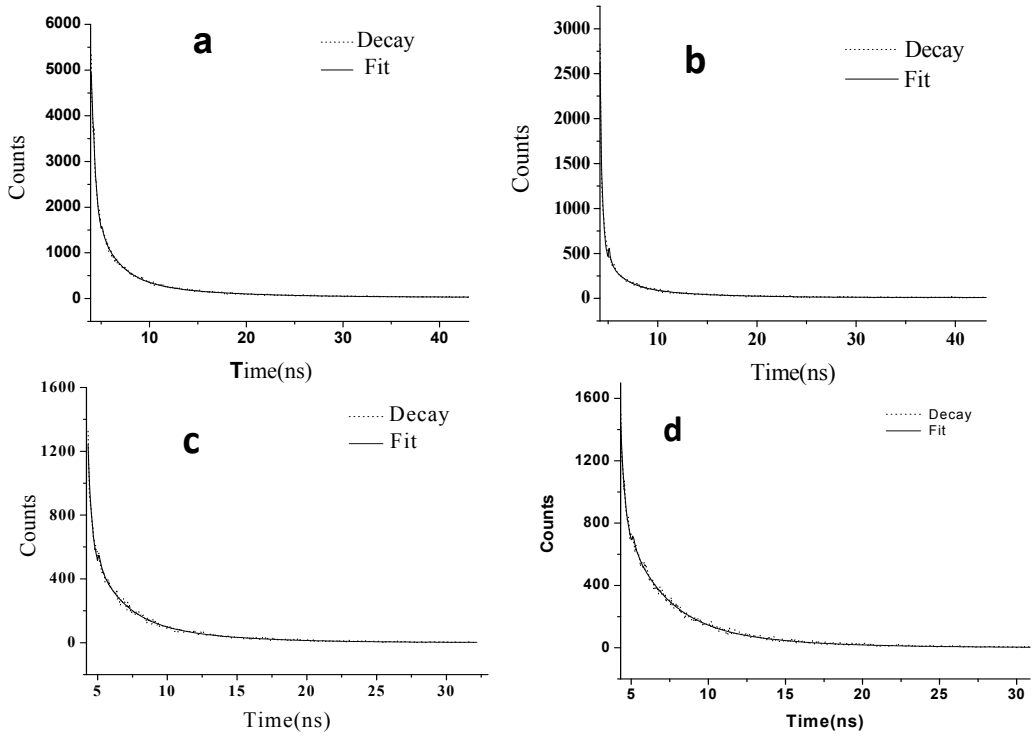

Figure 4.12: Fluorescence decay curves of (a) the as-prepared CdSe nanoparticles, (b) of mercaptopropionic acid linked CdSe nanoparticles (c) of CdSe nanoparticles linked by using a high concentration of ethanedithiol and (d) low concentration of ethane dithiol.(c) and (d) correspond to the PL spectra (b) and (c) in Figure 4.13.

exits for the different bridging structures, suggests that the luminescence spectra can be used to monitor ordering of nanocrystallites.

In order to understand the lifetimes and thereby the stability corresponding to each of the luminescence bands, we have performed time-resolved fluorescence experiments on the CdSe nanocrystalline aggregates with various linker groups in comparison with the pristine CdSe nanocrystals. The decay curves were measured at an emission wavelength of 564 nm for CdSe nanocrystals and at both 564 and 574 nm for the CdSe nanocrystalline aggregates formed with various linker molecules. Earlier reports suggest

that the fast initial decay is due to exciton energy transfer (<~2 nm) (*41, 42*). In Figure 4.14, we show typical decay curves. All the decay curves could be best fitted with three-exponential decay time components (Table 4.1). The significant changes that we find in the decay times of the small dimer type clusters and large aggregates are as

Table 4.1: Life time data (in nsec) for CdSe nanoparticles aggregates obtained by using various linker molecules.(1)–(3) correspond to the spectral characteristics shown in Figure 5.

	CdSe @ 564nm	(1) Mercapto propionic acid @ 584(532) nm	Ethanedithiol		(3) Click reaction @ 574(532) nm
			(2a) High conc. @ 574(532) nm	(2b) Low conc. @ 574 (532) nm	
τ_1	0.098	0.25(0.25)	0.2(0.29)	0.25(0.24)	0.25(0.25)
τ_2	3.14	1.96 (1.72)	1.81(2.11)	2.45(2.25)	2.21(1.96)
τ_3	6.81	6.37(6.37)	5.3(6.17)	6.37(6.56)	6.37(5.88)

follows. The τ_1 value increases markedly in the case of the small dimer type clusters. We also find a fairly substantial increase in τ_1 in the larger aggregates. The τ_2 values decrease significantly when the aggregates are small and there is a much less decrease in the larger aggregates. The τ_3 value does not appear to be sensitive to the size of the aggregates, and there is a general decrease of τ_3 in the aggregates. Due to the large distance between the nanocrystals, the exciton energy transfer gives the small initial decay parameter, which for the monomer case is of the order of 0.1 ns, while for the aggregate structures, it varies between 0.1 and 0.3 ns. Given that the excited state

lifetime may change during the measurement process even for an isolated nanocrystal, the aggregate structure would be expected to show many fluctuating dynamic quenching processes through both nonradiative and radiative channels. However, it remains true that larger the luminescence intensity, the longer would be the lifetime. The lifetime variation can therefore, be qualitatively understood, since the luminescence intensity corresponding to blue and red shifted bands of the aggregates are smaller compared to that of the luminescence bands of the pristine CdSe nanocrystals. Whether quenching processes and rates can be resolved from time-resolved fluorescence spectra requires further study.

4.5 Conclusions

The dependence of the magnetic properties of FePt nanoparticles on the interparticle separation has been studied by using of non-magnetic spacers of d<<D, the diameter of the nanoparticles. The observed variations of the blocking temperature and the Curie-Weiss temperature and also of the saturation magnetization with d, are found to be qualitatively consistent with a simple model of the nanomagnetic particles as finite dipoles coupled through anisotropic multipolar interactions. Basically, the magnetostatic interaction is the only relevant energy scale in the problem. Based on the present study, we are able to explain the results reported by other workers (*17, 20, 31, 32*). Almost all the data reported in the literature are for d << D. It is, therefore, understandable that they not only report a decrease in T_B with increase in interparticle separation, but also a variation similar to that in Figure 4.4 (b).

We have demonstrated that the optical luminescence spectra of CdSe nanocrystals can be modulated by means of coupling through bridging molecular units. When the thiolcarboxylic acid is used as the linker molecule, we obtain mainly dimers and trimers. The same is true when high concentrations of alknaedithiols are used. In both

these cases, the CdSe luminescence band splits into two bands, one red-shifted and another blue-shifted (3 and 2a in Figure 4.13). When a low concentration of an alkanedithiols or the click reaction is employed to link the CdSe nanocrystals to form higher order aggregates, one observes two (or one) red-shifted and two blue-shifted bands with a certain degree of symmetry with respect to the band of the as prepared (pristine) nanocrystals (see 2b and 3 in Figure 4.13). While the aggregate structure can be of higher order as the TEM images show, the luminescence spectra only capture the structures relevant within the dipolar coupling energy scale. The decay times also show significant changes in small and larger clusters compared to the pristine isolated nanocrystals.

REFERENCES

1. S. A. Empedocles, R. Neuhauser, K. Shimizu, M. G. Bawendi, *Adv. Mater.* **11**, 1243 (1999).
2. A. P. Alivisatos, *Science* **271**, 933 (1996).
3. Y. Yin *et al.*, *Science* **304**, 711 (2004).
4. R. Shenhar, T. B. Norsten, V. M. Rotello, *Adv. Mater.* **17**, 657 (2005).
5. C. B. Murray, C. R. Kagan, M. G. Bawendi, *Annu. Rev. Mater. Sci.* **30**, 545 (2000).
6. L. N. Lewis, *Chem. Rev.* **93**, 2693 (1993).
7. J. Kong, A. M. Cassell, H. Dai, *Chem. Phys. Lett.* **292**, 567 (1998).
8. T. Trindade, P. O'Brien, N. L. Pickett, *Chem. Mater.* **13**, 3843 (2001).
9. A. N. Shipway, E. Katz, I. Willner, *ChemPhysChem* **1**, 18 (2000).
10. K. S. Wilson, J. D. Goff, J. S. Riffle, L. A. Harris, T. G. St Pierre, *Polym. Adv. Technol.* **16**, 200 (2005).
11. J. P. Dailey, J. P. Phillips, C. Li, J. S. Riffle, *J. Magn. Magn. Mater.* **194**, 140 (1999).
12. H. L. N. Yockell-Leliavre, J. Desbiens, A. M. Ritcey, *Langmuir* **23**, 2843 (2007).
13. R. Matsuno, H. Otsuka, A. Takahara, *Soft Matt.* **2**, 415 (2006).
14. L. Motte, M. P. Pileni, *J. Phys. Chem. B* **102**, 4104 (1998).
15. B. L. Frankamp, A. K. Boal, V. M. Rotello, *J. Am. Chem. Soc.* **124**, 15146 (2002).
16. A. Verma, S. Srivastava, V. M. Rotello, *Chem. Mater.* **17**, 6317 (2005).
17. S. Srivastava, B. Samanta, P. Arumugam, G. Han, V. M. Rotello, *J. Mat. Chem.* **17**, 52 (2007).
18. S. Chen, *Langmuir* **17**, 2878 (2001).
19. D. S. Sidhaye, S. Kashyap, M. Sastry, S. Hotha, B. L. V. Prasad, *Langmuir* **21**, 7979 (2005).
20. B. L. Frankamp, A. K. Boal, M. T. Tuominen, V. M. Rotello, *J. Am. Chem. Soc.* **127**, 9731 (2005).
21. M. Li, H. Schnablegger, S. Mann, *Nature* **402**, 393 (1999).
22. Z. Nie, A. Petukhova, E. Kumacheva, *Nat. Nanotechnol.* **5**, 15 (2010).
23. E. V. Shevchenko, D. V. Talapin, N. A. Kotov, S. O'Brien, C. B. Murray, *Nature* **439**, 55 (2006).

24. S. A. Maier *et al.*, *Nat. Mater.* **2**, 229 (2003).
25. A. Imre *et al.*, *Science* **311**, 205 (2006).
26. R. P. Cowburn, M. E. Welland, *Science* **287**, 1466 (2000).
27. C. N. R. Rao, G. U. Kulkarni, P. J. Thomas, *Nanocrystals: Synthesis, Properties and Applications*. (Springer, Berlin, 2007).
28. L. Neel, Ed., *Low-Temperature Physics*, (Gordon and Breach, New York, 1962).
29. M. Ghosh, E. V. Sampathkumaran, C. N. R. Rao, *Chem. Mater.* **17**, 2348 (2005).
30. M. Ghosh, K. Biswas, A. Sundaresan, C. N. R. Rao, *J. Mater. Chem.* **16**, 106 (2006).
31. C. R. Vestal, Q. Song, Z. J. Zhang, *J. Phys. Chem. B* **108**, 18222 (2004).
32. K. Nakata, Y. Hu, O. Uzun, O. Bakr, F. Stellacci, *Adv. Mater.* **20**, 4294 (2008).
33. S. Sun, *Adv. Mater.* **18**, 393 (2006).
34. V. Nandwana *et al.*, *J. Phys. Chem. C* **111**, 4185 (2007).
35. L. V. Butov, C. W. Lai, A. L. Ivanov, A. C. Gossard, D. S. Chemla, *Nature* **417**, 47 (2002).
36. P. A. M. B. Erik, W. M. Albert, W. J. Leonardus, V. Daniël, *Angew. Chem. Int. Ed.* **39**, 2297 (2000).
37. V. Chernyak, T. Meier, E. Tsiper, S. Mukamel, *J. Phys. Chem. A* **103**, 10294 (1999).
38. V. A. Malyshev, H. Glaeske, K. H. Feller, *J. Chem. Phys.* **113**, 1170 (2000).
39. L. Cao *et al.*, *J. Chem. Phys.* **123**, 024702 (2005).
40. A. S. Davydov, *Theory of Molecular Excitons*. (Plenum, New York, 1971).
41. R. Koole, P. Liljeroth, D. Vanmaekelbergh, A. Meijerink, *J. Am. Chem. Soc.* **128**, 10436 (2006).
42. R. Koole *et al.*, *J. Phys. Chem. C* **111**, 11208 (2007).
43. U. K. Gautam, M. Rajamathi, F. Meldrum, P. Morgand, R. Seshadria, *Chem. Commun.*, 629 (2001).
44. J. L. Dormann, D. Fiorani, E. Tronc, in *Advances in Chemical Physics,* S. A. R. I. Prigogine, Ed. (2007), pp. 283-494.
45. J. L. Dormann, L. Bessais, D. Fiorani, *J. Phys. C: Solid State Phys.* **21**, 2015 (1988).
46. R. H. Kodama, *J. Magn. Magn. Mater.* **200**, 359 (1999).
47. D. Kechrakos, K. N. Trohidou, *App. Phys. Lett.* **81**, 4574 (2002).

48. J. D. Jackson, *Classical Electrodynamics*. (Wiley Eastern Ltd., New Delhi, 1978).
49. C. R. Kagan, C. B. Murray, M. G. Bawendi, *Phys. Rev. B* **54**, 8633 (1996).
50. L. E. Brus, *J. Chem. Phys.* **80**, 4403 (1984).
51. U. Banin *et al.*, *Phys. Rev. B* **55**, 7059 (1997).
52. A. Datta, S. K. Pati, *J. Chem. Phys.* **118**, 8420 (2003).
53. A. Datta, S. K. Pati, *Chem. Soc. Rev.* **35**, 1305 (2006).
54. M. Shim, P. Guyot-Sionnest, *J. Chem. Phys.* **111**, 6955 (1999).

CHAPTER 5

Extraordinary Sensitivity of the Electronic Structure and Properties of Carbon Nanotubes to Charge-Transfer Induced by Molecules and Metal Nanoparticles

Summary*

Single-walled carbon nanotubes (SWNTs) exhibit novel electronic structure and properties arising from the quantization of electron wave vector of the 1D system. Electron or hole doping influences the electronic structure of SWNTs and thereby their Raman spectra. We have studied the interaction SWNTs with electron-donor molecules such as anisole, aniline and tetrathiafulvalene (TTF) as well as –acceptor molecules such as chlorobenzene, nitrobenzene tetracyanoquinidomethane (TCNQ), tetracyanoethylene (TCNE) and observed significant changes in the electronic absorption and Raman spectra of the nanotubes. Electron-donating molecules (TTF and aniline) cause changes opposite to those caused by electron-withdrawing molecules (nitrobenzene and TCNE). Thus, a proportion of the semiconducting SWNTs become metallic on electron donation through molecular charge transfer. Electrical resistivity measurements reveal a systematic variation with electron-donating or –withdrawing power of the interacting molecules. This feature of SWNTs may be useful in many of the applications such as sensors and nanoelectronics.

SWNTs have been coated with gold and platinum nanoparticles either by microwave treatment or by the click reaction and the Raman spectra of these SWNT-metal

**** Papers based on these studies have appeared in Journal of Physical Chemistry C (Letter) (2008) and Journal of Physics: Condensed Matter (2008)***

nanoparticle composites have been investigated. Analysis of the G bands in the Raman spectra shows an increase in the proportion of metallic SWNTs on attachment with metal nanoparticles. This conclusion is also supported by the changes observed in the RBM bands. a*b-initio* calculations reveal that semiconductor-metal transition occurs in SWNTs due to Columbic charge transfer between the metal nanoparticles and the semiconducting SWNTs.

5.1 Introduction

Carbon nanotubes are one-dimensional (1D) materials with different chiralities and diameters (*1-3*). Single-walled carbon nanotubes (SWNTs) exhibit diverse electronic structure and properties arising from the quantization of electron wave vector of the 1D system. SWNTs exhibit significant changes in the electronic structure and chemical reactivity depending on the geometry, doping, chemical environment and solvent. SWNTs are formed by rolling two-dimensional graphene sheets into cylinders along a (n, m) lattice vector (C_h) in the graphene plane, where n and m are integers. We can obtain the diameter and chiral angle from the (n, m) values. Nanotubes with chiral numbers n=m are metallic, and quasi metallic if n-m is divisible by 3. The other nanotubes are semiconducting. As-prepared SWNTs generally contain a mixture of metallic and semiconducting species. In conventional synthetic processes employed for SWNTs, metallic nanotubes constitute 33 %, the remaining being semiconducting nanotubes. Metallic and semiconducting SWNTs are readily characterized by Raman and electronic spectra (*1-5*). The radial breathing mode (RBM) in the Raman spectrum of SWNTs is useful for determining the diameter and the (n, m) values of the nanotubes. Electronic properties of the nanotubes can be predicted by using the Kataura plots based on the RBM bands. The Raman band of SWNTs centered around 1580 cm^{-1} (G-band)

exhibits a feature around ~1540 cm^{-1} which is characteristic of metallic SWNTs (*4*). The G-band can be deconvoluted to get the relative proportions of metallic and semiconducting species. Absorption spectra of SWNTs in the visible and near IR regions contain characteristic bands due to the metallic and semiconducting species.

Ability to tune the electronic properties of SWNTs is important for many applications. A control of the carrier type and concentration has been achieved by electrochemical doping or chemical doping. Through electrochemical top-gating, it is possible to achieve a high level of doping (*6*). The electronic structure and phonon frequencies of SWNTs are affected on doping with electrons or holes. Changing the electronic properties of SWNTs by chemical means has attracted considerable attention. Chemical approaches employ covalent or noncovalent functionalization. Covalent functionalization methods include direct addition of fluorine atoms, cycloaddition reactions, radical and nucleophilic additions to side walls of nanotubes (*2, 7*). Another method is to introduce carboxylic groups on the side walls of SWNTs by oxidation. The carboxylic acid groups can be further transformed to amide or ester linkages. Attachment of various molecules also enables modification of the electronic structure of SWNTs (*2, 7*). The main problem with covalent functionalization is that it causes a change in hybridization of carbon from sp^2 to sp^3, and hence in the electronic structure. Excessive covalent functionalization completely destroys the electronic structure of SWNTs.

Noncovalent functionalization offers non-invasive approaches to modify SWNTs properties. Noncovalent modification can be brought by adsorption of aromatic compounds, surfactants or polymers and also through π-π stacking and hydrophobic interaction. Earlier studies of noncovalent modification focused on the solubilization and exfoliation of SWNT bundles. Another aspect which has come into light in recent years is to modify the electronic structure of SWNTs by interaction with electron-donor

and -acceptor molecules. This involves the adsorption of the electron-donor or -acceptor molecules on the surface of SWNTs. The advantage of molecular doping over other means is that one has an electronic system with less charged impurities. Furthermore, this effect of doping is reversible.

Metal to semiconductor transition in SWNTs has been induced by helical wrapping of DNA (*8*). Water appears to be critical to this reversible transition which accompanied by hybrid formation with DNA. It is predicted that a band gap can open up in metallic SWNTs wrapped with ssDNA in the presence of water molecules, due to charge-transfer. Kim *et al.* (*9*) have shown that adsorption of $AuCl_3$ to SWNTs results in high level of p-doping due to strong charge-transfer from the SWNTs to $AuCl_3$ and they have shown that sheet resistance was systematically reduced with the increasing doping concentration. Ehli *et al*. (*10*) have shown that charge-transfer between SWNTs and perylene dyes leads to individualized nanotubes and they have observed radical ion-pair state is formed in the excited state. There are reports of charge-transfer interaction of SWNTs with I_2 and Br_2 (*11, 12*). Doping of double-walled carbon nanotubes with bromine and iodine has been investigated (*13, 14*). Charge-transfer doping of DWNTs has been used to distinguish between the behavior of the S/M and M/S outer/inner semiconducting (S) and metallic (M) tube configurations. The binding of electron-accepting molecules (F_4TCNQ and NO_2) to SWNTs leads to a threshold voltage shift toward positive gate voltages, while the binding of electron donating molecules (NH_3 and polyethylenimine) leads to a shift toward negative gate voltages (*15-17*). Field-effect transistor devices made of semiconducting SWNTs have been used to obtain quantitative information on charge-transfer with aromatic compounds (*18*). Stoddart *et al.* (*19*) have fabricated SWNT/ FET devices to investigate the electron/charge-transfer with the donor-acceptor SWNT hybrids. A SWNT/FET device, functionalized

noncovaletly with a zinc porphyrin derivative shows that SWNTs act as electron donors and that the porphyrin molecules act as the electron acceptors.

There are various efforts in the literature to tune the electronic properties of SWNTs. We report the scope of the present investigation in the next section.

5.2 Scope of the present investigations

Controlling and/or tuning of the electronic properties of SWNTs, has numerous applications in designing of advanced electronic devices. However, the precise control of the carrier type and concentration has been achieved only recently, by electro-chemical doping. It has been reported that through electrochemical top-gating, it is possible to achieve a high level of doping (*6*). On the other hand, charge transfer is well known in molecular systems. This can be achieved either by intramolecular or by intermolecular charge-transfer pathway. For the intramolecular case, the donor and/or acceptor molecule has to form a new chemical bond with the nanotubes. Obviously, the formation of new covalent bonds through functionalizations of nanotubes may significantly modify the structure as well as its electronic properties. On contrary to that, one can self assemble some selective donor or acceptor molecules on the surface of SWNTs developing a possibility of through charge-transfer.

Various dispersants and solvents have been used to disperse carbon nanotubes. However, this often involves serious modification of their electronic structures (*7, 20*). For example, sodium dodecyl sulfate (SDS) and polythiophene are good dispersants, but they also modify the electronic structures (*21, 22*). Despite this, there have been few studies on the effect of the solvent on the electronic structures of carbon nanotubes. In general, donating and withdrawing groups in a π-system of the solvent are well known (*23*). The presence of functional groups might induce a permanent or induced dipole moment in a molecular solvent. This apparently involves charge transfer between the

adsorbates and carbon nanotubes, which modifies the electronic structures of carbon nanotubes. In order to tailor the electronic structures of carbon nanotubes to a desired direction, it is necessary to determine the effect of the solvent exclusively without dispersants. We have investigated the interactions of various electron-withdrawing (chlorobenzene, nitrobenzene, tetracyanoquinodimethane (TCNQ), tetracyanoethylene (TCNE)) and electron-donating (anisole, aniline, tetrathiafulvalene (TTF)) molecules with SWNTs to determine the sensitivity of their electronic structure and properties to molecular charge-transfer. We have investigated the effect of these donor and acceptor molecules as measured by both electronic and Raman spectra of the SWNTs. We have also measured the effect of the electron-donor and -acceptor molecules, electrical resistivity of the SWNTs. It is found that donor and acceptor molecules induce opposite effects in the electronic and Raman spectra as well as in electrical resistivity.

We have been interested in examining how the electronic structure of SWNTs are affected by attaching metal nanoparticles to them. In order to do this, we have coated SWNTs with nanoparticles of gold and platinum by microwave treatment (*24*). We have also covalently attached gold nanoparticles to the SWNTs through the click reaction. We have studied the Raman spectra of SWNTs attached to the metal nanoparticles in comparison with the spectrum of pure SWNTs. We have made use of the G-band in the Raman spectra to obtain the relative proportions of the semiconducting and metallic species. We have also used the radial breathing mode (RBM) bands in the Raman spectra to affirm the results obtained from the analysis of G-bands.

5.3 Experimental

5.3.1 Synthesis of SWNTs:

Arc discharge SWNTs were synthesized by the method as reported by Journet *et al.(25)* using a composite rod containing Y (1 at. %) and Ni (4.2 at. %) as the anode and a graphite rod as the cathode, under a helium pressure of 660 torr with a current of 100 A and 30 V. The nanotubes were heated in air at 300 ^{o}C for 12 h and then stirred in conc. HNO_3 and H_2SO_4 mixture at 60 ^{o}C for 24 h in order to dissolve the metal nanoparticles. The product was washed with distilled water, dried, dispersed in ethanol under sonication, and filtered using Millipore (0.3 μm) filter paper. The filtered product was dried in an oven at 100 ^{o}C for 2 h. The sample was heated to 1000 ^{o}C in a furnace at a rate of 3 ^{o}C per minute, in flowing hydrogen at 100 sccm and held at that temperature for 2 h. The resulting sample was again stirred in conc. HCl at 60 ^{o}C for 3 h and finally heated in a furnace at 1100 ^{o}C for 2 h in flowing hydrogen (100 sccm). The procedure was repeated until the removal of metal impurities and amorphous carbon.

5.3.2 Interaction SWNTs with electron-donors and –acceptors

In order to study the interaction of nitrobenzene and aniline, SWNTs were soaked in the corresponding liquid placed on a glass slide for 1 hour. The solids obtained after drying were examined by electronic absorption and Raman spectroscopies. Electronic spectra were recorded with thin films of SWNTs on a quartz plate. In order to study the interaction with TCNQ, TCNE and TTF, the compounds were added to a suspension of SWNTs in toluene. The suspensions were drop-coated on glass or quartz plates and dried in vacuum. In order to compare the effects of the different donor and acceptor molecules, we employed interaction with benzene as a reference.

5.3.3 Decoration of SWNTs with gold and platinum nanoparticles

The purified SWNTs were treated with a mixture of sulphuric and nitric acids under mild conditions. To coat the SWNTs by the metal nanopraticles, 1mg of nanotubes was taken in a 5ml Teflon-lined autoclave to which 1 ml of chloroauric acid (10mM, $HAuCl_4$) or chloroplatinic acid (10mM, H_2PtCl_6) and 1 ml of ethylene glycol were added. The autoclave was placed in a microwave oven equipped with a 700 W magnetron operating at 2.45 GHz for about 30min. The products were subjected to

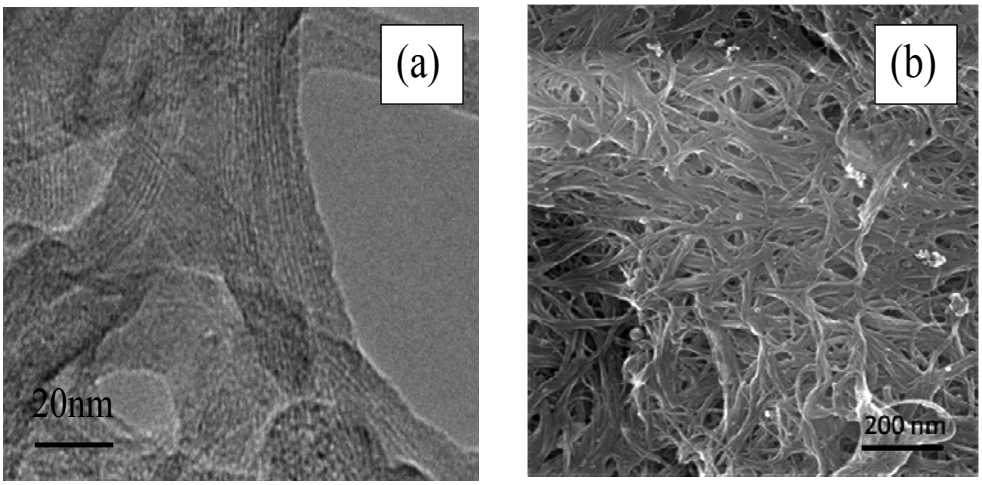

Figure 5.1: Typical (a) transmission electron microscope and (b) field emission scanning electron microscope images of SWNTs after purification.

centrifugation, filtration and thorough washing with deionized water to remove loosely bound nanoparticles and ethylene glycol. Gold nanoparticles of 3 and 12 nm prepared by literature procedures (*26, 27*) were covalently linked to SWNTs by the click reaction by the following procedure. SWNTs were first functionalized by the 4-azidobutane-1-amine by reacting acid-treated SWNTs with thionyl chloride, followed by reaction with 4-azidobutane-1-amine. These SWNTs were reacted with Au nanocrystals capped by hex-5-yne-1-thiol in the presence of $CuSO_4$ and sodium ascorbate as a catalyst. The occurrence of the click reaction was verified by infrared spectroscopy from the absence of the azide and acetylenic stretching bands.

5.3.3 Techniques used for characterization

Optical absorption spectroscopy

Optical absorption spectra were recorded using a Perkin-Elmer Lambda 900 UV/VIS/NIR spectrophotometer (200-3300 nm). Nanotube samples were deposited on quartz plate for this purpose.

Raman Spectroscopy

Raman spectra were recorded with a LabRAM HR high-resolution Raman spectrometer (Horiba-Jobin Yvon) using a He−Ne laser (λ = 632.8 nm) and Ar laser (514 nm).

Transmission electron microscopy:

For transmission electron microscopy (TEM), samples were dropped onto the holey carbon-coated Cu grids, and the grids were allowed to dry in the air. The grids were examined using a JEOL (JEM3010) microscope operating with an accelerating voltage of 300 kV.

5.4 Results and discussion

SWNTs are prepared by arc-discharge method and purified by successive acid and hydrogen treatment. The typical TEM and FESEM images of SWNTs after purification are shown in the Figure 5.1.

5.4.1 Extraordinary sensitivity of the electronic structure and properties of SWNTs to molecular charge-transfer

In order to study the interaction of various electron-donating and –withdrawing molecules with SWNTs, SWNTs were soaked in the corresponding liquid placed on a glass or quartz slide for 1 h. The solids obtained after drying were examined by electronic absorption and Raman spectroscopies.

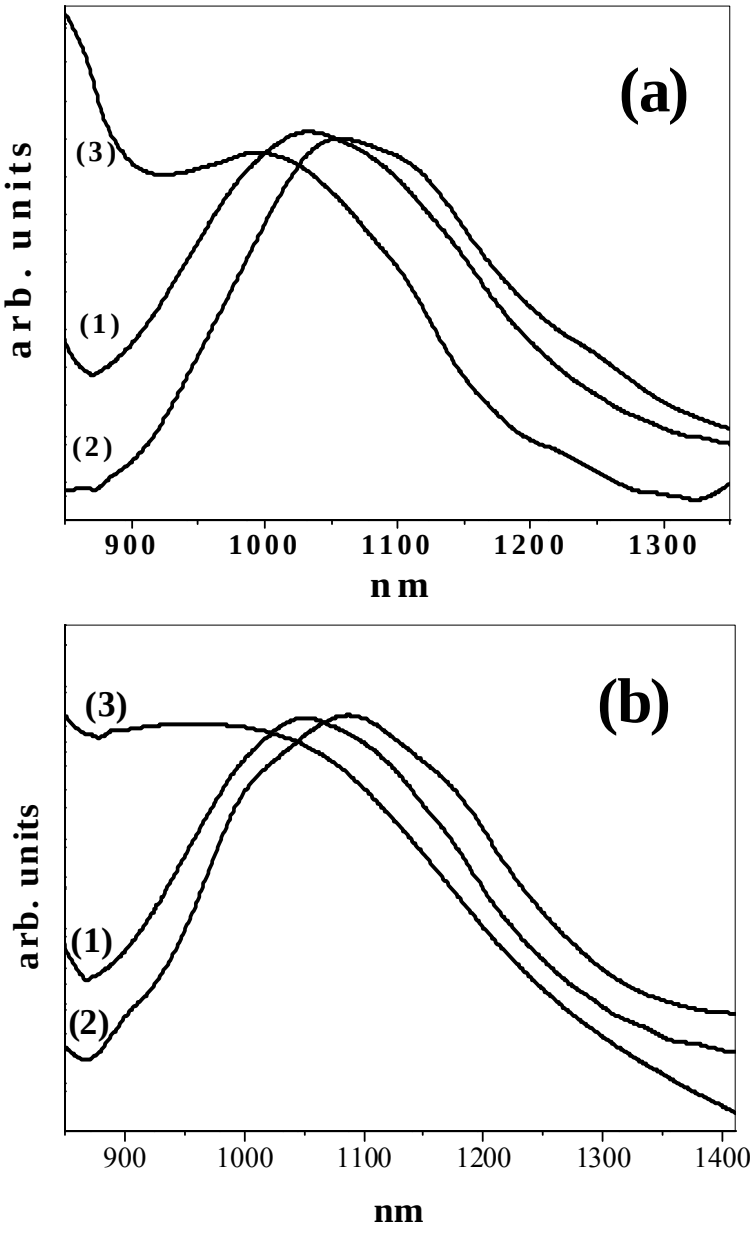

Figure 5.2: Electronic absorption spectra of SWNTs on interaction with electron-donor and -acceptor molecules: (a) (1) benzene, (2) aniline and (3) nitrobenzene; (b) (1) benzene, (2) TTF, and (3) TCNE.

Pristine SWNTs show bands around 750 nm (M_{11}) corresponding to the metallic nanotubes and around 1040 nm (S_{22}) and 1880 nm (S_{11}) due to the semiconducting species arising from the Van-Hove singularities in the optical absorption spectra. In

Figure 5.2, we show the S_{22} bands of SWNTs in the electronic absorption spectra. On interaction with nitrobenzene and aniline, the S_{22} band shifts in the opposite directions relative to the benzene reference. Thus, the positions of the S_{22} band maxima are 1010 and 1090 nm respectively on interaction with nitrobenzene and aniline, while the band maximum occurs at 1054 nm on interaction with benzene. Similarly, on interaction with TTF which is a good electron donor, the S_{22} band shifts to 1095 nm while with TCNE and TCNQ band shift to 990 nm and 1005 nm respectively. The changes in the optical absorption spectra can be attributed to the changes in the Fermi level of the semiconducting nanotubes.

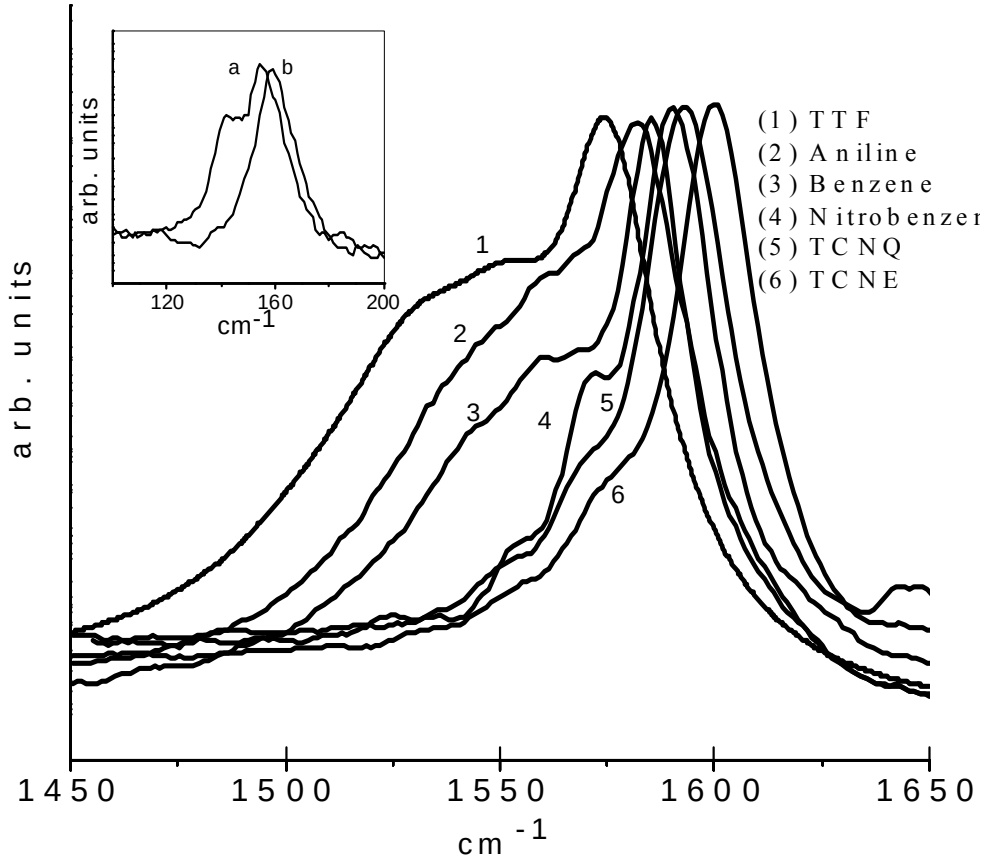

Figure 5.3: G-bands in the Raman spectra of SWNTs on interaction with electron donor and acceptor molecules. The inset shows RBM bands in the Raman spectra of SWNTs on interaction with (a) TTF and (b) TCNE.

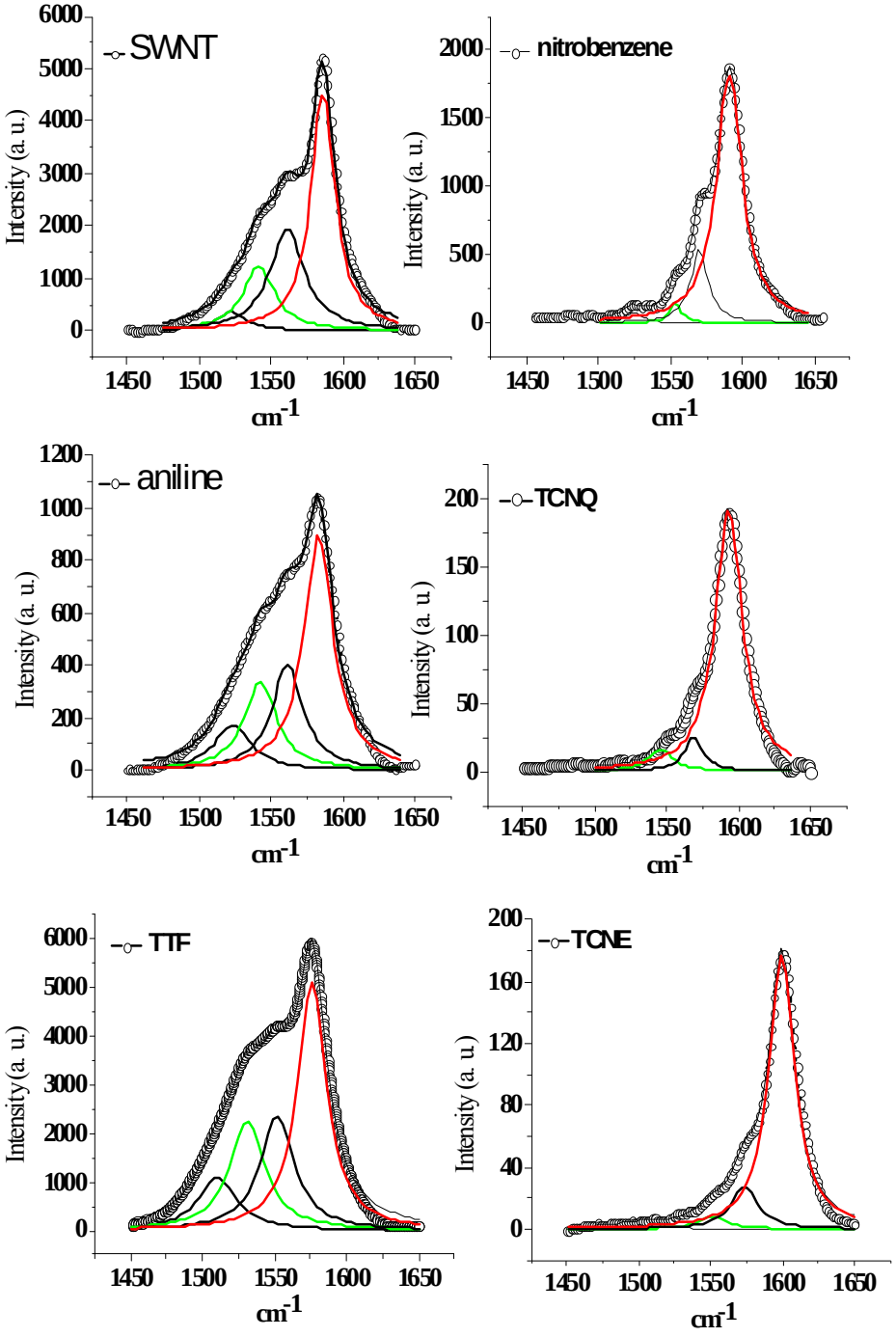

Figure 5.4: Decanvolution of Raman G-bands of SWNTs and SWNTs on interaction with electron-donors and –acceptors.

Considering that the G-band of SWNTs in the Raman spectrum is highly sensitive to the electronic effects, we have examined the changes in the G-band position on interaction with the electron-withdrawing and -donating molecules. In Figure 5.3, we show the G-bands recorded with different chemical surroundings. The G-band maximum is shifted to 1582 cm^{-1} and 1590 cm^{-1} respectively in the case of aniline and nitrobenzene, compared to 1585 cm^{-1} with benzene. These shifts are similar to those reported by Shin *et al.* (*28*) Carbon nanotubes doped with boron and nitrogen produce shifts in the opposite directions, just as nitrobenzene and aniline. While boron doping (p-type) increases the G-band frequency, nitrogen doping (n-type) decreases the G-band frequency (*29*). We, therefore, surmise that aniline causes n-type doping while nitrobenzene corresponds to p-type doping. Further, the band is shifted to 1574 cm^{-1} on interaction with TTF, while with TCNQ and TCNE the G-band maxima occur at 1593 and 1599 cm^{-1} respectively. These shifts are also consistent with the electron-donating or -withdrawing character of these molecules.

The Raman G-band of SWNTs exhibits a significant feature around 1540 cm^{-1} due to the metallic species (*4*). The Raman G-band can accordingly be deconvoluted to obtain approximate estimates of the metallic species relative to the semiconducting species (Figure 5.4). The metallic feature in the G-band appears prominently on interaction of the SWNTs with aniline and TTF, but nearly disappears on interaction with nitrobenzene, TCNQ and TCNE. Clearly, the donor molecules increase the proportion of the metallic species by transforming the semiconducting species to the metallic species through electron donation. Electron withdrawing molecules, on the other hand, decrease the apparent proportion of the metallic species by withdrawing carriers from the metallic species. This conclusion is consistent with the observation of Shin *et al.* (*28*) Thus, the percentage of metallic like species varies as TTF > aniline > benzene > nitrobenzene > TCNQ > TCNE. The percentage of the metallic species is estimated to

be less than 10 % on interaction with electron-withdrawing molecules, while it is in the range of 35-59 % on interaction with electron-donating molecules.

We have followed changes in the G-band with the concentration of TTF and TCNE (Figure 5.5). In Figure 5.6 (a) we have shown the variation of the position of the G-band maximum with the concentration of TTF and TCNE. We clearly see that shifts are in the opposite directions with TTF and TCNE. In Figure 5.6 (b), we have plotted the variation of full-width at half maximum (FWHM) of the G-band against the

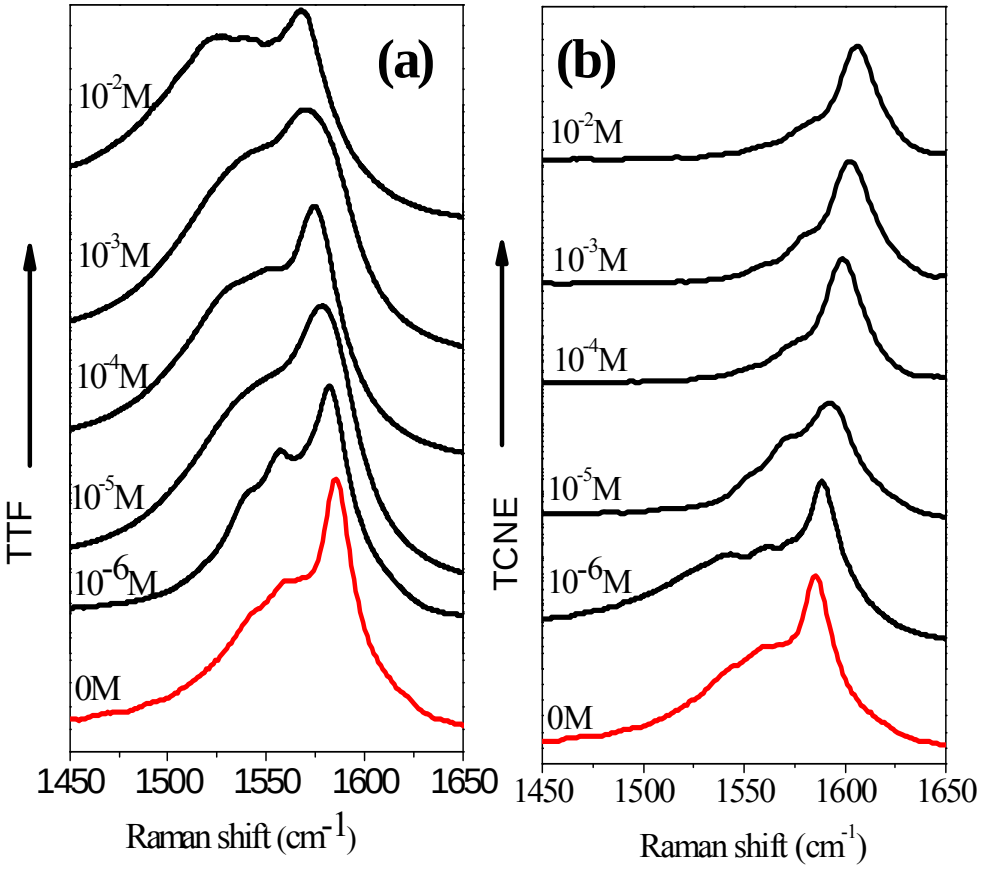

Figure 5.5: Effect of on interaction of varying concentrations of (a) TTF and (b) TCNE on the G-band of SWNTs.

concentration of TTF and TCNE. The FWHM shows opposite trends with concentration in the case of TTF and TCNE. The variation shown in Figure 5.6 is also obtained with

widths obtained by deconvoluting the G-band into metallic and semiconducting features. The spectra also show an increase in the intensity of the 1540 cm^{-1} feature due to the metallic species with an increase in TTF concentration and decrease in the intensity with an increase in TCNE concentration. These results demonstrate how carrier concentration is affected by the concentration of the electron-donor and -acceptor molecules.

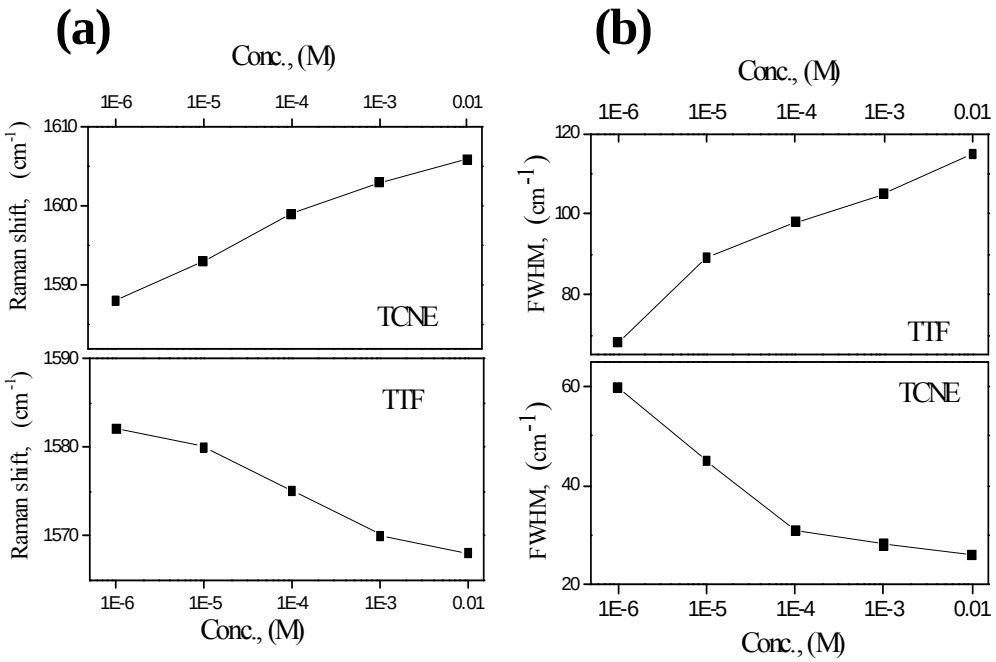

Figure 5.6: Variation of (a) the position and (b) the FWHM of G-band with the concentration of TTF and TCNE.

We find that molecular charge-transfer also affects the Raman bands due to the radial breathing modes (RBM) of SWNTs. Although it is difficult to estimate the proportions of the metallic and semiconducting species by making use of the RBM bands, the occurrence of marked changes in the band shapes due to molecular charge transfer is noteworthy (see inset of Figure 5.3). We have found the electronic absorption spectra of the donor and acceptor molecules are also affected on interaction with SWNTs. Thus, the $\pi - \pi^*$ band of aniline is slightly red-shifted on interaction with SWNTs.

In order to carry out electrical resistivity measurements, vertical SWNT devices were fabricated in a porous anodic alumina (PAA) template (*30-33*). The I-V characteristics of the SWNT bundle prepared as above and soaked in the liquids of electron-withdrawing and electron-donating molecules were measured using a Keithley 236 multimeter.

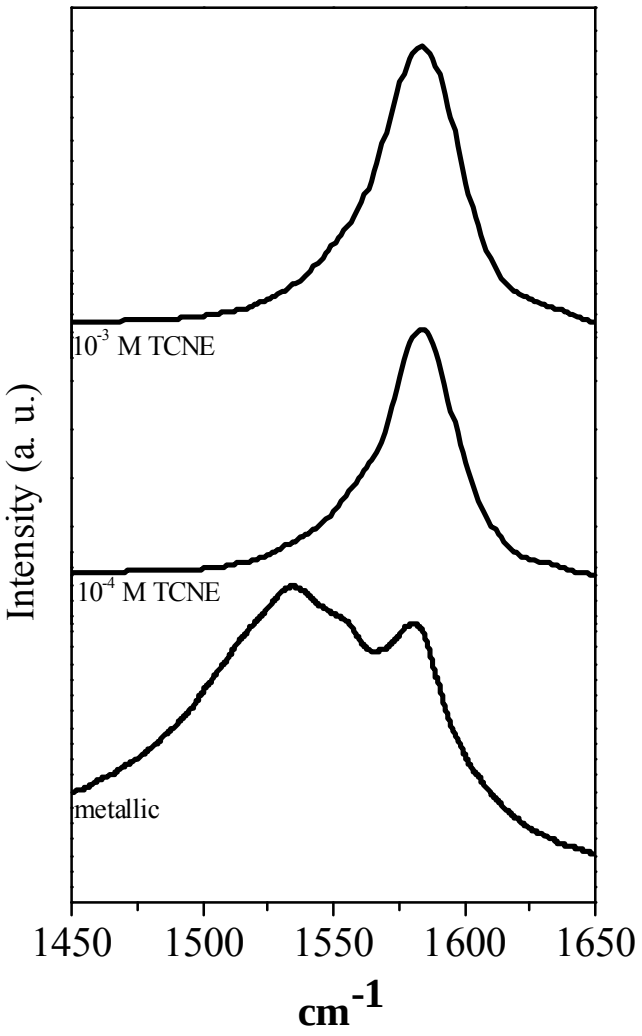

Figure 5.7: Changes in the G-band of metallic SWNTs on interaction with varying concentrations of TCNE.

The resistance of the SWNTs is 492 Ω in air at a bias voltage of 1 V. At a forward bias, the resistance decreases markedly in the presence of electron withdrawing molecules such as nitrobenzene and chlorobenzene, whereas it increases in the presence

of electron donating molecules such as aniline and anisole. Thus, the relative values of resistance (compared to pure SWNTs) were 5.1 and 1.5 respectively in the presence of aniline and anisole respectively at 1 V, the corresponding values in the presence of the chlorobenzene and nitrobenzene being 0.61 and 0.44 respectively. At a bias voltage of 0.05 V, the resistance of the SWNTs is 1.0 kΩ in air. In the presence of aniline, anisole, chlorobenzene and nitrobenzene, the relative values of resistance are 6.6, 1.7, 0.5 and 0.3 respectively. SWNTs under ambient conditions usually show p-type behavior (*34*). It is possible that in the presence of electron-donating molecules, the number of hole carriers is reduced, causing an increase in the resistance. In the presence of electron-withdrawing molecules more holes are generated in semiconducting SWNTs. Interestingly, that the resistance varies proportionally with the Hammett substituent constants, the order being $NH_2 > OCH_3 > Cl > NO_2$. This trend reflects the changes in the nature and the concentration of carriers as well as their motilities brought about by interaction with electron donor and acceptor molecules. The I-V curves become more nonlinear as one goes from aniline to nitrobenzene. The slope of the I-V curve also increases going from nitrobenzene to aniline, due to the presence of a higher proportion of metallic like nanotubes in the presence of aniline.

We have examined the interaction of electron donor and acceptor molecules with pure semiconducting and metallic SWNTs. On interaction with an electron acceptor molecule, TCNE, the 1540 cm^{-1} feature in Raman spectra due to metallic species disappears (Figure 5.8). This is due to change in the Fermi level of nanotubes. Electron donating molecules such as TTF have no effect on the Raman spectrum of metallic SWNTs. Interaction of electron donating molecule, TTF, with semiconducting carbon nanotubes, the 1540 cm^{-1} feature appears and increases significantly with increase in the concentration of TTF (Figure 5.8). This remarkable change on the electronic structure of SWNTs is reversible.

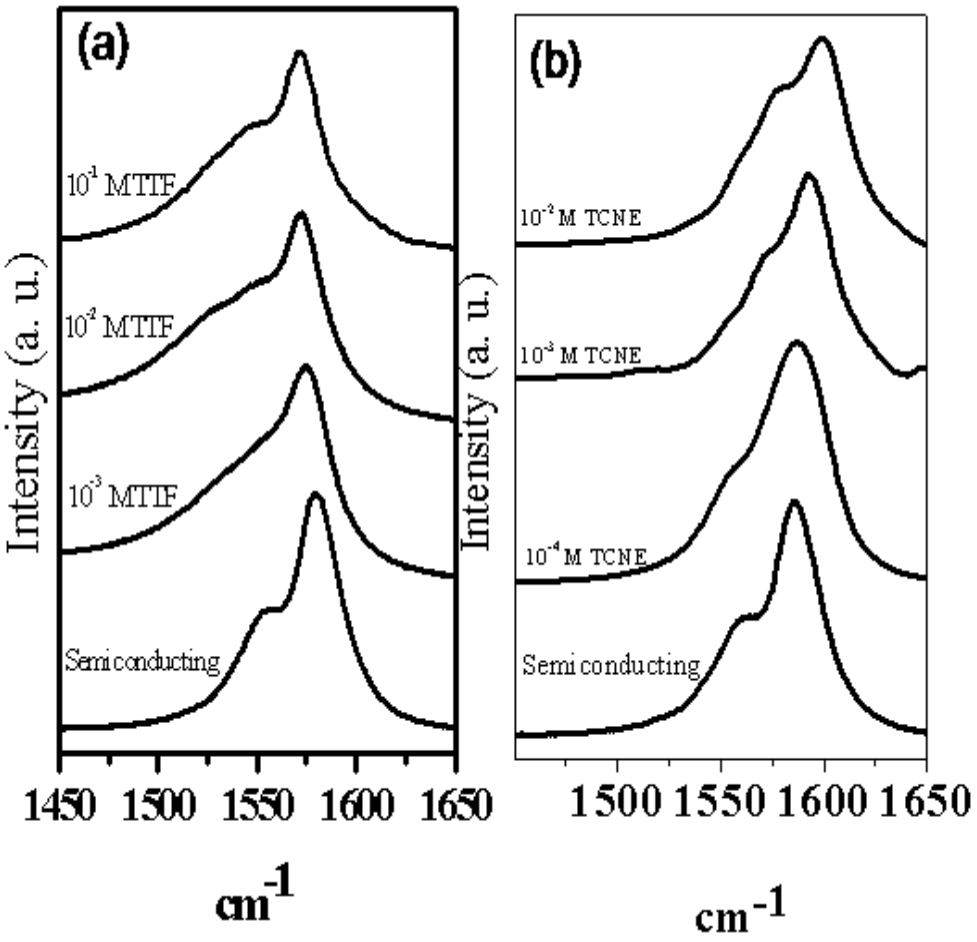

Figure 5.8: Shifts of the G-band of semiconducting SWNTs on interaction with varying concentrations of (a) TTF and (b) TCNE.

Calorimetric experiments on the interaction of SWNTs with molecules have provided an insight into the affinities of the different molecules (*35*). Interaction energies of electron acceptor molecules (e.g., TCNE) with SWNTs are higher than those of electron donor molecules (e.g., TTF). Metallic SWNTs interact reversibly with electron acceptor molecules such as TCNE, the interaction energy being higher than with as-prepared SWNTs (containing a mixture of metallic and semiconducting species). The interaction energy of metallic nanotubes with a donor molecule such as TTF is negligible and could not be measured by isothermal calorimentry (ITC). ITC measurements clearly show that metallic nanotubes specifically interact with electron-withdrawing molecules. The

interaction energy with acceptor molecules varies with the electron affinity as well as with the charge-transfer transition energy for different aromatics. Density functional theory calculations have shown that the nature of interaction is in physisorption regime and mainly governed by Coulombic forces *(36)*. The large band gap of semiconducting (8,0) SWNTs can be tuned through adsorption of selective organic molecules which gives mid gap localized molecular levels near the Fermi energy with tuning the band gap region. Metallic (5,5) SWNTs and semiconducting (8,0) SWNTs turn into semiconducting and metallic nanotubes respectively in the presence of adsorbed molecules.

The present study establishes the high sensitivity of SWNTs to molecular charge-transfer. This feature of SWNTs may be useful in many of the applications such as sensors and nanoelectronics.

5.4.2 Semiconductor to metal transition in SWNTs caused by interaction with gold and platinum nanoparticles

In Figures 5.9 (a) and (b) we show the TEM images of the SWNTs bundles coated with gold and platinum nanoparticles obtained by microwave treatment. The TEM images show the presence of uniform coatings on the SWNTs. The average diameters of the gold and platinum nanoparticles are around 3 and 2.5 nm respectively. Figures 5.9 (c) and (d) show the TEM images of SWNTs with covalently attached gold nanoparticles of average diameters of 3 and 12 nm through click chemistry.

Figure 5.10 (a) shows the Raman G band of SWNTs while Figures 5.10 (b) and (c) shows the G-bands of SWNTs bundles coated with gold and platinum nanoparticles obtained by microwave treatment and Figures 5.10 (d) and (e) the G-bands of SWNTs bundles with covalently attached gold nanoparticles of average diameters of 3 and 12 nm through click chemistry. The G band had been decomposed into four or six

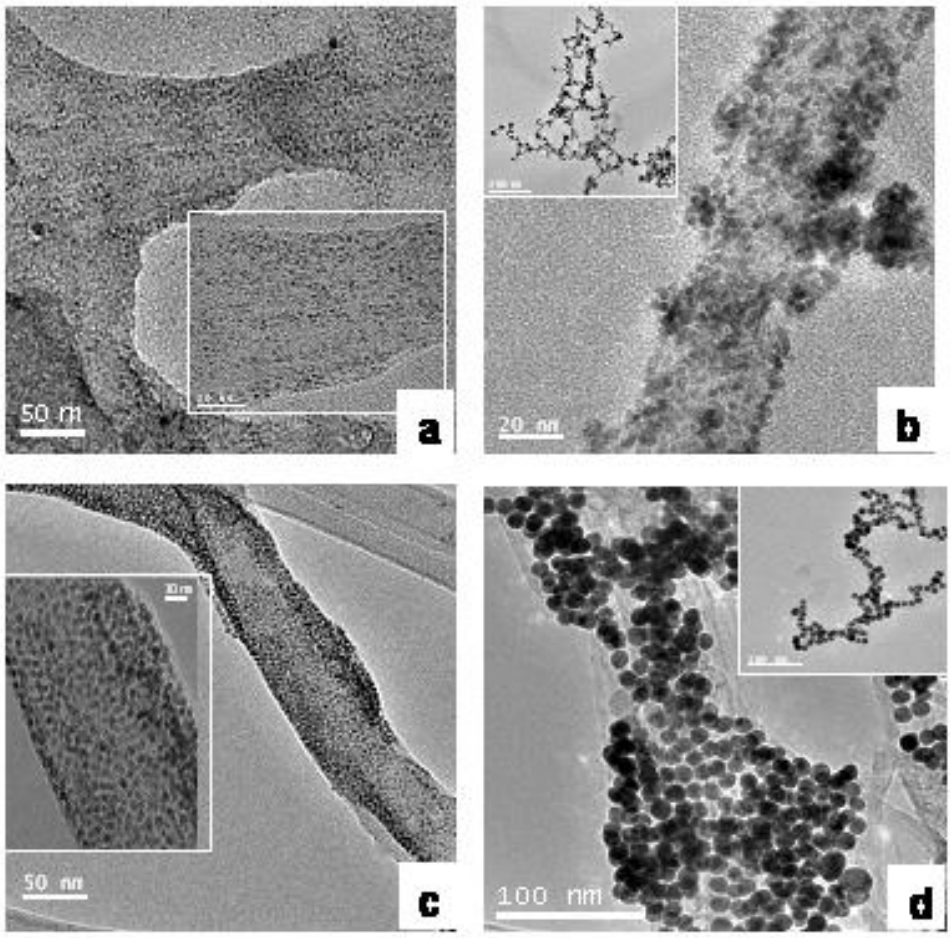

Figure 5.9: TEM images of SWNTs coated with (a) gold and (b) platinum nanoparticles by microwave treatment and of SWNTs covalently linked to (c) 3 nm and (d) 12 nm gold nanoparticles by click reaction.

Lorentzians in the literature (*6, 37, 38*). We first fitted the G bands using four Lorentzians centered at 1510, 1540, 1563 and 1579 cm^{-1}, of which first two are due to metallic species, while the 1563 cm^{-1} band has contributions from both the metallic and the semiconducting species. The band at 1579 cm^{-1} is mainly due to the semiconducting species. For the purpose of calculating the ratio of the metallic to the semiconducting species, we have used the ratio of areas of the 1540 (metallic, M) and 1579 cm^{-1} (semiconducting, S) bands. The M/S ratios so obtained for SWNTs coated with 3 nm gold nanoparticles by microwave treatment and click reaction are 0.61 and 0.72

respectively, compared to ~0.4 in the case of pure SWNTs. These values indicate a 40-80 % increase in the proportion of the metallic SWNT species on interaction with the

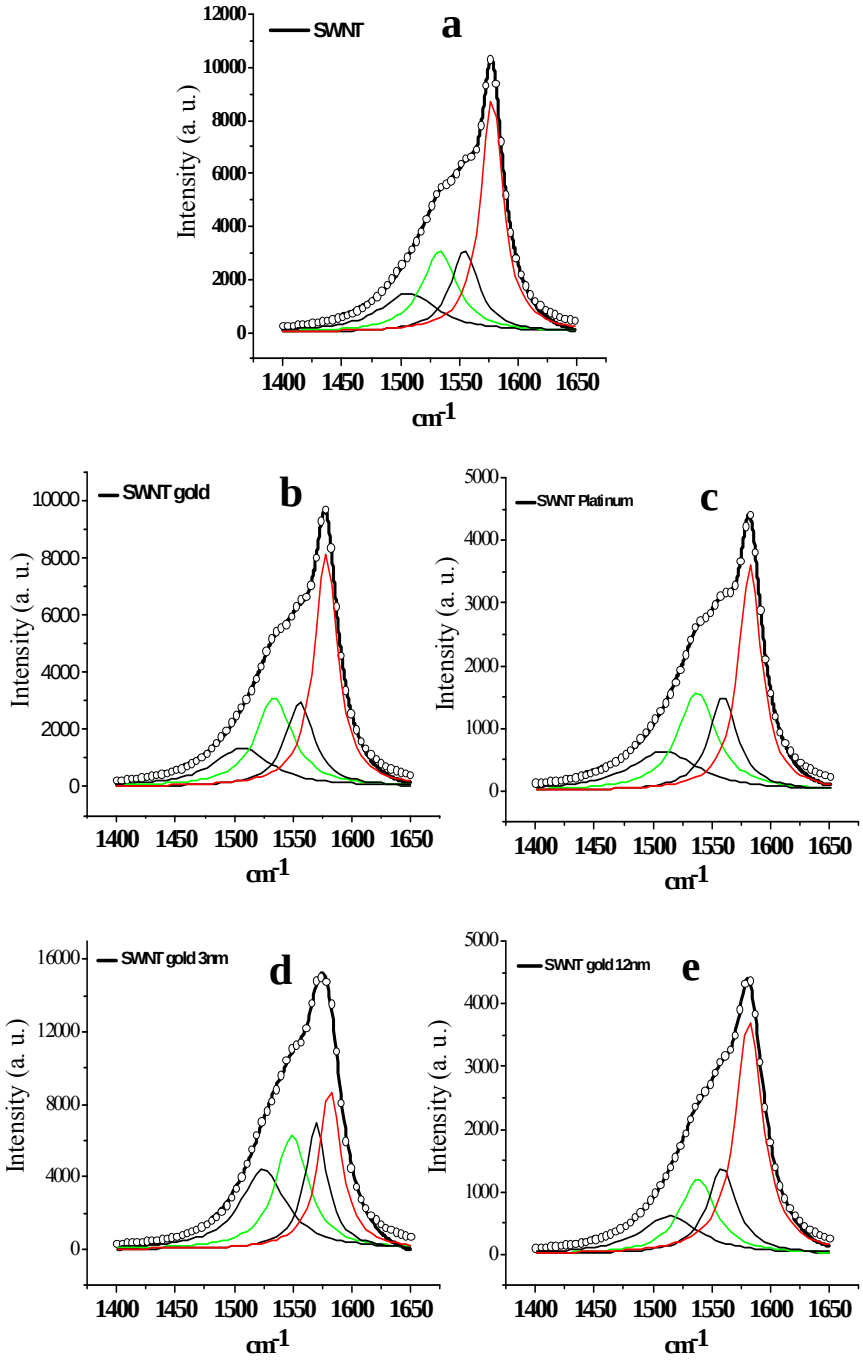

Figure 5.10: G-bands in the Raman spectra of (a) pure SWNTs and of SWNTs coated with (b) 3 nm gold and (c) 2.5 nm platinum nanoparticles by microwave treatement and (d) 3 nm and (e) 12 nm gold nanoparticles by click reaction.

Table 5.1: Intensity ratios of 1540 cm^{-1} feature with respect to the G-band at 1579 cm^{-1}.

By Microwave treatment		
	4 peak fit[a]	**3 peak fit[b]**
	1540/1579	**1540/1579**
SWNT	0.4	1.1
SWNT gold (3 nm)	0.61	1.2
SWNT platinum (2.5 nm)	0.73	1.6
By Click reaction		
	4 peak fit[a]	**3 peak fit[b]**
	1540/1579	**1540/1579**
SWNT gold 3nm	0.61	0.74
SWNT gold 12nm	o.43	0.91

[a] Ratios of intensities of the bands due to metallic to semiconduting species were obtained by fitting the G band into four Lorentzians at 1540 cm^{-1}, 1570 cm^{-1} (metallic species) and 1580 cm^{-1} , 1595 cm^{-1} (semiconducting species). The values in the parenthesis are obtained from the intensity ratios of the 1540 cm^{-1} and1580 cm^{-1} areas of the bands were used as intensities.

[b] Ratios of intensities of the bands due to metallic to semiconduting species were obtained by fitting the G band into three Lorentzians at 1540 cm^{-1}, 1570 cm^{-1} (metallic species) and 1579 cm^{-1} (semiconducting species).

3 nm gold nanoparticles. With 12 nm Au particles, the increase in the proportion of the metallic species is upto 13 %. SWNTs coated with 2.5 nm Pt particles by microwave treatment gave an M/S ratio of 0.73. Table 5.1 gives the M/S ratios obtained by fitting G-band with three Lorentzians. On fitting the G bands to six Lorentzians centered at

1515, 1540, 1555, 1570, 1580 and 1595 cm^{-1}, of which the bands at 1515, 1540 and 1570 cm^{-1} are due to the metallic species, the M/S values showed an increase in the proportion of the metallic species by 20-100 % on attachment of 3nm gold or platinum particles by either two methods. We also fitted the 1540 cm^{-1} band due to the metallic species to the Fano band shape and obtained the M/S ratios. This analysis showed a 30-40 % increase in the metallic species on attaching 3 nm Au nanoparticles to the SWNTs. The D-band shows a small increase on attachment of metal particles, but this is not too relevant to the present study.

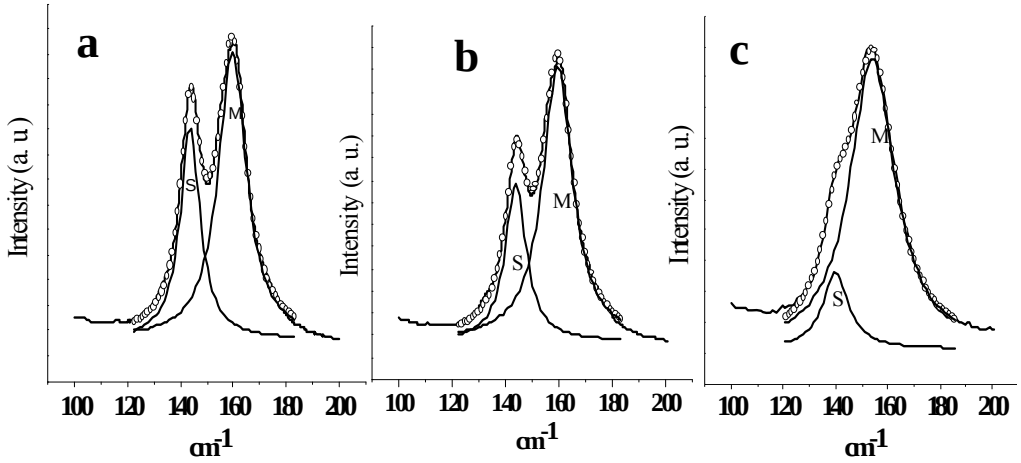

Figure 5.11: RBM bands in the Raman spectra of (a) pure SWNTs and of SWNTs coated with 3 nm gold nanoparticles (b) by microwave treatment and (c) by click reaction.

Pure SWNTs show two RBM bands in the Raman spectra at 145 cm^{-1} and 160 cm^{-1} when excited with 632 nm laser radiation, as can be seen from Figure 5.11 (a). Based on Kataura's plot, we assign the band at 145 cm^{-1} due to semiconducting species (S) and the band at 160 cm^{-1} to metallic species (M) (*39*). Accordingly, excitation by a 514 nm laser source exclusively showed only the band corresponding to the semiconducting species at 145 cm^{-1} (*40*). Figures 5.11 (b) and (c) show the RBM bands of SWNTs covered by 3 nm Au particles by microwave treatment and click reaction respectively. We see a clear increase in the M/S ratios, obtained by taking the ratios of band areas.

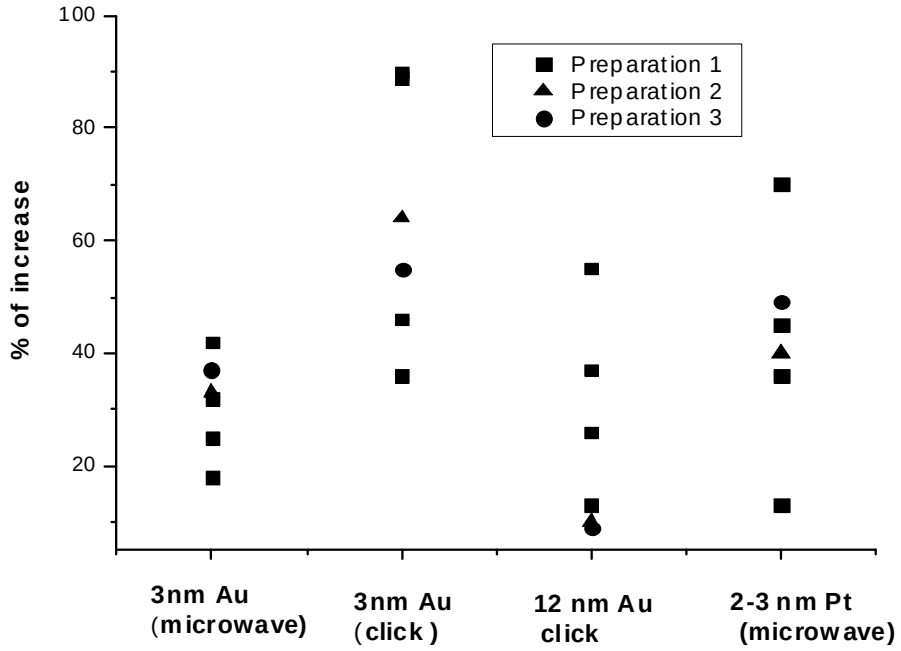

Figure 5.12: Percentage increase in the metallic SWNT species on interaction of Au and Pt nanoparticles found with different methods of analysis of the Raman G-band.

The ratios are higher in the case of the 3 nm Au particles compared to those with the 12 nm gold particles. The smaller Au particles get coated better and are also chemically more active. We found that the Pt particles also cause an increase in the M/S ratio. The results from the RBM bands confirm that there is a definitive increase in the proportion of the metallic species, on interaction of SWNTs with metal nanoparticles. It must however be noted that RBM bands are not suited to obtain quantitative changes in M and S bands unlike the G band.

In Figure 5.12 we show plots of the percentage increase in the metallic SWNT species found by us on different SWNT samples attached to Au (Pt) nanoparticles and by different methods of analysis of the G bands. This figure clearly establishes that the metal nanoparticles cause an increase in the proportion of the metallic SWNT species. Studies have shown that the intensities of the interband transitions show same changes.

Thus, the intensity of the M_{11} band in the electronic spectrum increases relative to the intensity of S_{22} band on attachment of SWNTs with gold nanoparticles.

To understand the above experimental results, Pati *et al.* have performed *ab-initio* studies on a variety of SWNT-Au and SWNT-Pt periodic composites, such as, gold and platinum wires, tubes and clusters adsorbed over the metallic as well as semiconducting SWNTs. A single chain of Au and Pt atoms periodically arranged on the surface of a (8,0) SWNT failed to sufficiently alter the electronic structure, although the semiconducting gap of Au-SWNT and Pt-SWNT composites reduced in proportions compared to the pristine (8,0) nanotube. Interestingly, however, the metal-SWNT system where the entire curved surface area of a semiconducting (8,0) SWNT is covered with a cylindrical metal monolayer is metallic. Furthermore, such extensive interactions between the metal atoms and the SWNT modify the electronic structure of the SWNTs as well, rendering them metallic. The density of states (DOS) projected out on the SWNT for both the Au-SWNT and Pt-SWNT show that there is sufficient electronic density around the Fermi energy. To understand the effect of metal clusters adsorbed on to the external curvature of the electronic structure of SWNTs, we considered Au and Pt clusters of various nuclearities adsorbed on the SWNTs. We present here the results of our calculations on Au-SWNT composites involving gold clusters of nuclearity 40, obtained by combining four unit cells of the (8,0) SWNT to ensure that consecutive clusters do not interact appreciably with one another along the direction of periodicity. The Au_{40} cluster was placed such that one vertex of the cluster was at a distance 3.0 Å from the nearest carbon atom. Interestingly, the Au_{40} cluster nearly retains its symmetrical structure, with the nearest proximity of the cluster to the curved surface of the SWNT being 2.4 Å. The optimized electronic structure shows that the DOS projected onto the SWNT had sufficient density around the Fermi energy indicating that the semiconducting SWNT transforms into a metallic one. Even Au clusters of smaller

nuclearity are found to transform the semiconducting SWNTs into metallic ones. Upon optimization, Au clusters of various nuclearities relax to highly symmetrical structures similar to the case with the Au_{40} cluster, giving rise to a semiconductor to metal transition. In contrast, the metallic SWNTs do not lead to any new phases for all these cases.

In order to understand the mechanism of semiconductor metal transition, the energy and charge densities of the composites have been calculated by varying the distance between the Au fragment and SWNT. The energy of interaction is found to change inversely with the distance between Au and SWNT, clearly indicating that such transition is due to Columbic interactions. Interestingly, such interactions are due to resonance between Au plasmon band and the excitation continuum of SWNTs. From the charge density analysis, we also find that the electron density at the outermost valence orbitals of Au reduces, while that at the orbitals of carbon in closest proximity to the Au fragments decreases. Thus our results indicate that such a phase transition is due to direct charge transfer between Au and Pt particles and the SWNT.

The present Raman studies establish that there is an increase in the proportion of the metallic SWNTs on interaction with Au and Pt nanoparticles. In other words, the metal nanoparticles cause a semiconductor to metal transition in the SWNT–nanoparticle composites.

5.5 Conclusions

In conclusion, the present study establishes the high sensitivity of SWNTs to molecular charge-transfer. Electron-donating molecules such as tetrathiafulvalene and aniline cause changes opposite to those caused by electron-withdrawing molecules such as nitrobenzene and tetracyanoethylene. Thus, a proportion of the semiconducting SWNTs becomes metallic on electron donation through molecular charge transfer.

This feature of SWNTs may be useful in many of the applications such as sensors and nanoelectronics.

The Raman studies establish that there is an increase in the proportion of the metallic SWNTs on interaction with Au and Pt nanoparticles. In other words, the metal nanopaticles cause a semiconductor to metal transition in the SWNTs-nanoparticle composites. These results find support from theoretical calculations which reveal that the interaction of SWNTs with small and reasonably large Au and Pt clusters, as well as cylindrical monolayers of these metals, leads to the modification of the electronic structure resulting in semiconductor to metal transition of the SWNTs. The primary interaction responsible for electronic transition is Coulombic charge transfer between the metal particles and SWNT surface. It is noteworthy that metallic SWNTs do not transform into semiconducting nanotubes upon interaction with metal particles.

REFERENCES

1. R. Saito, G. Dresselhaus, M. S. Dresselhaus, *Physical Properties of Carbon Nanotubes.* (Imperial College Press, London, 1998).
2. C. N. R. Rao, A. Govindaraj, *Nanotubes and Nanowires: RSC Nanoscience & Nanotechnology series.* (Royal Society of Chemistry, Cambridge, 2005).
3. C. N. R. Rao, R. Voggu, A. Govindaraj, *Nanoscale* **1**, 96 (2009).
4. M. S. Dresselhaus, G. Dresselhaus, A. Jorio, *J. Phys. Chem. C* **111**, 17887 (2007).
5. M. S. Strano, *J. Am. Chem. Soc.* **125**, 16148 (2003).
6. A. Das *et al.*, *Phys. Rev. Lett.* **99**, 136803 (2007).
7. D. Tasis, N. Tagmatarchis, A. Bianco, M. Prato, *Chem. Rev.* **106**, 1105 (2006).
8. M. Cha *et al.*, *Nano Lett.* **9**, 1345 (2009).
9. K. K. Kim *et al.*, *J. Am. Chem. Soc.* **130**, 12757 (2008).
10. C. Ehli *et al.*, *Nat. Chem.* **1**, 243 (2009).
11. A. M. Rao, P. C. Eklund, S. Bandow, A. Thess, R. E. Smalley, *Nature* **388**, 257 (1997).
12. J. Chen *et al.*, *Science* **282**, 95 (1998).
13. G. M. do Nascimento *et al.*, *Nano Lett.* **8**, 4168 (2008).
14. G. M. do Nascimento *et al.*, *J. Phys. Chem. C* **113**, 3934 (2009).
15. M. Shim, A. Javey, N. W. Shi Kam, H. Dai, *J. Am. Chem. Soc.* **123**, 11512 (2001).
16. J. Kong *et al.*, *Science* **287**, 622 (2000).
17. T. Takenobu *et al.*, *Adv. Mater.* **17**, 2430 (2005).
18. A. Star, T.-R. Han, J.-C. P. Gabriel, K. Bradley, G. Gruner, *Nano Lett.* **3**, 1421 (2003).
19. D. S. Hecht *et al.*, *Nano Lett.* **6**, 2031 (2006).
20. J.-H. Lee *et al.*, *J. Phys. Chem. C* **111**, 2477 (2007).
21. H.-Z. Geng *et al.*, *J. Am. Chem. Soc.* **129**, 7758 (2007).
22. K. K. Kim *et al.*, *Adv. Funct. Mater.* **17**, 1775 (2007).
23. J. March, Advanced Organic Chemistry. (Wiley, New York, ed. 4th 1992).
24. M. S. Raghuveer, S. Agrawal, N. Bishop, G. Ramanath, *Chem. Mater.* **18**, 1390 (2006).
25. C. Journet *et al.*, *Nature* **388**, 756 (1997).

26. D. G. Duff, A. Baiker, P. P. Edwards, *J. Chem. Soc.-Chem. Commun.*, 96 (1993).
27. J. J. Storhoff, R. Elghanian, R. C. Mucic, C. A. Mirkin, R. L. Letsinger, *J. Am. Chem. Soc.* **120**, 1959 (1998).
28. H.-J. Shin *et al.*, *J. Am. Chem. Soc.* **130**, 2062 (2008).
29. L. S. Panchakarla, A. Govindaraj, C. N. R. Rao, *ACS Nano* **1**, 494 (2007).
30. A. D. Franklin *et al.*, *J. Vacuum Sci. Tech.* B **25**, 343 (2007).
31. M. R. Maschmann *et al.*, *Nano Lett.* **6**, 2712 (2006).
32. M. R. Maschmann, A. D. Franklin, T. D. Sands, T. S. Fisher, *Carbon* **45**, 2290 (2007).
33. R. M. Matthew, *et al.*, *Nanotechnology* **17**, 3925 (2006).
34. C. Zhou, J. Kong, E. Yenilmez, H. Dai, *Science* **290**, 1552 (2000).
35. N. Varghese, A. Ghosh, R. Voggu, S. Ghosh, C. N. R. Rao, *J. Phys. Chem. C* **113**, 16855 (2009).
36. A. K. Manna, S. K. Pati, *Nanoscale*, DOI: 10.1039/c0nr00124d (2010).
37. A. M. Rao *et al.*, *Science* **275**, 187 (1997).
38. S. D. M. Brown *et al.*, *Phys. Rev. B* **61**, R5137 (2000).
39. H. Kataura *et al.*, S*ynth. Metals* **103**, 2555 (1999).
40. M. S. Dresselhaus, P. C. Eklund, *Adv. Phys.* **49**, 705 (2000).

CHAPTER 6

Selective Separation and Synthesis of Metallic SWNTs and Related Aspects

Summary*

This chapter describes our efforts towards selective separation and synthesis of metallic single-walled carbon nanotubes (SWNTs) and synthesis of Y-junction SWNTs. This chapter consists of three sections. The first section describes the separation of metallic and semiconducting SWNTs based on molecular charge-transfer. Interaction of as-prepared SWNTs, containing a mixture of metallic and semiconducting species with the potassium salt of coronenetetracarboxylic acid, **I**, in aqueous medium provides a simple method of separating semiconducting and metallic species. The metallic nanotubes precipitate out on interaction with **I**, while the semiconducting nanotubes remain in solution. The solution and precipitate was characterized by Raman spectroscopy, optical absorption spectroscopy, photoluminescence and thermo-gravimetric analysis (TGA). The separation was further confirmed from I-V and electrical resistivity measurements. This method avoids centrifugation and is amenable for large-scale separation, and can be used as a routine laboratory procedure.

The second section deals with a novel method for the synthesis of metallic SWNTs by arc discharge method. Arc-discharge with carbon electrodes containing Ni and Y_2O_3 in He atmosphere, in the presence of $Fe(CO)_5$ vapors have been investigated. It is found

**** Papers based on these studies have appeared in Journal of American Chemical Society (communication) (2010), Nanoscale (2009) and Journal of Nanoscience and Nanotechnology (2010)***

that unlike the cathode deposit, the web deposited in the chamber contains mainly metallic single-walled carbon nanotubes (SWNTs) as evidenced from Raman and optical absorption spectroscopy. The percentage of metallic SWNTs increases with the concentration of $Fe(CO)_5$. Under optimal conditions, the web contains over 90% of metallic SWNTs. This method enables the synthesis of nearly pure metallic SWNTs on a large scale.

The third section of the thesis presents our efforts to synthesize Y-junction SWNTs. Y-junction SWNTs were prepared by carrying out arc discharge of graphite over a Ni–Y_2O_3 catalyst in an atmosphere of thiophene and helium. The formation of junctions is established from transmission electron microscopy and atomic force microscopy.

6.1 Introduction

Carbon nanotubes exhibit fascinating electronic, chemical and mechanical properties with a wide range of applications (*1, 2*). Since the discovery of carbon nanotubes, several methods have been reported for the synthesis of multi-walled, double-walled and single-walled carbon nanotubes (*3*). The methods include arc-evaporation of graphite, laser ablation, chemical vapor deposition (CVD) and vapor phase decomposition or disproportionation of carbon-containing molecules. Among the various types of carbon nanotubes, single-walled carbon nanotubes (SWNTs) are of special interest because of their unique properties and potential applications. Specific methods have been found to obtain long SWNTs (*4-6*) as well as diameter-control of the nanotubes (*7, 8*). SWNTs of various forms such as rings (*9*), brushes (*10*) and films (*11*) have been prepared. Vertically aligned (*12, 13*) as well as horizontally aligned (*14, 15*) carbon nanotubes have been prepared on different substrates by several workers. Diameter selective dispersions of SWNTs are also reported (*16, 17*). As prepared

SWNTs contain a mixture of metallic and semiconducting species. It should be recalled that nanotubes having chiral numbers n=m are metallic and quasi metallic if n-m is divisible by 3, while all the other nanotubes are generally semiconducting. In conventional synthetic processes for SWNTs, metallic nanotubes constitute 33%, the remaining being semiconducting nanotubes. An important aspect of carbon nanotubes is to develop synthetic as well as separation strategies that provide narrow distributions of SWNTs of a specific electronic variety. Metallic SWNTs can function as leads in nanoscale circuits and conductive additives in composites (*18-20*), while the semiconducting ones can be used to design field effect transistors (*21*).

Methods to separate metallic and semiconducting SWNTs include dielectrophoresis, ultracentrifugation, and selective destruction of one type of nanotubes by irradiation or by chemical means, selective interaction with molecules and covalent or noncovalent functionalization. Thus, it is possible to produce SWNTs with a narrow size distribution and specific electronic properties by density gradient ultracentrifugation in the presence of surfactants(*22*). Sucrose has been used as the gradient medium along with surfactants to obtain semiconducting SWNTs with near 95 % purity (*23*). Making use of the differences in the relative dielectric constants of semiconducting and metallic species with respect to the solvent, alternating current dielectrophoresis has been employed to separate the two species (*24*). In this study, a drop of SWNT suspension was dropped on the microelectrode array. The metallic tubes which acquired the largest dipole moments migrated towards the electrodes, while the semiconducting tubes remained in suspension during this process. Selective adsorption of semiconducting nanotubes on agarose has also been used to separate metallic SWNTs (*25*). By making use of selective interaction of aliphatic amines with functionalized SWNTs, separation of metallic and semiconducting SWNTs has been achieved (*26-28*). Preferential charge-transfer interaction of bromine with the metallic species over the semiconducting

species in surfactant-stabilized SWNTs, followed by centrifugation, has been used to separate semiconducting from metallic SWNTs (*29*). Derivatized porphyrins selectively interact with semiconducting SWNTs through noncovalent interaction (*30*). Such interaction can be employed to obtain semiconducting species in solution, leaving the metallic species as residue. Smalley *et al*. (*31*) have employed diazonium reagents for selective functionalization of metallic nanotubes with near exclusion of semiconducting nanotubes under controlled conditions. Thus the hydroxybenzenediazonium salt selectively functionalizes metallic SWNT. Subsequent deprotonation in alkaline solution followed by electrophoretic separation results in the enrichment of the metallic and semiconducting fractions separately (*32, 33*). Density gradient separation of the hydroxybenzenediazoium salt-functionalized SWNTs produces two distinct density fractions corresponding to functionalized metallic and pure semiconducting SWNTs. A model for the differences in the reactivities of the metallic and semiconducting SWNTs with the diazonium salt has been proposed. Covalent functionalization with azomethine ylides has been employed to separate metallic from semiconducting nanotubes (*34, 35*). Wrapping SWNTs by single stranded DNA is found to depend on the tube diameter and the electronic properties of the nanotubes. This property has been used to enrich the metallic nanotubes (*36*). Fluorous chemistry has been effectively used to separate metallic from semiconducting nanotubes. Ghosh and Rao (*37*) have reported effective separation of semiconducting and metallic SWNTs by employing fluorous chemistry wherein the diazonium salt of 4-heptadecafluorooctylaniline reacts preferentially with metallic SWNTs present in the mixture of nanotubes.

An important aspect of nanotube synthesis is to develop strategies that provide narrow distributions of SWNTs of a specific electronic variety. There are reports on the diameter control of SWNTs by controlling the temperature (*38*), pressure (*39*), carbon feedstock (*40*), catalyst particle size (*41*) or catalyst material (*42*). Methods to obtain a

specific electronic type of SWNTs is of greater interest. Li *et al. (43)* and Qu *et al. (12)* have recently reported selective growth of semiconducting nanotubes using plasma-enhanced chemical vapor deposition. High-density arrays of horizontally aligned SWNTs consisting of over 95% semiconducting nanotubes were obtained on single crystal quartz substrates by Ding *et al. (44)*. Zhang *et al.* (*45*) were able to selectively etch semiconducting SWNTs by treating the mixture of SWNTs with SO_3 gas at 400 ^oC. Metallic SWNTs could be continuously extracted from a mixture of semiconducting and metallic species in a microfluidic channel using dielectrophoretic force fields (*46*). This is a nondestructive method yielding nearly complete selectivity. Wang *et al.* (*47*) have suggested that pyrolysis of monohydroxy aliphatic alcohols with long chains on a Fe-Co/MgO catalyst results in the enrichment of metallic SWNTs. They were able to produce SWNTs enriched up to 65 %. Selective etching by hydroxyl radicals of the alcohol molecules and protection of amorphous carbon might be responsible for the enrichment.

It has been theoretically predicted that carbon nanotubes with intramolecular junctions such as Y-junctions would possess unusual electronic properties (*48*). Electronic properties of SWNT/SWNT junctions can be metal-metal (M-M) junctions, metal-semiconductor (M-S) Schottky junctions or semiconductor-semiconductor (S-S) heterojunctions. A M-S junction would behave like a rectifying diode with non-linear transport characteristics (*49*). A S-S junction can also behave like a rectifying diode due to the different band gaps of the two semiconducting segments (*50*). These novel properties enable carbon nanotube junctions to be used in circuits and other applications (*51, 52*).

Synthesis of junction carbon nanotubes has been an important challenge. Earlier efforts focused on the generation of multi-walled carbon nanotubes by using template methods (*53*). To obtain large yields of branched CNTs, the most used route is to

introduce additives such as thiophene in the reactants. This was first reported by Rao *et al*. in 2000 (*54*). MWNT junctions were produced by the pyrolysis of nickelocene (which acts both as the catalyst source and the carbon feedstock) in the presence of thiophene. A similar CVD process with different additives has been employed to generate branched MWNTs (*55*). The role of sulfur (thiophene) in the branching process of nanotubes with stacked-cone morphologies has been explained (*56*). The growing branches appear to possess a minute amount of sulfur which is sufficient to promote the formation of heptagons (negative curvature) and pentagons (positive curvature).

Due to the advantages of multiterminal SWNTs over MWNTs in applications, there is effort to prepare Y-junction SWNTs. Y-junction SWNTs were seen in samples of STM samples produced by the thermal decomposition of C_{60} in the presence of transition metals like Ti, Cr, Fe, Co and Ni (*57*). Choi and coworkers (*58*) synthesized Y-junction SWNTs using thermal chemical vapor deposition of methane over Mo or Zr doped Fe nanoparticles supported on aluminum oxide. The presence of Mo or Zr in the Fe catalyst enhances the nucleation and growth of carbon nanotubes, and facilitates the growth of new nanotube branches when they are attached to the sidewalls of the existing nanotubes.

Although there are various reports in the literature to obtain SWNTs with desired electronic properties, developing strategies for selective synthesis of SWNTs and separation of SWNTs based on the electronic type still an active area of research. We report the scope of present investigation in the next section.

6.2 Scope of the Present Investigations

Selective synthesis and separation of metallic and semiconducting SWNTs are major challenges today. It is technologically important to separate these two types of SWNTs to fully realize the potential applications in nanoelectronics and other areas. Therefore,

we thought it is highly desirable to find out the simple and scalable methods to obtain the SWNTs with specific electronic properties.

Despite various reports in the literature on the separation of nanotubes, the yields after separation in most of the cases are not large enough to be used for an industrial scale. Most of the methods require cumbersome procedures such as high speed centrifugation which renders large scale processing difficult. It is, therefore, highly desirable to find a simple and scalable separation strategy which also avoids high speed centrifugation. In the first section we describe our efforts towards the separation of metallic and semiconducting nanotubes from the mixture of nanotubes. We have investigated whether molecular charge-transfer between SWNTs and an appropriate π-system can be exploited for the effective separation of metallic and semiconducting nanotubes, since π-π interaction with aromatic molecules enables the solubilization of SWNTs and there appears to be selectivity in the interaction of electron donor and acceptor molecules with SWNTs and graphene (*59*). With this purpose, we have made use of the potassium salt of coronene tetracarboxylic acid, **I,** which has a large π skeleton attached to four electron-withdrawing groups and exhibits charge-transfer interaction with graphene causing solubilization in aqueous medium. The separation process is simple which, involves sonication followed by the precipitation of metallic nanotubes. The solution contains semiconducting nanotubes exclusively. The simplicity of the method allows bulk separation of SWNTs, giving 100 % separation with the appropriate concentration of potassium salt of coronene tetracarboxylate.

Methods to prepare a specific electronic type of SWNT are of vital importance. Li *et al.(43)* and Qu *et al.*(*12*) have recently reported selective growth of semiconducting nanotubes using plasma-enhanced chemical vapor deposition. Enriched metallic SWNTs (up to 65%) seem to be produced by the pyrolysis of monohydroxy alcohols (*47*). A method for the synthesis of pure or nearly pure metallic SWNTs has not yet

been reported. We have carried out a systematic study of having iron pentacarbonyl vapors on the nature of SWNTs produced by arc discharge process. We find that the arc discharge of composite (Ni/Y_2O_3) graphite rods in the presence of iron pentacarbonyl, $Fe(CO)_5$, yields nanotube deposits on the walls of the discharge chamber, primarily containing metallic SWNTs($\geq$ 90%). The procedure is simple and provides a useful method to prepare metallic SWNTs.

There is no straight forward method for the synthesis of junction single-walled carbon nanotubes. Earlier efforts focused on the generation of multi-walled carbon nanotubes by using template methods and pyrolysis of nickelocene in the presence of thiophene. Due to the advantages of multiterminal SWNTs over MWNTs in applications, there are few efforts to prepare Y-junction SWNT in the literature. We have developed a procedure to synthesize Y-junction SWNTs by arc discharge methods. The method involves arc evaporation of graphite over a $Ni\text{-}Y_2O_3$ catalyst in an atmosphere of thiophene and helium. The products were characterized by transmission electron microscopy and atomic force microscopy.

6.3 Experimental

6.3.1 Separation of SWNTs by molecular charge-transfer

Synthesis of SWNTs: Arc discharge SWNTs were synthesized by the method as reported by Journet *et al.* (60) using a composite rod containing Y (1 at.%) and Ni (4.2 at.%) as the anode and a graphite rod as the cathode, under a helium pressure of 660 torr with a current of 100 A and 30 V. The nanotubes were heated in air at 300 ^oC for 12 h and then stirred in conc. HNO_3 and H_2SO_4 mixture at 60 ^oC for 24 h in order to dissolve the metal nanoparticles. The product was washed with distilled water, dried, dispersed in ethanol under sonication, and filtered using Millipore (0.3 μm) filter paper. The filtered product was dried in an oven at 100 ^oC for 2 h. The sample was heated to 1000

^{o}C in a furnace at a rate of 3 ^{o}C per minute, in flowing hydrogen at 100 sccm and held at that temperature for 2 h. The resulting sample was again stirred in conc. HCl at 60 ^{o}C for 3 h and finally heated in a furnace at 1100 ^{o}C for 2 h in flowing hydrogen (100 sccm). Procedure was repeated until the removal of metal impurities and amorphous carbon.

Separation of SWNTs:

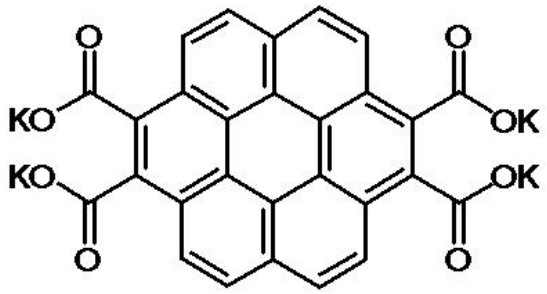

(I)

We have performed the separation of SWNTs with **I** by varying the concentrations of the latter. **I** was prepared starting from perylene by oxidative benzogenic Diels–Alder reaction with N-ethyl maleimide, followed by hydrolysis of the resulting diimide with KOH in methanol. To separate SWNTs, we have taken 1mg of pure SWNTs in 5 ml of 5 mM or 10 mM solution of **I** in water and sonicated the mixture at 50 ^{o}C for 3h. The mixture was then heated at 70 ^{o}C for 12 h under vigorous stirring. The resulting mixture was transferred to 5ml glass vial and kept aside without disturbance. The precipitate is collected at the intervals of 24 hours and 48 hours and there was no precipitate observed after 48 hours. Both the solution and precipitate were characterized separately. Before all the measurements the nanotubes were filtered through PTFE membrane and washed thoroughly with water to remove **I**. The compound **I** can be removed from the nanotubes by heating at 400 ^{o}C.

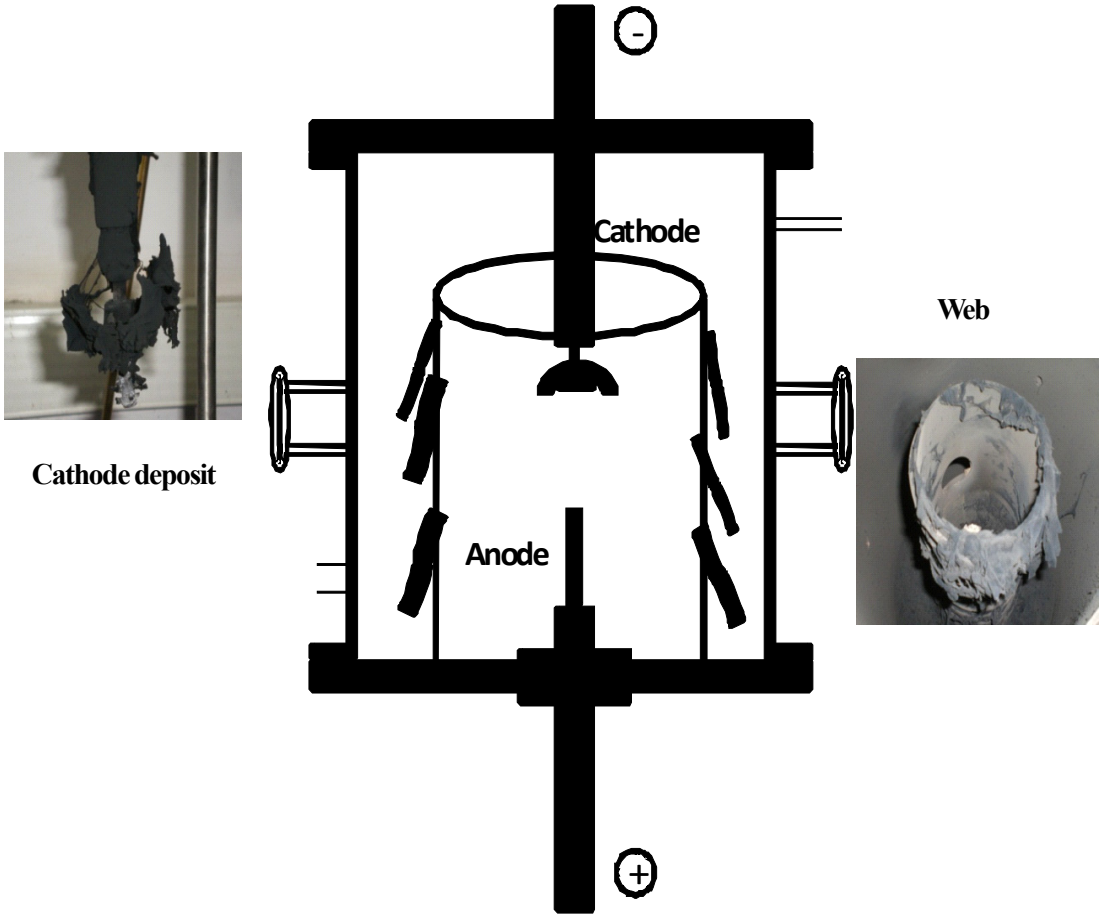

Figure 6.1: Schematic showing formation of SWNTs in the different regions of the arc-discharge chamber.

6.3.2 Synthesis of metallic SWNTs

The details of the method used by us to generate SWNTs by arc discharge are as follows. Arc discharge was carried out between the two graphite electrodes in an arc discharge chamber under a helium atmosphere at 600 mbar pressure using a DC power source with a current of ~100 A and a voltage of 38 V. The cathode was a pure graphite rod and the consumable anode was a composite graphite rod (6 mm diameter, 60 mm long) containing a mixture of Y_2O_3 (1 at.%) and Ni (4.2 at.%) catalyst. The discharge was maintained by continuously translating the anode to keep a constant distance (~3 mm) from the cathode. The composite graphite rod was consumed during the arcing process and the cob-web like structures deposited in the chamber contained SWNTs

(Figure 6.1). To prepare nearly pure metallic single-walled carbon nanotubes, the arc chamber was initially filled with helium (500 mbar), and helium bubbled through iron pentacarbonyl, $Fe(CO)_5$, was then passed through the chamber at a flow rate of 200 sccm until the pressure reached to 600 mbar. Arc-discharge experiments were carried out under the conditions mentioned earlier, with a continuous flow of the He+$Fe(CO)_5$ mixture, at different helium flow rates ranging from 100 to 400 sccm. Further increase in the flow rate of helium through $Fe(CO)_5$ did not favor nanotube formation. SWNTs were collected from the cathode region and from the web hanging at the sides of arc-discharge chamber as shown in the Figure 6.1. The samples collected from web and cathode region were separately subjected to purification by acid treatment followed by hydrogen treatment to remove metal and amorphous carbon impurities (*61*).

6.3.3 Synthesis of Y-junction SWNTs

Y-junction SWNTs are synthesized by striking an arc between the graphite rods in the arc discharge chamber under He atmosphere in presence of thiphene vapor. The graphite rods (anode 6mm dia. and 6 cm long, cathode 10 mm dia. and 4 cm long graphite rods) and filled with Y_2O_3 and Ni powder. The composite graphite rods were prepared by filling with Y_2O_3 & Ni powder ratio (Ni to Y) 4.1:1.1. The graphite rods were treated in H_2 atmosphere at 1100 ^oC for 15 hrs prior to arcing. He pressure of 450-550 torr was maintained in the chamber and dc at 30 V, 100 A was applied. During the arcing process, thiophene is passed with the flow of He gas and the electrode separation of ≈1 mm is kept to assure a sustained arc. Large quantities of web-like material were deposited at the chamber wall. The web comprises of SWNT bundles along with amorphous carbon and metal particles covered in graphene sheets. The samples collected from web and cathode region were separately subjected to purification by acid

treatment followed by hydrogen treatment to remove metal and amorphous carbon impurities (*61*).

6.3.4 Techniques used for characterization

Scanning electron microscopy

A field-emission scanning electron microscope (FESEM, FEI Nova-Nano SEM-600, Netherlands) was used to check the purity of the nanotubes.

Transmission electron microscopy

Transmission electron microscope (TEM) images of the nanotubes were obtained by taking a drop of nanotubes suspension in ethanol solution on the holey carbon-coated Cu grids. The grids were allowed to dry in the air and examined by using a JEOL (JEM3010) microscope operating with an accelerating voltage of 300 kV.

Optical absorption spectroscopy

Optical absorption spectra were recorded using a Perkin-Elmer Lambda 900 UV/VIS/NIR spectrophotometer (200-3300 nm). Nanotube samples were deposited on quartz plate for this purpose.

Raman Spectroscopy

Raman spectra were recorded with a LabRAM HR high-resolution Raman spectrometer (Horiba-Jobin Yvon) using a He−Ne laser (λ = 632.8 nm) and Ar laser (514 nm).

Themogravimetric analysis

Themogravimetric analyses (TGA) of the nanostructure were carried out using a Mettler Toledo Thermal Analyzer.

Electrical measurements:

I-V measurements were measured by two-point probe method between two gold electrodes having a probe separation of 20 μm using Keithley 236 multimeter. Temperature dependent resistivity measurements were carried out by the standard four-probe method using the resistivity option in the Physical Property Measurement System (PPMS), Quantum Design, USA.

6.4 Results and Discussion

6.4.1 Separation of SWNTs by molecular charge-transfer

We have investigated the interaction of SWNTs with **I** by varying the concentration of the latter and the time of interaction. For this purpose, we have taken pure SWNTs in a 5 mM or 10 mM solution of **I** in 5 ml water and sonicated the mixture at 50 °C for 3 h, followed by heating at 70 °C for 12 h (Figure 6.2). The resulting mixture was set aside for 24 h when a precipitate appeared at the bottom of the container. The precipitates as well as the solid extracted from the solution were examined by electronic absorption spectroscopy and Raman spectroscopy.

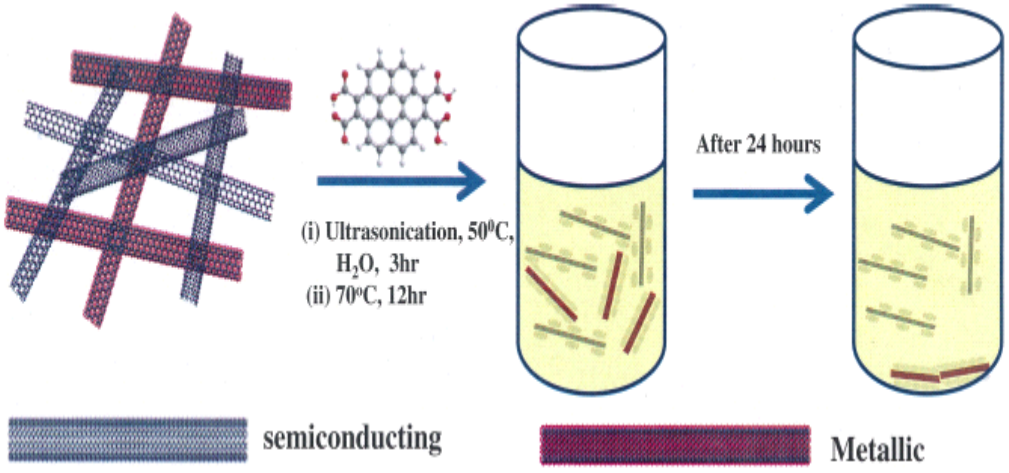

Figure 6.2: Schematic depicting the separation of SWNTs by **I**.

Pristine SWNTs show bands around 750 nm (M_{11}) corresponding to the metallic nanotubes and around 1040 nm (S_{22}) and 1880 nm (S_{11}) due to the semiconducting species which occurs because of Van-Hove singularities in the optical absorption spectra (Figure 6.3). SWNTs extracted from the solution exhibit only the S_{11} and S_{22}

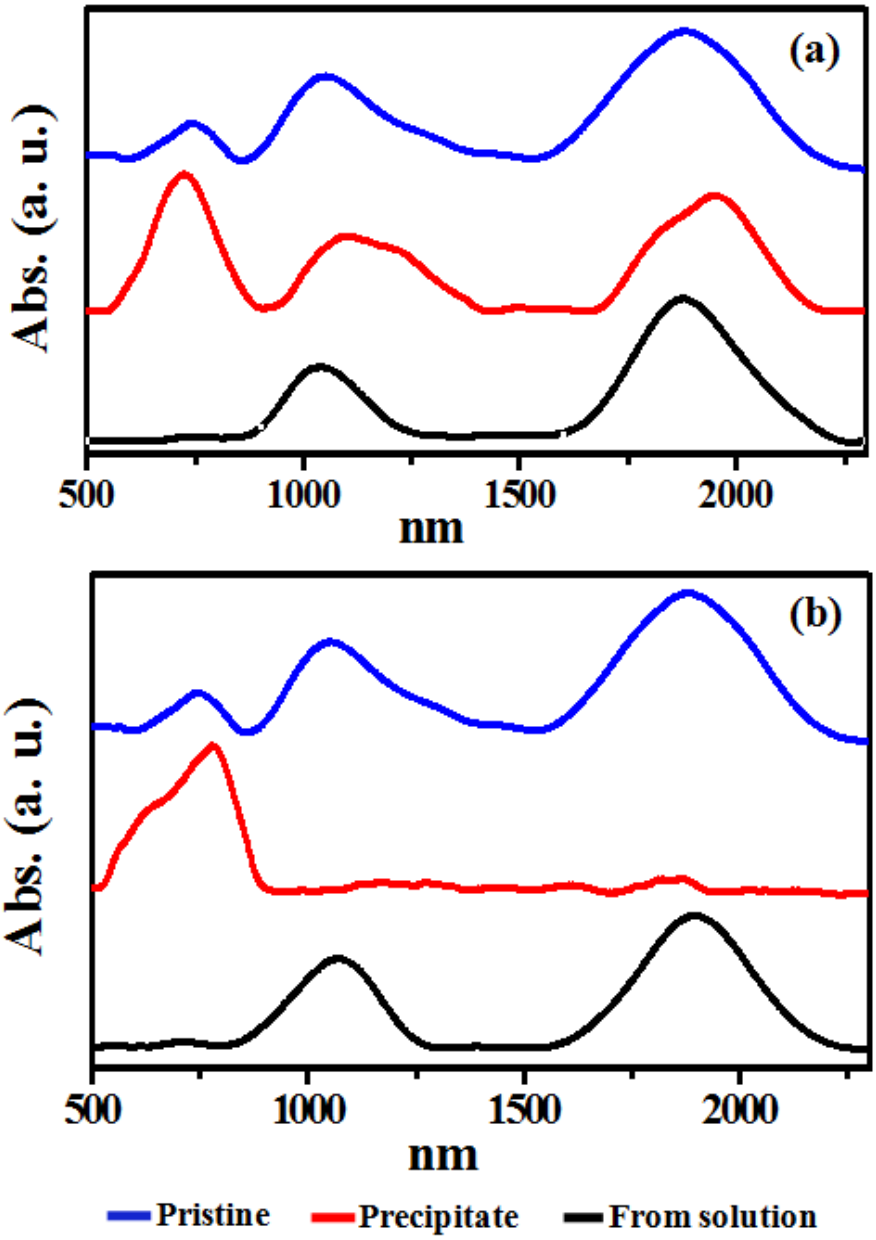

Figure 6.3: Optical absorption spectra of pristine SWNTs (blue), precipitate (red) and SWNTs from solution (black) obtained with (a) 5mM and (b) 10mM of **I**.

bands due to the semiconducting species as can be seen from Figure 6.3. SWNTs in the precipitate, however, exhibit bands due to both the metallic and semiconducting species when 5mM solution of I was used, but only the band due to the metallic species when 10 mM solution of I was used (compare Figures 6.3 (a) and (b)). Thus, optical absorption spectra clearly demonstrate the separation of metallic and semiconducting SWNTs on interaction with **I**.

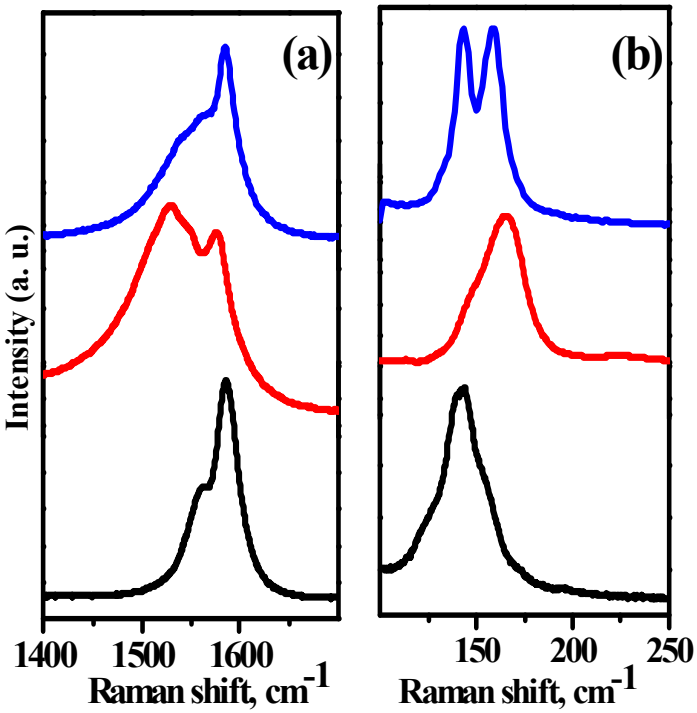

Figure 6.4: Raman (a) G-band and (b) radial breathing mode (RBM) of pristine SWNTs (blue), precipitate (red) and SWNTs from solution (black) with 10mM of **I.**

These results are supported by Raman spectra. SWNTs prepared by arc-discharge show Raman bands due to the radial breathing mode (RBM) in the Raman spectra in 100-200 cm^{-1} region and the G-band in the 1500-1600 cm^{-1} (G-band) region. The G-band of the semiconducting tubes consists of two features around 1570 cm^{-1} (radial) and 1590 cm^{-1} (longitudinal). The G-band of the metallic tubes shows bands around 1585 cm^{-1} (radial) and 1540 cm^{-1} (longitudinal), the latter broadened into a Breit-Wigner

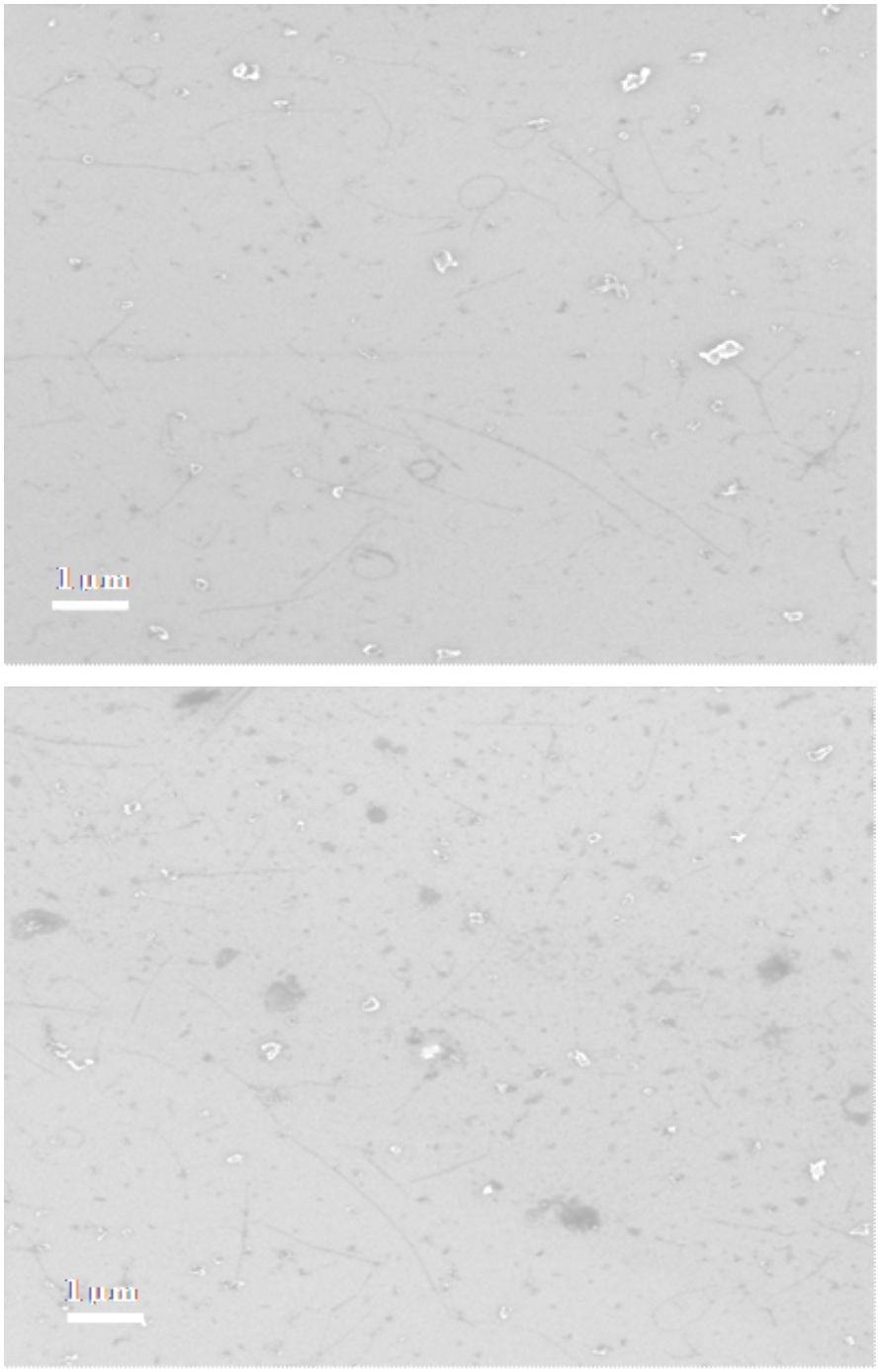

Figure 6.5: FESEM images showing unbundled single-walled carbon nanotubes.

Fano (BWF) line shape due to strong coupling in the density of states (*2, 62*). The 1540 cm^{-1} feature is generally used as a signature of metallic SWNTs. We have used 632 nm laser for Raman studies. The 632 nm excitation resonates roughly equal populations of both metallic and semiconducting tubes for the diameter range of the tubes used in this study (~1.2 to 1.8 nm), where as the 514 nm laser excites semiconducting nanotubes

exclusively (*36, 63*). SWNTs extracted from the 10 mM solution of **I** exhibit features of the G-band corresponding to the semiconducting species, where as the precipitate shows features of pure metallic species with the prominent feature around 1540 cm^{-1} (Figure 6.4 (a)). Pristine SWNTs show two RBM bands due to semiconducting and metallic species (Figure 6.4 (b)). SWNTs from the solution show only the bands due to the semiconducting ones and SWNTs in the precipitate correspond to the metallic species.

The method depends on the concentration of **I** and the time of interaction. The separation occurs due to molecular charge-transfer between **I** and SWNTs, and is accompanied by the debundling of the SWNTs as evidenced by electron microscope images (Figure 6.5). The separation process reported here involves sonication followed by the precipitation of metallic nanotubes. The solution contains semiconducting

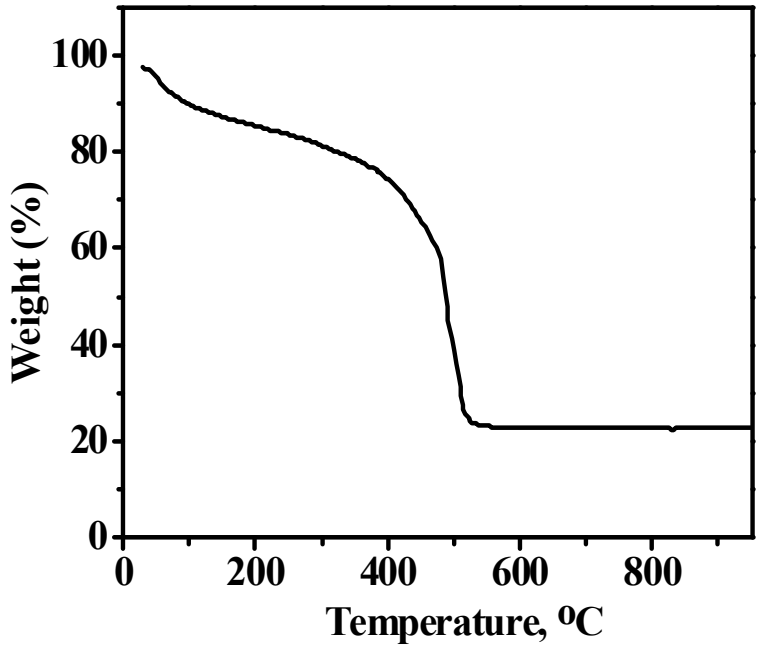

Figure 6.6: TGA of precipitate obtained after annealing under Ar.

nanotubes exclusively. The preferential precipitation of metallic nanotubes might be due to greater affinity of electron donating molecules to metallic ones in the mixture of

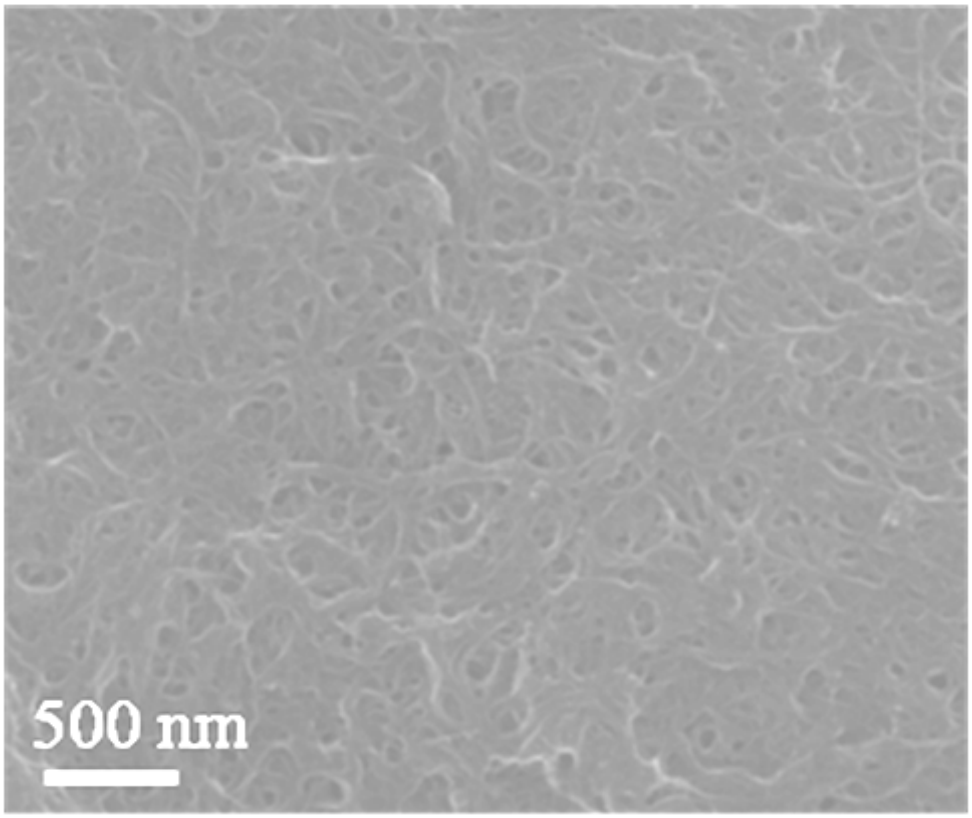

Figure 6.7: FESEM image of metallic SWNTs after washing with water to remove **I**.

SWNTs, which is confirmed by TGA. TGA analysis of the precipitate under argon atmosphere shows weight loss of 77 % in the temperature range of 30-530 ^{o}C and further increase in temperature does not result in additional weight loss (Figure 6.6). The weight loss corresponds to coronene molecules which are tethered with nanotubes. The residue after heating above 530 ^{o}C corresponds to the metallic SWNTs. **I** can be removed from metallic SWNTs by heating above 600 ^{o}C or by washing with water. Figure 6.7 shows the FESEM image of purified metallic SWNTs after removing **I**. The solubilization of semiconducting SWNTs in water can be attributed to the weak interaction with coronene salt **I**. This can be confirmed from the photoluminescence spectra of the solution obtained after the precipitation process (Figure 6.8). Coronene salt **I** shows intense blue fluorescence with emission maxima at 435 and 462 nm. The solution remained after precipitation containing semiconducting nanotubes and

coronene salt **I** shows an additional broad band around 575 nm in the PL spectra. This might be due to the weak interaction between the semiconducting SWNTs and coronene salt. Some of the semiconducting nanotubes were also precipitated after 48 hours. The use of coronene salt in excess of 10^{-2} M results in the formation of hydrogel with SWNTs.

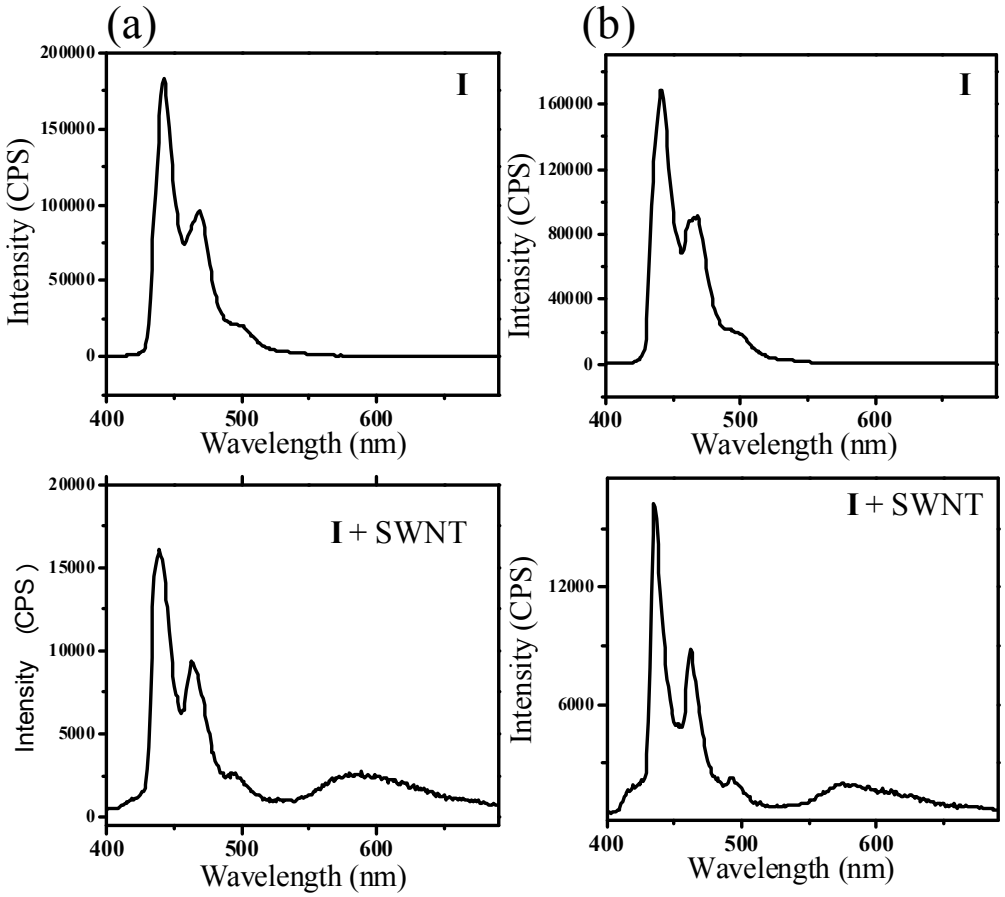

Figure 6.8: Photoluminescence spectra of I (coronene salt) and of I+SWNTs at two different concentrations of **I** (a) 5mM and (b) 10mM

We have compared the I-V characteristics of SWNTs (measured by the two-point probe method between two gold electrodes) from the solution and the precipitate and compared it with the pristine nanotubes. Pristine SWNTs show a nonlinear I-V curve while the metallic nanotubes show linear behavior with conductivities of 92.5 and 1538.5 mS/cm respectively at 300 K. The latter value is comparable to that in the literature (*64*). Semiconducting nanotubes exhibit a low conductivity of 53.5 mS/cm and

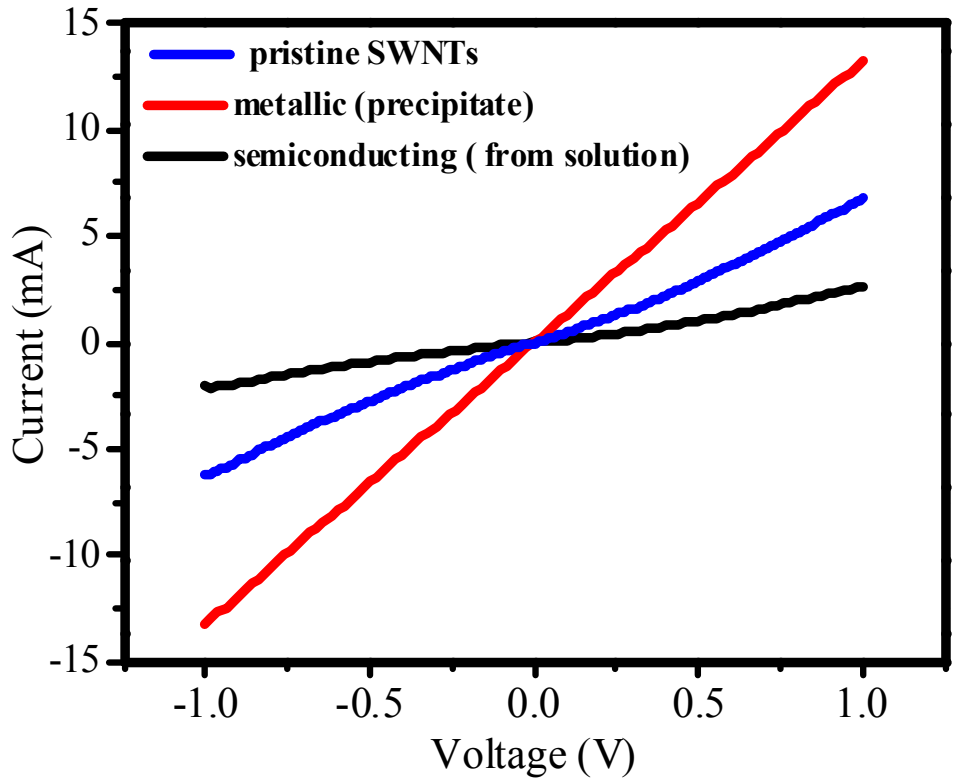

Figure 6.9: I-V measurements of pristine SWNTs (blue) as well as pure metallic (red) and semiconducting (black) nanotubes obtained by separation.

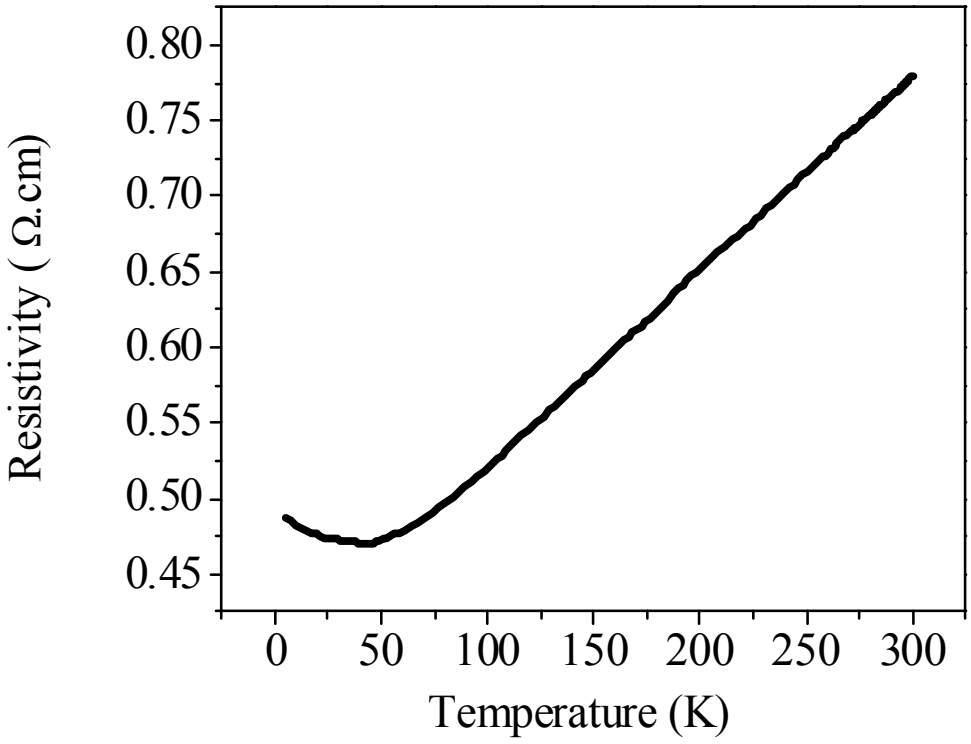

Figure 6.10: Resistivity of metallic SWNTs as a function of temperature.

a nonlinear I-V curve (Figure 6.9). These results are in accord with the spectroscopic data. To further confirm whether precipitate contains metallic nanotubes we have measured the resistivity of the samples by four probe measurement. For metallic nanotubes above 50 K resistivity increases linearly with temperature (Figure 6.10). These measurements clearly indicate metallic behavior at high temperatures with increasing resistivity approximately linearly with temperature. In addition to the high-temperature linear resistivity, measurement shows an upturn in the resistivity at low temperature. The observed dependence of this crossover on the sample morphology and quality suggests that disorder or other three-dimensional effects may actually control this low-temperature behavior. The high-temperature behavior is consistent with the predicted intrinsic metallic nature of the nanotubes (*65, 66*).

We believe that this method can be readily employed as a routine laboratory procedure.

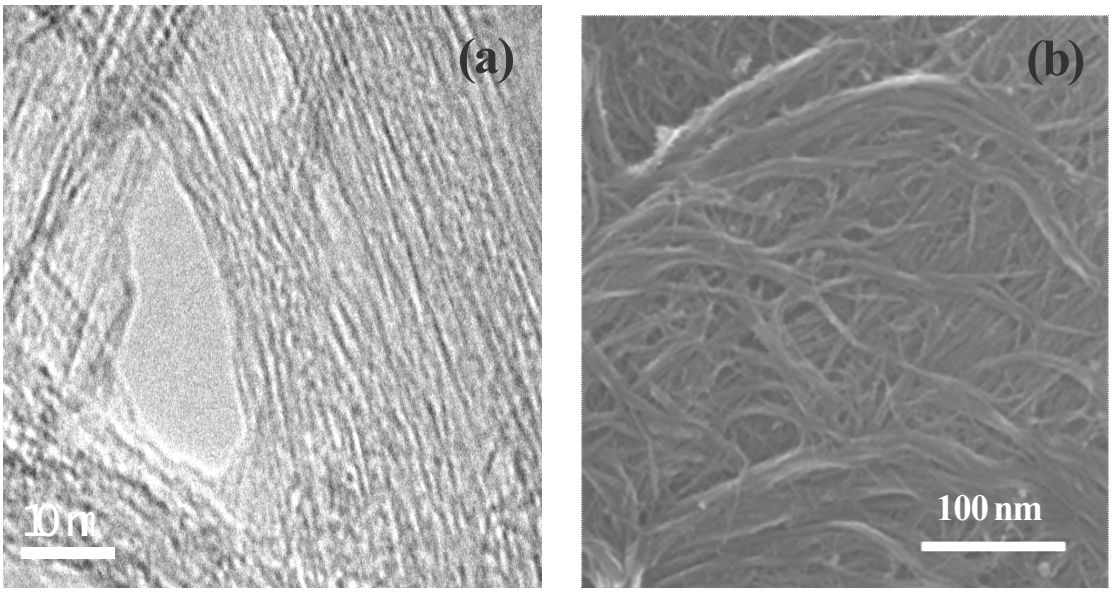

Figure 6.11: Typical (a) transmission electron microscopy and (b) field emission scanning electron microscopy images of metallic SWNTs after purification.

6.4.2 Synthesis of metallic SWNTs

We have studied the SWNTs obtained from the walls of the discharge chamber as well as from the cathode region (Figure 6.1) by optical absorption spectroscopy as well as Raman spectroscopy. These techniques specially electronic spectroscopy, being ideally suited to distinguish the metallic and semiconducting species. The spectra of the different nanotubes samples were recorded after purification (*61*). In Figure 6.11 we show typical TEM and FESEM image of SWNTs after purification.

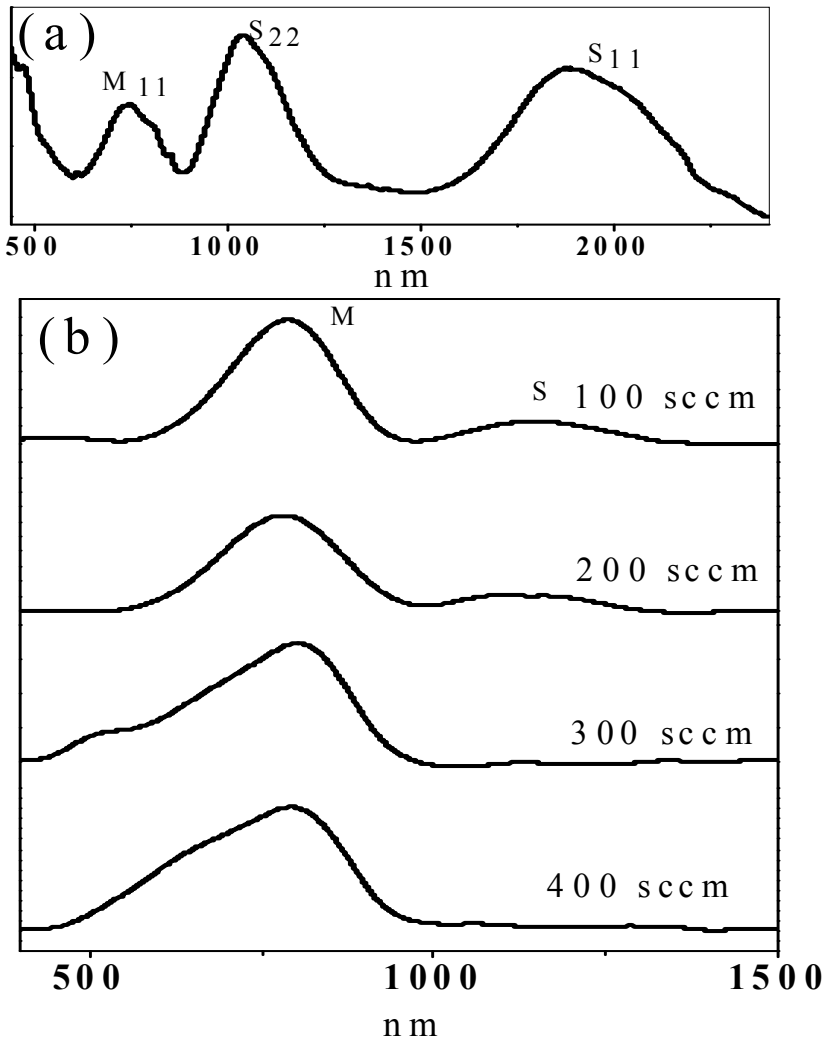

Figure 6.12: Optical absorption spectra of SWNTs samples (collected from the web region) (a) obtained with Ni+ Y_2O_3 catalyst alone and (b) with Ni+ Y_2O_3 in the presence of $Fe(CO)_5$.

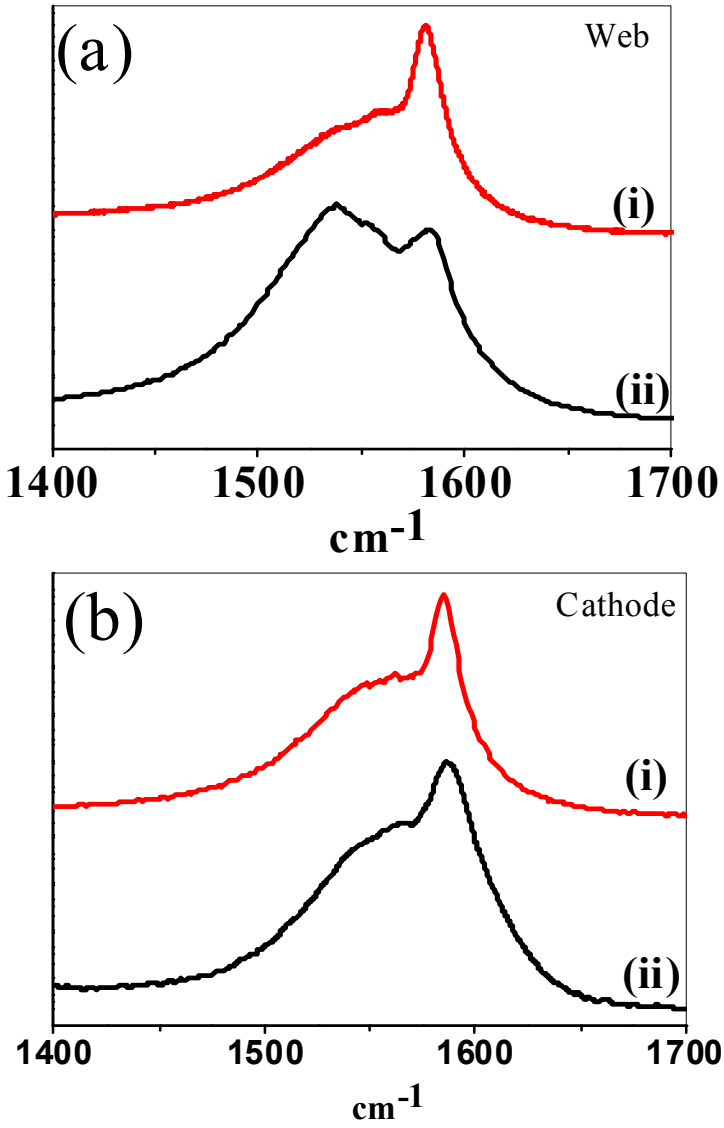

Figure 6.13: G-bands in the Raman spectra of SWNTs collected from (a) the web and (b) the cathode regions (i) with the catalyst Ni+ Y_2O_3 alone and (ii) with the Ni+ Y_2O_3 catalyst in the presence of $Fe(CO)_5$ vapor

In Figure 6.12, we show the background-subtracted optical absorption spectra of SWNTs samples prepared in the absence and presence of $Fe(CO)_5$. The sample prepared in the absence of $Fe(CO)_5$ shows three bands, a band centered around 750 nm corresponding to the metallic nanotubes (M_{11}) and the bands around 1040 nm (S_{22}) and 1880 nm (S_{11}) due to the semiconducting species as can be seen from Figure 6.12 (a). The optical absorption spectra from the samples prepared in the presence of $Fe(CO)_5$

mainly show the band due to metallic species (M_{11}) while the bands due to the semiconducting species nearly disappear as clearly seen from the Figure 6.12 (b). It may be noted that the presence of 750 nm band in the optical absorption spectra is taken as unequivocal evidence for the presence of metallic SWNTs (*63*). Furthermore, the intensity of the M_{11} band increases with the flow rate of $Fe(CO)_5$. From the integrated areas of the bands due to the metallic and semiconducting species, we estimate the relative percentage of the metallic species to be around 26 % and 94 % respectively in the absence and presence of $Fe(CO)_5$.

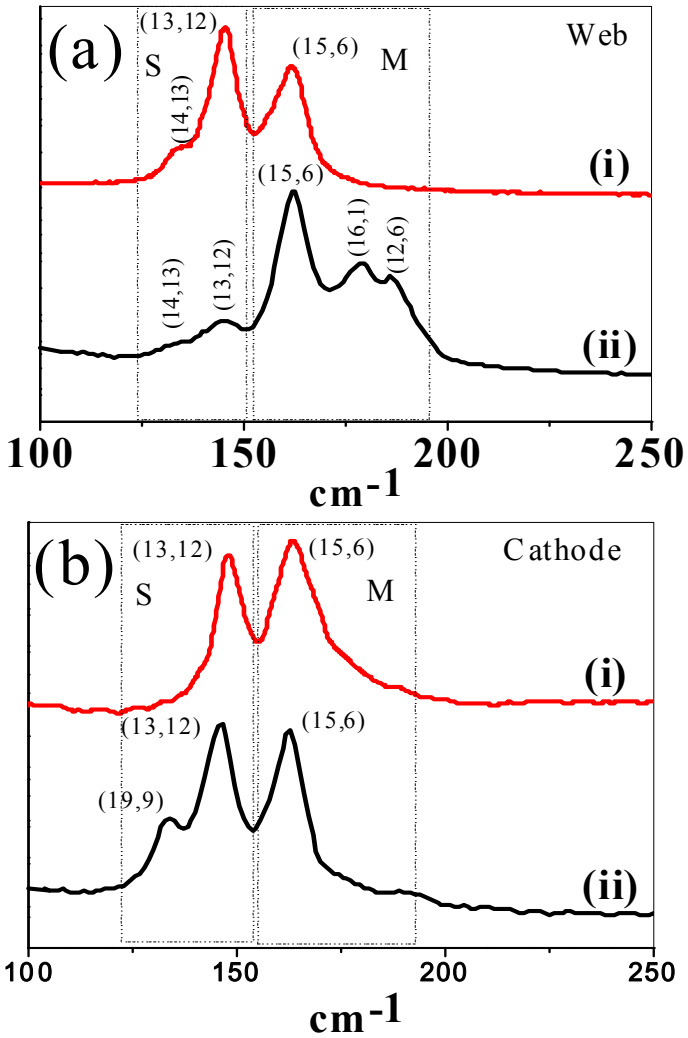

Figure 6.14: : RBM bands in the Raman spectra of SWNTs collected from (a) the web and (b) the athode (i) with the catalyst Ni+ Y_2O_3 alone and (ii) with the Ni+ Y_2O_3 catalyst in the presence of $Fe(CO)_5$ vapor.

In order to confirm that the SWNTs from the walls of the discharge chamber obtained in the presence of $Fe(CO)_5$ was primarily metallic, we carried out detailed Raman studies. SWNTs prepared by arc discharge exhibit bands due to the radial breathing mode (RBM) in the Raman spectra in 100-350 cm^{-1} region and the G-band in the 1500-1600 cm^{-1} (G-band) region (*67, 68*). The G band of the semiconducting tubes consists of two peaks at around 1570 cm^{-1} (radial) and at 1590 cm^{-1} (longitudinal). The G-band of the metallic tubes shows bands around 1585 cm^{-1} (radial) and at 1540 cm^{-1} (longitudinal), the latter broadened into a Breit-Wagner Fano (BWF) line shape caused by strong coupling in the density of states (*69, 70*). In Figure 6.13 we compare the Raman G-bands of SWNTs collected from the walls and the cathode regions in the absence and in the presence of $Fe(CO)_5$. The SWNTs collected from the cathode region show minor differences. This is not the case with SWNTs collected from the walls of arc chamber. The SWNTs prepared in the presence of $Fe(CO)_5$ show a marked increase in the metallic feature in the G-band. In fact, almost the entire band can be ascribed to the metallic species.

In Figure 6.14, we compare the RBM bands of SWNTs collected from web and cathode regions. The SWNTs prepared in the absence of $Fe(CO)_5$ show two RBM bands at 145 and 160 cm^{-1} when excited with 633 nm laser radiation. Based on the revised Kataura's plot, we assign the band at 145 cm^{-1} to the semiconducting species (S) and the band at 160 cm^{-1} to the metallic species (M) (*71*). Accordingly, excitation by a 514 nm laser exclusively showed only the band corresponding to the semiconducting species at 145 cm^{-1} (*72*). The sample prepared in presence of $Fe(CO)_5$ and collected from the web exhibits an enhanced intensity of the metallic RBM band at 160 cm^{-1} relative to the semiconducting band along with the evolution of two new bands at higher frequencies. The higher frequency bands which are absent in the Raman spectrum obtained with 514 nm laser excitation are attributed to the metallic nanotubes. The

samples collected from cathode regions do not show much variation in the RBM bands due to the presence of $Fe(CO)_5$.

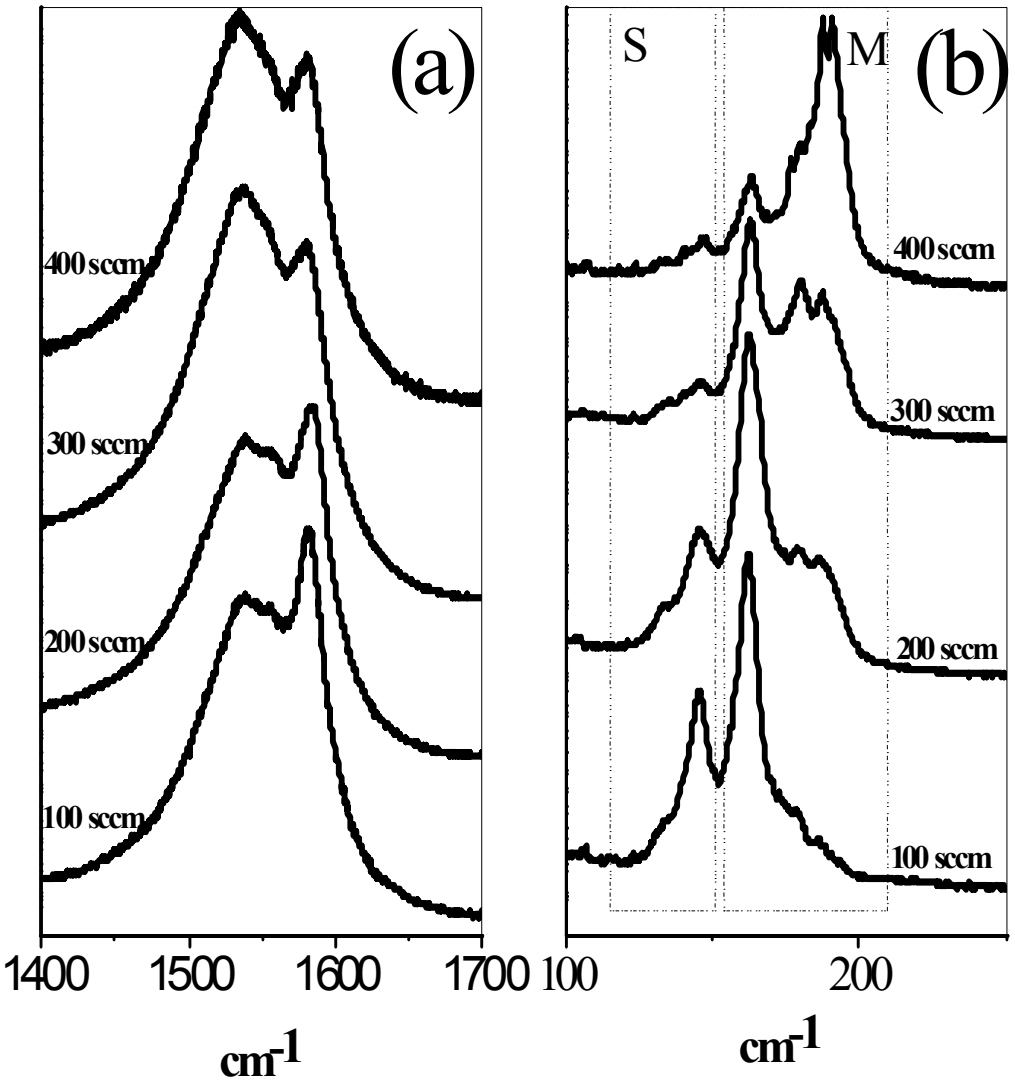

Figure 6.15: (a) G and (b) RBM bands in the Raman spectra of SWNTs (collected from the web) obtained at different flow rates of $Fe(CO)_5$.

In Figure 6.15 we show the variation of the G and RBM bands, of SWNTs (from web region) obtained at different flow rates of $Fe(CO)_5$. We readily see the increase in the metallic features with the increase in the flow rate. We have studied the different catalysts combination to elucidate the role of $Fe(CO)_5$ in the formation of metallic nanotubes. Table 6.1 gives the summary of various catalysts used. Only with the $Ni+Y_2O_3$ catalyst under optimal flow of $Fe(CO)_5$ metallic SWNTs are produced.

Table 6.1: SWNT formation with various catalysts in different atmospheres.

Catalyst			With $Fe(CO)_5$		With CO	
	Cathode	Web	Cathode	Web	Cathode	web
$Ni+Y_2O_3$	Metallic +Semi	Metallic +Semi	Metallic +Semi	**Metallic**	Metallic +Semi	Metallic +Semi
Ni	Not formed	Not formed	Not formed	Not formed	Not formed	Not formed
Fe	Not formed	Not formed	Not formed	Not formed	Not formed	Not formed
Ni + Fe *	Not formed	Metallic +Semi	Not formed	Metallic +Semi	Not formed	Metallic +Semi

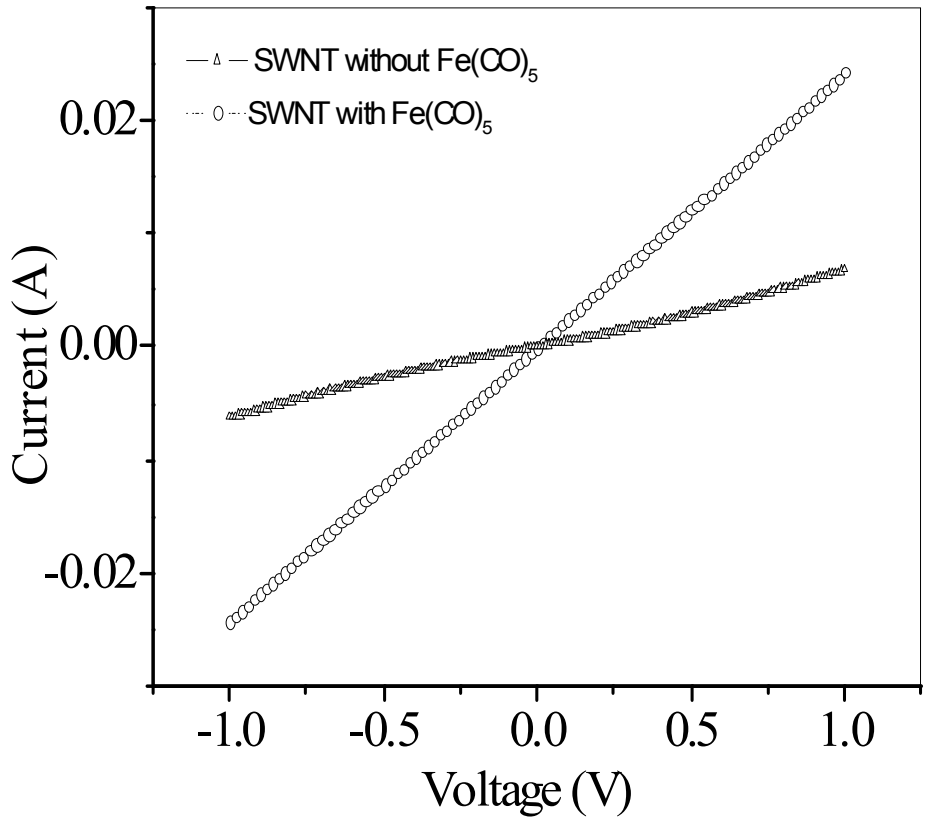

Figure 6.16: I-V measurements of SWNTs with and without $Fe(CO)_5$.

We have compared the I-V characteristics of metallic SWNTs with those of mixture of nanotubes. Pristine SWNTs show a nonlinear I-V curve while the metallic nanotubes show linear behavior with conductivities of 92.5 and 1720.1 mS/cm respectively at 300 K. The latter value is comparable to that in the literature (*64*).

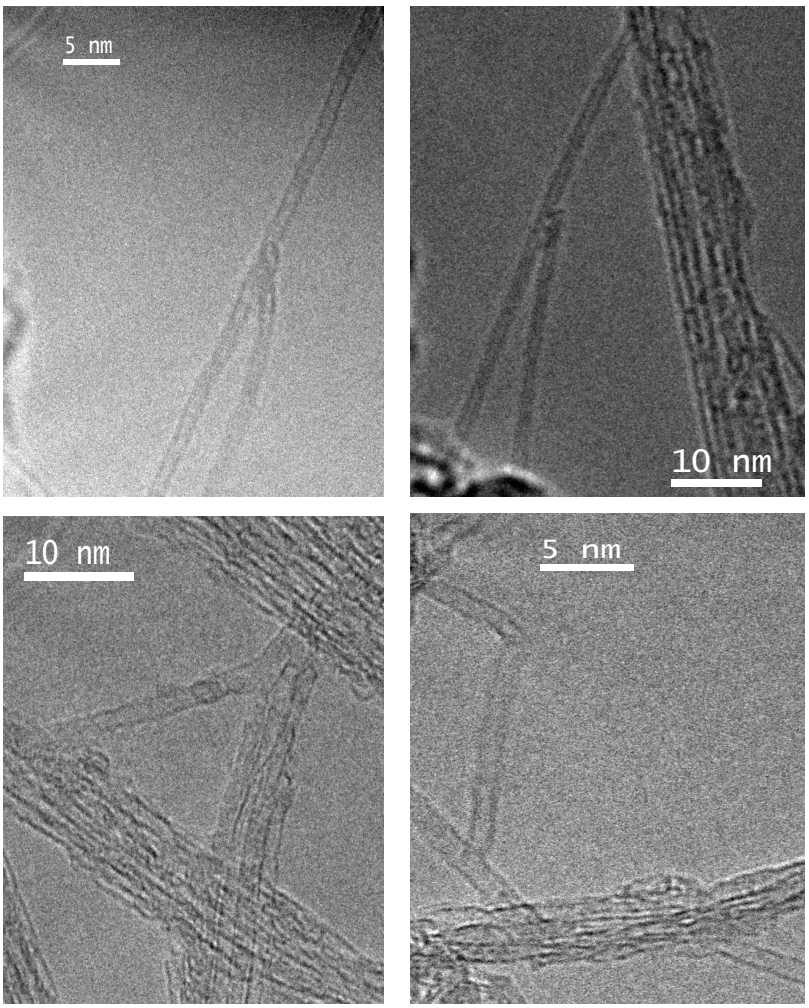

Figure 6.17: TEM images of Y-junction single-walled carbon nanotubes.

6.4.3 Synthesis of Y-junction SWNTs

The Y-junction SWNTs are obtained by arc-evaporation of graphite rods (filled Ni and Y_2O_3) in thiophene and He atmosphere (660 torr). The SWNTs were purified by acid and hydrogen treatment. We have characterized the purified nanotubes by TEM, AFM and Raman spectroscopy. Figure 6.17 shows TEM images of Y-junction SWNTs obtained in presence of thiophene. The angle enclosed between the upper arms of the *Y*-

junction nanotube is less than 60° in most cases, but occationally we have observed Y-junctions with 90^{o} angle between the upper arms. This is in contrast to the multi-walled nanotubes where they have often observed 90^{o} angles between the upper arms.

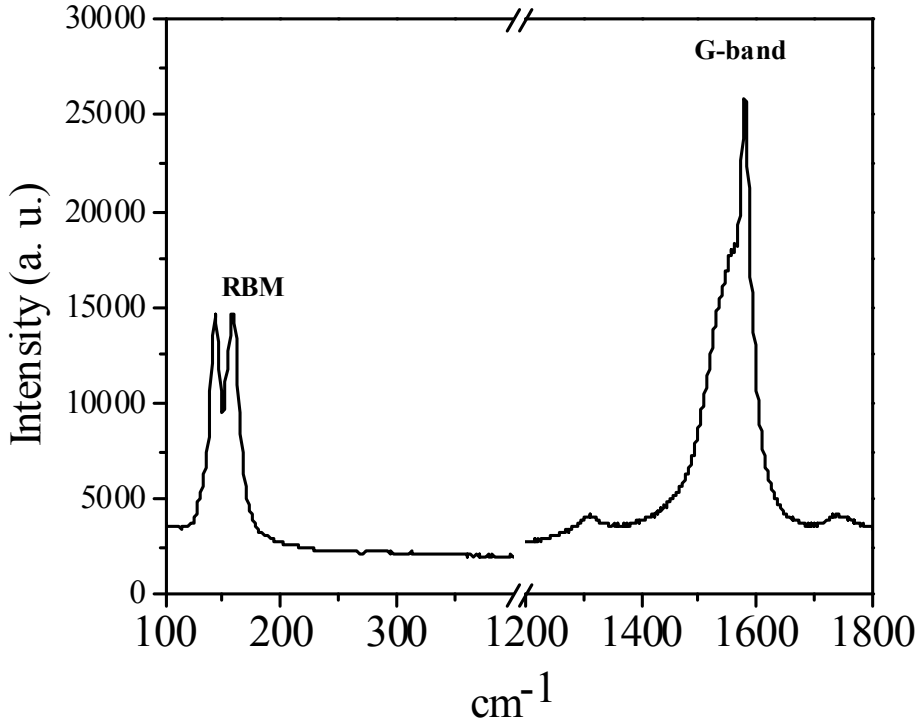

Figure 6.18: Typical Raman spectra of Y-junction single-walled carbon nanotubes.

The TEM images show that the diameter of arms in Y-junction SWNTs varies between 1.6 nm and 2 nm. Raman spectra of the Y-junction carbon nanotubes is given in Figure 6.18. The Raman signatures are similar in both in the presence and absence of thiophene. There are various reports in the literature on the synthesis of Y-junction carbon nanotubes. Most of them are directed towards the synthesis of multi-walled carbon nanotubes. Junction SWNTs are occasionally observed during the various conventional synthetic process. There is only one method in the literature on the synthesis of multiterminal SWNTs by thermal CVD process using Mo or Zr-doped Fe nanoparticles supported by aluminum oxide particles. Here junction growth is attributed to the excess nucleation by Mo or Zr. The mechanism of junction formation under thiophene is different from the above method. The presence of sulfur during the

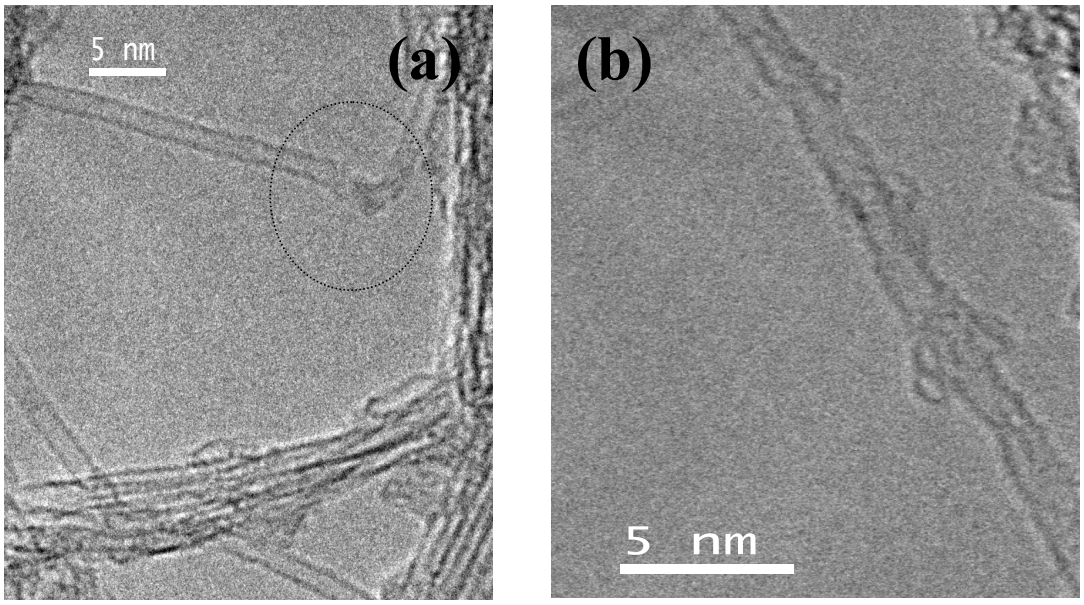

Figure 6.19: TEM images of intramolecular junctions in single-walled carbon nanotubes.

synthesis plays a key catalytic role in the branching mechanism. We did not observe the junction formation in the absence of sulfur. Recent theoretical calculation suggest that sulfur energetically favors pentagonal rings and heptagonal rings over hexagons, thereby introducing negative curvatures (heptagons, branch opening) or positive curvatures (pentagons, closing its tip) (*73, 74*). Their results suggest that sulfur is likely to induce the appearance of a bud along the structure and to promote the formation of junctions. Figure 6.19 shows intramoleuclar junctions in SWNTs. From the TEM images we can clearly show bud like protrusion on the walls of the nanotubes (Figure 6.19(b)). Accumulation of sulfur atoms on a cone wall then promotes the formation of a bump, which induces deformations on the opposite side of the growing tubule. The bump formation is supported by the fact that sulfur tends to promote heptagonal and pentagonal rings in the sp^2 carbon network. In Figure 6.20 we show the AFM image of the Y-junction SWNTs. Passing of excess thiophene in the arc chamber results in the lower yield. This might be due to the poisoning of catalyst particles by sulfur. At very higher concentration of thiophene we observed only carbon coated catalyst particles and MWNTs.

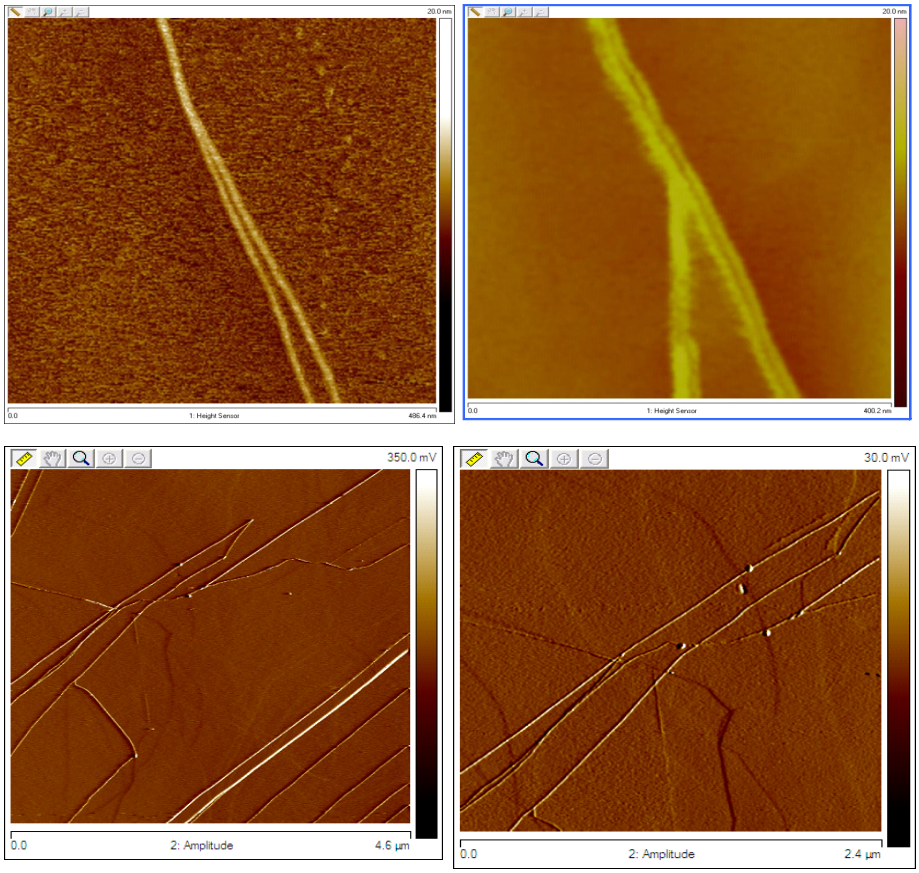

Figure 6.19: AFM images of Y-junction SWNTs.

6.5 Conclusions

we have been able to separate semiconducting and metallic SWNTs from the mixture in the as-prepared sample by employing the interaction with **I**. The method depends on the concentration of **I** and the time of interaction. The separation occurs due to molecular charge-transfer between **I** and SWNTs, and is accompanied by the debundling of the SWNTs as evidenced by electron microscope images. We believe that this method can be readily employed as a routine laboratory procedure.

A new method of obtaining high enrichment of the metallic SWNTs has been discovered. The method involves the arc evaporation of graphite electrodes containing the Ni+Y_2O_3 catalyst in the presence of $Fe(CO)_5$ vapor. Although we cannot comment on the mechanism of formation of metallic nanotubes in the presence of $Fe(CO)_5$ vapor, the method itself is new and simple. It can be of value in the practical use of SWNTs.

Y-junction SWNTs could be prepared by carrying out arc discharge of graphite over a Ni–Y_2O_3 catalyst in an atmosphere of thiophene and helium.

REFERENCES

1. C. N. R. Rao, A. Govindaraj, *Nanotubes and Nanowires: RSC Nanoscience & Nanotechnology series*. (Royal Society of Chemistry, Cambridge, 2005).
2. R. Saito, G. Dresselhaus, M. S. Dresselhaus, *Physical Properties of Carbon Nanotubes*. (Imperial College Press, London, 1998).
3. S. Iijima, *Nature* **354**, 56 (1991).
4. R. E. Smalley *et al.*, *J. Am. Chem. Soc.* **128**, 15824 (2006).
5. S. Chakrabarti, H. Kume, L. Pan, T. Nagasaka, Y. Nakayama, *J. Phys. Chem. C* **111**, 1929 (2007).
6. M. Keidar *et al.*, *App. Phys. Lett.* **92**, 043129 (2008).
7. J. Lu, D. Yuan, J. Liu, W. Leng, T. E. Kopley, *Nano Lett.* **8**, 3325 (2008).
8. C. L. Pint *et al.*, *Nano Lett.* **8**, 1879 (2008).
9. L. Song *et al.*, *Adv. Mater.* **18**, 1817 (2006).
10. S. Chakrabarti, T. Nagasaka, Y. Yoshikawa, L. Pan, Y. Nakayama, *Jpn. J. Appl. Phys.* **45**, L720 (2006).
11. Y.-H. Li *et al.*, *Small* **2**, 1026 (2006).
12. L. Qu, F. Du, L. Dai, *Nano Lett.* **8**, 2682 (2008).
13. D. H. Lee, W. J. Lee, S. O. Kim, *Chem. Mater.* **21**, 1368 (2009).
14. C. Kocabas, M. Shim, J. A. Rogers, *J. Am. Chem. Soc.* **128**, 4540 (2006).
15. N. Yoshihara *et al.*, *J. Phys. Chem. C* **113**, 8030 (2009).
16. R. M. Tromp, A. Afzali, M. Freitag, D. B. Mitzi, Z. Chen, *Nano Lett.* **8**, 469 (2008).
17. S. Niyogi, C. G. Densmore, S. K. Doorn, *J. Am. Chem. Soc.* **131**, 1144 (2008).
18. M. Lee *et al.*, *Nat. Nanotechnol.* **1**, 66 (2006).
19. P. G. Collins, M. S. Arnold, P. Avouris, *Science* **292**, 706 (2001).
20. S. G. Rao, L. Huang, W. Setyawan, S. Hong, *Nature* **425**, 36 (2003).
21. J. A. Misewich *et al.*, *Science* **300**, 783 (2003).
22. M. S. Arnold, A. A. Green, J. F. Hulvat, S. I. Stupp, M. C. Hersam, *Nat Nanotechnol.* **1**, 60 (2006).
23. K. Yanagi, T. Iitsuka, S. Fujii, H. Kataura, *J. Phys. Chem. C* **112**, 18889 (2008).
24. R. Krupke, F. Hennrich, H. v. Lohneysen, M. M. Kappes, *Science* **301**, 344 (2003).
25. T. Tanaka *et al.*, *Nano Lett.* **9**, 1497 (2009).

26. D. Chattopadhyay, I. Galeska, F. Papadimitrakopoulos, *J. Am. Chem. Soc.* **125**, 3370 (2003).
27. S.-Y. Ju, M. Utz, F. Papadimitrakopoulos, *J. Am. Chem. Soc.* **131**, 6775 (2009).
28. Y. Maeda *et al.*, *J. Am. Chem. Soc.* **128**, 12239 (2006).
29. Z. Chen *et al.*, *Nano Lett.* **3**, 1245 (2003).
30. H. Li *et al.*, *J. Am. Chem. Soc.* **126**, 1014 (2004).
31. M. S. Strano *et al.*, *Science* **301**, 1519 (2003).
32. W.-J. Kim, M. L. Usrey, M. S. Strano, *Chem. Mater.* **19**, 1571 (2007).
33. W.-J. Kim, N. Nair, C. Y. Lee, M. S. Strano, *J. Phys. Chem. C* **112**, 7326 (2008).
34. V. Georgakilas *et al.*, *J. Am. Chem. Soc.* **124**, 760 (2002).
35. C. Menard-Moyon, N. Izard, E. Doris, C. Mioskowski, *J. Am. Chem. Soc.* **128**, 6552 (2006).
36. M. Zheng *et al.*, *Science* **302**, 1545 (2003).
37. S. Ghosh, C. Rao, *Nano Research* **2**, 183 (2009).
38. S. Bandow *et al.*, *Phys. Rev. Lett.* **80**, 3779 (1998).
39. B. Wang *et al.*, *J. Phys. Chem. C* **111**, 14612 (2007).
40. B. Wang *et al.*, *J. Am. Chem. Soc.* **129**, 9014 (2007).
41. S. B. Sinnott *et al.*, *Chem. Phys. Lett.* **315**, 25 (1999).
42. S. M. Bachilo *et al.*, *J. Am. Chem. Soc.* **125**, 11186 (2003).
43. Y. Li *et al.*, *Nano Lett.* **4**, 317 (2004).
44. L. Ding *et al.*, *Nano Lett.* **9**, 800 (2009).
45. H. Zhang *et al.*, *Adv. Mater.* **21**, 813 (2009).
46. D. H. Shin *et al.*, *Nano Lett.* **8**, 4380 (2008).
47. Y. Wang *et al.*, *Small* **3**, 1486 (2007).
48. A. N. Andriotis, M. Menon, D. Srivastava, L. Chernozatonskii, *Phys. Rev. Lett.* **87**, 066802 (2001).
49. Z. Yao, H. W. C. Postma, L. Balents, C. Dekker, *Nature* **402**, 273 (1999).
50. Y. Yao *et al.*, *Nat. Mater.* **6**, 283 (2007).
51. C. Zhou, J. Kong, E. Yenilmez, H. Dai, *Science* **290**, 1552 (2000).
52. P. R. Bandaru, C. Daraio, S. Jin, A. M. Rao, *Nat. Mater.* **4**, 663 (2005).
53. J. Li, C. Papadopoulos, J. Xu, *Nature* **402**, 253 (1999).
54. B. C. Satishkumar, P. J. Thomas, A. Govindaraj, C. N. R. Rao, *App. Phys. Lett.* **77**, 2530 (2000).

55. F. L. Deepak, A. Govindaraj, C. N. R. Rao, *Chem. Phys. Lett.* **345**, 5 (2001).
56. J. M. Romo-Herrera *et al.*, *Angew. Chem., Int. Ed.* **47**, 2948 (2008).
57. M. Terrones *et al.*, *Phys. Rev. Lett.* **89**, 075505 (2002).
58. D.-H. Kim, J. Huang, H.-K. Shin, S. Roy, W. Choi, *Nano Lett.* **6**, 2821 (2006).
59. N. Varghese, A. Ghosh, R. Voggu, S. Ghosh, C. N. R. Rao, *J. Phys. Chem. C* **113**, 16855 (2009).
60. C. Journet *et al.*, *Nature* **388**, 756 (1997).
61. S. R. C. Vivekchand, A. Govindaraj, M. M. Seikh, C. N. R. Rao, *J. Phys. Chem. B* **108**, 6935 (2004).
62. M. S. Dresselhaus, G. Dresselhaus, A. Jorio, *J. Phys. Chem. C* **111**, 17887 (2007).
63. H. Kataura *et al.*, *Synt. metals* **103**, 2555 (1999).
64. Y. Maeda *et al.*, *J. Am. Chem. Soc.* **127**, 10287 (2005).
65. C. L. Kane, et al., *Europhysics Lett.* **41**, 683 (1998).
66. J. E. Fischer *et al.*, *Phys. Rev. B* **55**, R4921 (1997).
67. M. S. Dresselhaus *et al.*, *Acc. Chem. Res.* **35**, 1070 (2002).
68. A. Jorio *et al.*, *Phys. Rev. Lett.* **86**, 1118 (2001).
69. S. D. M. Brown *et al.*, *Phys. Rev. B* **63**, 155414 (2001).
70. A. Jorio *et al.*, *Phys. Rev. B* **65**, 155412 (2002).
71. M. S. Strano, *J. Am. Chem. Soc.* **125**, 16148 (2003).
72. M. S. Dresselhaus, P. C. Eklund, *Adv. Phys.* **49**, 705 (2000).
73. J. M. Romo-Herrera *et al.*, *Angew. Chem., Int. Ed.* **47**, 2948 (2008).
74. J. M. Romo-Herrera *et al.*, *Adv. Funct. Mater.* **19**, 1193 (2009).

CHAPTER 7

Sensitivity of the Electronic Structure of Graphene to Molecular Charge Transfer

Summary*

Graphene is a fascinating two-dimensional nanomaterial with unique electronic structure and properties. The Fermi energy can be shifted by doping due to stiffening or softening of phonons and other effects which modify the phonon dispersion by changing the carrier concentration and mobility. Effects of interaction of few-layer graphene with electron-donor (anisole, aniline and TTF) and -acceptor (chlorobenzene, nitrobenzene, TCNE) molecules have been investigated by employing Raman spectroscopy and the results compared with those of electrochemical doping. The G-band softens progressively with the increasing concentration of aniline and tetrathiafulvalene (TTF) which are electron-donors, while the band stiffens with increasing concentration of nitrobenzene and tetracyanoethylene (TCNE) which are electron-acceptor molecules. Both electron-donor and –acceptor molecules broaden the G-band. The 2D-band position is also affected by interaction with electron-donors and -acceptors. The intensity of the 2D-band decreases markedly with the concentration of either. The ratio of intensities of the 2D- and G- bands decreases with increase in electron-donors and -acceptors concentrations. The electrical resistivity of graphene varies in opposite directions on interaction with electron-donors and -acceptors. All these effects occur due to molecular charge-transfer, as evidenced by the observation of

Papers based on these studies have appeared in Chemical Communications (2008), Journal of Physics: Condened Matter (Fast Track Communication) (2008) and Journal of Physical Chemistry Letters (perspective) (2010)

charge-transfer bands in the electronic absorption spectra. The present study, demonstrates how the electronic structure and phonons of graphene are markedly affected by interaction with electron-donor and –acceptor molecules. It is significant that we observe such marked effects due to molecular charge-transfer even with multi-layered graphene of 3-4 layers.

7.1 Introduction

Graphene, the mother of all graphitic materials, has emerged to become an exciting two-dimensional material with wondrous properties (*1-4*). Some of the significant properties include ballistic electron transport, anomalous integer quantum Hall effect at room temperature and fractional quantum Hall effect at low temperatures and ability to sustain very high current densities. Atomic and electronic structures of graphene have been investigated by employing a variety of microscopic, spectroscopic and other techniques. Direct imaging of individual carbon atoms in single layer graphene by aberration-corrected transmission electron microscopy has shown the formation and annealing of Stone-Wales defects (*5*). Studies of graphene are not limited to one-atom thick single-layer graphene alone but also include bi- and few-layer (< 10 layers) graphenes. As a 2D crystal, graphene was found to exhibit high crystal quality (*6-8*) in which charge carriers can travel thousands of interatomic distances without being scattered (*9-11*). In particular, due to its special honeycomb structure, the band structure of graphene exhibits two intersecting bands at two inequivalent K points in the reciprocal space, and its low energy excitations are massless Dirac Fermions near these K points because of the linear (photon-like) energy momentum dispersion relationship. This results in very high electron mobility in graphene, which can be further improved significantly, even up to $\approx 10^5$ $cm^2/V \cdot s$. Electron or hole transport in field-effect devices

based on graphene can be controlled by an external electric field. Moreover, Park (*12*) demonstrated theoretically that the chiral massless Dirac Fermions of graphene propagate anisotropically in a periodic potential, which suggests the possibility of building graphene based electronic circuits from appropriately engineered periodic surface potential patterns, without the need for cutting or etching. Graphene-based devices can be expected to have many advantages over silicon-based devices.

However, precise control of the carrier type and concentration in graphene is not easy, especially for p-type. Up to now, most of the graphene samples were either deposited on a SiO_2 surface or grown on a SiC surface, and these epitaxial graphenes are usually electron doped by the substrate (*13*). Alkali metal atoms can be deposited on graphene to selectively control the n-type carrier concentration in the graphene layers. However, distribution of the metal atoms on the graphene surface is usually inhomogeneous, and the resulting charged impurities cause significant reduction of the carrier mobility (*14*). The single, open-shell NO_2 molecule is found to be a strong acceptor, whereas its equilibrium gaseous state N_2O_4 acts as a weak dopant and does not result in any significant doping effect (*15*). Boron or nitrogen substitutional doping is also not reliable and always induces defects that destroy the promising electronic property of graphene. Thus, it is desirable and crucial to develop new methods to precisely control the carrier type and concentration in graphene for further development of graphene-based nanoelectronics. In addition, pristine graphene is a zero-gap semiconductor, and its Fermi level exactly crosses the Dirac point. For practical application, an energy gap is essential.

Raman spectroscopy has emerged as an effective probe to characterize graphene samples in terms of the number of layers and their quality. Single-layer graphene shows the well-known G-band characteristic of the sp^2 carbon network around 1580 cm^{-1}. The D band around 1350 cm^{-1} and D' band around 1620 cm^{-1} are both defect-induced. The

2D band at ~ 2680 cm^{-1} differs in single and few-layer graphene and can be understood on the basis of the double resonance Raman process involving different electronic dispersions (*16*). The 2D band can be employed to determine the number of layers in few-layer graphene. By combining Raman experiments with *in-situ* transport measurements of graphene in field-effect transistor geometry, it has been shown that the G-modes of single and bi -layer graphenes blue shift on doping with electrons as well as holes (*17, 18*). On the other hand, the 2D band blue-shifts on hole doping whereas it red shifts on doping with electrons. The relative intensity of the 2D band is quite sensitive to doping. Theoretical calculations based on time-dependent perturbation theory have been employed to explain the observed shifts of the G-band. Comparison between theory and experiment, however, is not entirely satisfactory at high doping levels (> $1x10^{13}/cm^2$) and the disagreement is greater for the 2D band. In the case of bilayer graphene (*18*), the blue-shift of the G-band with doping has contributions from phonon-induced inter-band and intra-band electronic transitions, thereby giving an experimental measure of the overlap integral between A and B atoms in the two layers. Furthermore, the in-plane vibration in bilayer graphene splits into a symmetric Raman active mode (E_g) and an anti-symmetric infrared active mode (E_u). Doping dependence of these modes has been examined by Raman scattering (*19*) and infrared reflectivity measurements (*20*). The latter show a drastic enhancement of intensity and a softening of the mode as a function of doping, along with a Fano-like asymmetric line shape due to a strong coupling of the E_u mode to inter-band transitions.

Graphene is a nearly semimetal membrane, whose extreme physical strength (*21*) and high electron mobility at room temperature result from extensive electron conjugation and delocalization. Charge transfer to and from adsorbed species can shift (*22, 23*) the graphene Fermi level by a large fraction of an electron volt. Such adsorption-induced chemical doping adjusts the Fermi level without introducing

substitutional impurities, or basal plane reactions, that interrupt the conjugated network. Adsorption induced chemical doping may well become an important aspect of future graphene technologies. In graphenes consisting of only a few layers, chemical doping can result from both surface adsorption and intercalation between layers.

Organic molecules containing aromatic π systems can be used to solubilize and modify the electronic structure of graphene. Charge-transfer with coronene tetracarboxylate (CT) has been exploited recently to solubilize graphene sheets (*24*). It was shown that the CT molecules help to exfoliate few-layer graphene and selectively solubilize single- and double-layer graphenes. Graphene quenches the fluorescence of aromatic molecules, probably due to the electron transfer, a feature of possible use in photovoltaics. Charge-transfer from fluorescent molecules to graphene has been utilized in visualization of graphene sheets by fluorescence microscopy (*25*) and in the use of graphene as a substrate for resonance Raman spectroscopy (*26*).

This chapter describes our efforts towards understanding the effect of adsorbing various electron-donor and –acceptor molecules on graphene. We report the scope of the present investigation in the next section.

7.2 Scope of the Present Investigations

The extremely high mobility of electrical carriers in graphene makes it an ideal candidate for next-generation nanoelectronics. However, lacking a band gap, graphene as a semimetal has been limited from some direct applications in electronics such as a channel material for field-effect transistors. Therefore, opening and tuning the bandgap of graphene, a crucial step to the wider device applications of graphene electronics, has attracted great scientific interest. To date, many methods have been developed to open the band gap of graphene, including hydrogenation (*27*), electrically gated bilayer

graphene (*28-34*), Stone–Wales defects (*35*), graphene-substrate interaction (*13, 36*) and absorption of molecules (*37*).

Charge-transfer between electron–donor and –acceptor molecules is a widely studied subject of great chemical interest. Some of the charge-transfer compounds in solid state exhibit novel electronic properties. We considered it is important to investigate the effects of doping graphene through molecular charge-transfer by the interaction of graphene with electron-donor and -acceptor molecules and compare the results from electrochemical doping. For this purpose, we have prepared graphene samples by the exfoliation of the graphitic oxide (*38, 39*). First we have studied the interaction of monosubstituted benzenes such as nitrobenzene, chlorobenzene, anisole and aniline by employing Raman spectroscopy. Raman spectroscopy provides the most useful signature for examining the changes brought about in the electronic structure of graphene. Interestingly the results have been correlated with Hammett substituent constant.

Encouraged by the results on monosubsituted benzenes we studied the interaction of graphene with tetrathiafulvalene (TTF) which is a powerful electron-donor and tetracyanoethylene (TCNE) which is an excellent electron-acceptor. We have employed Raman spectroscopy as well as electronic spectroscopy, the former enabling us to monitor the changes with the concentration of the donor and acceptor molecules. Optical absorption spectroscopy gave clear evidence of charge transfer in these systems. We have also measured the effect of interaction of the donor and acceptor molecules on the electrical resistivity of graphene.

7.3 Experimental

7.3.1 Synthesis of graphene

Graphene samples were prepared by the exfoliation of the graphitic oxide. Graphite oxide (GO) was synthesized by employing the literature procedure (*38, 39*). Briefly, a reaction flask containing a magnetic stir bar was charged with sulfuric acid (18 ml) and fuming nitric acid (9 ml) and cooled by immersion in an ice bath. The acid mixture was stirred and allowed to cool for 20 min, and graphite microcrystals (0.5 g) were added under vigorous stirring to avoid agglomeration. After the graphite powder was well dispersed, potassium chlorate (10 g) was added slowly over 5 min to avoid sudden increase in temperature. The reaction flask was loosely capped to allow evolution of gas from the reaction mixture and allowed to stir for 120 h at room temperature. The resulting product was suction filtered and washed thoroughly with distilled water. The product was dried under vacuum for 24 hours. The graphite oxide so obtained was exfoliated in a furnace preheated to 1050 ^{o}C under argon flow for about 30s.

7.3.2 Techniques used for characterization

The number of layers in the graphene samples prepared by us was 3 to 4 as indicated by AFM. TEM images were obtained with a JEOL JEM 3010 instrument fitted with a Gatan CCD camera operating at an accelerating voltage of 300 kV. FESEM images were obtained using a FEI NOVA NANOSEM 600. AFM measurements were performed using a CP2 atomic force microscope. Raman spectra were recorded with a LabRAM HR high-resolution Raman spectrometer (Horiba-Jobin Yvon) using a He−Ne laser (λ = 632.8 nm). For Raman measurements, one milligram of the graphene sample was dispersed in 3 ml of benzene containing appropriate concentrations of electron-donor and -acceptor molecule and sonicated. The resulting solution was filtered through an anodisc filter (Anodisc 47, Whatman) with a pore size of 0.1 μm. Electronic

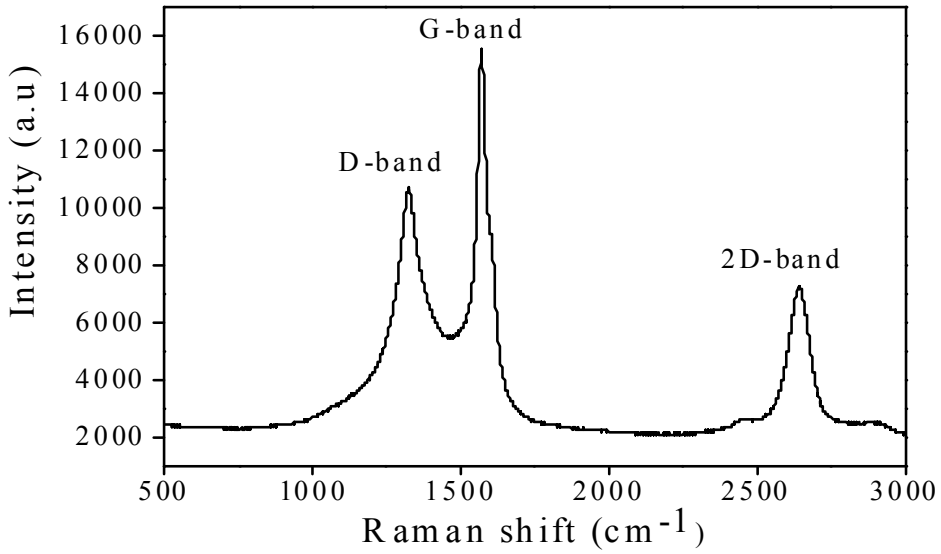

Figure 7.1: Raman spectrum of as prepared graphene prepared by exfoliation of graphite oxide.

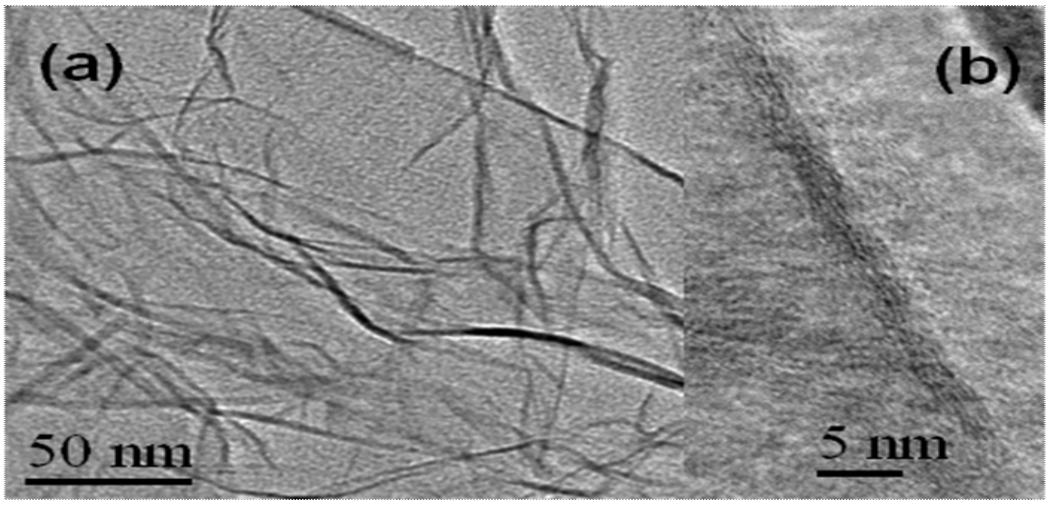

Figure 7.2: (a) TEM and (b) HR-TEM images of graphene prepared by exfoliation of graphite oxide.

absorption spectra were recorded with a Perkin–Elmer UV/VIS/NIR spectrometer. In order to study the interaction of graphene with TTF and TCNE by electronic absorption spectroscopy, the compounds were added to a suspension of graphene in spectroscopy grade acetonitrile. The suspensions were drop-coated on a quartz plate and dried. Electrical resistance measurements were carried out by drop-coating the graphene

sample on Au-gap electrodes patterned on glass substrates. The thickness of the sample was 1µm as measured from optical profiler

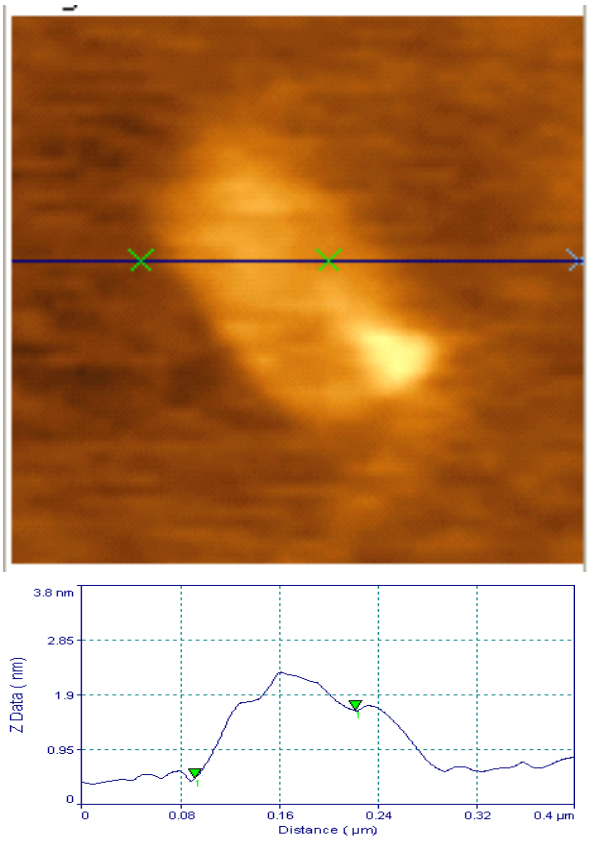

Figure 7.3: AFM image and corresponding height profile of exfoliated graphene.

7.4 Results and Discussion

We have prepared graphene by the exfoliation of graphite oxide by employing the literature procedure (*38, 39*) and characterized the samples by Raman spectroscopy (Figure 7.1), transmission electron microscopy (Figure 7.2) and atomic force microscopy (Figure 7.3) as described in the literature (*39, 40*). The number of layers in the graphene samples prepared by us was three to four. In Figure 7.4, we show the G-band of the graphene after interaction with 1 M solutions of various monosubstituted benzenes with electron-donating and -withdrawing groups. While nitrobenzene causes stiffening of the G-band or an increase in the frequency, aniline causes softening or a shift to a lower frequency. The stiffening or softening of the

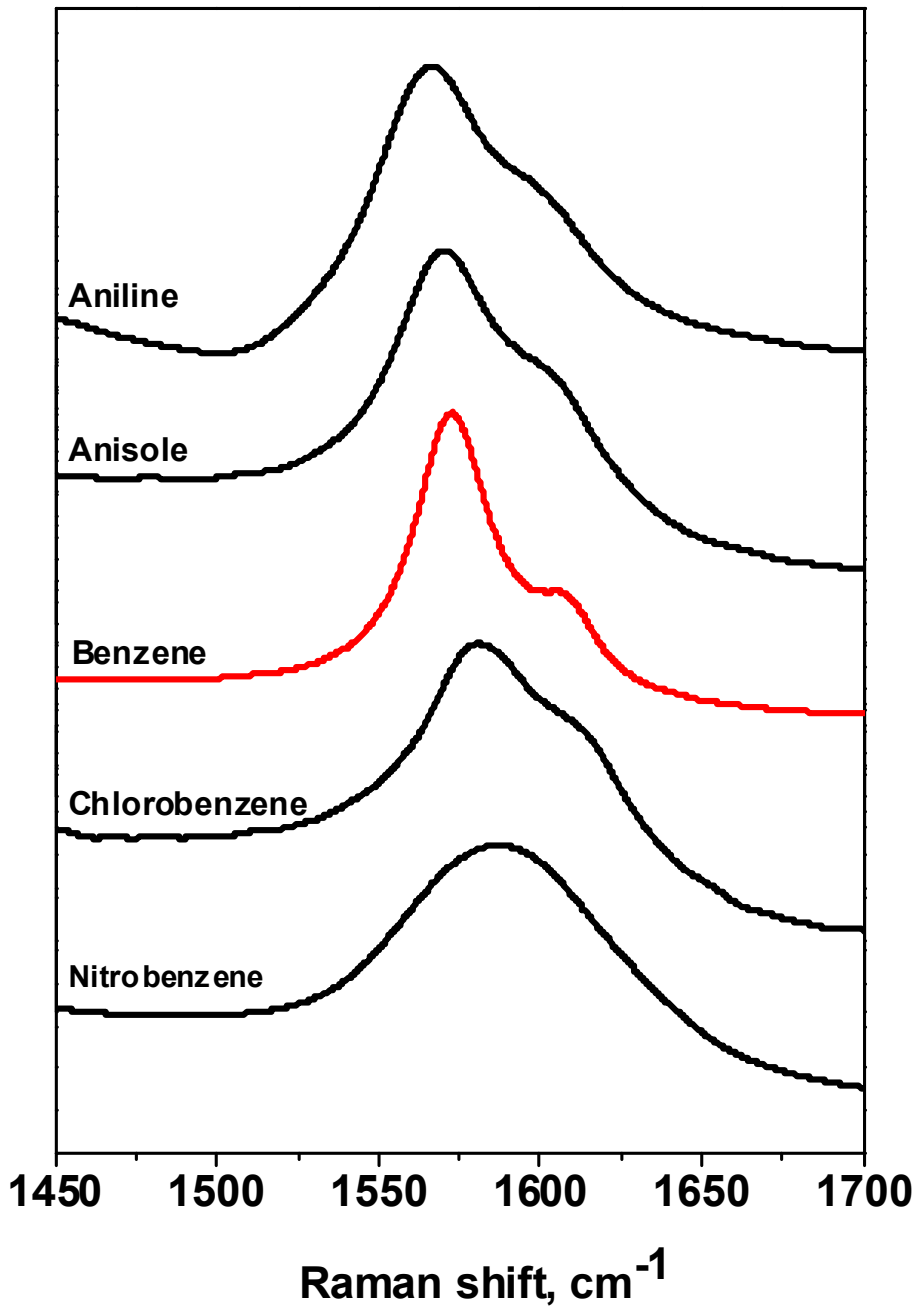

Figure 7.4: Raman shift of the G-band of graphene on interaction with 1M solutions of monosubstituted benzenes.

G-band depends on the electron-donating or -withdrawing power of the substituent on benzene. This observation is similar to that reported with SWNTs where charge-transfer to potassium, bromine and iodine is also known to cause similar shifts of the G-band (*41*). In nanotubes, n-type and p-type doping causes opposite shifts of the G-band similar to the effects of molecular charge-transfer with donor and acceptor

molecules found here. The G-band has a feature on the higher frequency side around 1607 cm^{-1} due to the defect-related G' band (*42*). We are able to deconvolute the observed G-band to get the characteristics of the G'-band. We have followed the changes in the positions and intensities of both the G and G' bands on interaction with donor and acceptor molecules.

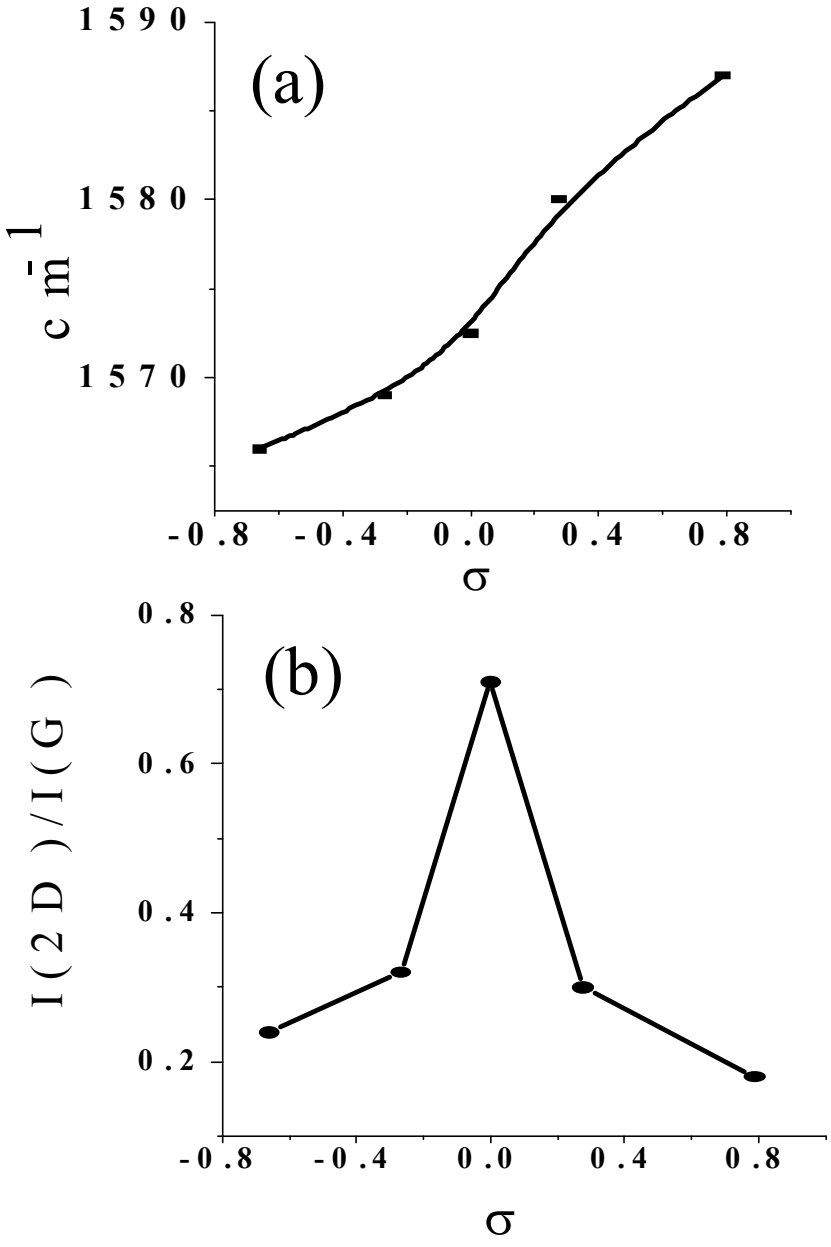

Figure 7.5: Variation of (a) the G-band frequency and (b) the ratios of intensities of the 2D and G bands (I(2D)/I(G)) against the Hammett substituent constant, σ.

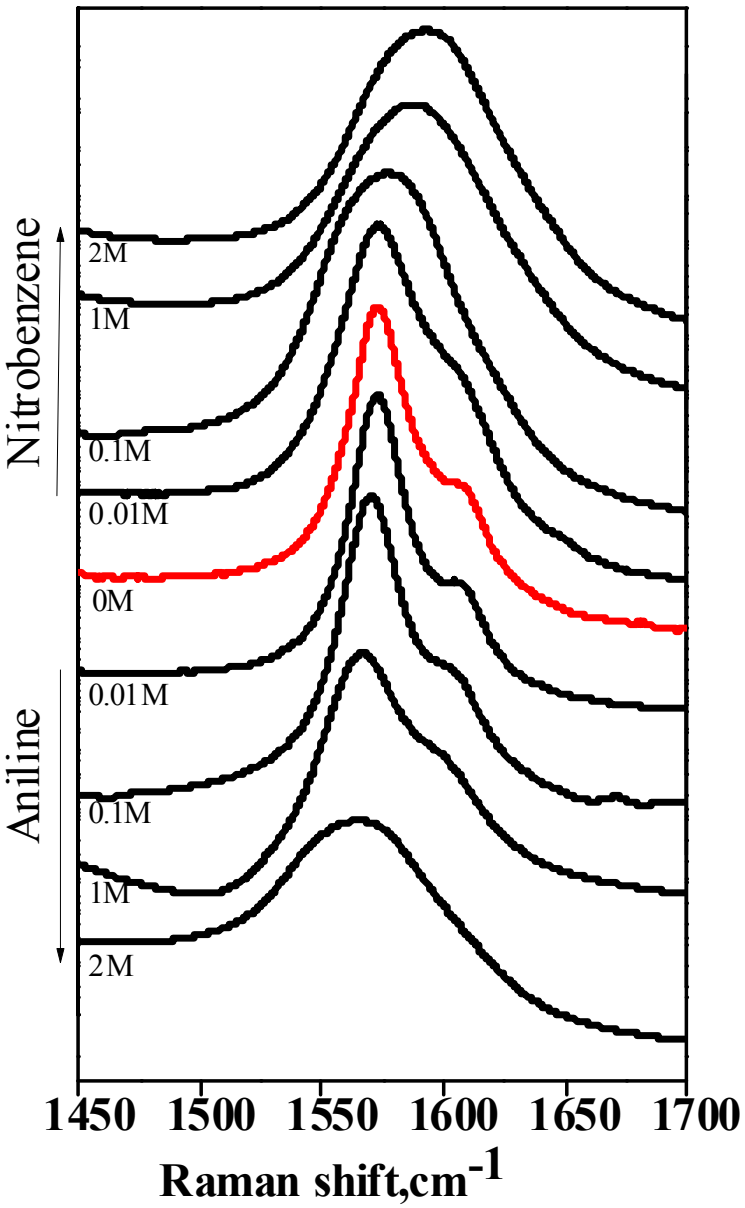

Figure 7.6: Shifts in the Raman G-band of graphene caused by interaction with varying concentrations of aniline and nitrobenzene.

In Figure 7.5 (a) we have plotted the position of the G-band maximum against the Hammett σ substituent constant to show how the frequency decreases with the decreasing electron-withdrawing power or increasing electron-donating power of the substituent. Figure 7.5 (b) we show the ratios of intensities of the 2D and G bands (I(2D)/I(G)) against the Hammett substituent constant, σ which is discussed later. Encouraged by this result, we have examined the dependence of the G-band on

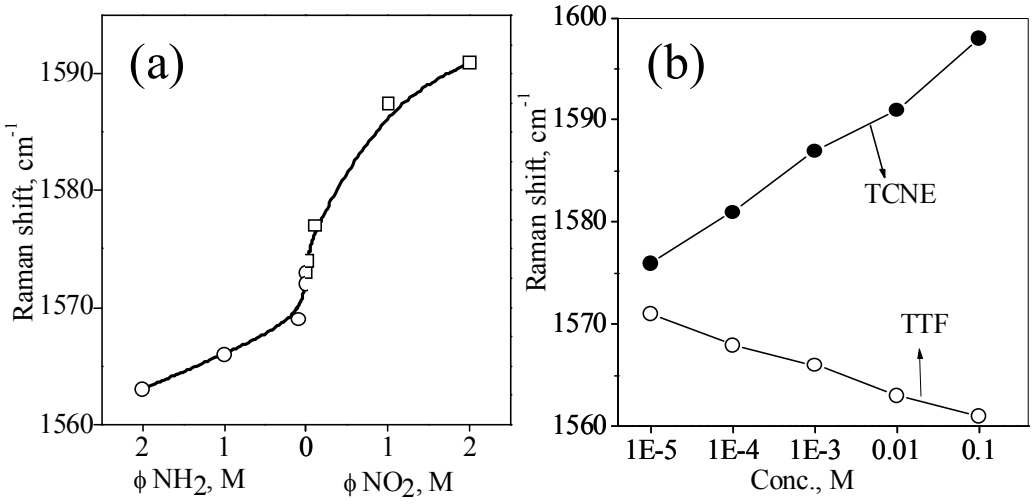

Figure 7.7: Variation in the position of graphene G-band caused by interaction with varying concentrations of (a) aniline and nitrobenzene and (b) TTF and TCNE.

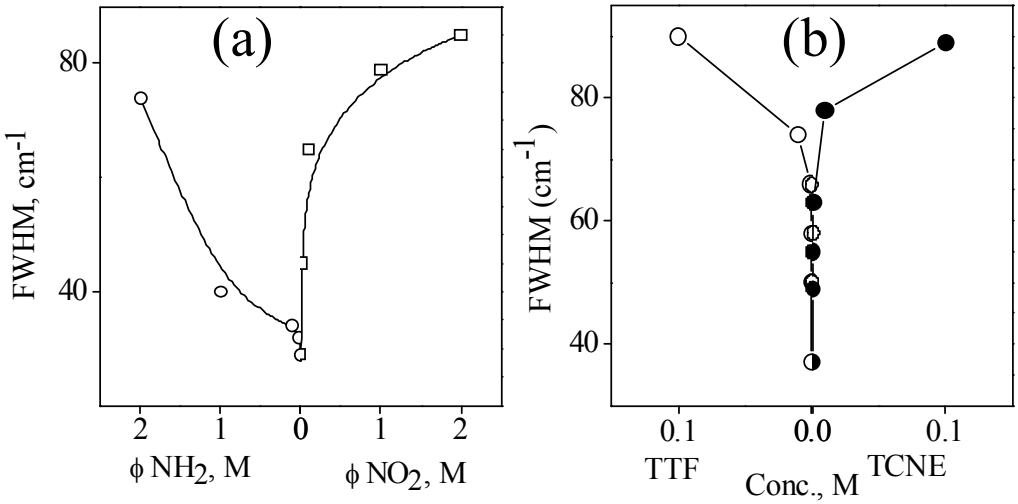

Figure 7.8: Variation in the FWHM of Raman G-band caused by interaction with varying concentrations of (a) aniline and nitrobenzene and (b) TTF and TCNE.

the concentrations of nitrobenzene and aniline in benzene solutions. Figure 7.6 shows the G-bands at different concentrations of aniline and nitrobenzene. We show the variation in the position of the G-band maximum with the concentration of aniline and nitrobenzene in Figure 7.7(a). Interaction with aniline and nitrobenzene causes shifts in the opposite directions, the magnitude of the shift increasing with the concentration. The full-width-at-half-maximum (FWHM) of the G-band

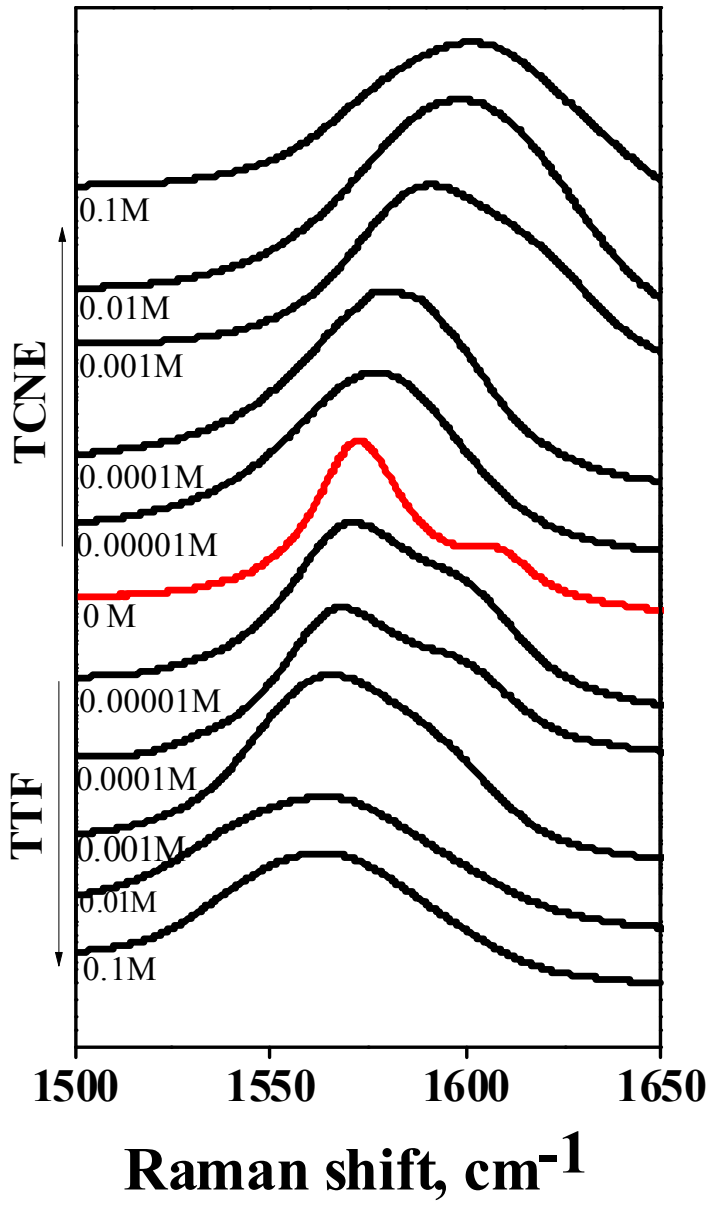

Figure 7.9: Shifts in the Raman G-band of graphene caused by interaction with varying concentrations of TTF and TCNE.

increases with the concentration of aniline and nitrobenzene, as can be seen from the Figure 7.8(a).

Encouraged by the results on monosubsituted benzenes we have studied the interaction of graphene with tetrathiafulvalene (TTF) which is a powerful electron-donor and tetracyanoethylene (TCNE) which is an excellent electron-acceptor. In Figure 7.9 we show the Raman G-band of graphene recorded after interaction with

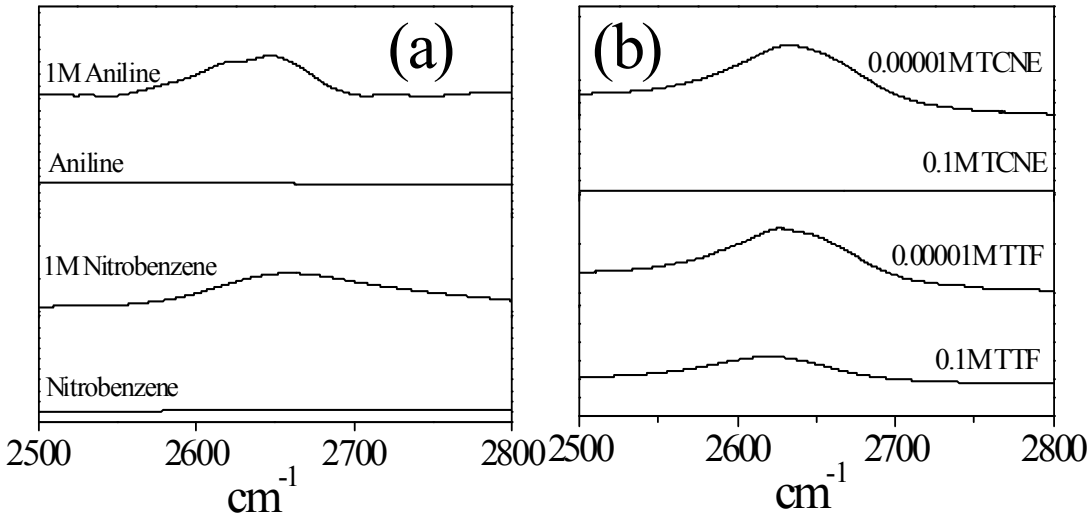

Figure 7.10: Variation in the Raman 2D-band with the concentration of (a) aniline and nitrobenzene and (b) TTF and TCNE.

varying concentrations of TTF and TCNE. We see a feature on the right-side of the G-band (~ 1570 cm^{-1}) due to the defect-related G'-band. Similar to aniline and nitrobenzene, with increase in the concentration of TTF, there is softening of the G-band, while there is stiffening of the G-band with increasing concentration of TCNE. The G-band broadens with increase in the concentration of either TTF or TCNE. In Figure 7.7 (b) we show the change in the position of the G-band maximum with the variation in concentrations of TTF and TCNE. The figure clearly shows how interaction with TTF and TCNE causes shifts in the opposite directions, the magnitude of the shift increasing with concentration. This is in contrast to the stiffening observed with electron and hole doping by electrochemical means (*17*). The FWHM of the G-band increases on interaction with both TTF and TCNE, as can be seen from Figure 7.8(b). On the other hand, the G-band sharpens on electrochemical hole or electron doping. The G'-band around 1607 cm^{-1} exhibits shifts similar to the G-band on interaction of graphene with donor and acceptor molecules, accompanied by an increase in the FWHM.

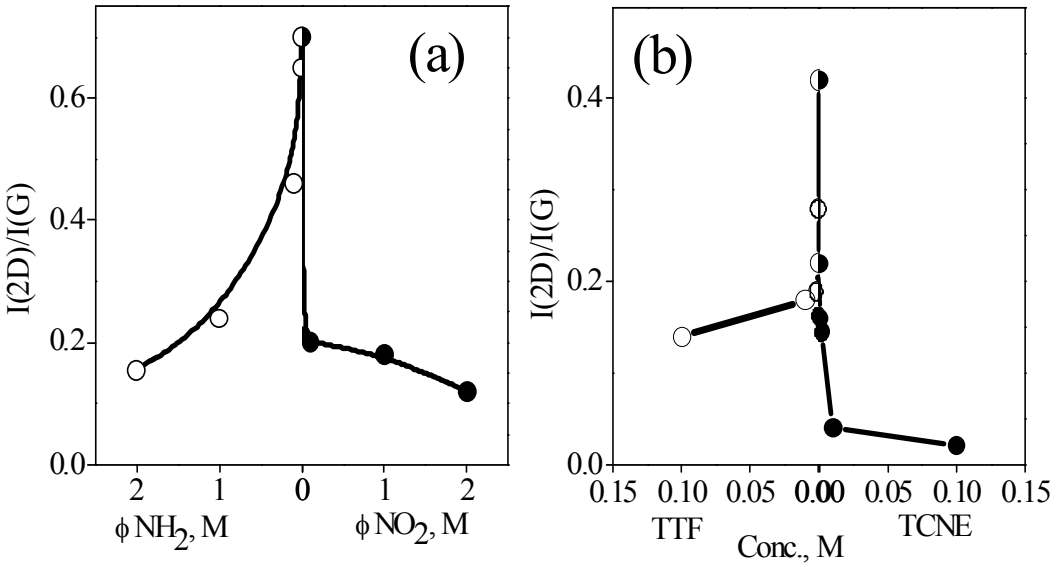

Figure 7.11: Variation in the I(2D)/I(G) ratio of the graphene Raman bands caused by interaction with varying concentration of (a) aniline and nitrobenzene and (b) TTF and TCNE.

The position of the D-band (~1320 cm^{-1}) of few layer graphene does not vary systematically on interaction with electron-donors (TTF and aniline) and –acceptors (TCNE and nitrobenzene). The position of the 2D-band, however, varies on interaction with electron-donors (TTF and aniline) and –acceptors (TCNE and nitrobenzene), the latter causing an increase in the frequency. The ratio of the intensities of 2D and G bands, (I(2D)/I(G)), is considered to be sensitive to doping. More interestingly, the intensity of the 2D-band decreases markedly on interaction with either electron-donors (TTF and aniline) or –acceptors (TCNE and nitrobenzene) as shown in Figure 7.10. The ratio of intensities of the 2D- and G-bands, (I(2D)/I(G)), decreases markedly with increasing concentration of electron-donor and -acceptor as shown in Figure 7.11. This behaviour is similar to that found in the case of electrochemical doping (*17*). The I(2D)/I(G) ratio obtained with 1M solutions of monosubstituted benzenes shows a maximum when plotted against the

Hammett σ substituent constant as shown in Figure 7.5(b), indicating that both electron-donating and -withdrawing substituents cause a decrease in the intensity ratio. The relative intensity of the D-band shows behaviour different from that of the

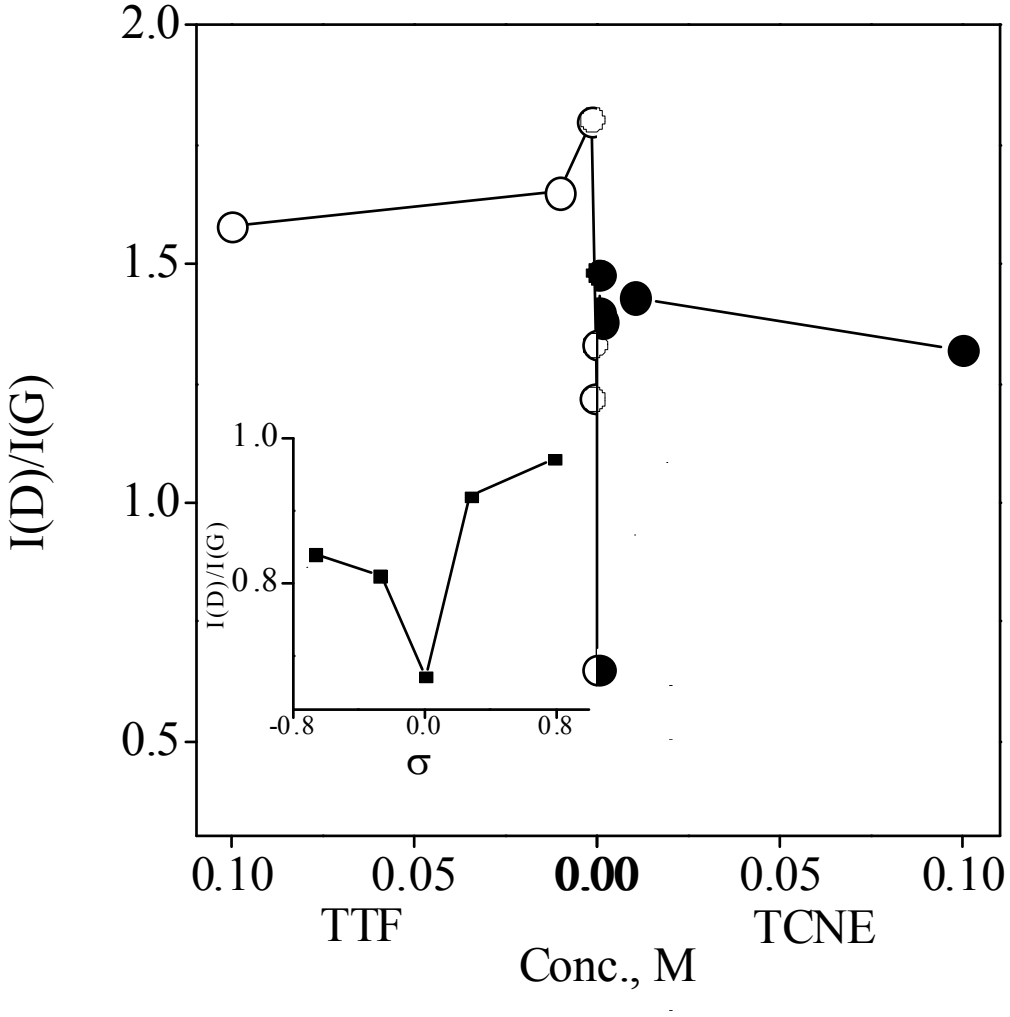

Figure 7.12: Variation in the I(D)/I(G) ratio of graphene Raman bands caused by interaction with varying concentrations of TTF and TCNE. Inset shows variations of the ratio of the D/G band intensities caused by interaction with 1M solutions of monosubstituted benzenes, against Hammett substituent constant, σ

2D-band, in that its intensity increases on interaction with donor or acceptor molecules, with the minimum value in the absence of interaction. In the Figure 7.12, we show the variation of the I(D)/I(G) intensity ratio with the concentrations of TTF and TCNE. The I(D)/I(G) ratio, shows a minimum with both the donor and acceptor molecules by increasing the ratio as shown in the inset of Figure 7.12. The above

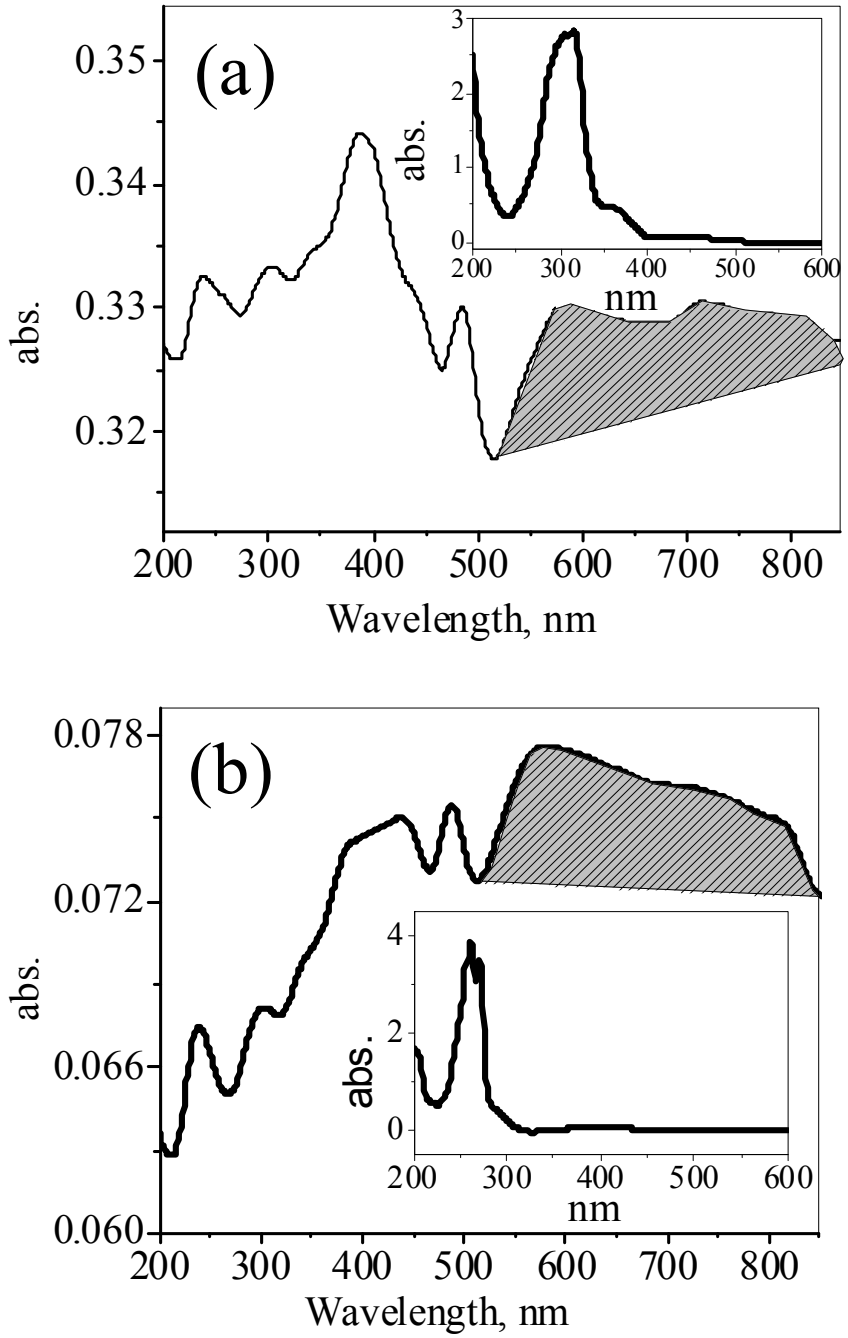

Figure 7.13: Electronic absorption spectra of (a) graphene +TTF and (b) graphene +TCNE. Inset in (a) and (b) show the spectra of TTF and TCNE respectively. The shaded regions correspond to the charge-transfer bands.

results reveal how the Raman spectrum of few-layer graphene is highly sensitive to charge-transfer from electron-donor and -acceptor molecules. Besides showing how the different Raman bands (G, D and 2D) exhibit different sensitivities to interaction with electron-donor and -acceptor molecules, the present study shows significant

differences between electrochemical doping and doping by molecular charge-transfer. The difference between the sensitivities of the D- and the 2D- bands is likely to be because of the nature of origin of these bands as discussed later.

Since we consider the interaction between graphene and TTF and TCNE to be due to molecular charge-transfer, we have examined the UV-visible absorption spectra of graphene with the varying concentration of TTF and TCNE to look for possible evidence for charge transfer. TTF has a strong absorption band in the region of 305 to 316 nm, a shoulder at 361 nm and a broad band around 445 nm. The charge-transfer band of TTF with aromatics is in the 400-700 nm region (*43*). We find a broad band in the 500-800 nm region in the TTF-graphene system as shown in Figure 7.13 (a). TCNE has a strong absorption band in the 250-270 nm region, while the charge transfer band of TCNE with aromatics is in the 550-750 nm region (*44, 45*). On interaction of TCNE with graphene, we observe a broad charge-transfer band between 520 and 800 nm (Figure 7.13 (b)). In addition, bands possibly due to radical anions of TCNE seem to appear (*45*).

In Figure 7.14 (a) we show the I-V characteristics of the graphene films after treatment with 1M solutions of monosubstituted benzenes. The I-V characteristics remain linear showing metallic behaviour. The resistance itself is lowest in the presence of nitrobenzene and highest in the presence of aniline. There is a systematic dependence of resistance with the electron-donating and -withdrawing power of the substituents. The value of resistance varies with the concentration of aniline and nitrobenzene as shown in Figure 7.14 (b). At a bias voltage of 0.5 V, the resistance of the graphene is ~1.0 kΩ. The resistance increases linearly with increasing aniline concentration, while it decreases abruptly at low concentrations of nitrobenzene. Thus, hole-doping brought about by interaction with nitrobenzene has a marked effect even at low concentrations.

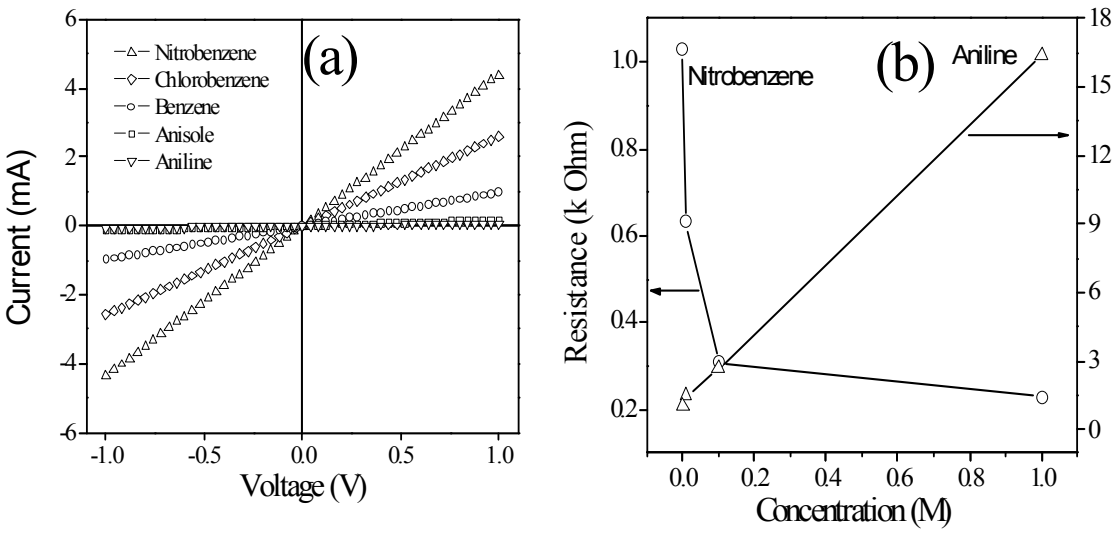

Figure 7.14: (a) I-V characteristics of the graphene in the presence of benzene and 1 M solutions of nitrobenzene, chlorobenzene, anisole and aniline in benzene (b) Variation of the resistance with the concentration of nitrobenzene and aniline at a bias voltage of 0.5 V.

Similarly, we have measured the I-V characteristics of graphene after interaction with different concentrations of TTF and TCNE (Figure 7.15). The I-V plot always remains linear, but the slope decreases with increasing concentration of TTF and increases with the increase in the concentration of TCNE. Thus, the resistance increases with increasing TTF concentration, and decreases with increasing TCNE concentration. The variation of resistance with the concentration of TTF and TCNE is shown in the inset of Figure 7.15 (a), reflecting the dependence of resistance on carrier concentration

The above results clearly demonstrate the extra-ordinary sensitivity of the Raman bands of few-layer graphene to molecular charge-transfer and also significant differences in the sensitivities of the different Raman bands to doping by charge-transfer. This is clearly reflection of the differences in the effects of the electronic structure and electron-phonon interaction and many of the results can be understood on the basis of following considerations (*42*). The G-band is a doubly degenerate phonon

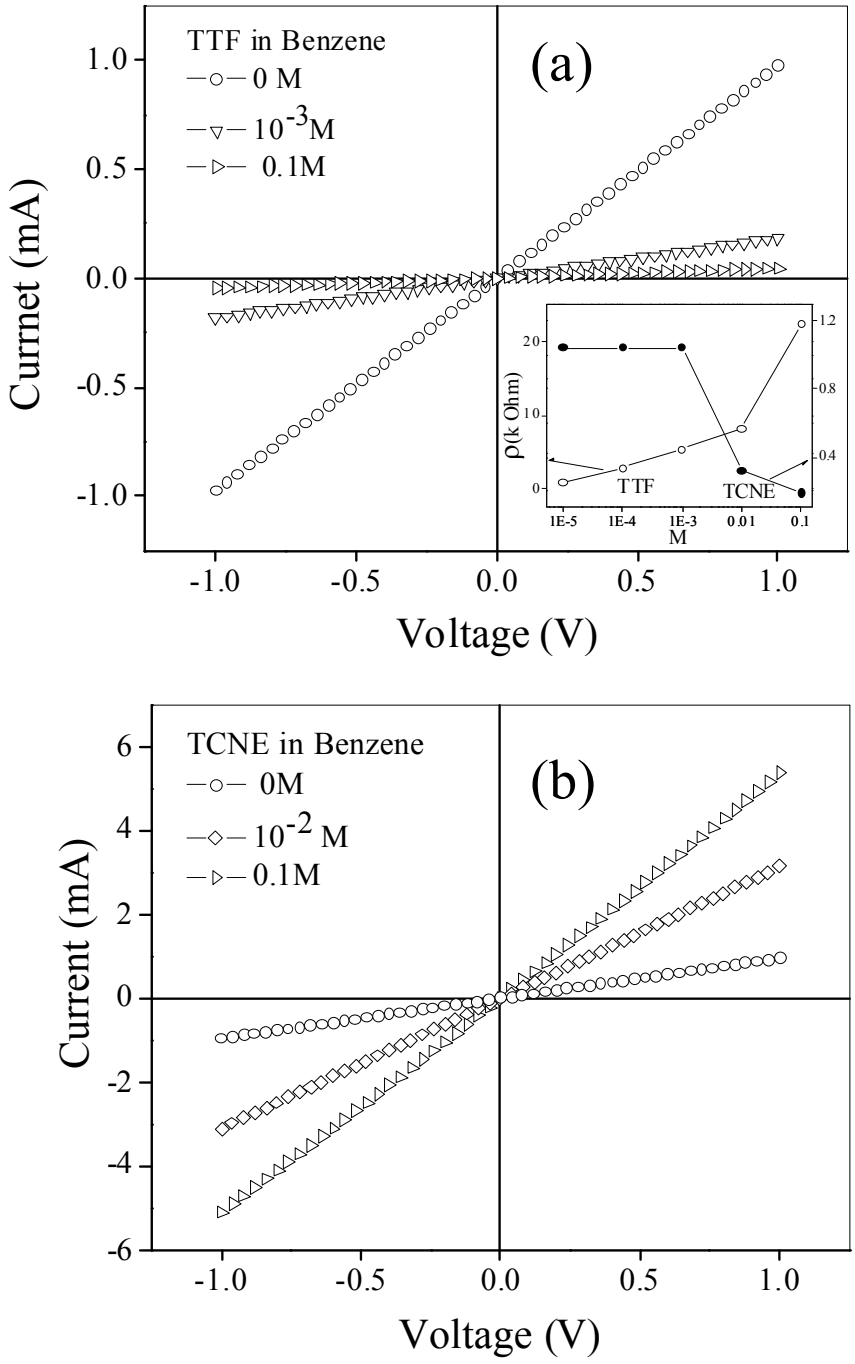

Figure 7.15: I-V characteristics of graphene on interaction with different concentrations (M) of (a) TTF and (b) TCNE. Inset in (a) shows the variation in the resistance, ρ, with the concentration of TTF and TCNE at a bias voltage of 0.5 V.

mode (E_{2g}) at BZ center of the sp^2 carbon network. It is truly characteristic of the sp^2 framework. The electron-phonon coupling in graphene causes Kohn anomalies in the phonon dispersions which can give rise to phonon softening (*46, 47*). Stiffening of the G-band arises from the non-adiabatic removal of the Kohn anomaly at the Γ point (*48*)

The band broadening suggests the absence of blockage of the decay channels of the phonons into electron-hole pairs in the present situation. The D and 2D bands originate from a double resonance Raman process. The D band couples preferentially to the electronic states with wave vector k such that 2q=k (*49*). It appears that an internally double resonance process involving electronic states around two ineqvivalent K points is responsible for this band. The scattering events involving defects occur in the case of the D band, both processes are inelastic involving phonons in the case of the 2D band (*42*). This high intensity and other features of the 2D band may be because of a triple-resonant process arising from processes involving both electrons and holes (*49*).

Recent experimental results have shown that the magnitude of interaction between graphene and donor/acceptor molecules seems to depend on the surface area of the graphene sample (*50*). More importantly isothermal titration calorimetry (ITC) measurements show that the interaction energies of graphene with electron-acceptor molecules are higher than those with -donor molecules (*51*). DFT calculations confirm the occurrence of charge-transfer induced changes in graphene giving rise to mid-gap molecular levels with tuning of band gap region near the Dirac point and show how they are different from the effects of electrochemical doping (*52, 53*). It has been shown that n-type and p-type graphenes result from charge-transfer interaction of graphene with donor and acceptor molecules respectively. It is also predicted that the extent doping depends on the coverage of organic molecules. Synchrotron-based high-resolution photoemission spectroscopy studies reveal that charge transfer from graphene to adsorbed F_4-TCNQ is responsible for the p-type doping of graphene (*54*). Recent studies of the core-level spectra of the dopant molecules (TTF and TCNE) provide direct evidence for charge transfer involving graphene (*55*).

It is interesting to compare the effects of doping graphene by gating (*17*) or chemical doping (*56*) with those caused by molecular charge-transfer. The G-band is shifted to

higher frequencies when an electron acceptor molecule is adsorbed on graphene, while it is shifted to lower frequencies when an electron donor molecule is adsorbed. This is in contrast to the gate-induced or chemical doping, where the G-band increases in frequency for both the electron and hole doping.

7.5 Conclusions

In conclusion, the present study demonstrates how the electronic structure and phonons of graphene are markedly affected by interaction with electron-donor and -acceptor molecules. It is significant that we observe such marked effects due to molecular charge-transfer even with multi-layered graphene of 3-4 layers. These effects would be expected to be prominent in single-layered graphene as well. Comparing our results with those reported for electrochemically doped single-layer graphene, it appears that only static contributions are involved in the spectral changes observed by us. Dynamic contributions may become negligible due to the defects in multilayered graphene. It is noteworthy that the results reported here are consistent with the changes in the G-band of nanographite caused by interaction with potassium and halogens.

The magnitude of changes in the Raman spectra found here is quite large and is comparable to that found with electrochemical doping (*17*). The G, D and 2D bands show different sensitivities to molecular charge-transfer, the 2D/G intensity ratio providing a probe to determine the magnitude of doping through charge-transfer. The changes in the Raman spectra brought about by the interaction of few-layer graphene with electron-donor and –acceptor molecules differ to some extent from those observed on electrochemical doping of graphene.

REFERENCES

1. A. K. Geim, K. S. Novoselov, *Nat. Mater.* **6**, 183 (2007).
2. C. N. R. Rao, A. K. Sood, K. S. Subrahmanyam, A. Govindaraj, *Angew. Chem. Int. Ed* **48**, 7752 (2009).
3. M. J. Allen, V. C. Tung, R. B. Kaner, *Chem. Rev.*, DOI: 10.1021/cr900070d (2009).
4. A. K. Geim, *Science* **324**, 1530 (2009).
5. J. C. Meyer *et al.*, *Nano Lett.* **8**, 3582 (2008).
6. S. Stankovich *et al.*, *Nature* **442**, 282 (2006).
7. K. S. Novoselov *et al.*, *Science* **306**, 666 (2004).
8. J. C. Meyer *et al.*, *Nature* **446**, 60 (2007).
9. K. S. Novoselov *et al.*, *Nature* **438**, 197 (2005).
10. K. S. Novoselov *et al.*, *Proc. Natl. Acad. Sci. U.S.A.* **102**, 10451 (2005).
11. Y. Zhang, Y.-W. Tan, H. L. Stormer, P. Kim, *Nature* **438**, 201 (2005).
12. C.-H. Park, L. Yang, Y.-W. Son, M. L. Cohen, S. G. Louie, *Nat. Phys.* **4**, 213 (2008).
13. S. Y. Zhou *et al.*, *Nat. Mater.* **6**, 770 (2007).
14. J. H. Chen *et al.*, *Nat. Phys.* **4**, 377 (2008).
15. T. O. Wehling *et al.*, *Nano Lett.* **8**, 173 (2007).
16. A. C. Ferrari *et al.*, *Phys. Rev. Lett.* **97**, 187401 (2006).
17. A. Das *et al.*, *Nat. Nanotechnol.* **3**, 210 (2008).
18. A. Das *et al.*, *Phys. Rev. B* **79**, 155417 (2009).
19. L. M. Malard, D. C. Elias, E. S. Alves, M. A. Pimenta, *Phys. Rev. Lett.* **101**, 257401 (2008).
20. A. B. Kuzmenko *et al.*, *Phys. Rev. Lett.* **103**, 116804 (2009).
21. C. Lee, X. Wei, J. W. Kysar, J. Hone, *Science* **321**, 385 (2008).
22. X. Wang *et al.*, *Science* **324**, 768 (2009).
23. F. Schedin *et al.*, *Nat. Mater.* **6**, 652 (2007).
24. A. Ghosh, K. V. Rao, S. J. George, C. N. R. Rao, *Chem. European J.* **16**, 2700 (2010).
25. J. Kim, L. J. Cote, F. Kim, J. Huang, *J. Am. Chem. Soc.* **132**, 260 (2009).
26. L. Xie, X. Ling, Y. Fang, J. Zhang, Z. Liu, *J. Am. Chem. Soc.* **131**, 9890 (2009).
27. D. C. Elias *et al.*, *Science* **323**, 610 (2009).

28. T. Ohta, A. Bostwick, T. Seyller, K. Horn, E. Rotenberg, *Science* **313**, 951 (2006).
29. E. V. Castro *et al.*, *Phys. Rev. Lett.* **99**, 216802 (2007).
30. J. B. Oostinga, H. B. Heersche, X. Liu, A. F. Morpurgo, L. M. K. Vandersypen, *Nat. Mater.* **7**, 151 (2008).
31. Y. Zhang *et al.*, *Nature* **459**, 820 (2009).
32. K. F. Mak, C. H. Lui, J. Shan, T. F. Heinz, *Phys. Rev. Lett.* **102**, 256405 (2009).
33. H. Min, B. Sahu, S. K. Banerjee, A. H. MacDonald, *Phys. Rev. B* **75**, 155115 (2007).
34. L. Liu, Z. Shen, *App. Phys. Lett.* **95**, 252104 (2009).
35. X. Peng, R. Ahuja, *Nano Lett.* **8**, 4464 (2008).
36. G. Giovannetti, P. A. Khomyakov, G. Brocks, P. J. Kelly, J. van den Brink, *Phys. Rev. B* **76**, 073103 (2007).
37. J. Berashevich, T. Chakraborty, *Phys. Rev. B* **80**, 033404 (2009).
38. H. C. Schniepp *et al.*, *J. Phys. Chem. B* **110**, 8535 (2006).
39. K. S. Subrahmanyam, S. R. C. Vivekchand, A. Govindaraj, C. N. R. Rao, *J. Mater. Chem.* **18**, 1517 (2008).
40. A. Ghosh *et al.*, *J. Phys. Chem. C* **112**, 15704 (2008).
41. A. M. Rao, P. C. Eklund, S. Bandow, A. Thess, R. E. Smalley, *Nature* **388**, 257 (1997).
42. M. A. Pimenta *et al.*, *Pys. Chem. Chem. Phys.* **9**, 1276 (2007).
43. M. R. Bryce, *Adv. Mat.* **11**, 11 (1999).
44. M.-S. Liao, Y. Lu, V. D. Parker, S. Scheiner, *J. Phys. Chem. A* **107**, 8939 (2003).
45. H. Hartmann, B. Sarkar, W. Kaim, J. Fiedler, *J. Organomet. Chem.* **687**, 100 (2003).
46. S. Piscanec, M. Lazzeri, J. Robertson, A. C. Ferrari, F. Mauri, *Phys. Rev. B* **75**, 035427 (2007).
47. M. Lazzeri, S. Piscanec, F. Mauri, A. C. Ferrari, J. Robertson, *Phys. Rev. B* **73**, 155426 (2006).
48. S. Pisana *et al.*, *Nat. Mater.* **6**, 198 (2007).
49. R. Saito *et al.*, *Phys. Rev. Lett.* **88**, 027401 (2001).
50. K. S. Subrahmanyam, R. Voggu, A. Govindaraj, C. N. R. Rao, *Chem. Phys. Lett.* **472**, 96 (2009).

51. N. Varghese, A. Ghosh, R. Voggu, S. Ghosh, C. N. R. Rao, *J. Phys. Chem. C* **113**, 16855 (2009).

52. A. K. Manna, S. K. Pati, *Chem. Asian J.* **4**, 855 (2009).

53. S. K. Saha, R. C. Chandrakanth, H. R. Krishnamurthy, U. V. Waghmare, *Phys. Rev. B* **80**, 155414 (2009).

54. W. Chen, S. Chen, D. C. Qi, X. Y. Gao, A. T. S. Wee, *J. Am. Chem. Soc.* **129**, 10418 (2007).

55. D. Choudhury, B. Das, C. N. R. Rao, D. D. Sarma, *To be published*.

56. L. S. Panchakarla *et al.*, *Adv. Mat.* **21**, 4726 (2009).